



**Numerical investigation of homogeneous
expansion and lateral solid mixing in
gas-fluidized beds**

Oyebanjo Stephen Oke

Department of Chemical Engineering

University College London

A thesis submitted for the degree of
Doctor of Philosophy of University College London
March 2016

I, Oyebanjo Oke, confirm that the work presented in this thesis is my own. Where information has been derived from other sources, I confirm that this has been indicated in the thesis.

To Ifedolapo

But there is a spirit in man, and the breath of the Almighty gives him understanding.

(Job 32:8)

Abstract

This research project is concerned with the numerical investigation of the behaviour of homogeneous and bubbling gas-fluidized beds. We started by investigating the homogeneous expansion of gas-fluidized beds using the Richardson & Zaki (1954) equation. We modelled the stable expansion of gas-fluidized beds of different diameter, accounting for enduring contacts among particles and wall effects. We solved the model numerically to obtain the bed expansion profiles, back-calculating from them the values of the expansion parameter n . To validate our model, we carried out fluidization and defluidization experiments, analyzing the results by means of the Richardson & Zaki equation. We obtained a reasonable agreement between numerical and experimental findings; this suggests that enduring contacts among particles, which are manifestations of cohesiveness, affect homogeneous bed expansion. The results showed that homogeneous gas-fluidized beds do not consist of particles floating freely; rather they are made up of particles in sustained frictional contacts.

We then investigated the process of lateral solid mixing in bubbling fluidized beds, adopting the Eulerian-Eulerian modeling approach. To quantify the rate at which solids mix laterally, we used a lateral dispersion coefficient (D_{sr}). The values of D_{sr} obtained numerically are larger than the experimental ones, within the same order of magnitude. The overestimation has a twofold explanation. On one side, it reflects the different dimensionality of simulations (2D) as compared with real fluidized beds (3D), which affects the degrees of freedom of particle lateral motion. On the other, it relates to the way frictional solid stress was modelled. To investigate how sensitive the numerical results are on the constitutive model adopted for the frictional stress, we ran the simulations again using different frictional models and changing the solid volume fraction at which the bed is assumed to enter the frictional flow regime (ϕ_{min}). We observed that D_{sr} is quite sensitive to the latter. The results show that accurate prediction of lateral solid dispersion depends on adequate understanding of the frictional flow regime, and accurate modelling of the frictional stress which characterizes it.

We further examined the influence of simulation dimensionality in numerical results. We ran 3D CFD simulations using the same powder, the same operational conditions and the same computational setup as in the previous 2D simulations. The 3D simulations predicted D_{sr} more accurately than the 2D simulations, the simulation dimensionality appearing to be an important factor. To analyse further the role of frictional stress models, we ran 3D DEM simulations. The simulation results agreed reasonably well with the empirical data, but their accuracy depended on the values used for the collision parameters; also, the 3D CFD simulations matched the empirical data more closely. Altogether, we thus concluded that the simulation dimensionality plays a dominant role in predicting D_{sr} accurately.

Aknowledgements

My profound gratitude goes to Dr Luca Mazzei for his support throughout this PhD project. I would like to say thank you for giving me the privilege to work with you during my master's programme; this is where I drew my strength and motivation to carry out research in multiphase flows. I am sincerely grateful for all you taught me and your constant advice to think critically and logically. Indeed, I would say that you have made a significant contribution to my personal and professional development.

I would also like to thank Professor Paola Lettieri for her advice and suggestions during my PhD. I am particularly thankful for her support in setting up my fluidization experiments and the x-ray machine.

My heartfelt gratitude goes to Clara Vascello and Massimiliano Materazzi for their support and encouragement. I am especially thankful to them for their assistance and patience while working for long hours in the Lab.

A special thanks to Pastor Frank Oyibo and his wife, and indeed to all members of Deeper Life Bible Church, Borough Region, for their moral and spiritual support throughout my studies at UCL. Your contribution to the successful completion of my PhD is very substantial. Thank you so much for always being there.

My warmest and heartfelt thanks to Mr & Mrs I.O. Awopegba for their constant love and care. Your prayers and words of encouragement were very valuable and comforting. Thank you so much for being so dependable.

My sincere gratitude to my fellow PhD colleagues and Erasmus students: Carla, Luigi, Marco, Sara, Alex, Shane, Olga, Max, Sri, Andrea and Marianna. You all made my stay in UCL exciting and fun.

I would like to also acknowledge the financial support of UCL graduate school.

I am greatly indebted to my family for their love and care, and constant source of encouragement throughout my entire life. Especially, I would like to appreciate Ifedolapo, my wife, for her true and matchless love. She is indeed a true companion and a dependable friend. I am very grateful also to our son, Dara, for your patience and understanding when Daddy had little time to play and read with you.

Finally, my heartfelt gratitude goes to Jesus Christ, the giver of life, whose enduring mercies saw me through the challenges of this PhD, and who is my hope and strength for the days to come.

Notation

Units are expressed using the SI system. Some symbols used infrequently are not listed, but are defined where they first appear in the text.

a	positive constant	-
a_i	linear acceleration of particle i	m/s^2
b	positive constant	-
B_n	granular bond number	-
c	positive constant	-
C	void-free solid concentration	kg/m^3
C_e	experimental void-free solid concentration	kg/m^3
C_D^*	drag coefficient	-
C_D	drag coefficient	-
D	vessel diameter	m
d_p	particle diameter	m
d_b	bubble diameter	m
D_f	averaged rate of deformation tensor of the fluid	1/s
D_i	averaged rate of deformation tensor of the i th particle phase	1/s
D_{sa}	axial dispersion coefficient	m^2/s
D_{sr}	lateral dispersion coefficient	m^2/s
E_i	elastic modulus of particle i	N/m^2
E_w	elastic modulus of the wall	N/m^2
f	interaction force per unit particle	N
f_i^s	averaged buoyancy force	N

Notation

f_i^d	averaged drag force	N
$F_{c,i}$	total contact force	N
$F_{ext,i}$	total external force	N
$F_{s,i}$	sum of other particle-particle forces	N
F_{ij}	contact force exerted by particle j on particle i	N
$F_{g,i}$	gravitational force on particle i	N
$F_{d,i}$	drag force on particle i	N
$F_{p,i}$	pressure forces on particle i	N
F_r	Froude number	-
g	gravitational acceleration	m ² /s
G_i	shear modulus of particle i	N/m ²
h_{mf}	bed height at minimum fluidization	m
H_o	initial bed height	m
H	bed height	m
I_j	moment of inertia of particle j	kg.m ²
I_i	moment of inertia of particle i	kg.m ²
j	janssen coefficient	-
J	impulse	N.s
k	ratio of aggregate size to particle size	-
k_c	particle cohesion coefficient	N/m ²
K_t	tangential spring constant	N/m ^{3/2}
K_n	normal spring constant	N/m ^{3/2}
m	total mass of particle	kg
n	Richardson & Zaki exponent	-
n^*	experimental Richardson & Zaki exponent	-
n_{ij}	normal unit vector	-
N	number of particles per aggregates	-

Notation

n_p	number of particles per unit volume	m^{-3}
p_s	total solid pressure	N/m^2
p_i	averaged pressure of particle phase i	N/m^2
p_i^f	frictional pressure of the i th particle phase	N/m^2
p_i^v	pressure of the i th particle phase in the viscous regime	N/m^2
p_f	averaged fluid pressure	N/m^2
Q_{mf}	minimum fluidization flow rate	m^3/s
Q_{mb}	minimum bubbling flow rate	m^3/s
\mathbf{r}_i	position vector of particle i	-
\mathbf{r}_j	position vector of particle j	-
Re_t	terminal Reynolds's number	-
Re_p	particle Reynold's number	-
\mathbf{S}_f	averaged fluid stress tensor	N/m^2
\mathbf{S}_p	averaged particle stress tensor	N/m^2
\mathbf{S}_i	averaged stress tensor of particle phase i	N/m^2
t	time	s
\mathbf{t}_{ij}	tangential unit vector	-
\mathbf{T}_i	torque on particle i	N.m
u	superficial fluid velocity	m/s
\mathbf{u}_i	averaged velocity of particle i	m/s
\mathbf{u}_f	averaged fluid velocity	m/s
\mathbf{u}_p	averaged particle velocity	m/s
u_{mf}	minimum fluidization velocity	m/s
u_{mb}	minimum bubbling velocity	m/s
u_e	kinematic wave velocity	m/s
u_ε	dynamic wave velocity	m/s
u_t	particle terminal velocity	m/s

Notation

u_t^*	experimental terminal velocity	m/s
u_a	terminal settling velocity of aggregates	m/s
v_j	linear velocity of particle j before collision	m/s
v_j'	linear velocity of particle j after collision	m/s
v_{ij}	linear velocity of i relative to j before collision	m/s
V_L	volume of vertical layer	m^3

Greek Symbols

α_i	angular acceleration of particle i	rad/s^2
β	coefficient of tangential friction	-
δ	bubble fraction	-
ε	fluid volume fraction	-
ε_{mf}	bed voidage at minimum fluidization	-
ε_{mb}	bed voidage at minimum bubbling	-
η_t	tangential damping coefficient	N.s/m
η_n	normal damping coefficient	N.s/m
Θ_i	granular temperature of the i th particle phase	m^2/s^2
κ_f	dilatational fluid viscosity	kg/(m.s)
κ_i	dilatational viscosity of i th particle phase	kg/(m.s)
μ	friction coefficient	-
μ_f	fluid viscosity	kg/(m.s)
μ_i	viscosity of particle phase i	kg/(m.s)
μ_s	solid viscosity	kg/(m.s)
μ_i^v	viscosity of the i th particle phase in the viscous regime	kg/(m.s)
μ_i^f	frictional viscosity of the i th particle phase	kg/(m.s)
ρ_f	fluid density	kg/m^3
ρ_p	particle density	kg/m^3

Notation

ρ_{PL}	bulk density obtained under loose packing	kg/m ³
ρ_{LP}	bulk density obtained under prolonged packing	kg/m ³
σ_i	poisson ratio of particle i	-
ϕ	solid volume fraction	-
ϕ_a	volume fraction of aggregates	-
ϕ_{min}	solid volume fraction at which enduring contacts vanish	-
ϕ_{max}	maximum value of solid volume fraction	-
$\bar{\phi}$	average solid volume fraction	-
ω_j	angular velocity of particle i before collision	rad/s
ω_i	angular velocity of particle j before collision	rad/s

Table of Contents

1.0 General Introduction	1
1.1 An introduction to fluidization.....	1
1.2 The phenomenon of fluidization	4
1.3 Computational modelling of fluidized suspensions	8
1.4 Computational fluid dynamic codes	11
1.5 Research questions	12
1.6 Research objectives	13
1.7 Thesis outline	14
2.0 The stability of gas-fluidized beds	15
2.1 Introduction.....	15
2.2 Interparticle forces in fluidized beds.....	20
2.2.1 <i>Van der Waals forces</i>	20
2.2.2 <i>Electrostatic forces</i>	21
2.2.3 <i>Capillary forces</i>	21
2.3 Solid-like behaviour of Geldart A gas-fluidized beds.....	23
2.4 Fluid-like behaviour of particles fluidized by liquids	31
2.5 Fluid-like behaviour of fine particles fluidized by gas	36
2.5.1 Fluidization assisting methods	36
2.6 Conclusions.....	42

3.0 Theoretical and experimental investigation of the behaviour of homogeneous gas-fluidized beds	44
3.1 Introduction.....	45
3.2 The Richardson & Zaki (1954) equation and homogeneous expansion of gas-fluidized beds	45
3.3 The processes of fluidization and defluidization of fine particles	50
3.4 Theoretical analysis	53
3.5 Experimental	59
3.5.1 Powder preparations.....	59
3.5.2 Fluidization and defluidization experiments.....	62
3.5.3 Determination of the powder compressive yield stress.....	64
3.6 Results and discussion	69
3.7 Solid volume fraction profiles.....	74
3.8 Richardson & Zaki equation and homogeneous expansion in gas-fluidized beds	77
3.9 Conclusions.....	81
4.0 Literature review on solid mixing in gas-fluidized beds.....	82
4.1 Introduction.....	83
4.2 The mechanism of solid mixing in gas-fluidized beds.....	85
4.3 Axial and lateral solid mixing in gas-fluidized beds.....	87
4.4 Estimating lateral dispersion coefficients in gas-fluidized beds	94
4.5 Conclusions.....	101
5.0 2D CFD simulations of lateral solid mixing in gas-fluidized beds.....	103
5.1 Introduction.....	104
5.2 Lateral dispersion coefficient – Definition and estimation	104
5.3 Multiphase fluid dynamic model	109
5.3.1 Fluid-particle interaction forces	110
5.3.2 Particle-particle interaction force.....	111
5.3.3 Effective stress	111
5.4 Boundary and initial conditions	115
5.5 Results.....	115
5.5.1 Effect of superficial gas velocity	119
5.5.2 Effect of bed height.....	123
5.5.3 Effect of bed width.....	126

Table of contents

5.6 Discussion.....	128
5.7 Influence of hydrodynamic models.....	129
5.8 Effect of simulation dimensionality.....	142
5.9 Conclusions.....	143
6.0 3D numerical simulations of lateral solid mixing in gas-fluidized beds: CFD and DEM studies	145
6.1 Introduction.....	146
6.2 2D versus 3D simulations of gas-fluidized beds.....	147
6.2.1 Results and discussion on 3D Eulerian-Eulerian simulations.....	150
6.3 Eulerian-Lagrangian (DEM) Simulations	158
6.3.1 Hard-sphere approach	158
6.3.2 Soft-sphere Model.....	161
6.3.3 Comparison between hard-sphere and soft-sphere approaches.....	168
6.3.4 DEM simulation results and discussion	169
6.4 DEM vs. CFD simulations.....	178
6.5 Conclusions.....	180
7.0 Conclusions and future work	181
7.1 Future work.....	186
APPENDIX A: Setting up Eulerian-Lagrangian simulations.....	188
A.1 Preliminaries	188
A.2 Setting up simulations.....	189
A.3 Visualization and post-processing.....	199
APPENDIX B: Creating geometries in ANSYS Workbench.....	202
B.1 Procedures	202
B.2 Loading the mesh in Fluent	204
B.3 Creating a 3D geometry	205
APPENDIX C: Setting up simulations in ANSYS FLUENT	207
C.1 Introduction	207
C.2 Procedures	207
APPENDIX D: Experimental Results	214
D.1 Particle size distributions for Powder 1(Alumina).....	214
D.2 Particle size distributions for Powder 2(Ballotini).....	216

Table of contents

D.3 Pressure drop curves for fluidization and defluidization (Powder 2).....	217
D.4 Bed height curves for fluidization and defluidization (Powder 2)	219
Bibliography	221

Chapter 1

General Introduction

In this chapter, we provide a general overview on the process of fluidization, its applications and different fluidization regimes. We summarize the main goals of this research work, and finally we provide an outline of the thesis.

1.1 An introduction to fluidization

Fluidization is an operation in which a bed of granular material is made to behave like a fluid by contact with gas or liquid. This is usually achieved by feeding the fluid through the granular material at a rate that is sufficient to exert a force on the particles that at least counter-balances its weight, making the bed acquire fluid-like properties such as: *ability to flow freely under gravity, ability to deform or to be pumped using fluid-type technologies*. The bed of granular material is then said to be *fluidized*. In the fluidized state there is extremely high surface contact between the fluid and the solid per unit volume of the bed, high level of mixing of the particulate phase(s) which promotes heat and mass transfer and high relative velocity between the fluid and the dispersed solid phase. These properties allow fluidized beds to find applications in many industrial operations.

The first application of fluidized beds was in Germany, where they were used in the Winkler process for coal gasification to produce synthesis fuel. Following this, fluidized beds were employed in the fluid catalytic cracking (FCC) of heavy oils to convert them to light products such as gasoline, kerosene, diesel and light olefins. This process is by far the largest application of fluidized bed technology. Similar to FCC applications, the Fischer-Tropsch (F-T) process is another catalytic gas-phase process that relies on fluidized bed technology. The F-T process is used to synthesize carbon monoxide (CO) and hydrogen (H_2), which are used to produce long chain hydrocarbons. This process draws on the advantage of excellent heat transfer rate in the fluidized beds which ensures uniform temperature is achieved in the process, thus improving the efficiency of the process. Other catalytic gas-phase processes where fluidized beds are employed are production of phthalic anhydride, acrylonitrile, aniline, ethylene dichloride, polyethylene and polypropylene.

In recent times, fluidized beds have been used in the incineration of solid wastes. This application is the most widely used of all the waste-to-energy technologies. Incineration is particularly useful for getting rid of harmful materials and for the utilization of heat produced for electricity generation. Consequently, fluidized beds have been employed extensively in the incineration of municipal and industrial wastes, offering distinct advantages such as ability to handle different feed materials, homogeneous combustion and lack of moving part in the combustion zone.

The world-wide campaign for environmental sustainability and green technology has caused a great shift of attention to the use of renewable sources for energy generation, with biomass as one of the preferred energy resources. Gasification of biomass offers an efficient way of controlling emissions, offering a simpler way of removing pollutant gases such as sulphur dioxide, nitrogen oxides and carbon dioxide. It also produces synthesis gas which is used to produce different environmentally friendly gaseous and liquid fuels. The conversion of biomass to these fuels relies on fluidized bed technology, making the latter a contributor to sustainable development.

Table 1.1: Applications of fluidized bed technology

Polymeric materials	<ul style="list-style-type: none"> • Synthesis of polyethylene, polypropylene • Production of silicon for semi-conductor applications
Pharmaceutical & Biochemical applications	<ul style="list-style-type: none"> • Cultivation of microorganisms for food and pharmaceutical applications e.g. fluidized bed bioreactors • Continuous and batch processing to produce antibiotics, enzymes, fermentation products, proteins, vitamins.
Chemical synthesis	<ul style="list-style-type: none"> • Synthesis of varieties of products such as phthalic anhydride, Fischer-Tropsch synthesis of hydrocarbons, acrylonitrile, maleic anhydride, activated carbon
Petroleum processing	<ul style="list-style-type: none"> • Fluid catalytic cracking for production of gasoline from oil • Fluid coking
Combustion & Gasification	<ul style="list-style-type: none"> • Coal combustion • Solid waste incineration • Biomass gasification • Chemical looping combustion
Other applications	<ul style="list-style-type: none"> • Coating of particulate material • Drying of solids • Granulation • Adsorption of solvents • Metallurgical applications

Another area of fluidized beds application that is worth mentioning is in the mineral and metallurgical processes. The use of fluidized beds for these processes commenced in the late 1940s in Ontario, Canada, where these systems were used for the roasting of arsenopyrite (Kunii & Levenspiel, 1991). Fluidized beds are suitable for this application because of the excellent heat and mass transfer rates which they promote. Subsequently, fluidized beds have

been employed in a wide range of mineral and metallurgical processes such as roasting of pyrites, pyrrhotite, zinc sulfide, copper and cobalt concentrates.

The application of fluidized beds is not limited to processes where chemical reactions take place, such as those described above. They are also employed in many physical operations. We mention for instance, their use in drying operations. This has been used in many industries such as food and agriculture industry, pharmaceutical industry and chemical process industries. Other physical processes in which fluidized beds are employed include coating, granulation, solid mixing, food freezing, solvent adsorption and heat treatment. Table 1 summarizes some applications of fluidized bed technology.

1.2 The phenomenon of fluidization

When a fluid is passed upwards through a bed of particles as shown in Figure 1.1, at low flow rate, the fluid just moves through the spaces between the particles while the particles remain stationary in their positions. This is referred to as *fixed bed* or *packed bed*. As the flow rate of the fluid is increased, the particles move apart and a few of them vibrate and move in restricted regions. As the flow rate is further increased, a point is reached where all particles are just suspended by the upward flowing fluid. At this point, the drag force on the particles counterbalances their effective weight (real weight minus buoyant force). When this happens, the bed is considered to be just *fluidized* and is referred to as *incipiently fluidized bed* or bed at *minimum fluidization*. For a bed fluidized by liquid, a further increase in flow rate above the minimum fluidization flow rate Q_{mf} will result in a smooth, progressive expansion of the bed and the bed remains in a homogeneous state. The superficial gas velocity corresponding to Q_{mf} , obtained by dividing the latter by the cross sectional area A of the vessel, is a property of the fluid-particle system, referred to as *minimum fluidization velocity*, u_{mf} . A bed such as this is called a *particulately fluidized bed* or *homogeneously fluidized bed*. This behaviour is observed in gas-fluidized beds only when small, light particles are fluidized.

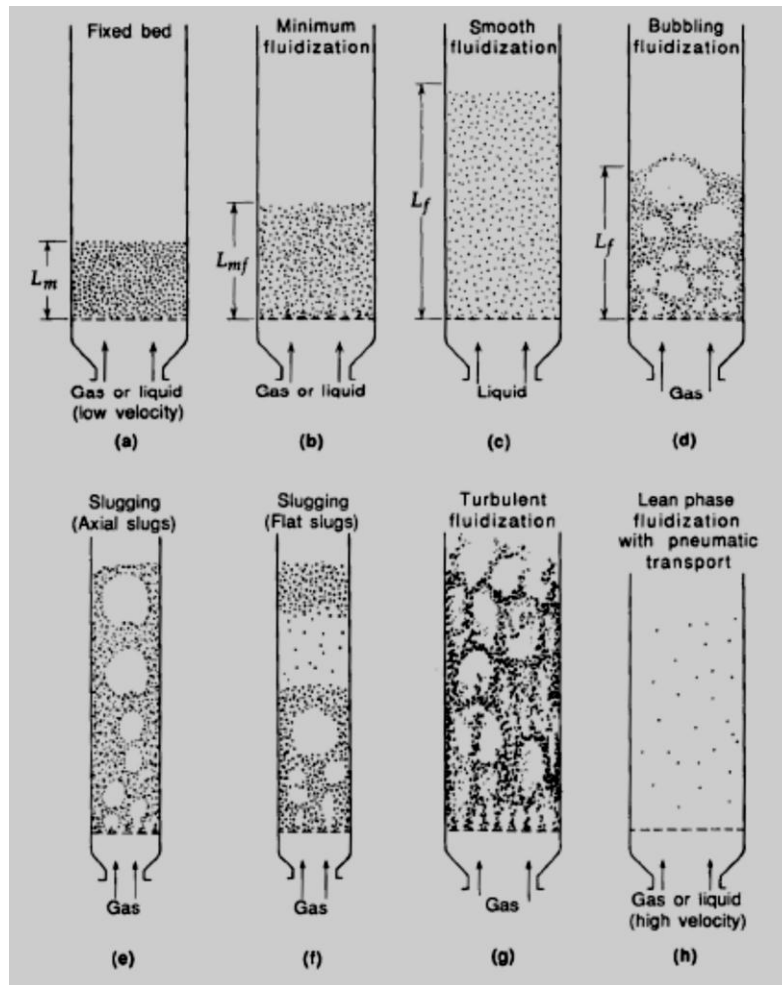


Figure 1.1: Fluidization regimes (Kunii & Levenspiel, 1989).

Typically, in gas-fluidized beds, when the flow rate is increased beyond that which is needed for minimum fluidization, bubbles begin to form and movement of particles become more vigorous. Unlike the situation obtained for liquid-solid systems, the bed does not expand much beyond its volume at minimum fluidization. This type of bed is called an *aggregative fluidized bed* or a *bubbling fluidized bed*. This type of bed rarely occurs in liquid-solid systems, except with very dense solids fluidized by low density liquids. The velocity u_{mb} at which the first bubble forms is also a property of the fluid-particle system, and it is called the *minimum bubbling velocity*. With further increase in gas flow rate, bubbles coalesce as they rise through the bed, and in a bed that is deep and of small diameter, they may eventually become large enough to spread across the vessel. This is called *slugging fluidization*. At sufficiently high gas flow rate, the

terminal velocity of the solid is exceeded, making the upper surface of the bed disappear, and instead of bubbles, one observes a turbulent motion of solid clusters and voids of gas of various sizes and shapes. This is called a *turbulent fluidized bed*. A further increase in gas velocity drives the bed into the *pneumatic transport* regime, where the particles are carried out of the bed. We summarize the different regimes of fluidization in Figure 1.1. In this work, we focus on two regimes: the homogeneous and bubbling regimes. The former is our main focus in Chapters 2 and 3, while the latter is addressed in Chapters 4 through 6.

The fluidization behavior described above provides a generalization of how particles behave when subjected to an increasing upward flow of gas. However, the behavior of gas-fluidized beds depends largely on the physical properties of the particles and the operating conditions. In trying to describe this dependence, Geldart (1973) characterized the behavior of particles fluidized by gas into four distinct groups. Figure 1.2 reports the classification of powders fluidized by air at ambient temperature.

Group A powders have small sizes (30 - 100 μm) and/or low density (typically less than 1.4 g/cm^3). A notable example is FCC catalyst. When they are fluidized by gas they expand homogeneously at superficial gas velocities between u_{mf} and u_{mb} . The physical mechanism responsible for this homogeneous expansion has been a subject of controversy among researchers (Foscolo & Gibilaro, 1984; Mutsers & Reitema, 1977; Tsinontides & Jackson, 1993; Fortes et al., 1998); some argue that the homogeneous expansion (or the stability) is due to the existence of interparticle forces in the bed, while others sought for a purely fluid dynamic explanation. In Chapter 2, we provide an extensive review of this lingering controversy, while in Chapter 3 we address the subject, providing further insight using theoretical and experimental methods.

Group B contains powders in the mean size range of 40 – 500 μm , and density range 1.4 – 4 g/cm^3 . An example is sand. When these particles are fluidized, bubbles start to appear at minimum fluidization velocity or at a velocity slightly higher than the latter. Group D consists

of large and/or dense particles whose minimum fluidization velocity coincides with the minimum bubbling velocity; thus powders belonging to this group begin to bubble as soon as they are fluidized.

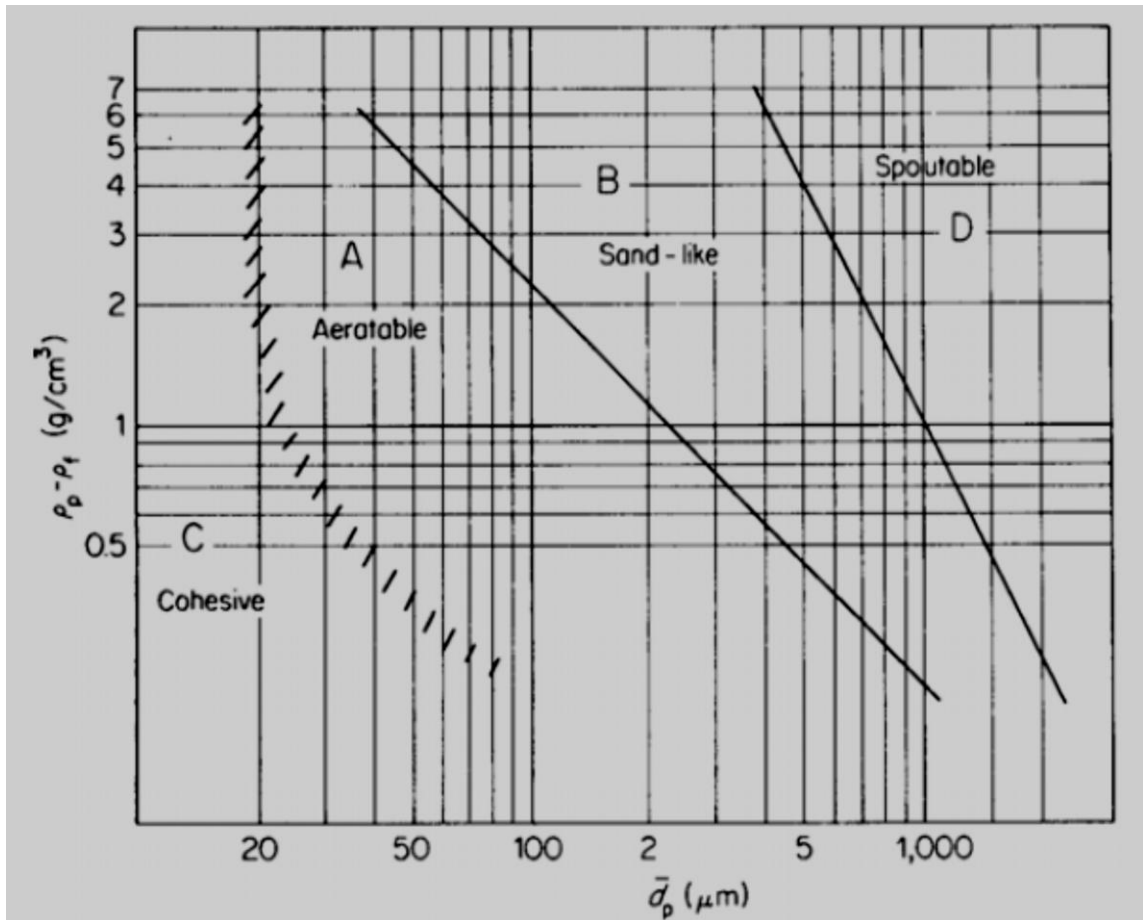


Figure 1.2: Fluid-particle system classification for air at ambient temperature (Geldart, 1973)

Group C consists of cohesive powders characterized by very small particles of size range 20 – 50 μm . Fluidization of this group of powder is difficult because of the strong interparticle forces among the particles which dominate the fluid dynamic forces. Their fluidization usually leads to undesirable processes such as *plugging*, *channeling* and *formation of stable cakes* (Chaouki et al., 1985; Molerus, 1982; Özcan & Tüzün, 2006). To fluidize this group of powder, researchers have developed various methods including *sound assisted fluidization* (Morse, 1955), *vibro-fluidization* (Mori et al., 1990), *magnetically assisted fluidization* (Lu & Li, 2000), *electro-fluidization* (Kashyap et al., 2006), *addition of foreign particles* (Brereton, 1987) and the *use of tapered fluidized beds* (Venkatesh et al., 1996). As we shall later see in this work,

successful fluidization of Group C powders makes them behave in a similar way to Group A powders, having in particular a stable interval of homogeneous expansion before transiting to the bubbling regime.

1.3 Computational modelling of fluidized suspensions

Despite the extensive applications of fluidized beds, their design is quite challenging. The usual way is to construct them on a laboratory scale, construct a bigger pilot plant, and then scale-up the pilot plant to a commercial size. This approach has some problems associated with it - many of the essential operating parameters are scale-dependent, a change in one parameter affects several other parameters, making the scaled fluidized bed have a significantly different hydrodynamics. In addition to this, fluidized beds operate in different regimes (bubbling, turbulent, spouting etc.); therefore, it is difficult to come up with a general rule on fluidized bed scale-up. While describing the complexity of fluidized bed scale-up, Matsen (1996) stated that *“scale-up is not an exact science, but is rather that mix of physics, mathematics, witchcraft, history and common sense that we call engineering”*. Matsen’s statement clearly revealed the difficulties inherent in the design of fluidized beds using the scale-up method.

As interest in understanding the mechanisms responsible for complex fluid dynamic interactions in fluidized systems grew, a more fundamental approach based on equations of motion for interacting fluid and particles was developed. These equations nevertheless were seen as a means of understanding the mechanisms responsible for complex behaviour of fluidized systems rather than as a basis for engineering design. However, in the 1980s, researchers began to attempt using differential equations of continuity and momentum as a basis for quantitative design calculations. This effort was greatly complemented by rapid improvements in the speed and memory capacity of digital computers, coupled with the development of better numerical methods for solving equations of motion. Consequently, researchers began to attempt predicting bubble formation in dense fluidized beds by direct integration of these equations (Pritchett et al., 1978; Gidaspow & Ettehadieh, 1983; Gidaspow et al., 1986).

Nowadays, computer simulations have proven to be a useful tool in the design and scale-up of fluidized bed processes, allowing researchers to obtain fundamental insights into the complex behaviour of dense fluidized suspensions. Computer simulations are also employed as a design tool, where numerical models are used to predict the behaviour of dense gas-particle flows encountered in engineering-scale equipment. The use of computational methods in the design of fluid bed processes has led to reduction in cost of product and process development, reduced the need for physical experiment, improved design reliability, increased conversions and yield and facilitated the resolution of environmental, health and right-to-operate issues (Davidson, 2002).

Although empirical correlations are still employed in many practical engineering designs, attention is gradually shifting towards the use of computational methods. This is because the latter are able to provide answers to questions that cannot be addressed using empirical correlations. For example, empirical correlations are unable to tell us the effect of introducing internals or changing the designs of distributor plates on fluid dynamics and performance, whereas computational codes are able to solve the governing equations to answer these questions.

The equations used for investigating the behaviour of fluidized systems can be formulated at different levels of detail. At the most fundamental level, the particles are treated individually and their motion is determined by Newtonian equation of motion for translational and rotational motion, thus retaining the discrete nature of the particles. The interstitial fluid, on the other hand, is modelled as a continuum whose dynamics is described by Navier-Stokes and continuity equations, satisfied at every point of the fluid itself. Each set of equations is coupled by no-slip boundary condition between solid and fluid on each particle boundary, the fluid also satisfying no-slip condition on the remaining boundaries of the computational domain. The main advantage of this modelling approach lies in the simplicity of the equations; the latter do not contain indeterminate terms that need closure – except the fluid stress tensor, for which the classical Newtonian equation holds, and particle-particle collisions. Despite the simplicity of this approach, it is seldom used. This is because of its enormous computational demand. Indeed,

simulations at this level of detail have only been carried out for very dilute systems (Pan et al., 2002). Quite recently, Kriebitzsch et al. (2013) carried out simulations of gas-fluidized beds using this approach, but in the simulations they considered only 2000 particles, owing to the significant computational effort required.

Another modelling approach, which provides a lower level of detail, can be obtained by averaging the fluid velocity over a spatial domain large enough to contain many particles but still small compared to the whole computational domain. The Newtonian equations of motion are solved for each particle, and the force exerted on each particle is related to the particle's velocity relative to the locally averaged fluid velocity. This modelling approach, referred to as discrete element modelling (DEM), is less computationally demanding compared to that reported in the preceding paragraph, and has been widely employed to investigate the behaviour of fluidized suspensions (Tsuji et al., 1993; Hoomans et al., 1996; Ouyang & Li, 1999; Kafui et al., 2002; Lu et al., 2005; Sun, et al., 2007; Liang – wan & Zhan, 2010; Zhu et al., 2011). The approach provides enormous information on the fluid bed dynamics, and is an approach of choice for researchers who are interested in gaining deeper insight into the dynamics of granular media. Nonetheless, discrete particle modelling has its own drawbacks – it requires enormous computational effort and can rarely be employed to investigate the dynamics of large-scale fluidized systems. We provide further detail on this modelling approach in Chapter 6.

At an even lower level of detail, both the fluid velocity and particle velocity are averaged over the local spatial domain; thus the resulting equations resemble those that one would write for n imaginary fluids capable of interpenetrating each other while occupying the same volume simultaneously. The model, referred to as Eulerian-Eulerian, therefore takes the form of coupled differential equations subject to boundary conditions at the boundaries of the whole system. The numerical solution of the Eulerian averaged equations of motion is known as *computational fluid dynamics (CFD)*. This modelling approach, when compared to those described previously, is computationally less demanding, and is often used by researchers who are interested in investigating the behaviour of large-scale systems. The approach has been successful in

investigating the behaviour of full-scale systems, thus offering a more reliable way of designing and investigating industrial size fluidized beds.

Although the Eulerian-Eulerian modelling approach is very attractive to researchers and engineers who are interested in investigating the behaviour of industrial scale fluidized systems, it has a major drawback: the equations are mathematically unclosed; therefore closures must be formulated for indeterminate terms resulting from the averaging process. To close these equations, we must formulate models for the *fluid-particle interaction force* and the *effective fluid dynamic stress* of the fluid and solid phases. To express the former, we employ empirical correlations together with results of classical fluid dynamics, while the Newtonian equation is used to express the effective fluid dynamic stress of the fluid phase. Modelling interaction forces between particles of different phases and effective fluid dynamic stress of solid phase is very challenging. Many researchers resort to the kinetic theory of granular flow (Haff, 1983; Jenkins & Savage, 1983; Lun et al., 1984; Jenkins, 1987; Lun, 1991; Gidaspow, 1994; Goldshtein & Shapiro, 1995; Mazzei et al., 2010; Oke, et al., 2014). However this approach is inadequate to describe correctly the behaviour of dense fluidized systems where particle interact through enduring frictional contacts; hence several approaches originating from the field of soil mechanics have been adopted (Savage, 1982; Johnson & Jackson, 1987; Makkawi & Ocone, 2006). In Chapter 5 we discuss this modelling approach in greater detail, reporting its governing equations and demonstrating its capability to investigate the process of mixing in fluidized beds.

1.4 Computational fluid dynamic codes

The numerical solution of averaged equations of motion consists of three basic steps – pre-processing, solving and post-processing. These steps are briefly described below.

1. Pre-processing:

In this step we set up the physical problem. This involves creating the geometry, generating the mesh, specifying the number of Eulerian phases and their physical and/or chemical properties, time-step, initial and boundary conditions.

2. Solving:

Most commercial CFD codes use the finite volume method. The code integrates the differential transport equations over each computational cell, generating a set of integral equations on a control volume basis. Then, the code converts these equations into algebraic form using discretization techniques. Finally, the code solves the set of algebraic equations and finds the cell-centre values of the flow variables.

3. Post-processing:

The raw outputs from the solver consist of huge data sets that have to be analysed in order to obtain useful information. The modeller therefore uses analysis tools to extract and manipulate the data and generate diagrams and snapshots.

1.5 Research questions

This research project is concerned with the investigation of the fluid dynamic behaviour of homogeneous and bubbling regimes of gas-fluidized beds. Knowing how fluidized beds behave will greatly allow us to model and design them more accurately. The research aims to answer some fundamental questions relating to the dynamics of fluidized bed suspensions. These involved answering, among others, questions such as how do particles interact in homogeneous gas-fluidized beds? Do homogeneous fluidized beds consist of free-floating particles having no form of particle-particle interactions? How applicable are the existing fluid dynamic correlations, often used to analyse bed expansion, to the solid-like regime of fluidized beds? What roles do interparticle forces play in the homogeneous expansion of gas-fluidized beds. These questions have lingered for quite a while in the fluidization community. Answering these questions will provide deep insight into the complex fluid dynamic relationships in fluidized beds and will enhance our ability to better model their behaviour. The investigations in this work also cover the bubbling regime of fluidized beds. In this regime, the process of lateral solid mixing is examined. Lateral solid mixing is crucial for assessing the performance of large-scale fluidized beds. The influence of operational and design conditions on lateral solid mixing is investigated. In this part of the research, we aim to investigate how well the two widely used

modelling approaches, the Eulerian-Eulerian and the Eulerian-Lagrangian, can estimate lateral solid dispersion coefficients.

1.6 Research objectives

The main goals of this research are:

1. Presenting clearly the process of homogeneous fluidization in gas-fluidized beds; investigating the distinctive features of solid-like and fluid-like regimes of homogeneous fluidization.
2. Elucidating the fluid dynamic behaviour of homogeneous gas-fluidized beds; providing deeper insight into the mechanisms responsible for the stability observed in gas-fluidized beds.
3. Modelling the stable expansion in gas-fluidized beds, accounting for enduring particle contacts and wall friction; examining the roles played by enduring particle contacts and wall friction on the homogeneous expansion of gas-fluidized beds.
4. Conducting fluidization and defluidization experiments to investigate the expansion process in gas-fluidized beds; carrying out experiments to determine yield stresses in gas-fluidized suspensions; analysing the expansion profiles of gas-fluidized beds using the Richardson & Zaki (1954) equation, and examining the applicability of the latter in describing the expansion profiles in gas-fluidized beds.
5. Modelling lateral solid mixing in gas-fluidized beds using the Eulerian-Eulerian approach; quantifying lateral solid mixing using a lateral dispersion coefficient and validating numerical results with empirical data.
6. Investigating the effects of operational and design factors on the lateral solid mixing in gas-fluidized beds; in particular the influence of *superficial gas velocity*, *bed diameter* and *bed height*.
7. Examining the influence of frictional models and dimensionality on the numerical simulations of lateral solid mixing; comparing the numerical results obtained from 2D

and 3D simulations of lateral solid mixing; analysing the effects of frictional packing limit, frictional pressure and frictional viscosity models on lateral solid mixing.

8. Investigating the capability of Eulerian-Lagrangian modelling approach in estimating lateral solid dispersion coefficients; comparing the predictive ability of this modelling approach with that of Eulerian-Eulerian methods.

1.7 Thesis outline

Chapter 2 reports on the stability of gas-fluidized beds, discussing on the lingering controversy among researchers about its origin. We then report on the homogenous expansion of gas-fluidized beds, revealing the distinct peculiarities of the solid-like and fluid-like regimes. In Chapter 3, we investigate the mechanics of homogeneous expansion in gas-fluidized beds using theoretical and experimental methods. In Chapter 4, we report on the process of mixing in bubbling fluidized beds and how it is quantified. We highlight the importance of *axial* and *lateral* solid mixing and report on the dominant mechanisms by which these processes occur. In Chapter 5, we model lateral solid mixing using the Eulerian-Eulerian approach. We solve the 2D governing equations numerically to determine the lateral dispersion coefficients. We finally investigate the influence of design and operating conditions on the latter. We then examine the influence of frictional stress models on our numerical results. In Chapter 6, we investigate the effect of simulation dimensionality on the numerical results obtained in Chapter 5. We run 3D CFD simulations comparing the results with those obtained in the latter. We later review the Eulerian-Lagrangian approach and we use it to investigate lateral solid mixing in gas-fluidized beds. We compare our numerical results with those obtained from the Eulerian-Eulerian modelling approach.

Chapter 2

The stability of gas-fluidized beds

This chapter reviews various mechanisms proposed for the stability of gas-fluidized beds.

1. We present a brief account on the lingering controversy on the mechanism responsible for the stability of gas-fluidized beds.
2. We report on the experimental and theoretical works supporting the fluid dynamic stability of gas-fluidized beds.
3. We review the experimental evidence put forward to support the idea that stability in gas-fluidized beds is due to interparticle forces.
4. We present the fluid-like and solid-like behaviour of gas-fluidized beds.

Parts of this chapter have been published:

Oke, O., Lettieri, P., Mazzei, L. (2015). An investigation on the mechanics of homogeneous expansion in gas-fluidized beds. *Chemical Engineering Science*, 127, 95-105.

2.1 Introduction

Generally liquid-fluidized beds display a smooth appearance and expand progressively as the fluid flow rate is increased, while gas-fluidized beds display heterogeneous appearance,

containing rising pockets of gas, referred to as bubbles. The former behaviour is referred to as homogeneous (particulate) fluidization, while the latter is termed bubbling (aggregative) fluidization. Although gas-fluidized beds generally exhibit bubbling fluidization, small particles with low density (Geldart A powders) fluidized by gas displays an interval of smooth expansion when the gas flow is increased above the minimum fluidization rate (Tsinontides & Jackson, 1993). The origin of the stable behaviour of Group A powders has been a subject of controversy in the fluidization community. On one side of the argument are those ascribing the stability to the existence of *interparticle forces* in the bed and on the other side are those seeking for a purely *fluid dynamic* explanation.

Over 60 years ago, Wilhelm & Kwauk (1948) proposed an empirical fluid dynamic criterion for stability in fluidized beds. They based their criterion on the Froude number F_r :

$$F_r = \frac{(u_{mf})^2}{gd_p} \quad (2.1)$$

where d_p is the particle diameter, g is the gravitational acceleration and u_{mf} is the minimum fluidization velocity. They observed that a bed is fluidized homogeneously if $F_r \leq 1$, while it bubbles otherwise.

Jackson (1963) sought to derive a theoretical justification for the criterion proposed by Wilhelm & Kwauk (1948) using a linear stability analysis. This was based on the continuity and linear momentum balance equations for the fluid and particle phase. Unfortunately, the analysis yielded a physically unacceptable behaviour: it predicts that all fluidized suspensions should be unstable and that the rate of growth of instability should increase monotonically as their wavelengths tend to zero. However, the analysis predicted correctly that the rate of growth of instability in gas-fluidized beds is generally greater than in beds of comparable particles fluidized by liquids.

The physically unacceptable behaviour predicted by the linear stability analysis is because the particle-phase momentum balance equation adopted by Jackson did not include terms

representing viscous dissipation (Anderson & Jackson, 1967). The latter accounts for the physical mechanisms responsible for momentum transport associated with fluctuations in particle velocity. When such terms are added to the particle-phase momentum balance equation (Pigford & Baron, 1965; Anderson & Jackson, 1967) there is a bounded value of the wavelength for which the disturbances grow.

The foregoing attempts simply attribute the difference between liquid and gas-fluidized beds to the greater growth of disturbance, but could not establish a sharp dividing line between homogeneous and bubbling fluidization, neither did they say anything about the ultimate fate of the disturbance nor provide a justification on why disturbances in liquid fluidized beds do not grow into bubbles. The failure of linear stability analysis to establish a clear distinction between homogeneous and bubbling fluidization has led researchers to take into account non-linearities in the equations of motion (Liu, 1982; Needham & Merkin, 1983; Ganser & Drew, 1990). Nevertheless these attempts, based only on fluid dynamic considerations, have neither revealed any qualitative distinction between the predicted behaviour of gas and liquid fluidized beds, nor provided convincing evidence for stability due to fluid dynamic forces.

Verloop & Heertjes (1970) investigated the transition from homogeneous to bubbling fluidized beds, considering only the fluid dynamic forces in the bed. Following Wallis (1962), they viewed bubbles as shock waves propagating in the bed. They reported that shock waves originate in the latter when the velocity of *kinematic wave* is greater than that of *dynamic wave*. Kinematic waves propagate between two regions of different voidage where equilibrium of fluid dynamic forces exists and there is no inertia effect (Cherntongchai & Brandani, 2013). Lighthill & Whitman (1955) describes kinematic waves using a road-traffic flow analogy. They reported that kinematic wave is comparable to a 'traffic concentration wave' which arises when an interruption of traffic flow occurs at some distance ahead. This traffic concentration wave propagates backwards at a constant speed from the point of obstruction. Drivers who are far away from the point of obstruction are forced to slow down and move closer as the wave passes over them. We should note that the kinematic description just described does not take into

account the inertial effects due to breaking and acceleration. A dynamic wave, on the other hand, arises as a result of a force considered to be a component of the drag, which accelerates the particles as a result of the concentration gradient. This wave is likened to the inertial effects of breaking and deceleration. Verloop & Heertjes (1970) described the condition for transition from homogeneous to bubbling fluidization as:

$$u_\varepsilon = u_e \quad (2.2)$$

where u_ε is the kinematic wave velocity and u_e is the dynamic wave velocity. Accordingly, a bed manifests homogeneous behaviour when $u_\varepsilon < u_e$, and bubbling behaviour when $u_\varepsilon > u_e$. It is important to note that the considerations by Verloop & Heertjes assumed that the fluid is incompressible; hence, these considerations are valid for liquid-fluidized beds. For beds fluidized by gas, their propositions are invalid.

Similar to Verloop & Heertjes (1970), Fanucci et al. (1979) described bubbles as shock waves which propagate in the bed when the velocity of kinematic wave is greater than the velocity of dynamic wave. By solving the mass and linear momentum balance equations for the fluid and particle phase, they demonstrated that shock waves can indeed form in the bed. They investigated the effects of several parameters on the formation of shock waves. Their results showed that decreasing particle size, increasing bed density, increasing fluid viscosity and decreasing particle density delay the formation of shock waves. These results are consistent with experimental data on bubble formation in fluidized beds.

In the same vein, Foscolo & Gibilaro (1984) derived a stability criterion based on fluid dynamic arguments, resorting to the stability theory of Wallis (1969) to show that stability depends on the relative magnitude of the kinematic and dynamic waves that propagate in the bed. They argue that the drag force should include an addition term proportional to the gradient of void fraction. This led to a criterion for instability of the form:

$$\frac{(gd_p)^{1/2}}{u_t} \left(\frac{\rho_p - \rho_f}{\rho_p} \right)^{1/2} < 0.56n(1 - \varepsilon)^{1/2} \varepsilon^{n-1} \quad (2.3)$$

where g is the acceleration of gravity, u_t is the terminal velocity of a particle, ρ_p is the particle density, ρ_f is the fluid density, n is the Richardson & Zaki (1954) exponent and ε is the void fraction. Although the authors claimed that Eq. 2.3 is valid for investigating the stability of a wide range of gas-fluidized beds, experimental observations revealed that the criterion failed when applied to certain liquid-fluidized systems. Researchers (Anderson & Jackson, 1969; El-Kaissy & Homsy, 1976; Ham et al., 1990) reported that certain water-fluidized beds of glass beads predicted to be stable by Eq. 2.3 are actually unstable, though the instabilities never grow into bubbles.

Another approach, based on fluid dynamic considerations, was adopted by Batchelor (1998). He showed that stability could arise due to random fluctuations in particle velocity and related this to diffusion of particles in the suspension. He proposed the following criterion for instability:

$$\frac{(gd_p)^{1/2}}{u_t} \left(\frac{a_1}{2(1+a_2)} \right)^{1/2} < n(1-\varepsilon)\varepsilon^{n-1} \quad (2.4)$$

where a_1 and a_2 are parameters related to the virtual mass effects and the particle phase pressure. Batchelor reported that the value of $(1+a_2)$ lies between 1 and 2, and a_1 is of order unity.

The foregoing works, based on fluid dynamic considerations, assume that particles are free floating in the fluid during fluidization, without any form of particle-particle interaction. On the other side of the argument are those attributing the stability to the existence of interparticle forces. They argue that the stability of gas-fluidized beds arises due to interparticle forces holding the particles together and delaying their bubbling over a range of superficial gas velocity. Those upholding this view report that interparticle forces keep the particles together in permanent contacts, conferring to the expanded bed a *solid-like* structure. Indeed, most experimental results, as we shall later report in this chapter, suggest that Group A powders behave like a weak solid rather than a fluid in the homogeneous fluidized state, due to enduring interparticle contacts. The weight of the fluidized particles are therefore not fully supported by

the upward flow of gas, but also supported in part by interparticle forces among the particles. Before reporting on this solid-like behaviour, we will review the nature of interparticle forces that are often at play in gas-fluidized beds.

2.2 Interparticle forces in fluidized beds

Interparticle cohesion in fluidized beds may arise from the interplay of different forces. These forces, as we shall see, affect the fluidization behaviour of powders and have been closely linked to the stability observed in gas-fluidized beds. Some notable examples of interparticle forces are reported below.

2.2.1 Van der Waals forces

This is due to the interaction between instantaneous dipoles formed in the atoms by their orbiting electrons. The rapidly changing dipole of one atom generates an electric field that induces the polarization of the neighbouring atom. The induced dipole of the latter produces an attractive interaction known as the van der Waals force. We should note that this type of attractive force does not only exist between atoms and molecules, but also between macroscopic particles. The van der Waals force F_w between two smooth spheres of radius R and separation r is given by:

$$F_w = \frac{h_w}{8\pi z^2} R \left(1 + \frac{h_w}{8\pi^2 r^3 h_r} \right) \quad (2.5)$$

where h_w is the Lifshits-van der Waals coefficient; the latter depends on the nature of bodies in contact and the surrounding medium. h_r is a coefficient characterising the hardness of the bodies in contact (Krupp, 1967; Molerus, 1982; Massimilla & Donsi, 1976). The Van der Waals force is generally more significant than other interparticle forces for fine particles of diameter less than 100 μm fluidized by dry gas, dominating over their fluid dynamic counterpart (Visser, 1989; Valverde et al., 1998; Seville et al., 2000).

2.2.2 Electrostatic forces

In addition to van der Waals forces, electrostatic forces can also contribute to interparticle cohesion in fluidized beds. When non-conducting particles come into contact with surfaces of dissimilar material or slide along such surfaces, for example particles sliding along the wall of fluidized beds, there is generally an exchange of electrons in the surface layer. This causes the particles to be electrically charged. The motion of a charged particle in the fluidized bed is influenced by the neighbouring charged particle, therefore creating an electrostatic force between them. According to Coulomb's law, the electrostatic force F_e between two charged objects a and b is proportional to the product of their charges and inversely proportional to the square of the distance r between them (Fan & Zhu, 1998). Coulomb's law is expressed as:

$$F_e = \frac{1}{4\pi\epsilon} \frac{q_a q_b}{r^2} \quad (2.5)$$

where q_a and q_b are the charges on a and b , respectively, and ϵ is the permittivity of the surrounding medium. In general, when compared to van der Waals forces, electrostatic forces are not significant in a fluidized bed (Reitema, 1991). Nevertheless significant electrostatic forces can be generated in the bed depending on the material from which the fluidizing vessel is constructed. For instance, we see significant electrostatic effects when a fluidized bed reactor is made from Perspex.

2.2.3 Capillary forces

This arises when moisture from the surrounding gas condenses on the surface of particles, forming a liquid bridge in the gap between neighbouring particles. This produces a resultant attractive force on the two particles. Capillary forces can dominate the gravitational force on particles when the vapour pressure of surrounding gas is near the saturation vapour pressure and can be larger than van der Waals forces (Lian et al., 1993). The magnitude of capillary forces is very challenging to calculate. One method, proposed by Lian et al. (1993), is the boundary

method, where the total capillary force F_c is calculated at the liquid-solid contact. The capillary force is given by:

$$F_c = 2\pi\gamma R \sin\alpha \sin(\theta + \beta) + \pi R^2 \Delta P \sin^2\theta \quad (2.6)$$

where γ is the surface tension of the liquid, θ is the half-filling angle, β is the contact force and ΔP is the pressure drop across the air-liquid interface. It is worth mentioning that in most fluidized beds applications, capillary forces are always small and can be neglected (Reitema, 1991).

Researchers have made considerable headway in investigating the role of interparticle forces on the behaviour of gas-fluidized beds. For instance, the understanding of the effects of interparticle forces on fluidization behaviour has led to the re-interpretation of Geldart's (1973) classification of powders, using a dimensionless number known as the granular Bond number B_n . The latter is defined as the ratio of interparticle forces to the weight W_p of a particle. Powders having $B_n < 1$ are generally non-cohesive and bubble as soon as they are fluidized; these powders are classified by Geldart (1973) as Group B and D powders. Those powders for which $B_n \gg 1$ are very cohesive and generally difficult to fluidize; they are classified as Group C powders in the Geldart classification. Furthermore, powders having $B_n \cong 1$ exhibit smooth expansion over a range of superficial gas velocity as soon as they are fluidized; these are Geldart A powders. The fluidization behaviour of the latter is discussed in the next section.

We should note that the Geldart classification was intended to predict the behaviour of powders fluidized by air at ambient conditions. Reitema (1984, 1991) pointed out that it is more appropriate to speak in terms of *Geldart's A, B, C or D behaviour* instead of *Geldart's A, B, C or D powders*, since the same powder can exhibit different fluidization behaviour depending on experimental conditions. For example, Geldart B materials can be fluidized homogeneously with substantial expansion under conditions of high temperature and pressure. Under these conditions, there is a significant increase in the interparticle forces among the particles, causing the granular bond number to take a value very close to unity; hence the shift in behaviour from

Geldart B to Geldart A. Likewise, a powder which shows Geldart C behaviour may exhibit Geldart A behaviour when fluidized by a gas of high viscosity or when certain additives (such as fumed silica) are added. This decreases the interparticle forces among the particles, causing a reduction in the granular bond number. These observations show that the behaviour of a fluid-particle system depends largely on the ratio of interparticle forces to the weight of a particle, B_n .

2.3 Solid-like behaviour of Geldart A gas-fluidized beds

The controversy on the origin of stability of Group A powders started over 60 years ago when Wilhelm & Kwauk (1948) proposed their empirical criterion based on the Froude number. Since then researchers, some of which were reported in Section 2.1, have carried out theoretical and numerical studies to emphasize the role of fluid dynamic forces on the stability of Group A powders. Contrary to the views expressed by these authors, Reitema (1973) stated the stability of gas-fluidized particles is due to the existence of interparticle forces. He stated that the latter confer to the bed an effective *elastic modulus* that could stabilize the bed against small perturbations, making the bed behave like a weak solid rather than a fluid; this behaviour is referred to as *solid-like* behaviour. In their earlier studies, Reitema (1967) measured the electrical conductivity of a fluidized bed of coke particles. He observed that, during all fluidization stages, there is a considerable amount of electrical conductivity in the bed, signifying that particles are in frictional contacts with each other. On this basis he reported that particles in a fluidized bed arrange themselves in a string, with the latter behaving as a mechanical system, and exhibiting elastic behaviour. He stated further that a fluidized bed of cohesive particles, in a way, can be compared to a cigarette-tobacco consisting of crumpled strings. When a certain mass of tobacco is strongly compacted it is stable, but within certain limits displays elastic behaviour. When the tobacco is loosened, a more porous structure is obtained which is also stable and shows elastic behaviour. In the same way, a fluidized bed of cohesive particles displays an elastic property where the elasticity decreases as the porosity of the bed increases. To further provide evidence in support of fluidized bed stability by interparticle forces, Reitema & Mutsers (1973) conducted a tilting bed experiment. In the

experiment they tilted a homogeneously fluidized bed over the horizontal axis. They observed that the bed remains stable until a critical *tilting angle* is reached where the bed surface suddenly shears off. Their experimental set-up is reported in Figure 2.1. The critical tilting angle depends on bed expansion, particle size and particle density. When the bed is tilted, the direction of the drag force on the particles changes, whereas the surface of the bed does not slide. This implies that the change is being compensated by some other forces in the bed. Reitema (1973) referred to these forces as interparticle forces in bed. The experiment demonstrates that the homogeneous fluidized bed has a certain mechanical strength caused by a network of interparticle contacts.

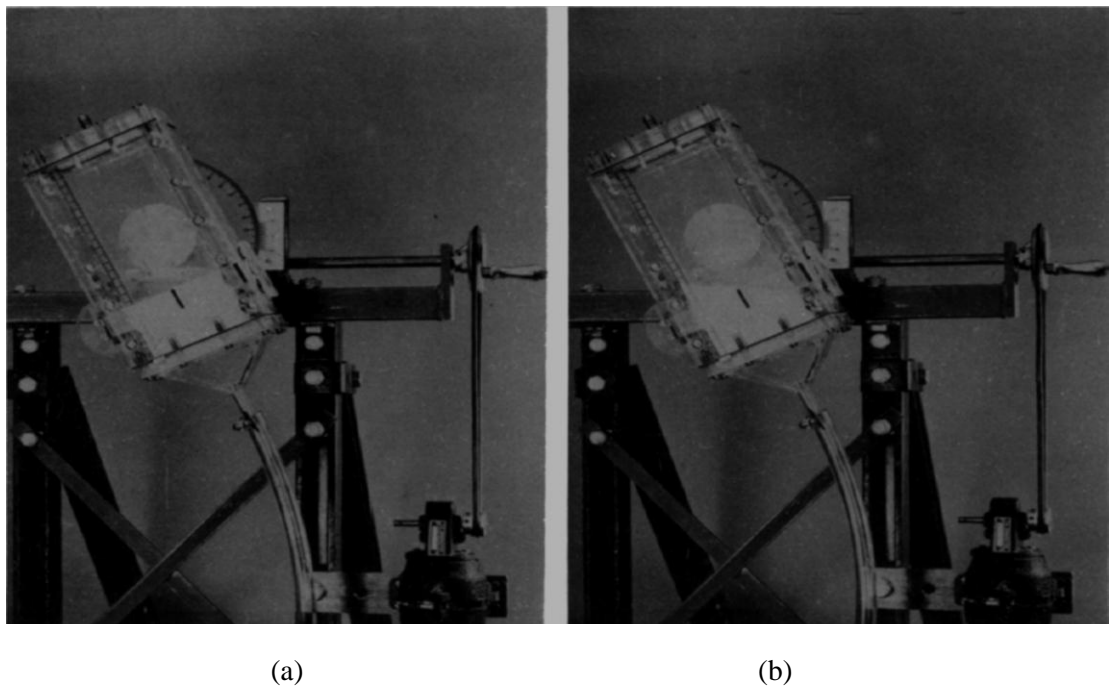


Figure 2.1: Tilting bed experiments (a) before shearing off (b) after shearing off. (Reitema & Piepers, 1990)

The idea of interparticle forces as a stabilizing agent for gas-fluidized beds led Mutsers & Reitema (1977) to conclude that an elasticity term ($E \partial \varepsilon / \partial z$, where E is the elasticity modulus of the bed and z is the vertical coordinate) should be added to the solid phase linear momentum balance equation. They employed Wallis (1969) criterion to show that a fluidized bed is unstable if:

$$\frac{\rho_p^3 d_p^4 g^2}{\mu_f^2 E} > \left[\frac{150(1 - \varepsilon)}{\varepsilon^2(3 - 2\varepsilon)} \right]^2 \quad (2.7)$$

where ρ_p is the particle density, d_p is the particle diameter, μ_f is gas viscosity and ε is the void fraction. Whenever there are perturbations in the bed, such as those arising from gas fluctuations, hydrodynamic stress is generated in the bed. Reitema (1977) stated that for a bed to be stable it must have a sufficiently large elasticity to compensate for the stress caused by perturbations in the bed.

To highlight the solid-like behaviour of Geldart A powders, Donsi et al. (1984) carried out experiments similar to those of Reitema (1973). They measured the tilting angles of Geldart A and B powders. They observed for the latter powder that the tilting angle tend to zero when the particles are fluidized, implying that the upper surface of the bed shears off at minimum fluidization velocity. Conversely the tilting angle of Geldart A powders takes non-zero values throughout the period of homogeneous expansion. They explained that the tilting angle of Geldart B powders becomes zero at minimum fluidization because the particles do not maintain a network of interparticle contacts when they are fluidized; hence they do not have mechanical strength that such enduring contacts bring and therefore they bubble as soon as they are fluidized. Donsi et al. (1984) also measured the *angle of internal friction* of Group A powders, starting from the packed state (when the fluid flow rate is zero) to the minimum bubbling point. They reported that the angle of internal friction measured when the bed is fluidized accounts for the contribution of cohesive forces in the bed. They could not measure the angle of internal friction for Group B powders because they bubble as soon as they are fluidized.

Although the above experiments provide evidence that stability of gas-fluidized particles is due to interparticle forces in the bed, Gilbertson & Yates (1996) expressed doubts on the use of such experiments for obtaining information on the stability of gas-fluidized beds. They carried out tilting bed experiments using the same powder investigated by Reitema, but they used metal as the bed container as opposed to perspex used by the latter author. They reported a radically

different observation from Reitema: the surface of the bed shears off as soon as the particles are fluidized. They attributed the difference in observation to the different materials used for the fluidized bed container. Reitema used Perspex, which is more prone to cause electrostatic charges within bed. The interparticle forces generated by these charges are sufficient to stabilize the bed during tilting, thus validating Reitema's conclusions. However, Gilberton & Yates (1996) reported that Reitema's results may only be applicable to their experiments and should not be generalized for all Group A powders. This is because they observed that the angle of tilt of the bed is different from the angle of tilt of the container. They argued that if the particles are held together by interparticle forces the two angles should be the same. They concluded that interparticle forces should not be ruled out as a potent factor responsible for the stability of Geldart A powders, but they should not be invoked as the sole explanation for their stability. Although their experiments seem to contradict the solid-like structure of gas-fluidized particles, they reported that there are possibilities of smaller, temporary structures in the bed due to fluid dynamic interactions, but they did not provide detailed explanation on the physical mechanisms governing the evolution of these structures.

Empirical observations on magnetically stabilized beds (MSBs) appear to cast doubt on Gilberton & Yates (1996) conclusions. In these experiments, interparticle forces are induced on fluidized particles by applying an external magnetic field. Rosensweig (1979) carried out the fluidization of magnetisable particles by a gas stream in the presence of a uniformly applied magnetic field. He reported that fluid dynamic instability due to formation of bubbles was curtailed. The fluidized suspension expanded uniformly in a manner typical of Geldart A powders. Visual observations of the bed suggested that the MSB is free of agitation and solid recirculation, implying that the bed acquired a solid-like structure where particles are held together in enduring contacts by the magnetically induced interparticle forces. If interparticle forces did not play a dominant role in the stabilization, as Gilberton & Yates (1996) suggested, then the application of external magnetic field on the fluidized bed would not result in a dramatic change in the fluidization behaviour. Figure 2.2 shows Rosensweig's comparison of

ordinary fluidized beds and MSBs. Further experimental studies revealed that the fluidity of MSBs decreases continuously as the magnetic field strength is increased, indicating that the bed becomes more solid-like. Lee (1983) measured the yield stress in a MSB. He reported that there is an appreciable yield stress in the bed which increased monotonically as the magnetic field strength is increased. The yield stress arises owing to the sustained contacts among particles as the interparticle forces increased.

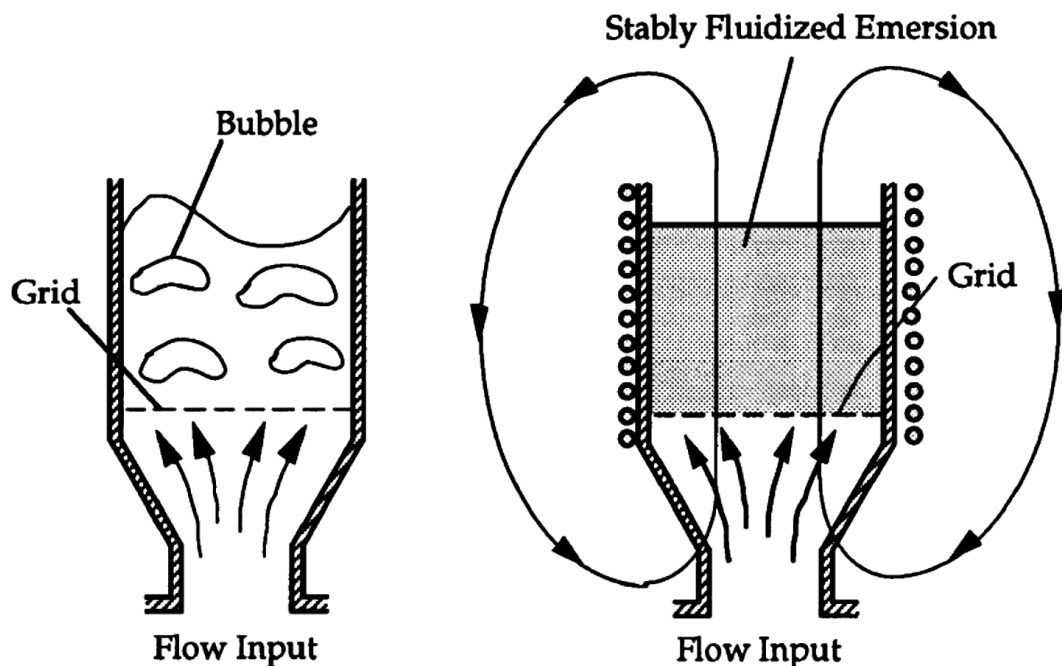


Figure 2.2: Comparison between an ordinary fluidized bed and a magnetized fluidized bed (Rosensweig, 1979)

The dynamics of magnetically fluidized beds, as revealed by Valverde (2003), is controlled by the balance between the magnetically induced interparticle forces and the drag force. As the strength of the field increases, particles tend to form chains due to the prevalence of magnetic attractive forces over the drag force that tends to separate them. Further increase in the magnetic field strength leads to crowding of these chains of particles, causing the suppression of bubbles. To further investigate the solid-like structure of gas-fluidized beds, Espin et al. (2011) applied an external magnetic field to a naturally stabilized bed. They observed that the field does not

cause a remarkable increase in yield stress as one would expect. The reason for this, they reported, was that the field was applied when the particles were already fixed and therefore they were not free to rearrange. Their experimental results showed that interparticle forces provide the bed with a yield stress that stabilizes it, thus delaying the formation of bubbles.

Tsinontides & Jackson (1993) investigated the stability of gas-fluidized beds by carrying out fluidization and defluidization of FCC particles. They measured the pressure drop and bed height as a function of superficial gas velocity. Their measurements revealed hysteresis between the fluidization and defluidization pressure drop and bed height curves. This strongly suggests the existence of compressive yield stress in the particle assembly which forms the expanded bed. Tsinontides & Jackson also demonstrated that the fluidized particles behave like a weak solid with an effective elastic modulus, revealing a solid-like behaviour of fluidized systems. To do this, they slowly increased the superficial gas velocity of a partially compacted bed. They observed no significant change in bed height, signifying that the bed has an ability to resist compression and confirming that it has a measure of elasticity arising from the sustained contacts among particles. Similar conclusions were made by several authors; see for instance Loezos et al., 2002; Srivastava & Sundaresan, 2002; Jackson, 2000. Tsinontides & Jackson measured the axial solid volume fraction along in the bed using a high resolution gamma-ray densitometer. Their measurements showed that a solid volume fraction profile developed along the vertical bed axis, implying that the particles are in contact and a finite yield stress exists.

To further demonstrate the existence of yield stresses in a homogeneous gas-fluidized bed, Menon & Durian (1997) studied the motion of particles in a gas-fluidized bed. They measured the reflection of laser light from fluidized glass beads using diffusion-wave spectroscopy. They found no fluctuations in the interval of stable expansion. Their results revealed the presence of enduring contacts among particles due to the existence of interparticle forces in the bed. Fluctuations in particle motion, according to Reitema (1973), can only be initiated by instability due to bubbling. This observation revealed that the homogeneous state of the bed behaves like a

weak solid, supporting the solid-like behaviour of Geldart A powders. Similar measurements were made by Cody et al. (1996). They measured bed expansion and shot noise due to particle impacts on the wall of a bed of FCC powder. They reported that the bed was completely silent in the stable interval of homogeneous expansion until the superficial gas velocity reached a certain critical value.

The fundamental role of interparticle forces in stabilizing the fluidization of Geldart A powders was demonstrated by Marzocchella & Salatino (2004). They fluidized the particles using carbon dioxide at pressures ranging from subcritical to supercritical conditions. As they varied the pressure, the fluid density changed from the values typical of gases to those of liquids, and hence the fluid dynamic behaviour of the bed changed. They observed that the increase in fluid density causes the interval of bubble-free expansion to be extended. They carried out a statistical analysis of the heat transfer coefficient fluctuations in the bed. The analysis revealed a negligible fluctuation in the interval of homogeneous expansion, signifying that particle mobility is substantially hindered at superficial gas velocities within the range of homogeneous expansion. This observation supports the solid-like behaviour of Geldart A powders.

The solid-like behaviour of Geldart A powders is not only demonstrated by experimental investigations. Koch & Sangani (1999) studied the behaviour of Geldart A powders using the kinetic theory. They derived the particle-phase pressure for a homogeneous suspension of particles, and carried out a linear stability analysis of the system. Their results indicated that a gas-fluidized bed where there are no enduring particle contacts is also always unstable. This led them to conclude that bubbling can only be restrained by a solid-like behaviour of expanded beds.

Similarly, Fortes et al. (1998) used a theoretical approach to provide further insight into the solid-like behaviour of Geldart A powders. They adopted the Eulerian-Eulerian modelling approach to describe the fluidized suspension. The results of their investigation show that the stability of Geldart A powders has two distinct origins: one that is fluid dynamic, arising from

the interactions between the solid and fluid phases, and one that is not, arising from interparticle forces. Their results also revealed that the latter are responsible for the formation of clusters in gas-fluidized beds and deposition of particles on the vertical walls of the bed.

Ye et al. (2005) investigated the influence of interparticle forces on the fluidization behaviour of Geldart A powders using the Discrete Element Methods (DEM). They modelled the interparticle forces by adopting the Hamaker expression for van der Waals force between two spheres. They reported that interparticle van der Waals force delays the transition from homogeneous to bubbling regime. In particular, they noted that the minimum bubbling velocity increases as the granular bond number (the ratio of interparticle forces to the weight of a particle) increases, signifying that bubbling is delayed because the interparticle forces are increased.

Experimental and theoretical investigations such as those reported above provide evidence that homogeneous gas-fluidized particles maintain a network of enduring contacts which stabilizes the bed against small perturbations. The bed thus behaves like a weak solid with an effective elastic modulus, having ability to resist compression. In contrast to the *solid-like* behaviour of gas-fluidized Geldart A powders, most beds of granular material fluidized by liquids exhibit a non-bubbling *fluid-like* behaviour; they expand homogeneously without having any form of enduring particle contacts. Therefore gas-fluidized and liquid-fluidized beds are considered as systems displaying a radically different behaviour. However, experimental observations show that gas-fluidization of fine powders also display a non-bubbling fluid-like behaviour. This observation appears to reconcile the different opinions about the forces responsible for the stability of gas-fluidized beds; the solid-like behaviour on the one hand supports the idea that interparticle forces are responsible for the stability, while the fluid-like behaviour strengthens the view of those ascribing stability to fluid dynamic forces. Before reporting on the fluid-like behaviour of gas-fluidized fluidized beds, we report its distinctive features in liquid-fluidized beds.

2.4 Fluid-like behaviour of particles fluidized by liquids

Generally, granular materials fluidized by liquid display a smooth expansion without formation of visible bubbles as the fluid velocity is increased. The particles are freely suspended in the liquid, being fully supported by the upward flow of the latter. Unlike gas-fluidized beds of Geldart A powders which show solid-like behaviour, liquid-fluidized beds display a fluid-like behaviour, having in particular no ability to transmit stress through the particulate assembly, since there are no enduring contacts among the particles. In this condition, the stability of the fluidized particles is solely due to the fluid dynamic forces arising from the interaction between the fluid and the particles.

Researchers have made considerable efforts to predict the expansion profiles of liquid-fluidized beds. These profiles provide the velocity-voidage relationship which is often of great interest in fluidized bed applications. Numerous empirical and semi-empirical correlations have been developed for the velocity-voidage relationship in liquid-fluidized beds. Most of these correlations, summarized by Jamialahmadi & Müller-Steinhagen (1992), are reported in Table 2.1. Most of the correlations reported in Table 2.1 are applicable over a restricted range of Reynolds number, except for the Richardson & Zaki (1954) equation which covers the fluid dynamic regime from viscous to inertial flow. The Richardson & Zaki (1954) equation is the most widely used of all; hence we will place more emphasis on it. Although it was developed for particles falling in a stationary liquid under the influence of gravity, it is justifiable to use the equation for liquid fluidized beds, since sedimentation and fluidization are similar processes viewed from different frames of reference. When the Richardson & Zaki equation is employed in fluidization processes, the sedimentation velocity u becomes the superficial liquid velocity. Over the years, the equation has proved to be accurate in providing an excellent account of expansion profiles of non-bubbling liquid-fluidized beds.

Table 2.1: Correlations for predicting bed expansion in liquid-fluidized beds

Author	Equation	Range of Application	Type of equation
Steinour (1944)	$\frac{u}{u_t} = \varepsilon^2 \exp[-4.19(1 - \varepsilon)]$	$Re_t < 0.2$; $\varepsilon < 0.85$	Semi-empirical
Brinkman (1947)	$\frac{u}{u_t} = 1 + 0.75(1 - \varepsilon) \left[1 - \left(\frac{8}{1 - \varepsilon} - 3 \right) \right]^{0.5}$	$Re_t < 2$	Theoretical
Lewis et al. (1949)	$\frac{u}{u_t} = \varepsilon^{4.65}$	$1.1 < Re_t < 2.6$	Empirical
Hawksley (1951)	$\frac{u}{u_t} = \varepsilon^2 \exp\left(-\frac{2.5(1 - \varepsilon)}{1 - 39(1 - \varepsilon)/64}\right)$	$0.001 < Re_t < 58$	Semi-empirical
Jottrand (1952)	$\frac{u}{u_t} = \varepsilon^{5.6}$	$0.001 < Re_t < 0.4$	Empirical
Lewis & Bowerman (1952)	$\frac{u}{u_t} = 0.9\varepsilon^{2.97}$	$2 < Re_t < 500$	Empirical
Richardson & Zaki (1954)	$n = 4.65 + 20d_p/D$ $\frac{u}{u_t} = \varepsilon^n$ $n = (4.4 + 18d_p/D)Re_t^{-0.03}$ $n = (4.4 + 18d_p/D)Re_t^{-0.1}$ $n = 4.4Re_t^{-0.1}$ $n = 2.4$	$Re_t < 0.2$ $0.2 < Re_t < 1$ $1 < Re_t < 200$ $200 < Re_t < 500$ $Re_t > 500$	Semi-empirical
Happel (1958)	$\frac{u}{u_t} = \frac{3 - 4.5(1 - \varepsilon)^{\frac{1}{3}} + 4.5(1 - \varepsilon)^{\frac{5}{3}} - 3(1 - \varepsilon)^2}{3 + 2(1 - \varepsilon)^{\frac{5}{3}}}$	$Re_t < 0.2$	Theoretical
Oliver (1961)	$\frac{u}{u_t} = (1 - 2.15(1 - \varepsilon)) \left[1 - 0.75(1 - \varepsilon)^{\frac{1}{3}} \right]$	$Re_t < 0.4$	Semi-empirical
Letan (1974)	$\frac{u}{u_t} = \frac{(1 + 0.15Re_t^{0.687})\varepsilon^{4.5}}{1 + 0.15 \left(Re_t \frac{u}{u_t} \right)^{0.687} \varepsilon^{1.033}}$	$1.5 < Re_t < 2200$	Semi-empirical
Foscolo et al. (1983)	$\frac{u}{u_t} = \frac{\varepsilon^4}{4(1 - \varepsilon) + \varepsilon^3}$ $\frac{u}{u_t} = \frac{0.0777Re_t(1 + 0.01941Re_t)\varepsilon^{4.8} - 1}{0.0288Re_t}$ $\frac{u}{u_t} = \left[\frac{\varepsilon^4}{3.55(1 - \varepsilon) + \varepsilon^3} \right]^{0.5}$	$Re_t < 0.2$ $0.2 < Re_t < 500$ $Re_t > 500$	Theoretical

It is important to note that the Richardson & Zaki (1954) equation, and indeed other correlations reported in Table 2.1, are purely fluid dynamical and entirely unrelated to particle-particle interactions in the bed. These correlations were derived for monodisperse spherical particles which are *uniformly* suspended in the fluid; hence they are appropriate for investigating fluidized systems manifesting fluid-like behaviour. Nonetheless, as we shall see in Chapter 3, these equations (in particular the Richardson & Zaki equation) have also been employed to study the behaviour of gas-fluidized in the solid-like regime, such as those reported in Section 2.2.

Although most liquid-fluidized beds exhibit non-bubbling behaviour, displaying smooth appearance and expanding progressively as fluid velocity is increased, Anderson & Jackson (1969) reported a different observation in their liquid-fluidized bed of glass beads. Their experiment was carried out in a 1.8 m tall cylindrical tube. They observed that the bed of glass beads was traversed by one-dimensional travelling voidage wavefronts. They observed that the amplitude of these waves increased exponentially as the distance from the distributor plate increased, signifying that the bed is by no means uniform beyond a certain extent of bed expansion. Similar observations were reported by Ham et al. (1990). They studied the homogeneous fluidization of small particles with liquid. They conducted a wide range of experiments changing the particle size, particle density and fluid properties. They measured instabilities in the bed using light extinction technique proposed by Anderson & Jackson (1969). This technique measures the amount of light attenuation by particles in suspension and uses this to calculate particle concentration in the bed. Ham et al. (1990) reported that uniform fluidization exists between the minimum fluidization velocity and a certain critical velocity u_c beyond which the bed began to be unstable with significant particle velocity fluctuations. These observations made researchers conclude that non-uniform structures (bubbles) do exist also in liquid-fluidized beds, but they occur very slowly, whereas in gas-fluidized beds the evolution of

these non-uniform structures occurs very rapidly (Anderson et al., 1995; Glasser et al., 1997; Homsy, 1998; Duru & Guazzelli, 2002).

Table 2.2: Cases of bubbling behaviour in liquid-fluidized beds

Author	Powder	Experimental method	Observations
Wilhelm & Kwauk (1948)	1.3mm lead shot	Visual observations	Bubbling and intermittent motion
Peck & Watkins (1956)	7mm glass beads	Visual observations	Bubbling fluidization with pockets of water
Hanratty & Bandukwala (1957)	0.56mm steel spheres	Visual observations	Motion of solids similar to gas-solid systems
Cairns & Prausnitz (1960)	3mm glass and lead spheres	Visual observations	Bubbling and void waves moving upwards
Harrison et al. (1961)	0.7mm lead shot	Visual and still photographs	Bubbling behaviour
Hasset (1961a,b)	1-1.5mm glass ballotini	Visual and still photographs	Partial voids and bubbles observed
Kelly (1961)	9-19mm steel ball	Gamma rays absorption	Slugging bed with large density fluctuations
Simpson & Roger (1961)	1.71mm lead shot	Visual observations	Lens-shaped bubbles at the bed wall and top
Reuter (1964)	1mm lead shot	Photographs	Bubble shape similar to gas-fluidized beds
Volpicelli et al. (1966)	3mm plastic and steel spheres	Photographs	Non-uniform particle distribution
Bicknell & Whitmore (1967)	9-12mm resin spheres	Visual observations	Waves of high voidages travelling upwards
Trupp (1968)	1.2-9.7mm glass and lead spheres	Visual observation and high-speed movie	Parvoids for glass bed and Sloshing of the lead bed
Garside & Al-Dibouni (1973)	1.8-3mm glass ballotini	Visual observations	Boiling appearance of bed surface
Kwauk (1973)	0.5-4mm glass spheres	Still photographs	Dense and dilute region present in the bed
El-Kaissy & Homsy (1976)	0.5-1.4mm glass beads	Visual observations and light transmitting techniques	Horizontal waves and high voidage regions measured
Kmiec (1978)	6mm glass beads	Photographs	Inhomogeneity in particle distribution
Didwania & Homsy (1981a)	0.5-1.1mm glass beads	Light transmission and optical scanning	Wavy, turbulent and bubbling regimes
Dorgelo et al. (1985)	10mm marble	Visual observations	Slugging behaviour observed

The experimental evidence reported above demonstrates that liquid-fluidized beds (*in general fluidized beds in the fluid-like regime*) are not uniform over the entire range of bed expansion, although these non-uniform structures rarely develop into macroscopic bubbles. To the naked eye, a fluidized bed in the fluid-like regime appears smooth and uniform; nonetheless the existence of mesoscale non-uniform structures proves that such beds are not really homogeneous.

The origin of non-uniform structures in liquid-fluidized beds has been associated with particle inertia, resulting from the relative motion between the fluid and particles. The relative motion between them is assumed to impart a fluctuating velocity on the particles. The velocity fluctuations generate a particle phase pressure p_s and viscosity μ_s , both of which are functions of ϕ . This in turn generates an effective elasticity on the particle phase $dp_s/d\phi$. If the latter is greater than zero and is sufficiently large to overcome the destabilization arising from particle inertia and voidage dependence on the drag, the bed is stable; otherwise the bed becomes unstable (Sundaresan, 2003).

Although, generally, liquid fluidization of granular materials can be extremely smooth, and in some cases characterised by the evolution of mesoscale structures, such as those reported in the preceding paragraphs, it is indeed possible for such beds to exhibit macroscopic bubbling. This was first observed by Wilhelm & Kwauk (1948) for the fluidization of lead spheres by water. Since then, several other experimental works which confirmed the bubbling behaviour of liquid-fluidized beds have been reported in the literature. These are summarized in Table 2.2.

It is interesting to note that the similarity between liquid-fluidized beds and gas-fluidized beds is quite remarkable. Some liquid-fluidized beds reported in Table 2.2 bubble as soon they are fluidized; a behaviour typical of Geldart B powders fluidized by gas, while some expand over a substantial interval of superficial gas velocity before bubbling, similar to what is observed for

Geldart A powders. In the latter, however, the bubble-free expansion is usually characterised by solid-like behaviour, while for liquid-fluidized beds the behaviour is completely fluid-like.

2.5 Fluid-like behaviour of fine particles fluidized by gas

We reported in Section 2.2 that gas-fluidization of Geldart A powders results in homogeneous expansion over an interval of superficial gas velocity. Experimental observations revealed that such homogeneous expansion is possible because the fluidized particles maintain a network of enduring contacts. The latter, as said, confers to the bed an effective elastic modulus which stabilizes the bed against small perturbations and delays their bubbling. The bed therefore behaves like a weak solid having the ability to resist compression – a behaviour referred to as solid-like behaviour. In this section we wish to clarify that the solid-like behaviour is not a necessary condition for the homogeneous gas-fluidization of all kinds of particles. Indeed, as experimental observations reveal, highly cohesive powders (such as Geldart C powders) fluidized by gas can exhibit non-bubbling fluid-like behaviour typical of granular materials fluidized by liquids reported in Section 2.3. However, to achieve this, fluidization assisting methods need to be used. These methods act in a way to reduce the interparticle forces in the bed, thus enhancing the fluidization of these highly cohesive powders. Before reporting on the fluid-like behaviour of gas-fluidized fine particles, we will briefly review the various assisting methods that have been employed to enhance the fluidization of highly cohesive powders.

2.5.1 Fluidization assisting methods

The assisting methods used in fluidization of highly cohesive powders include the use of acoustic wave, mechanical vibration, magnetic/electric field, tapered beds and the addition of foreign materials (also called flow control additives).

2.5.1.1 Sound assisted fluidization

Morse (1955) was the first author to study the fluidization behaviour of cohesive powders under the influence of acoustic fields of various sound pressure levels and frequencies. He applied an acoustic field to the bottom of the bed using loudspeakers. He found that submicron particles which had shown intense channelling were smoothly fluidized when he applied an acoustic field with a frequency in the range of 50 to 500 Hz. Other researchers (Chirone et al., 1992, 1993; Russo et al., 1995; Levy et al., 1997; Guo et al., 2005, 2006) have reported enhanced fluidization with the use of acoustic waves. The common observation among these researchers is that there is a minimum sound pressure level below which the acoustic field does not have any effect on the fluidization quality of fine powders. They reported that when the sound pressure level is below this minimum, the acoustic oscillation strength is not high enough to initiate fluidization. They also observed that large agglomerates are formed in the bed when the sound pressure level is very high due to greater collisions between the particles and smaller agglomerates.

2.5.1.2 Mechanical vibrations

Fluidization of highly cohesive powders has been achieved with the aid of mechanical vibrations. Dutta & Dullea (1991) used external mechanical vibrations to improve the fluidization quality of fine powders. Several others (Marring et al., 1994; Noda et al., 1998; Wank et al., 2001; Tasirin & Anuar, 2001; Mawatari et al., 2002; Xu et al., 2004; Valverde & Castellanos, 2006; Levy & Celeste, 2006; Harris, 2008; Zhang & Zhao, 2010; Wang et al., 2010; Kaliyaperumal et al., 2011) have also achieved a smooth fluidization of Geldart C powders with the aid of mechanical vibrations. Despite the success of this method in enhancing the fluidization of highly cohesive powders, more research is needed to clarify the effects of vibration frequency and amplitude on fluidization behaviour (Shabaniyan et al., 2012).

2.5.1.3 Magnetically assisted fluidization

This method involves the use of oscillating magnetic fields to enhance the fluidization of fine and ultrafine particles. This method has been generally implemented to enhance either the

fluidization of magnetic particles or a mixture of magnetic and non-magnetic particles. To achieve fluidization, the particles reorganize themselves to form a chain structure along the lines of the magnetic field. Zhu & Li (1994, 1996) reported that the chain structures block the channels and eventually eliminate them, allowing for even distribution of gas through the bed and thus enhancing fluidization.

2.5.1.4 Electrically assisted fluidization

Kashyap et al. (2006, 2008) investigated the influence of electric fields on the fluidization behaviour of fine particles. They reported that cohesive particles were fluidized with a considerable bed expansion under the influence of an electric field. The latter breaks the cohesive forces among the particles, thus enhancing their fluidization. Several others (Valverde, 2008; Quintanilla et al., 2008; Leppek et al., 2010) have also reported improved fluidization of fine particles with the aid of externally applied electric fields.

2.5.1.5 Centrifugal fluidized beds

Qian et al. (2001) studied the effect of centrifugal force on the fluidization of fine particles theoretically. They reported that particles belonging to Geldart C classification will manifest Geldart A behaviour under the action of a centrifugal force. To confirm their theoretical studies, they fluidized $7\mu\text{m}$ alumina particles (Geldart C powder) in centrifugal fluidized bed operating at a high rotating speed. They reported that at a sufficiently high speed of rotation, the bed behaves like a Geldart A powder.

2.5.1.6 Tapered fluidized beds

Vankatesh et al. (1996) showed that using a fluidized bed with a conical base, having an expanding section along the direction of flow, greatly enhanced the fluidization of fine particles. Others (Yang, 2005; Tong et al., 2004) have also reported improved fluidization quality with the use of tapered beds.

2.5.1.7 Addition of foreign particles

This method has significant advantages over those previously discussed. Most methods described above are difficult to implement for large-scale applications, requiring significant modifications to the fluidized bed reactors (Valverde, 2003). Some of these methods are not economically feasible except for selected applications, for instance the use of external mechanical vibrations and oscillating magnetic field (Ajbar et al., 2011). Addition of foreign particles however does not need any change to the reactor. This method can be used for a wide range of particle size, shape and density (Zhou & Li, 1999; Song et al., 2009; Ajbar et al., 2005). Owing to the advantages of this method over others, it has been widely adopted to investigate the fluid-like behaviour of fine powders.

Valverde et al. (2001) investigated the non-bubbling fluid-like behaviour of gas-fluidized beds by adding foreign particles, to which they referred as *flow control additives*, to the fine powder. Their investigations revealed that the non-bubbling fluidization of these conditioned powders exhibit both solid-like (the Geldart A behaviour reported in Section 2.2) and fluid-like (the general behaviour of liquid-fluidized beds reported in Section 2.3) behaviour. They reported that the solid-like behaviour was observed at superficial gas velocities below a critical value v_g , and the fluid-like behaviour was observed for higher values of the superficial gas velocity. To demonstrate this, they fluidized toner powders of two different colours – yellow and magenta, having mean size of $8.53\mu m$. To enhance their fluidization, the powders were conditioned by adding flow control additives. They placed the powders in a container divided into two equal halves by a vertical removable partition; the magenta powder on one side and the yellow powder on the other side of the partition. The powders were then subjected to an upward flow of air. When the powders were fluidized, the partition was carefully removed. For values of superficial gas velocities below v_g no mixing was observed between the yellow and magenta powders, signifying that the particles were held in permanent contacts – a solid like behaviour. In this condition, they observed that the gas pressure drop was below the weight of the particles

per cross sectional area, implying that a fraction of particles derive support from their mutual permanent contacts and that the bed has a certain measure of mechanical strength. To further confirm this, they did a similar experiment to Reitema (1973). They tilted the bed slowly and observed that the bed remained stable while its upper surface was also tilted. When the superficial gas velocity was increased above v_g , a radically different behaviour was observed. Even though the bed did not manifest bubbling behaviour, the yellow and magenta powders mixed successfully. The bed weight was fully supported by the gas flow; the gas pressure drop being exactly equal to the bed weight per cross sectional area. In this state, stresses due to enduring interparticle contacts vanished. Stresses in the bed were now generated by collisions among the particles due to fluctuations in their motion and the non-bubbling fluidized state is purely a result of fluid dynamic interactions in the bed, as in the case of liquid-fluidized beds discussed in the preceding section. Valverde et al. (2001) reports that the non-bubbling fluid-like bed has some properties of a liquid. For instance, when the bed enters the fluid-like regime, its upper surface remains horizontal when it was tilted just like one would expect a liquid to behave. They also measured the diffusion coefficient of magenta powder as it mixes with the yellow powder. They reported that the diffusion coefficient is a strong function of superficial gas velocity, increasing exponentially with the latter.

Valverde (2003) investigated the effect of particle size on the fluid-like regime of gas-fluidized powders. They reported that the range of superficial gas velocity in which the bed manifests fluid-like behaviour increased as the particle size reduces. From their results they sought to establish a link between the two agents of stabilization proposed for gas-fluidized beds – fluid dynamic and interparticle forces. They reported that the reduction in the extent of fluid-like regime as the particle size is increased revealed the reduced contribution of fluid dynamic forces on bed stability. They observed that when the particle size is such that the granular Bond number was $B_n \leq 1$, the fluid-like regime disappeared completely, indicating that the stability of the bed is due to enduring contacts in the particulate assembly. The fluidization behaviour is now similar to what one observes in the fluidization of Geldart A powders.

The non-bubbling fluid-like behaviour of gas-fluidized beds is quite similar to the fluid-like behaviour of liquid-fluidized beds. In the latter, as reported in Section 2.3, the absence of macroscopic bubbling does not necessarily mean that the bed is stable (Homsy, 1998; Jackson, 2000; Duru & Guazzelli, 2002). Similarly, the smooth expansion of gas-fluidized bed in the fluid-like regime does not mean that the bed is stable. Experimental observations by Valverde (2003) revealed the existence of mesoscale structures in the bed. As they increased the superficial gas velocity the number of local voids detected in the bed increased until the bed enters the bubbling regime. Furthermore density fluctuations, measured by fluctuations in light reflectance, increase with bed height for values of gas velocities below the minimum bubbling velocity. For velocities above the latter, these fluctuations continue to grow without limit. A similar result was obtained by Duru & Guazzelli (2002) by direct visualization of liquid-fluidized beds.

Although there are similarities between non-bubbling fluid-like regime of gas-fluidized beds and liquid-fluidized beds, we should note that one striking difference exists. The non-bubbling fluid-like regime of fine powders is characterised by the dynamic aggregation of freely suspended particles. The aggregation is caused by attractions among the particles, which make them form light aggregates in the suspension. The size of the aggregates, according to Castellanos (2005), is dictated by the dynamic equilibrium between the interparticle forces and the flow shear on the surface of aggregates. The fluid-like regime of gas-fluidized beds of fine particles therefore consists of light aggregates uniformly suspended in the fluid. This type of dynamic aggregates has not been reported for liquid-fluidized beds, raising a question of whether the empirical correlations reported in Section 2.3 can be employed to investigate the fluid dynamic behaviour of non-bubbling fluid-like gas-fluidized beds.

Castellanos (2005) investigated the sedimentation of a gas-fluidized bed in the non-bubbling fluid-like regime using a modified Richardson & Zaki (1954) equation. The latter has to be modified to account for the presence of clusters. Castellanos (2005) described the settling velocity of the aggregates using the following equation:

$$u = u_a(1 - \phi_a)^n \quad (2.8)$$

where u is the superficial gas velocity, u_a is the terminal settling velocity of individual aggregates, ϕ_a is the volume fraction of aggregates and n is the Richardson & Zaki exponent. The terminal settling velocity of individual aggregates u_a and the volume fraction of aggregates ϕ_a are expressed in terms of the number of particle N per aggregate as follows:

$$u_a = u_t N/k; \quad \phi_a = \phi k^3/N \quad (2.9)$$

where k is the average ratio of aggregate size to particle size, u_t is the terminal settling velocity of a particle and ϕ is the particle volume fraction. If we substitute Eq.2.9 into Eq.2.8 we obtain:

$$\frac{u}{u_t} = \frac{N}{k} \left(1 - \frac{\phi k^3}{N} \right)^n \quad (2.10)$$

Eq. 3.0 is the modified Richardson & Zaki (1954) equation for investigating the non-bubbling fluid-like behaviour of fine powders.

2.6 Conclusions

There has been a long controversy regarding the mechanism responsible for the stability of Geldart A powders. On one side of the argument are those proposing that fluid dynamic forces are responsible for the stability, on the other side others ascribed the stability to the existence of interparticle forces in the bed. Experimental observations revealed that gas-fluidized beds of Geldart A powders have an effective elastic modulus which stabilizes the bed against small perturbations. The elastic modulus arises because particles in the bed form a network of enduring contacts which confers to the bed a certain mechanical strength which allows the particles to be stable over a certain range of superficial gas velocity before transiting to bubbling; a behaviour referred to as solid-like. The solid-like behaviour strengthens the idea that interparticle forces are responsible for the stability of Geldart A powders. The solid-like behaviour of gas-fluidized particles is different from the fluid-like behaviour observed in liquid-fluidized beds. In liquid-fluidized beds particles are uniformly suspended in the fluid and

enduring particle contacts are absent. In the fluid-like state, the stability of the bed is purely a result of fluid dynamic forces arising from fluid-particle interactions.

Valverde (2001) sought to reconcile the arguments on the stabilizing agents of gas-fluidized beds. He demonstrated that the homogeneous regime of gas-fluidized particles consists of both solid-like and fluid-like regimes. The latter prevails when the superficial gas velocity is increased above a certain critical value, and the bed is fluidized in a manner similar to liquid-fluidized beds. He showed that the extent of the fluid-like regime reduces as the particle size increases; most gas-fluidized beds of Geldart A particles are fluidized in the solid-like regime. In the following chapter the behaviour of this class of powder is studied more closely using theoretical and experimental methods.

Chapter 3

Theoretical and experimental investigation of the behaviour of homogeneous gas-fluidized beds

This chapter is concerned with an investigation on the mechanics of homogeneous expansion in gas-fluidized beds using experimental and theoretical approaches.

1. We recap some salient points raised in Chapter 2 regarding the solid-like behaviour of gas-fluidized powders.
2. We introduce the Richardson & Zaki (1954) equation, discussing on its ability to describe the expansion profiles in gas-fluidized beds.
3. We describe the process of fluidization and defluidization in gas-fluidized beds.
4. We model the homogeneous expansion in gas-fluidized beds using a linear momentum balance equation, and accounting for enduring contacts among the particles.
5. We perform fluidization and defluidization experiments to validate our numerical results.

Parts of this chapter have been published:

Oke, O., Lettieri, P., Mazzei, L. (2015). An investigation on the mechanics of homogeneous expansion in gas-fluidized beds. *Chemical Engineering Science*, 127, 95-105.

3.1 Introduction

Gas-fluidized beds of Geldart A powders manifest homogeneous expansion over a certain range of superficial gas velocity before transiting to the bubbling regime. Experimental observations have shown that this behaviour results from enduring particle contacts which confers to the bed a measure of mechanical strength which stabilizes it and therefore delays its bubbling. Conversely, for most gas-fluidized beds such enduring contacts are absent and therefore they bubble as soon as they are fluidized. These considerations have been reported in Chapter 2. In this chapter we intend to provide further insight into the stable behaviour of cohesive homogeneous gas-fluidized beds. We believe that the effect of cohesiveness in such beds is reflected by the presence of enduring contacts among the particles. These enduring contacts are characteristic of the homogeneous gas-fluidized beds in the solid-like regime; therefore we focus our analysis on it. To do this, we carried out fluidization and defluidization experiments, analysing the results using the Richardson & Zaki (1954) equation. We believe that such experiments will further give us insight into the behaviour of homogeneous gas-fluidized beds. In our analysis we also employed the linear momentum balance equation proposed by Jackson (2000), which accounts for enduring contacts among the particles, to investigate the stable behaviour of gas-fluidized particles. In what follows, we briefly review the Richardson & Zaki equation, discussing on its ability to predict the expansion profiles of gas-fluidized beds.

3.2 The Richardson & Zaki (1954) equation and homogeneous expansion of gas-fluidized beds

The expansion characteristics of homogeneous fluidized beds have been of great interest to researchers. This is because knowing the expansion of a fluidized bed is crucial to its design and operation. For liquid-fluidized beds, many empirical and semi-empirical correlations have been developed to predict the expansion profiles (refer to Table 2.1 in Chapter 2). The most widely used of these correlations is the Richardson & Zaki (1954) equation; a simple, but powerful

equation that correctly captures bed expansion over the entire fluid-dynamic regime from viscous to inertial flow. The equation reads:

$$u = u_t \varepsilon^n \quad (3.1)$$

where n is an empirical parameter which depends on the free fall particle Reynolds number Re_t , and u_t is the unhindered terminal settling velocity of the particles. Several correlations have been proposed for determining the value of n . In particular, we report the empirical relationship proposed by Rowe (1987), which we used in this work:

$$n(Re_t) = \frac{A + B \times 0.175 Re_t^{3/4}}{1 + 0.175 Re_t^{3/4}} \quad (3.2)$$

Here A and B are the values ascribed to n in the limits of viscous and inertial regimes, respectively. Richardson & Zaki (1954) take A and B to be equal to 4.65 and 2.39, respectively; Rowe (1987) employs the values of 4.70 and 2.35, while Khan & Richardson (1989) and Gibiliaro (2001) use 4.80 and 2.40. The unhindered terminal settling velocity u_t , on the other hand, can be obtained in the creeping flow regime using the well-known Stokes equation:

$$u_t = \frac{(\rho_p - \rho_f) g d_p^2}{18 \mu_f} \quad (3.3)$$

Here μ_f and ρ_f are the viscosity and density of the fluid, respectively, d_p and ρ_p are the particle diameter and density, respectively, and g is the gravitational acceleration. Other expressions have been suggested as an improvement to the Richardson & Zaki (1954) equation, but their ability to predict the expansion profiles of homogeneous fluidized beds do not differ significantly from the latter (see for instance Garside & Al-Dibouni, 1977; Riba & Couderc, 1977; Hirata & Bulos, 1990).

The Richardson & Zaki (1954) equation and the correlations proposed for estimating the exponent n are found to hold for liquid-fluidized systems, where they are very accurate in providing an excellent account of the expansion profiles of such systems. The values of the parameter n in such systems range from 2.35 to 4.8 in the limits of inertial and viscous regimes.

But questions were raised regarding the applicability of this correlation to gas-fluidized systems. While trying to answer these questions, Godard & Richardson (1968) conducted several experiments on powders fluidized by air and characterized by extremely narrow size distributions. They found that the relationship between the superficial fluid velocity and the void fraction could be expressed in the Richardson & Zaki form, given in Eq. 3.1; however, the values of the exponent n for all the powders tested were found to be greater than those predicted by Eq. 3.2. They also found that the values of the parameter u_t determined by extrapolating the logarithmic void fraction-velocity plots were greater than the terminal velocity of the particles. To emphasize this, we shall denote these experimental values as n^* and u_t^* . The latter, as said, differ from the fluid dynamic values of n and u_t observed in liquid-fluidized beds and predicted by Eqs. 3.2 and 3.3, respectively.

Lettieri et al. (2002) studied the homogeneous bed expansion of FCC catalysts fluidized by gases at high temperatures. They employed the Richardson & Zaki equation to describe the homogeneous expansion of these particles, estimating the values of the parameters in the equation. These values were compared with those of n and u_t predicted by Eqs. 3.2 and 3.3, respectively; for all the FCC catalysts considered, they found that the former (that is, n^* and u_t^*) were much higher than the latter (that is, n and u_t). They attributed this to the formation of clusters in the bed, which are caused by the presence of interparticle forces.

In the same vein, Geldart & Wong (1984, 1985) investigated the bed expansion characteristics of Group A powders. They fluidized different materials with different gases and found the values of n^* between 4 and 60, showing that materials with higher cohesiveness have greater values of the exponent. The summary of their experimental work is reported in Table 3.1. Moreover, they observed that in non-cohesive systems, the value of the terminal velocity given by the Stokes equation is very close to that extrapolated from the logarithmic plot of the Richardson & Zaki equation, whereas for cohesive systems it is greater.

Table 3.1: Richardson & Zaki (1954) exponent (Geldart & Wong, 1984)

Fluid	Powder Type	Geldart Group	n
Air	$\alpha 320 - N$	AC	6.60
	$\alpha 320 - O$	A	6.82
	$\alpha 360$	AC	12.24
	$A4$	AC	7.55
	$FRF5$	A	5.21
	$FRF20$	C	15.75
	$FRF40$	C	60.00
	$FRF85$	C	51.00
	$9G4$	A	4.38
	CI	A	5.95
	II	A	4.00
	$F0.3$	A	7.76
	$F3/7$	A	5.19
	FSG	A	4.96
	$F2/5$	A	4.48
$Lactose$	C	35.03	
Nitrogen	$\alpha 320 - N$	AC	6.61
	$A4$	AC	7.55
	$9G4$	A	5.20
	$FRF5$	A	4.38
	CI	A	5.91
	$B20$	A	5.50
Arction - 12	$A4$	AC	8.00
	$FRF5$	A	7.21
	$B20$	A	5.21

All the foregoing experimental evidence, and much more not reported here, allow us to conclude that the Richardson & Zaki equation is capable of describing the bed expansion of gas-fluidized particles, but the values of the equation parameters are greater than those required for liquid-fluidized systems (in general, fluidized systems in which fluid dynamic forces dominate over interparticle forces). Researchers have presented compelling experimental evidence to show that the greater values obtained for the parameters are indications of the presence of interparticle forces. For instance, Geldart & Wong (1984) correlated the $n / 4.65$ to the Hausner

ratio, ρ_{PL} / ρ_{LP} (where ρ_{PL} is the bulk density of the powder under prolonged tapping and ρ_{LP} is the bulk density obtained under loose packing condition). The higher the Hausner ratio, the more significant is the role of interparticle cohesive forces. Similarly, Lettieri et al. (2002) reported an increase in the value of n with temperature. These observations appear to support the idea that these forces play a crucial role in the stabilization of gas-fluidized fine powders.

We should note that the expansion of non-cohesive homogeneous powders depends only on the drag force exerted by the fluid on the particles, in addition to the effective weight of the latter; as a consequence, the values of n and u_t (which refer to liquid-fluidized beds, in which interparticle forces are negligible compared to their fluid dynamic counterpart) are directly related to the drag force magnitude. Conversely, the expansion of cohesive powders depends not only on the fluid dynamic forces just mentioned, but also on the forces that the particles exert on one another; accordingly, the values of n^* and u_t^* (which refer to gas-fluidized beds, in which interparticle forces are often as important as their fluid dynamic counterpart) lump together the effects of both forces and are not directly related only to the drag force magnitude. This observation is important when one intends to model the drag force.

In this chapter, our goal is to investigate the homogeneous regime in gas-fluidized beds, intending to show that the stress transmitted through sustained contacts among particles plays a role in the bed homogeneous behaviour and is responsible for the higher values of n^* and u_t^* observed experimentally for fine particles. To this end, we employed a theoretical model to analyse the expansion of gas-fluidized powders, taking into consideration enduring particle-particle contacts. We used the model to determine the axial void fraction profiles through the bed at different superficial gas velocities. By plotting the mean void fraction against the superficial gas velocity in the Richardson & Zaki form, we then computed the values of the parameters n and u_t which appear in the correlation. We then conducted fluidization and defluidization experiments to validate our theoretical results. Before presenting the model, we

briefly report on the processes of fluidization and defluidization, on which the remaining part of this work focuses.

3.3 The processes of fluidization and defluidization of fine particles

In describing these processes, we find it more convenient to examine defluidization first. Consider a fluid bed of small, light particles, such as those belonging to Group A of the Geldart (1973) classification. We assume that the bed is homogeneous and in the *fluid-like* regime, so that *no enduring contacts are present* among the particles. These, in consequence, are fully supported by the fluid. Being the bed homogeneous, the volume fraction of solid, denoted as ϕ , is uniform throughout it. If we slightly decrease the fluid flow rate, the bed contracts, remaining uniform and in the fluid-like regime, until ϕ attains the value needed by the drag force to balance the effective weight of the bed. If we continue to decrease the fluid flow rate, the volume fraction of solid will eventually reach a value ϕ_{\min} at which the granular material is able to resist compression. When the bed reaches this compaction, it enters the *solid-like* regime, in which *particles do form enduring contacts* and the bed starts behaving like a weak solid. The more ϕ exceeds the value ϕ_{\min} (that is, the more compact the bed), the larger the stress needed to cause compressive yield (that is, further bed compaction). We assume that the compressive yield stress tends to infinity at some value ϕ_{\max} ; when the bed reaches this compaction, it cannot compact further, no matter how large the compressive stress to which it is subjected becomes. Hence, with Tsinontides & Jackson (1993), we can model the compressive yield stress using the following constitutive equation:

$$\begin{aligned} \sigma_c(\phi) &= c \frac{(\phi - \phi_{\min})^a}{(\phi_{\max} - \phi)^b} & \phi_{\min} < \phi < \phi_{\max}, \\ &= 0 & \phi < \phi_{\min} \end{aligned} \quad (3.4)$$

where a , b and c are positive constants which must be determined experimentally. As said, ϕ_{\min} denotes the lowest solid volume fraction at which the assembly of particles is capable of supporting stress through a structure of enduring contacts, whilst ϕ_{\max} denotes the

highest solid volume fraction that one can obtain in a defluidization process without resorting to mechanical means. The interval between ϕ_{\max} and ϕ_{\min} is largely determined by the *cohesiveness* of the material. For large, smooth, non-cohesive particles, such as those belonging to Groups B and D of the Geldart (1973) classification, ϕ_{\max} and ϕ_{\min} are very close; this is because particles are brought to random close packing under very small compressive stress, insofar as they are unable to form a network of enduring contacts. For small, rough, cohesive particles, which are able to form such a network, the interval between ϕ_{\max} and ϕ_{\min} is instead much larger. These groups of particles are able to form extended structures which can resist compressive stress over a broader range of particle concentration. This might explain why, during fluidization, they can expand homogeneously over a wide range of superficial gas velocity before transiting to the bubbling fluidization regime. In this work, we focus on this second group of particles.

When the bed enters the solid-like regime, its structure is uniform – the solid volume fraction being equal to ϕ_{\min} everywhere. In this condition, the bed is still fully supported by the fluid. But when the fluid flow rate is decreased further, the bed compacts non-uniformly, the mean bulk density increasing progressively from the top of the bed to its bottom: *a solid volume fraction profile develops along the vertical bed axis*. In particular, if we assume that the bed is in a condition of incipient yield everywhere, in each location the solid volume fraction takes the value required by the compressive yield stress to equate the compressive stress present at that location. The bed is only *partially fluidized*, being partly supported by the distributor plate and partly by the frictional forces acting between the walls of the vessel and the particles. And even if the bed may look homogeneous to the naked eye, it is not. When the fluid flow rate vanishes, the bed is completely defluidized and fully supported by the distributor plate and the vessel walls; also in this case, the bed is inhomogeneous, the solid volume fraction increasing towards the bed bottom.

Consider now the bed of granular material that is resting on the distributor plate. If an upward flow of gas is established, the bed structure, and in particular the solid volume fraction profile

along the vertical axis of the bed, initially remains unchanged, the pressure drop through the bed rises, and the particles become partly supported by the drag force exerted on them by the fluid. At a sufficiently large flow rate, the bed weight is entirely supported by the drag force, but in general the bed retains its structure, without dilating (in other words, it does not fluidize). A further increase in gas flow rate generates tensile stress within the granular material. When the latter exceeds the tensile yield stress which the material may sustain, the bed breaks and fluidization begins. When this happens, the pressure drop, and hence the drag force, is equal to the sum of the weight of the bed and the tensile yield stress which must be exceeded before the bed dilates (Tsinontides & Jackson, 1993; Watson et al., 2001).

The condition for the bed to dilate, according to Tsinontides & Jackson (1993), is first met at the contact surface between the bed and the distributor plate; thus, the fluidization process commences by the fracture of the bed at its lowest point. When this happens, the stress at the bottom and top of the bed vanishes and the bed accelerates upwards. The acceleration is caused by the imbalance between the bed weight and the drag force; the latter, as said, is greater than the former when the bed detaches from the distributor plate. As the bed travels upwards, its bottom part, which is a free surface, gradually erodes, generating a rain of particles behind it. These particles recompact to form a new, more dilute bed. While the fluid flow rate is kept constant, the original packed bed continues to travel upward, gradually becoming shorter in length as its lower region progressively disappears, until it is entirely replaced by the new bed. This dynamic process is complex, and since we also lack an exact understanding of the mechanics of erosion, predicting how the newly-formed bed is structured (particularly, how the solid volume fraction varies along the bed axis) is not possible. We do not expect the bed to be at incipient yield conditions, but nothing can guarantee that it is fully supported by the fluid (and therefore fully fluidized).

The above description presents a contrary view to the conventional idea that sees fluidization as a uniform dilation process taking place throughout the particle assembly. It also makes us regard homogeneous beds differently, not necessarily as systems with uniform solid volume fraction

which are entirely supported by the fluid: this is only observed in beds that are in the fluid-like regime. More often, homogeneous beds are in the solid-like regime, and so are only partly fluidized, presenting a solid volume fraction gradient along the bed axis. Homogeneous beds do not always consist of particles which float freely in the fluid with no form of particle-particle contact. The presence of structures of sustained particle contacts in uniform beds presents a view that has to be further investigated. One often uses the Richardson & Zaki (1954) equation to describe the bed expansion of any kind of homogeneous bed, although the equation was derived merely for beds in the fluid-like regime, in which interparticle forces are absent or negligible. Also this aspect has to be investigated in more detail. This is what we now intend to do.

3.4 Theoretical analysis

The Eulerian averaged equations of motion have been used extensively to study the dynamics of fluidized particles (Oke et al., 2015; Mazzei et al., 2010; Mazzei et al., 2008; Lettieri & Mazzei, 2009; Owoyemi et al., 2007). These equations, reported hereunder, express the conservation of mass and linear momentum for the solid and fluid phases. Here we intend to use them, making necessary assumptions and simplifications, to investigate the homogeneous expansion in gas-fluidized beds. As said, solid-like homogeneous expansion occurs when the particles are able to form a network of enduring contacts; these contacts confer mechanical strength to the bed, making the latter expand over a range of fluid flow rates before the onset of bubbling. The averaged equations of motion for the fluid phase are:

$$\frac{\partial \varepsilon}{\partial t} + \nabla \cdot (\varepsilon \mathbf{u}_f) = 0 \quad (3.5)$$

$$\rho_f \frac{\partial (\varepsilon \mathbf{u}_f)}{\partial t} + \rho_f \nabla \cdot (\varepsilon \mathbf{u}_f \mathbf{u}_f) = \nabla \cdot \mathbf{S}_f - n_p \mathbf{f} + \varepsilon \rho_f \mathbf{g} \quad (3.6)$$

Those for the solid phase are:

$$\frac{\partial \phi}{\partial t} + \nabla \cdot (\phi \mathbf{u}_p) = 0 \quad (3.7)$$

$$\rho_p \frac{\partial(\phi \mathbf{u}_p)}{\partial t} + \rho_p \nabla \cdot (\phi \mathbf{u}_p \mathbf{u}_p) = \nabla \cdot \mathbf{S}_p + n_p \mathbf{f} + \phi \rho_p \mathbf{g} \quad (3.8)$$

Here ε , ϕ , ρ_f , ρ_p , \mathbf{u}_f , \mathbf{u}_p , \mathbf{S}_f and \mathbf{S}_p are, respectively, the volume fractions, densities, mean velocities and effective stress tensors for the fluid and particle phases; n_p is the particle number density, \mathbf{g} is the gravitational acceleration vector and \mathbf{f} is the interaction force per unit particle exerted by the fluid phase on the particle phase.

To apply these equations in our case, we refer to the processes of fluidization and defluidization described in the previous section. At each stage of fluidization or defluidization, the particulate assembly is assumed to be in an equilibrium state, so that the local mean value of the particle velocity is zero everywhere in the bed. This is what we try to achieve in fluidization and defluidization experiments when, at each increase or decrease of fluid flow rate, we wait for a certain period of time to allow the bed to attain fluid dynamic equilibrium before taking measurements. If the local average velocity of the particles vanishes, the linear momentum balance equation for the solid phase reduces to a force balance that one obtains by setting the left-hand side of Eq. 3.8 to zero:

$$\nabla \cdot \mathbf{S}_p + n_p \mathbf{f} + \phi \rho_p \mathbf{g} = \mathbf{0} \quad (3.9)$$

The first term in Eq. 3.9 has two major contributions: the stress transmitted through contact forces $\boldsymbol{\sigma}$ and that generated by collisions and momentum transfer owing to fluctuations in particle velocity around its local average (Jackson, 2000). Several authors have examined the magnitude of the contribution of the latter stress to \mathbf{S}_p in beds operating in the solid-like regime (see, for instance, Cody et al., 1996 and Menon & Durian, 1997). They measured the particle granular temperature, because this provides a direct indication about the contribution of collisional and kinetic stress to the total stress \mathbf{S}_p . Cody et al. (1996) measured bed expansion and shot noise resulting from the collisions of particles against the vessel walls. Their results revealed that, over a substantial range of bed expansion, the bed is completely silent, indicating that the contributions of collisional and kinetic stress are negligibly small. This observation is consistent with the conclusion of Tsinontides & Jackson (1993) that particle assemblies form a

network of enduring contacts that stabilizes the bed throughout the range of solid-like homogeneous expansion, and demonstrates that stress transmitted through enduring particle contacts plays a major role in stabilizing gas-fluidized suspensions, contributing significantly to the effective stress tensor of the particulate phase. So, in the present considerations, we neglect the contributions of kinetic and collisional stress, considering only the stress transmitted through particle-particle contacts.

Let us consider again the processes of homogeneous fluidization and defluidization of particles in a vessel of diameter D . We assume that the particles are constrained to move in one dimension; thus, we consider only the component of $\mathcal{S}_p = \sigma$ acting on the planes normal to the direction of motion: the normal stress σ . This represents the stress transmitted through a network of enduring particle contacts. If we account for the frictional force between the particles and the vessel walls, Eq. 3.9 becomes:

$$\frac{d\sigma}{dz} \pm \frac{4}{D} \mu j \sigma = \phi \rho_p g - n_p f \quad (3.10)$$

Eq. 3.10 is a force balance in the z -direction, assumed to be vertical, for a particle assembly in the regime of stable bed expansion. In Eq. 3.10, σ is the zz -component of the stress, z is the vertical coordinate *measured downwards from the upper surface of the bed*, D is the bed diameter, μ is the coefficient of wall friction, j is the Janssen coefficient, while u is the superficial velocity of the fluid.

The first term on the left-hand side of Eq. 3.10 relates to the forces transmitted via particle-particle contacts. In this work, we aim to investigate how their presence influences the behaviour of the bed, in particular its homogeneous expansion. The second term represents the frictional force exerted on the particle assembly by the walls of the vessel containing the fluid bed; the positive sign applies to the defluidization process, in which the bed slowly consolidates, while the negative sign applies to the fluidization process. The first term on the right-hand side is the gravitational force acting on the particles, while the second term models the fluid-particle interaction force. With Jackson (2000), we consider the drag and buoyancy

forces to be the main contributors to $n_p f$; hence, other contributions, such as lift or virtual mass forces, are neglected. The constitutive equation used to model the fluid-particle interaction force is:

$$n_p f = \frac{\phi(\rho_p - \rho_f)g}{(1 - \phi)^n} \frac{u}{u_t} + \phi \rho_f g \quad (3.11)$$

where u_t is the unhindered terminal settling velocity of a particle and n is the *fluid dynamic* Richardson & Zaki (1954) exponent. The first term of Eq. 3.11 represents the drag force component of the fluid-particle interaction force, while the second term is the buoyancy force. We point out that the hydrodynamic value of n is used because the drag force is hydrodynamic and entirely unrelated to particle-particle interaction forces. If we employed the experimental value of n in Eq.3.11, we would no longer be modelling the drag force: we would be modelling an '*effective force*' that combines the drag and interparticle forces – this has been mentioned in Section 3.2. Therefore, to calculate the value of n in Eq. 3.11, we employed Eq. 3.2, which is purely fluid dynamical and unrelated to particle-particle contacts.

The force balance on the fluid phase yields:

$$\frac{dp}{dz} = \frac{\phi(\rho_p - \rho_f)g}{(1 - \phi)^n} \frac{u}{u_t} + \rho_f g \quad (3.12)$$

where p is the fluid pressure. If we combine Eq. 3.10 and 3.11, we obtain the following equation:

$$\frac{d\sigma}{dz} \pm \frac{4}{D} \mu_j \sigma = \phi(\rho_p - \rho_f)g \left[1 - \frac{1}{(1 - \phi)^n} \frac{u}{u_t} \right] \quad (3.13)$$

In Eq. 3.13 there are two unknown functions: $\sigma(z)$ and $\phi(z)$. To find the solid volume fraction profile $\phi(z)$ in the bed, we need to express the normal stress σ as a function of ϕ and then substitute this expression in the linear momentum balance equation. During *defluidization*, the variables σ and ϕ are related, if we assume that the bed is in conditions of incipient yield everywhere; thus, following Tsinontides & Jackson (1993), we can employ Eq. 3.4. In Section

3.5, we will report how we obtained the values of the constants in the equation. Consequently, for a defluidization process, we can write:

$$\frac{d\phi}{dz} = \frac{d\sigma}{dz} \left[\frac{d\sigma}{d\phi} \right]^{-1} = \left\{ (\rho_p - \rho_f) \phi g \left[1 - \frac{u}{u_t} \frac{1}{(1 - \phi)^n} \right] - \frac{4}{D} \mu j \sigma \right\} \left[\frac{d\sigma}{d\phi} \right]^{-1} \quad (3.14)$$

where the derivative of $\sigma(\phi)$ can be calculated by means of Eq. 3.4. The value of j is related to the angle of internal friction φ as follows:

$$j = \frac{(1 - \sin\varphi)}{(1 + \sin\varphi)} \quad (3.15)$$

To estimate the coefficient of wall friction μ , following Mabrouk et al. (2008), we use the relationship reported below:

$$\mu = \frac{k_c}{\sigma} + \tan\varphi \quad (3.16)$$

where k_c is the particle-wall cohesion coefficient, which we assume to be negligibly small since no strong cohesion is present between the particles and the steel walls of the vessel.

To calculate the solid volume fraction profile in the bed at each operating condition, we integrate Eq. 3.14, using the following boundary condition:

$$z = 0, \quad \phi = \phi_{\min} \quad (3.17)$$

This condition is given at the lower limit of the integration domain, which coincides with the top surface of the bed. The upper limit of the integration domain, which coincides with the bottom surface of the bed, located at $z = H$, where H denotes the bed height at the given operating condition, is unknown at the start of the numerical integration of Eq. 3.14. To determine it, we start integrating Eq. 3.14 from the top of the bed, terminating the integration at the value of H which satisfies the following condition:

$$\rho_p \int_0^H \phi(z) dz = m \quad (3.18)$$

where m is the particle mass loading, that is, the mass of particles per unit cross-sectional area. Thus, by imposing the condition reported in Eq. 3.18 on the solution of Eq. 3.14, we can

determine the solid volume fraction profile $\phi(z)$ and the bed height H for a given superficial fluid velocity. Knowing $\phi(z)$ allows us to integrate Eq. 3.12 to obtain the fluid pressure profile at different values of u .

In the *fluidization* process, if we assume that the tensile yield stress of the powder is vanishingly small, we can argue that, as the velocity is gradually increased from zero, σ at the bottom of the bed decreases to finally vanish when the minimum fluidization velocity u_m is reached. Following this argument, we can determine the value of u_m as follows. During fluidization, Eq. 3.13 reads:

$$\frac{d\sigma}{dz} - \frac{4}{D}\mu_j\sigma = (\rho_p - \rho_f)\phi g \left[1 - \frac{u}{u_t} \frac{1}{(1-\phi)^n} \right] \quad (3.19)$$

In this case, σ and ϕ are no longer functionally related; so, Eq.3.19 cannot be solved to obtain $\phi(z)$ at each superficial gas velocity, as we did during the defluidization process. For fluidization velocities lower than the minimum fluidization velocity, this does not present a problem, because the bed retains the structure acquired during the defluidization process, and therefore the solid volume fraction profile $\phi(z)$ is known, being equal to that obtained during defluidization for a zero fluid velocity. This allows us to solve Eq. 3.19 to determine the stress profile $\sigma(z)$. We can easily solve the differential equation by using the integrating factor e^{-pz} , where $p \equiv 4\mu_j/D$. If we multiply both sides of Eq.3.19 by e^{-pz} and then integrate with respect to z , we obtain:

$$\sigma(z=H)e^{-pH} - \sigma(z=0) = \rho_p g \int_0^H \phi e^{-pz} dz - \frac{\rho_p g u}{u_t} \int_0^H \frac{\phi}{(1-\phi)^n} e^{-pz} dz \quad (3.20)$$

As reported in Section 3.3, at the minimum fluidization point σ vanishes at the top and bottom of the bed and so the left-hand side of Eq. 3.20 vanishes. In these conditions, the velocity u is equal to the minimum fluidization velocity u_m ; therefore, we obtain:

$$\frac{u_m}{u_t} = \left(\int_0^H \phi e^{-pz} dz \right) \left(\int_0^H \frac{\phi}{(1-\phi)^n} e^{-pz} dz \right)^{-1} \quad (3.21)$$

Eq. 3.21 allows calculating the value of the minimum fluidization velocity given the axial profile $\phi(z)$. The latter, as said, is the solid volume fraction profile obtained in the defluidization process when the gas flow rate is zero (that is, the bed is fully defluidized).

3.5 Experimental

We investigated two types of powders: Powder 1 (Alumina) and Powder 2 (Ballotini). Their properties are reported in Table 3.2. For each powder we performed two sets of experiments: first, fluidization and defluidization experiments, which allowed us to determine the pressure drop and bed height profiles in the bed; second, experiments aimed to determine the compressive yield stress σ of the powder, which allowed us to obtain the values of the parameters appearing in Eq. 3.4. Before conducting the experiments, we carried out sieve analysis to determine the mean sizes of the powders.

3.5.1 Powder preparations

Particle size analysis using test sieves is, and has been, the standard for many years. Other methods have been developed, but they are commonly used for sub-micron analysis where sieves are difficult to use. To obtain representative samples of the powders, avoid segregation and ensure homogeneity, we shuffled large batches of powders. To carry out the sieve analysis we weighed each sieve and recorded their weight. We placed a known mass of powder on the top sieve of a stack of sieves and covered the top. We shook the stack, keeping it in the vertical position, using a mechanical shaker for about five minutes. Figure 3.1 shows the arrangement of the sieve stack and the mechanical shaker. We weighed the powder retained on each sieve and the bottom pan and recorded their weight. This allowed us to calculate the percentage of powder on each sieve and the mean particle size. We carried out the experiments three times to ensure repeatability. Figures 3.2 – 3.5 report the normal and cumulative size distributions of the powders. Table 3.2 reports the properties of Powder 1 and 2.



Figure 3.1: Sieve stack and mechanical shaker arrangement

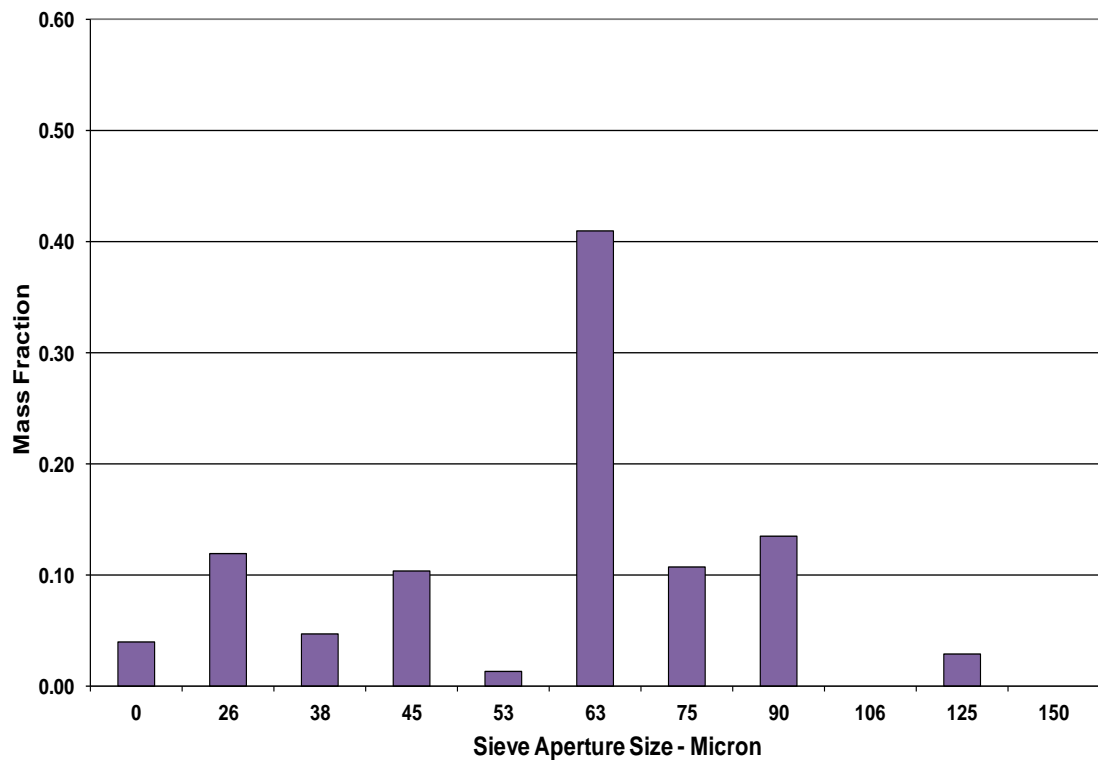


Figure 3.2: Normal particle size distribution of Powder 1

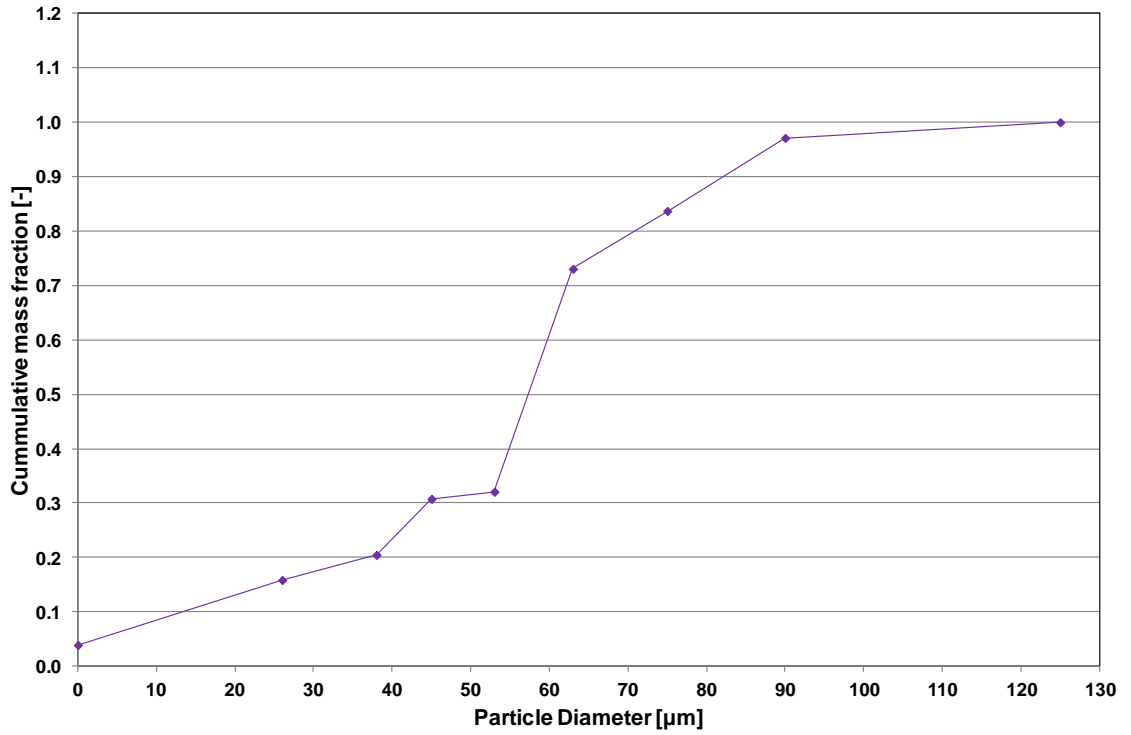


Figure 3.3: Cumulative particle size distribution of Powder 1

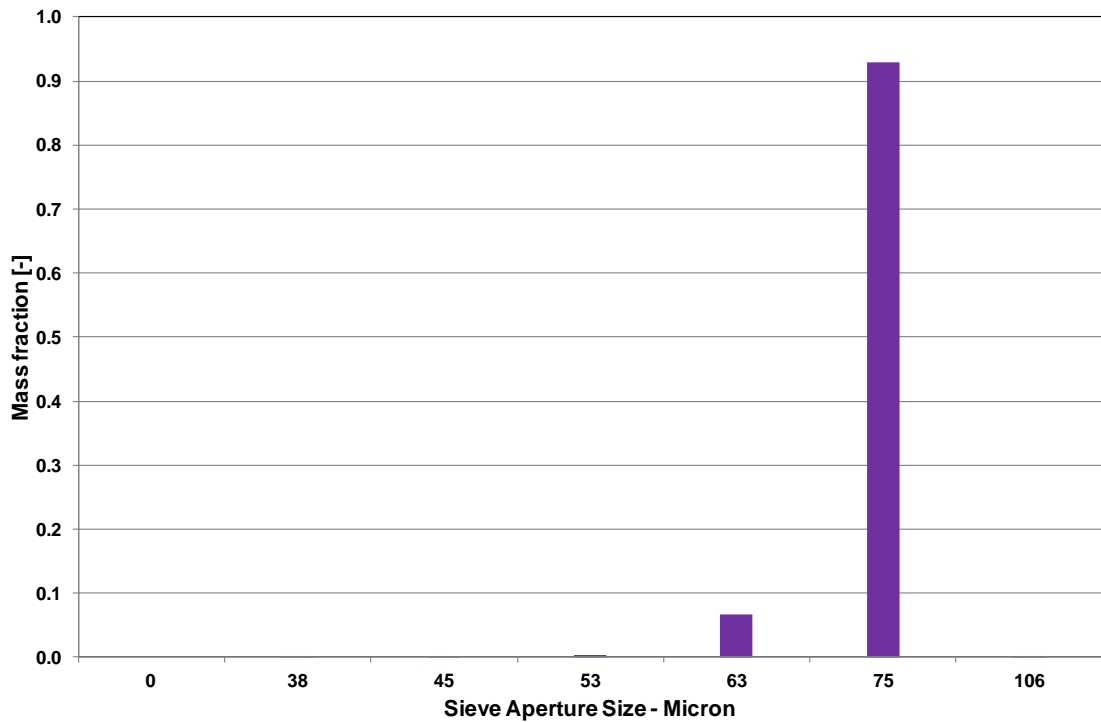


Figure 3.4: Normal particle size distribution of Powder 2

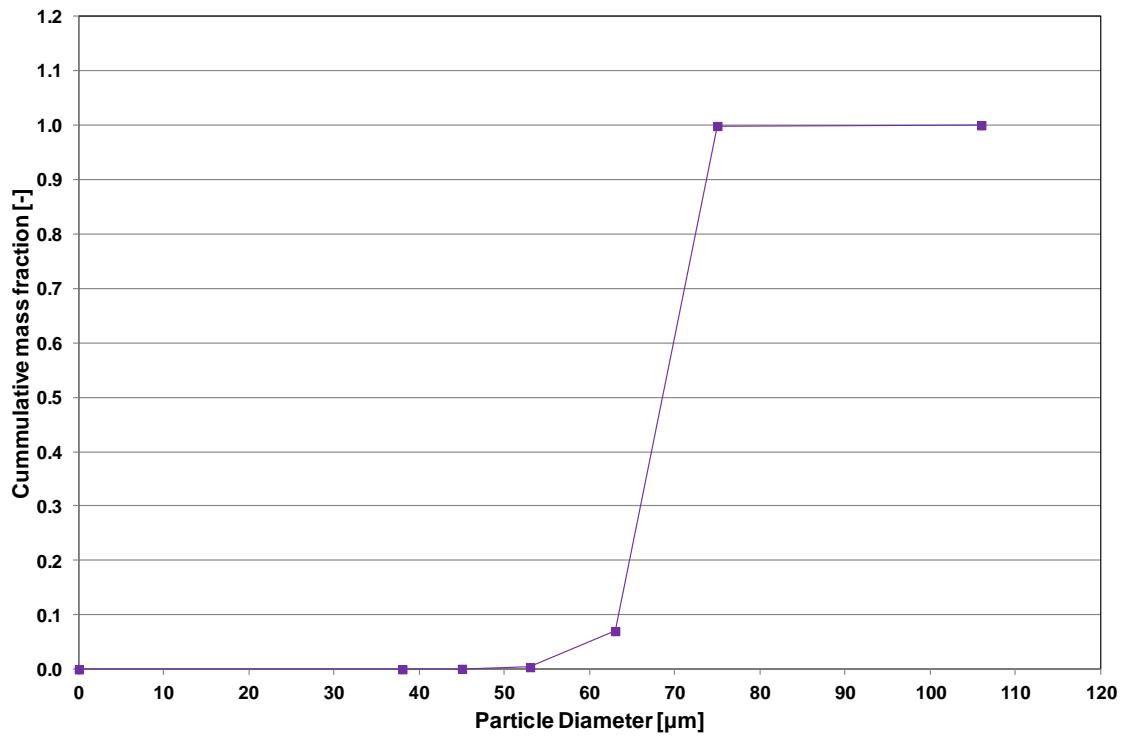


Figure 3.5: Cumulative particle size distribution of Powder 2

Table 3.2: Physical properties of powders (Oke et al., 2015)

	Powder 1	Powder 2
Mean particle diameter (μm)	53	66
Particle density, kg/m³	1730	2500
Angle of internal friction, φ	40 ^o	13 ^o
Minimum fluidization velocity (cm/s)	0.113	0.633
Minimum bubbling velocity (cm/s)	0.301	0.971

3.5.2 Fluidization and defluidization experiments

We carried out fluidization and defluidization experiments in three different tubes, made of stainless steel, with nominal internal diameters of 10 cm, 5 cm and 2.5 cm, and height of 1 m.

We chose stainless steel as vessel material to minimize electrostatic effects. The latter usually

arise as a result of continuous contact and separation between the particles and the vessel walls. Electrostatic effects create serious problems in fluidized beds, making particles adhere to the wall and in some cases generating channelling. One method suggested by Katz & Sears (1969) to minimize these effects is to increase the humidity of the fluidizing gas. We did not resort to this method, because it would increase the cohesiveness of the particles, making it impossible to distinguish between the effects of air humidity and those (that continue to be) present also in dry conditions. In any case, the electrostatic effects were reduced significantly with the use of stainless steel as vessel material. The gas distributor, made of a 5mm-thick sintered mesh with pore size of 20 μm , was mounted between the tubes and the windbox (whose diameter, in each case, was equal to that of the tube). We used dry air, from compressed air cylinders, as fluidizing medium, passing it through a pressure regulator to minimize flow fluctuations. We measured the gas flow rates by means of flow meters and the pressure drops across the bed by means of a digital manometer.

To visualize the bed, we used a pulsed x-ray system consisting of an x-ray generator, an x-ray tube and an image intensifier, respectively labeled 1, 2 and 3 in Figure 3.6. The x-ray tube and the image intensifier are mounted on a twin column suspension unit that allows them to be moved vertically or horizontally across the room. The horizontal movement allowed us to adjust the distance between the x-ray tube and the image intensifier, while the vertical movement allowed us to visualize different heights in the fluidized bed. Each column can be moved vertically independently or as a synchronized pair. The x-rays are produced from a high-voltage source ranging from 40 to 150 kV and frequencies up to 72 Hz, pulsed at 25 fps. The x-ray pulses, synchronized with an image capturing device, pass through the fluid bed. The absorption of the x-rays by the latter is proportional to the nature and quantity of the material along its path. The x-ray beam that emerges from the fluid bed is amplified by the image intensifier by converting the x-ray absorption pattern to an image of sufficient brightness and contrast. These are then recorded by a video camera. The images from the camera are sent by fibre optics to a

dual processor industrial PC that has the capacity to store real-time image sequences of high quality.

To start the experiments, we placed a known mass of particles in the tube. We aerated the bed at low flow rate for about 30 minutes to ensure that the particles were moisture-free. We then increased the flow rate, allowing the bed to bubble gently for a period of time. After, we decreased the air flow in small intervals until the bed was entirely defluidized. At each step, we let the bed equilibrate, subsequently measuring the bed height and pressure drop. After completing the defluidization process, we increased the air flow rate in small increments, measuring at each step the bed height and the pressure drop through the bed until the latter entered the bubbling regime.

3.5.3 Determination of the powder compressive yield stress

To determine the compressive yield stress of the powders investigated, we adopted a procedure proposed by Valverde et al. (1998). We placed a known mass of particles in the tube with diameter of 10 cm. We allowed the bed to bubble gently for a while, and then we slowly reduced the gas flow rate until it became entirely defluidized. We finally measured the bed height. We then added a known mass of particles to the bed, letting the latter bubble gently for a while; then, we slowly defluidized it, recording its resting height. By repeating this procedure, we obtained the bed height H as a function of the mass loading m . We then calculated the mean solid volume fraction $\bar{\phi}(H)$ for each value of H using this relation:

$$\bar{\phi}(H) = \frac{m}{\rho_p g H} \quad (3.22)$$

The variation with H of the experimental values obtained for $\bar{\phi}$, along with a curve fit, is shown in Figure 3.7 and 3.8 for Powders 1 and 2, respectively.

We see that $\bar{\phi}$ increases rapidly when the bed is shallow, remaining approximately constant when it becomes sufficiently deep. This constant value gives a rough estimate of ϕ_{\max} . We now use these figures to determine the compressive yield stress curves for the two powders.

The increase in $\bar{\phi}$ as the bed height increases is caused by an increase in compressive stress, owing to the weight of the particles; this makes the latter rearrange into a more compact ensemble in the lower parts of the bed. Assuming that wall friction plays a negligible role – this is why to carry out these measurements we used the vessel of largest diameter – we can calculate the compressive yield stress *at the bottom of the bed* using the following relation:

$$\sigma(H) = \rho_p \bar{\phi}(H) g H \quad (3.23)$$

If we now succeed in determining the corresponding values of $\phi(H)$, that is, of the solid volume fractions *at the bottom of the bed* for the various bed heights considered, combining the functions $\sigma(H)$ and $\phi(H)$ we can obtain the compressive yield stress locus $\sigma(\phi)$. Our task is thus finding a way to obtain the values $\phi(H)$. These differ from those of $\bar{\phi}(H)$: the former are the local values of the solid volume fraction at the bottom of the bed, whereas the latter are the mean values of the solid volume fraction, averaged over the entire bed.



Figure 3.6: Experimental set-up showing the x-ray machine employed to visualize the bed. 1: x-ray generator 2: x-ray tube 3: image intensifier.

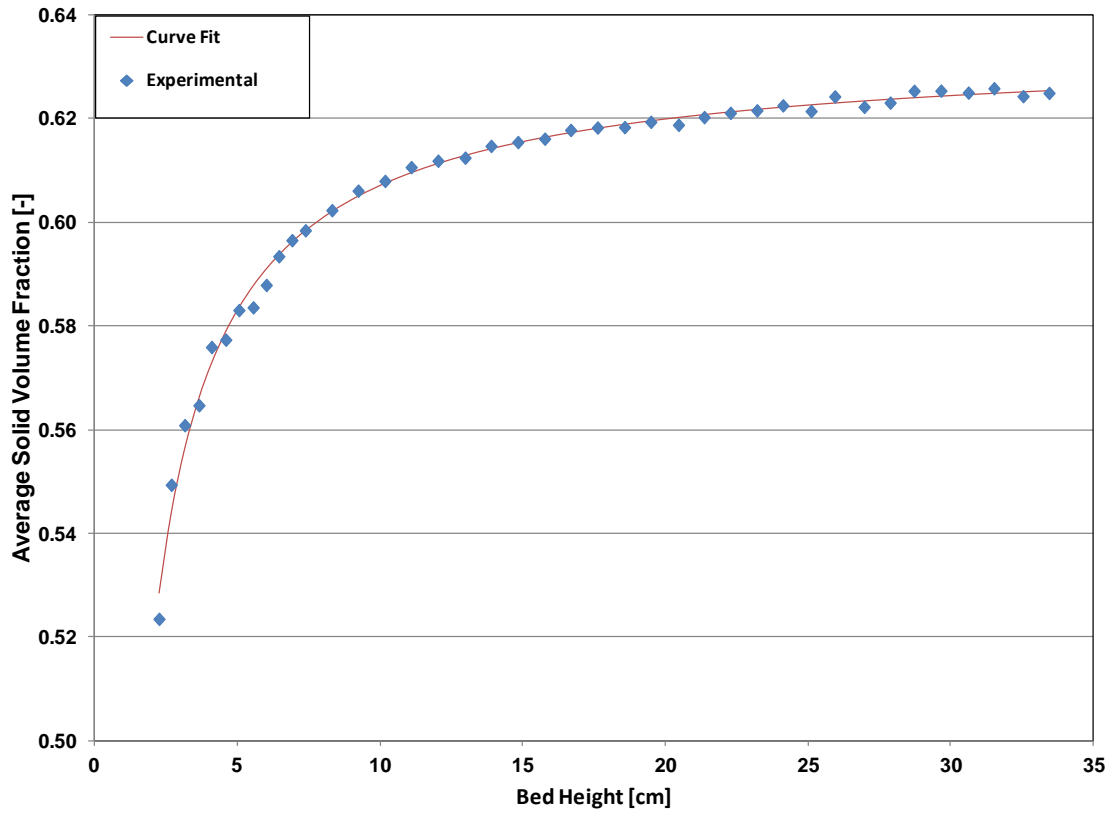


Figure 3.7: Average solid volume fraction against bed height for Powder 1

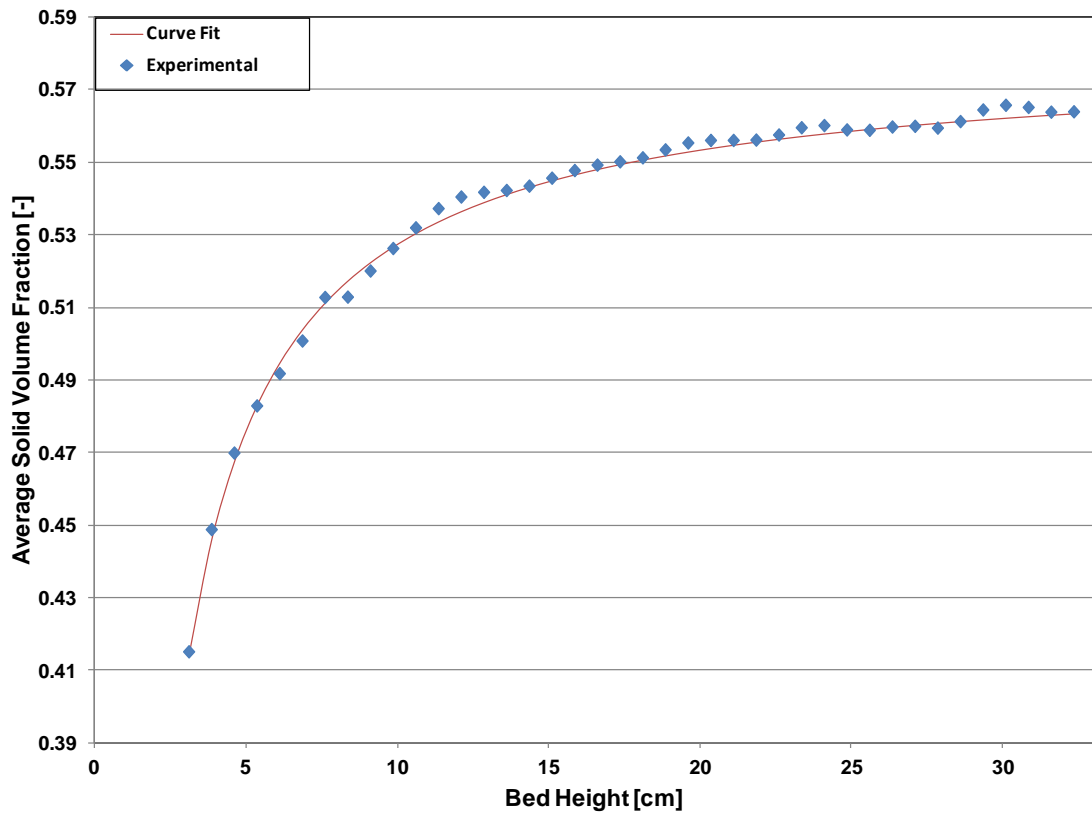


Figure 3.8: Average solid volume fraction against bed height for Powder 2

To derive an expression for $\phi(H)$, we proceed as follows. We begin by writing:

$$\int_0^H \phi(z) dz = \bar{\phi}(H)H \quad (3.24)$$

Differentiating both sides of Eq. 3.24 with respect to H , we obtain:

$$\phi(H) = \bar{\phi}(H) + H \frac{d\bar{\phi}}{dH} \quad (3.25)$$

We can now use the experimental curve $\bar{\phi}(H)$ reported in Figures 3.7 and 3.8 and Eq. 3.25 to evaluate $\phi(H)$ and use Eq. 3.23 to evaluate $\sigma(H)$.

Figures 3.9 and 3.10 report the curves $\sigma(\phi)$ for Powders 1 and 2 obtained with this method. The figure shows that the stress needed to cause compressive yield is small at low values of ϕ . But as the latter increases, σ rises slowly at first and then rapidly. To obtain the values of the parameters that appear in Eq. 3.4, we fitted the equation to the experimental curves in Figures 3.9 and 3.10; the results are reported in Table 3.3, along with other properties of the powders.

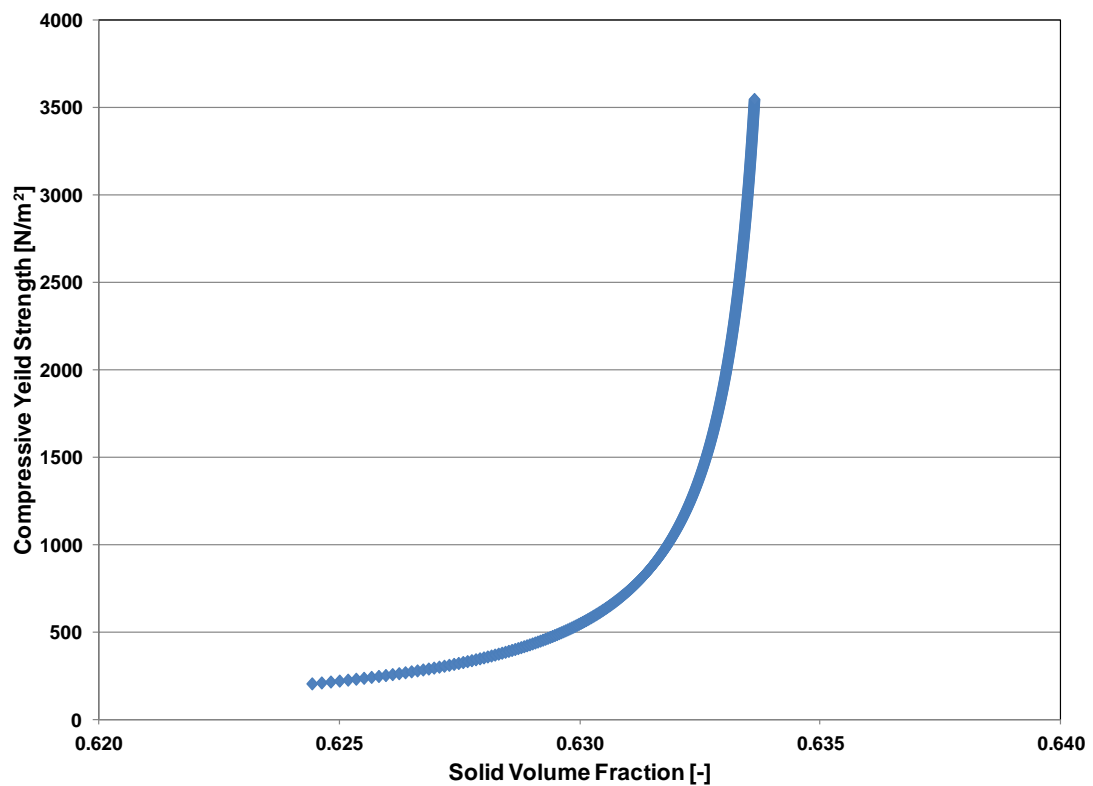


Figure 3.9: Compressive yield strength σ against solid volume fraction ϕ obtained experimentally for Powder 1.

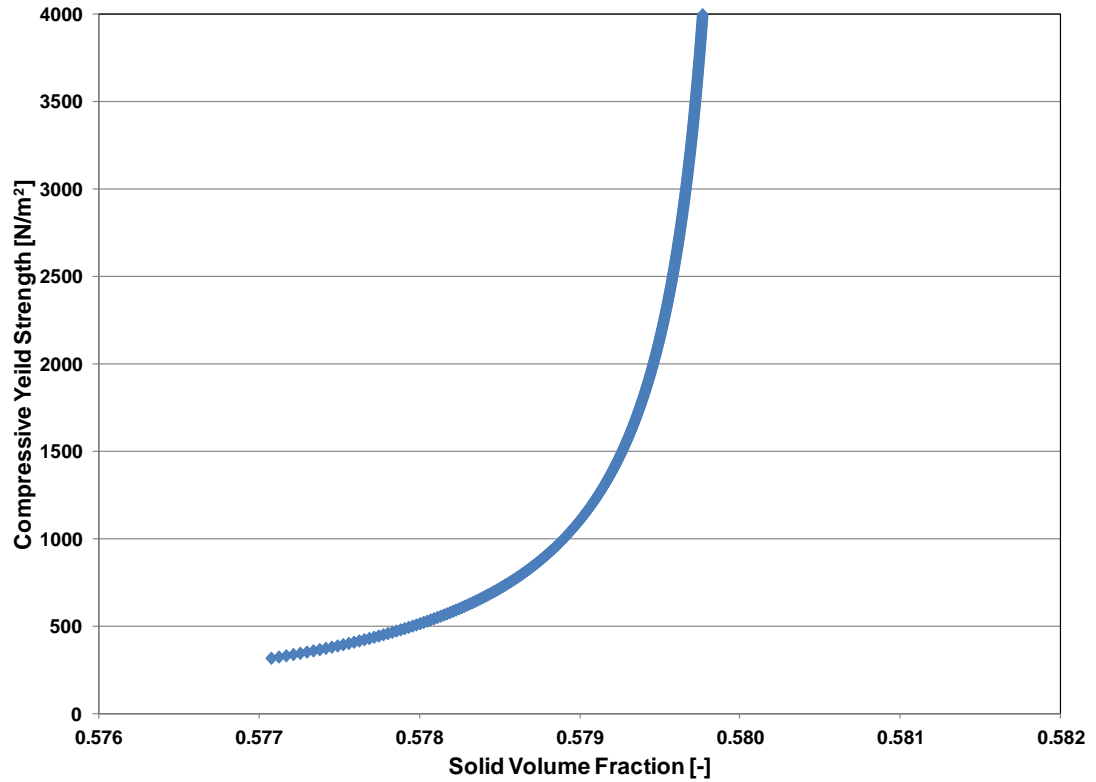


Figure 3.10: Compressive yield strength σ against solid volume fraction ϕ obtained experimentally for Powder 2.

Table 3.3: Simulation parameters

		Powder 1	Powder 2
Terminal velocity, m/s	u_t	0.10	0.25
Richardson & Zaki exponent	n	4.60	4.30
Coefficient of wall friction	μ	0.80	0.27
Solid volume fraction beyond which enduring particle contacts vanish	ϕ_{min}	0.5565	0.5486
Maximum solid volume fraction	ϕ_{max}	0.6343	0.5800
Janssen's coefficient	j	0.20	0.63
Positive parameter	a	1.00	1.00
Positive parameter	b	1.00	1.00
Positive parameter, N/m²	c	32.00	35.00

3.6 Results and discussion

Figures 3.11 – 3.13 refer to Powder 1 and report the plots, obtained through fluidization and defluidization experiments, of the pressure drop, normalized with respect to the bed weight per unit cross-sectional area of the tube, against the superficial gas velocity. The corresponding bed height profiles are reported in Figures 3.14 – 3.16. Similar profiles, reported in Appendix D, were obtained for Powder 2. In Figures 3.11 – 3.13, during the fluidization process, the normalized pressure drop rises linearly until the velocity reaches the minimum fluidization value. At this point, the normalized pressure drop increases above unity, revealing that the pressure drop through the bed exceeds the effective bed weight. This is observed for all the tube diameters investigated. There is a noticeable increase in the pressure drop overshoot as the bed diameter decreases; we attribute this to wall effects, which become more pronounced as the tube diameter becomes smaller. Similar pressure drop overshoots have been reported by several authors (see for instance, Tsinontides & Jackson, 1998; Valverde et al. 1998; Srivastava & Sundaresan, 2002). We observe that the normalized pressure drop at fluidization velocities beyond the point of initial expansion is less than unity; this means that the pressure drop does not support the full weight of the bed, and that in the latter compressive stress is at work. This is contrary to what one would expect in ideal fluid beds, where the pressure drop exactly balances the effective weight of the particles, the bed being unable to transmit stress. Although the bed expands, it is not fully fluidized, being in the solid-like regime over the entire interval of stable expansion, before transiting to the bubbling regime at a superficial gas velocity of 0.30 cm/s. This powder, therefore, never enters the fluid-like regime, even if, when the superficial gas velocity approaches the minimum bubbling velocity, the compressive yield stress almost vanishes (the normalized pressure drop being equal to 0.98). This kind of behavior is common to Group A powders, having been reported many times in the literature (Tsinontides & Jackson, 1998; Jackson, 2000; Srivastava & Sundaresan, 2002; Loezos et al., 2002). For more cohesive powders, such as those belonging to Geldart's Group C, the stable expansion interval features both solid-like and fluid-like regimes. This point has been discussed in Chapter 2.

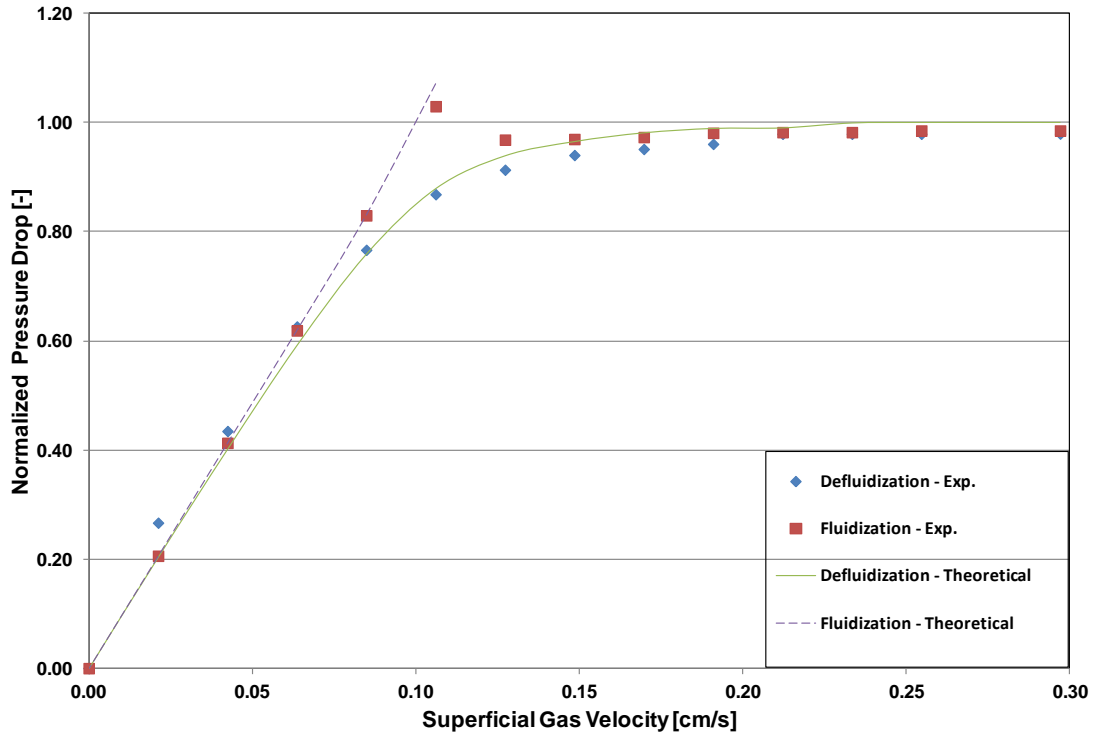


Figure 3.11: Normalized pressure drop (mg/A) against superficial gas velocity for Powder 1 obtained experimentally. m is the mass of the powder, A is the bed cross-sectional area and g is the acceleration due to gravity. Tube diameter - 10 cm.

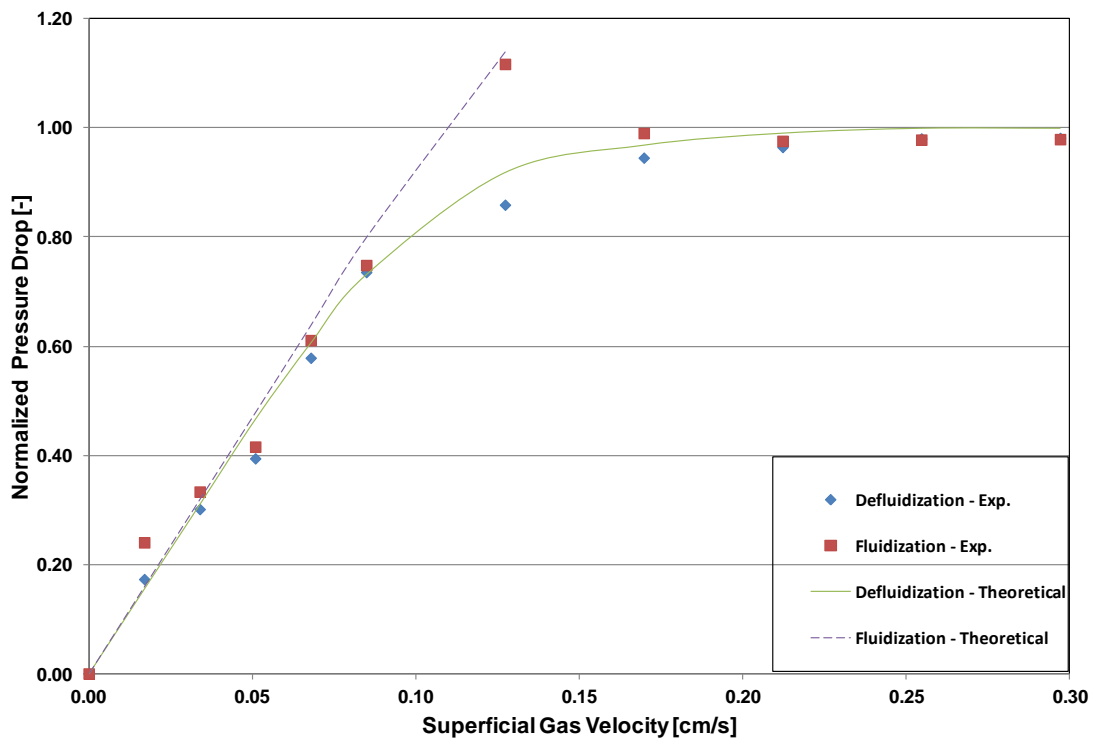


Figure 3.12: Normalized pressure drop (mg/A) against superficial gas velocity for Powder 1 obtained experimentally. m is the mass of the powder, A is the bed cross-sectional area and g is the acceleration due to gravity. Tube diameter - 5 cm.

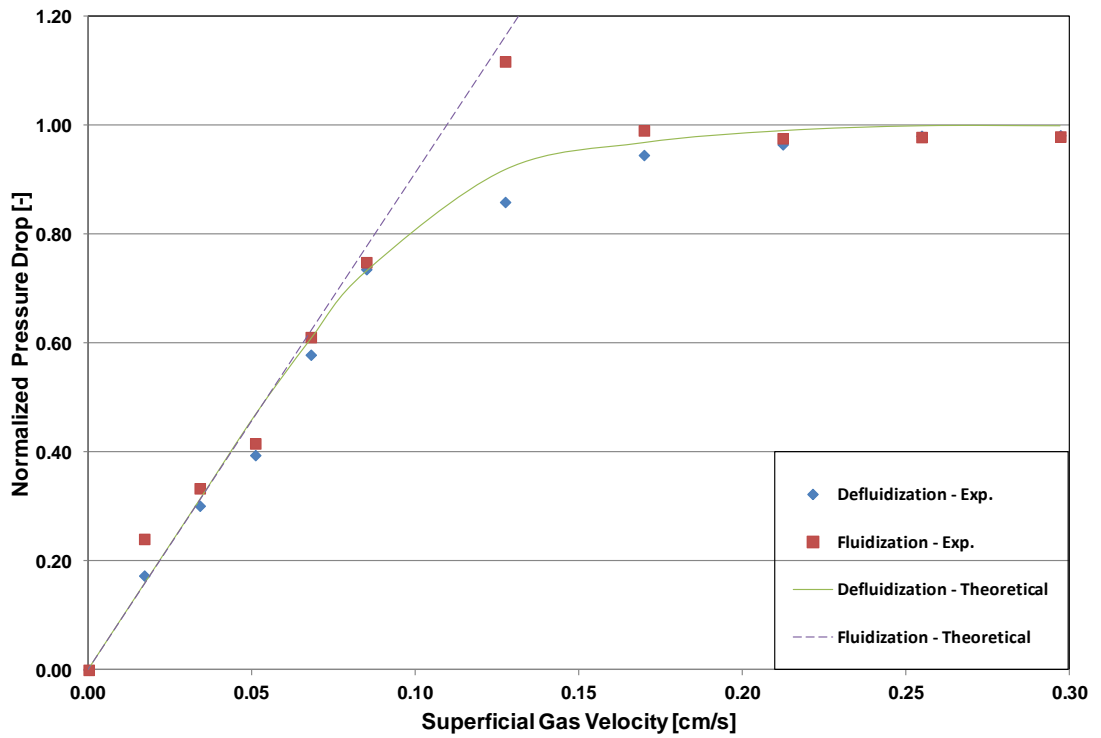


Figure 3.13: Normalized pressure drop (mg/A) against superficial gas velocity for Powder 1 obtained experimentally. m is the mass of the powder, A is the bed cross-sectional area and g is the acceleration due to gravity. Tube diameter – 2.5 cm.

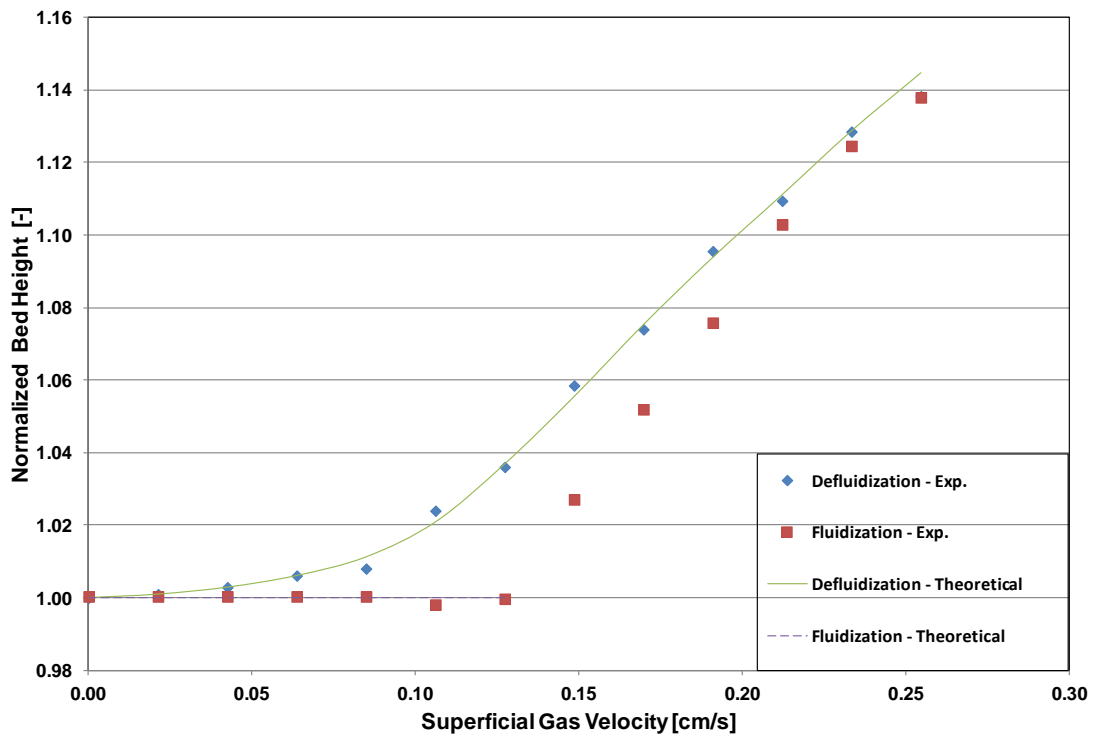


Figure 3.14: Normalized bed height (H/H_0) against superficial gas velocity obtained experimentally for Powder 1. H_0 is the initial bed height. Tube diameter – 10 cm.

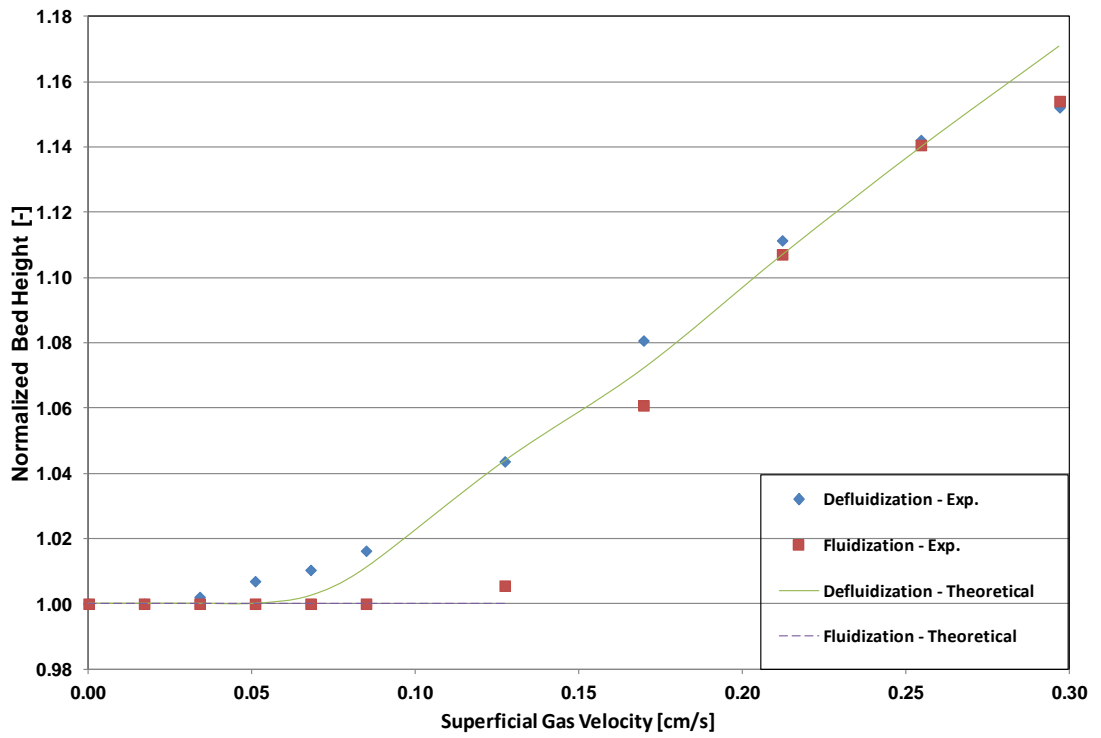


Figure 3.15: Normalized bed height (H/H_0) against superficial gas velocity obtained experimentally for Powder 1. H_0 is the initial bed height. Tube diameter – 5 cm.

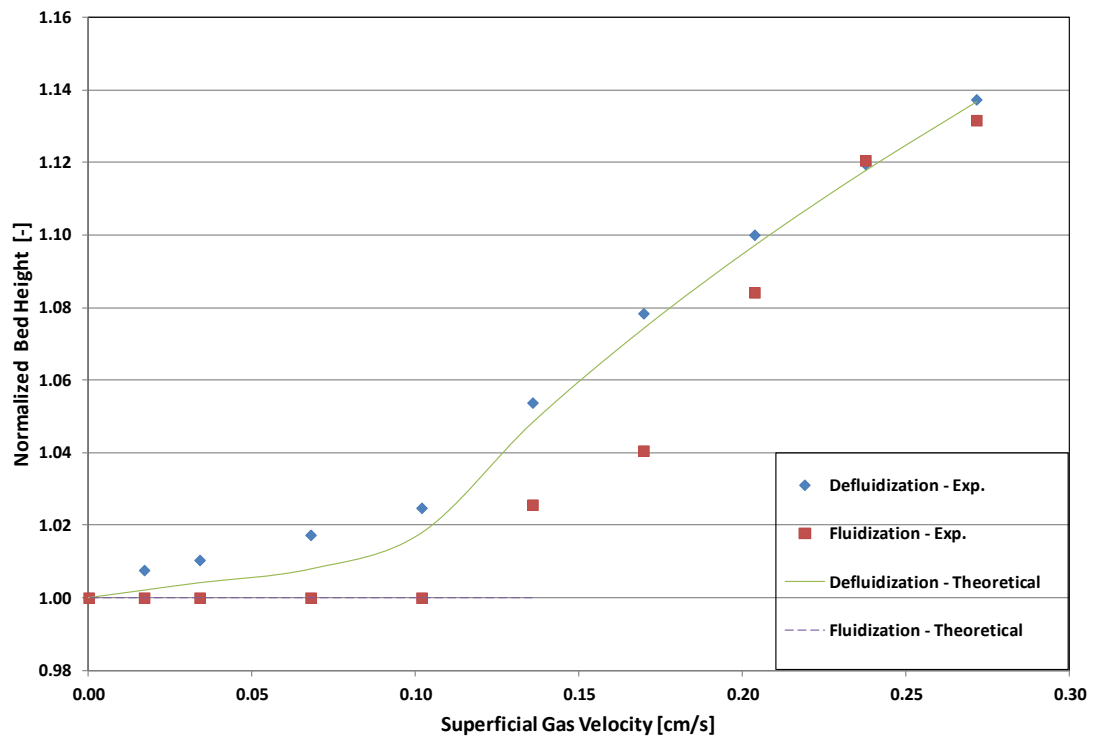


Figure 3.16: Normalized bed height (H/H_0) against superficial gas velocity obtained experimentally for Powder 1. H_0 is the initial bed height. Tube diameter – 2.5 cm.

Table 3.4: Experimental and theoretical values of minimum fluidization velocities

	Powder 1		Powder 2	
	Minimum Fluidization Velocity (cm/s)			
D (cm)	Experimental	Theoretical	Experimental	Theoretical
10.0	0.102	0.106	0.610	0.614
5.0	0.112	0.110	0.641	0.623
2.5	0.121	0.117	0.648	0.637

Figures 3.11 – 3.13 report also the theoretical fluidization and defluidization curves. The fluidization curves extend up to the superficial gas velocity at which the structure of the bed, acquired during defluidization, breaks down and fluidization begins; to continue these curves to higher superficial gas velocity values, we would have to assume something about the structure of the fluidized bed; the simplest assumption is that the bed is fully fluidized (*i.e.*, homogeneous and in the fluid-like regime), so that no compressive stress is present. However, as the experimental curves reported in Figures 3.11 – 3.13 reveal, this is untrue, because the normalized pressure drop is less than unity. As a consequence, we preferred to stop the fluidization curves at the end of the initial linear branch. The minimum fluidization velocities predicted theoretically and those obtained experimentally are reported in Table 3.4.

The theoretical and experimental fluidization/defluidization curves are very similar, except in one respect. The theoretical normalized pressure drop curves during defluidization approach a value of unity when the gas velocity exceeds 0.24 cm/s; the model, therefore, predicts that between this velocity and the minimum bubbling velocity the bed finds itself in the fluid-like regime. This is not observed experimentally, even if, for velocities larger than 0.24 cm/s, the bed is almost entirely fluidized. The reason for this, we believe, is that the value of ϕ_{\min} estimated experimentally (through the best-fit procedure reported in Section 3.5) and adopted in the model is slightly underestimated, so that the model predicts a transition of the system to the fluid-like regime when in reality the bed is still able to sustain a weak compressive stress.

3.7 Solid volume fraction profiles

By integrating Eq. 3.14 numerically, using for the parameters the values reported in Table 3.3, we determined the solid volume fraction profiles in the bed at various superficial gas velocities u during defluidization. Figures 3.15 and 3.16 report the solid volume fraction vertical profiles for Powders 1 and 2 at different superficial gas velocities. At each velocity, the volume fraction varies significantly near the top of the bed, remaining fairly constant at lower heights; this shows that the bed bulk density builds up with depth. The figure also shows that the solid volume fraction at the bottom of the bed decreases as the superficial velocity of the gas increases.

This is because at larger velocities the bed is more expanded, and we do expect lower and lower values of the solid volume fraction as the bed becomes progressively less packed; this indicates that as the gas velocity increases a larger fraction of the bed weight is supported by the fluid. The profiles of solid volume fraction show that the beds are not fully fluidized until the fluid velocity reaches the value of 0.24 cm/s for Powder 1 and 0.82 cm/s for Powder 2. At such values, the beds enter the fluid-like regime, becoming fully fluidized. We can tell because the solid volume fraction becomes constant over the entire depth of the bed: this implies that the particles are uniformly suspended into the fluid and particle-particle contacts are absent. In such a condition, the gradient of the normal stress vanishes, so that the beds can no longer transmit stress due to a network of particle-particle contacts; accordingly, spatial variations in solid volume fraction no longer exist.

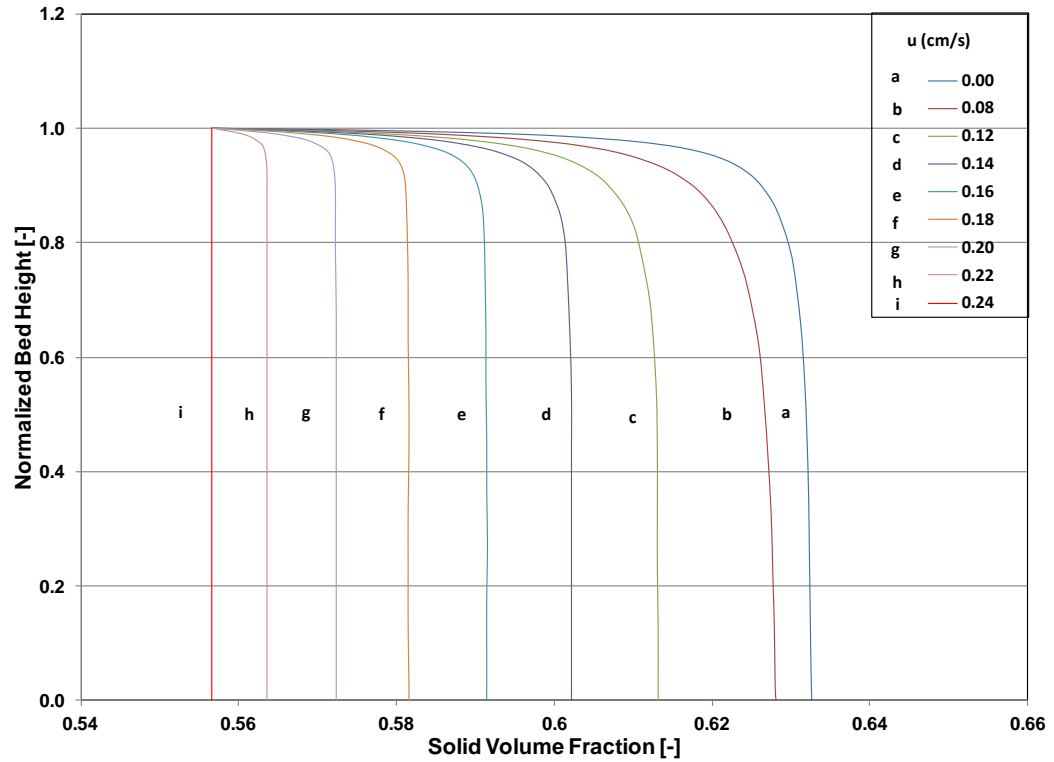


Figure 3.15: Normalized bed height (H/H_0) against solid volume fraction ϕ obtained theoretically for powder 1. H_0 is the initial bed height.

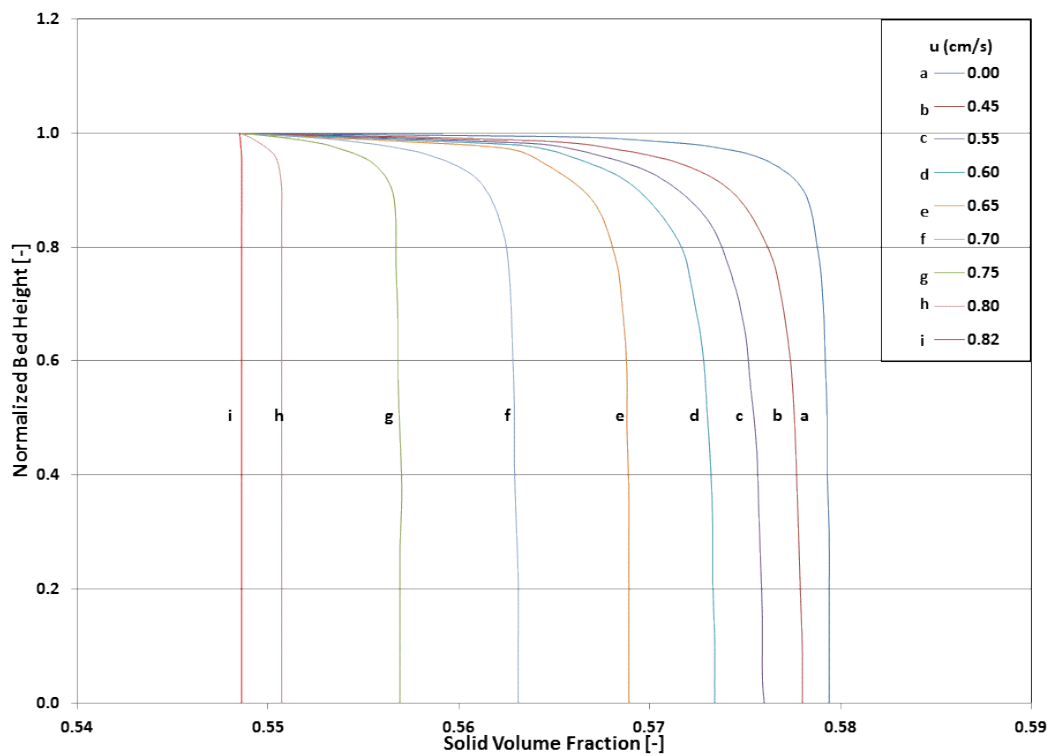


Figure 3.16: Normalized bed height (H/H_0) against solid volume fraction ϕ obtained theoretically for powder 2. H_0 is the initial bed height.

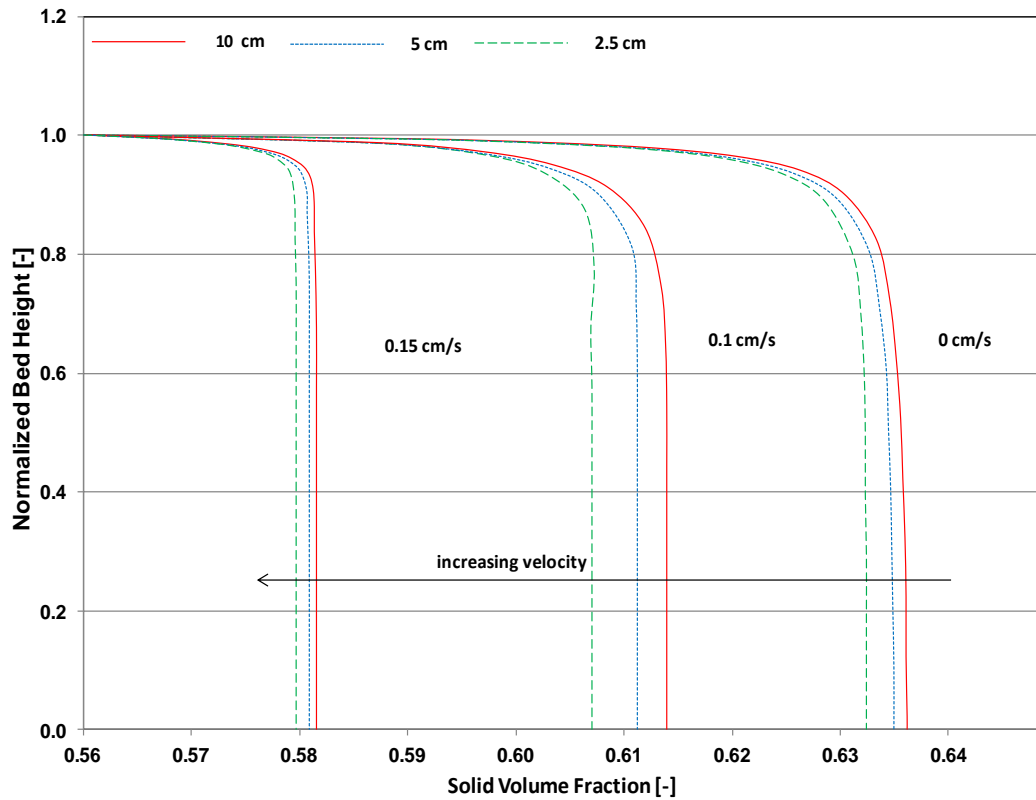


Figure 3.17: Normalized bed height (H/H_0) against solid volume fraction ϕ in tubes of different diameters obtained theoretically for Powder 1. H_0 is the initial bed height.

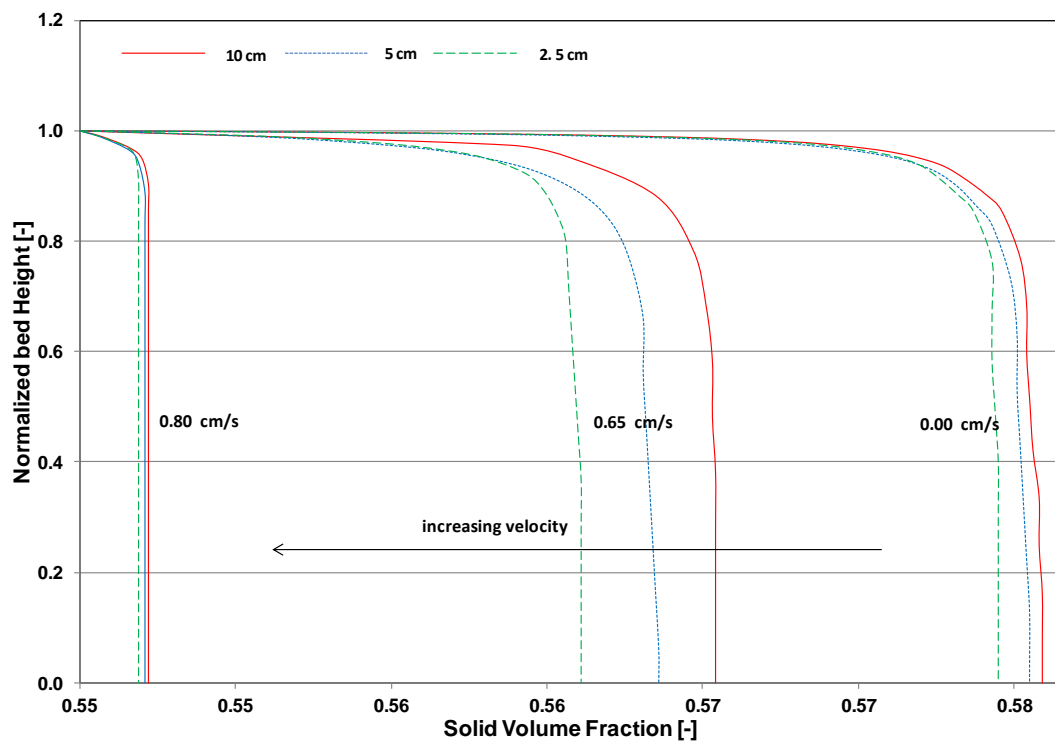


Figure 3.18: Normalized bed height (H/H_0) against solid volume fraction ϕ in tubes of different diameters obtained theoretically for Powder 2. H_0 is the initial bed height.

To see if wall friction affects the solid volume fraction profile in the bed, we ran simulations at various values of the bed diameter, keeping the superficial velocity of the fluid constant. Figures 3.17 and 3.18 show the plot of normalized bed height against solid volume fraction for Powders 1 and 2 respectively. We observe that, at a given value of the superficial fluid velocity, the solid volume fraction, in particular at the bottom of the bed, decreases as the value of D decreases. This is due to the additional support provided by the walls of the vessel, the latter reducing the component of the particle weight balanced by the action of the distributor plate. At larger velocity, the difference among the solid volume fraction profiles becomes less significant; the profiles at 0.15 cm/s for Powder 1 and 0.80 cm/s for Powder 2 are closer than those obtained at lower velocities. The reason for this is that at a high superficial gas velocity, the bed expands more, the enduring contacts among the particles reduce, and therefore the normal stress decreases considerably. This causes a corresponding decrease in the frictional force at the walls, since the latter is directly related to the normal stress σ (refer to the second term on the left-hand side of Eq.3.10). At these high velocities, the dependence of the frictional force on the normal stress outweighs that on the vessel diameter; hence, the solid volume fraction profiles do not vary appreciably as D changes.

3.8 Richardson & Zaki equation and homogeneous expansion in gas-fluidized beds

Before advancing further, let us briefly recap the aim of this chapter. We pointed out, in Section 3.2, that the correlation of Richardson & Zaki (1954) holds for both liquid-fluidized and gas-fluidized beds, but for the latter the values of the parameters n and u_t appearing in the correlation are greater than those predicted by the relations reported in the literature, which instead are reasonably accurate for liquid-fluidized beds. As said, we denote the larger values holding for gas-fluidized beds as n^* and u_t^* . These values reflect the effects of both fluid dynamic and interparticle forces, whilst the values of n and u_t reflect only the effects of the former, insofar as in liquid-fluidized beds the interparticle forces play a negligible role. We believe that the larger values of n^* and u_t^* are caused by the enduring contacts among the

particles, which in turn are a manifestation of cohesiveness. In homogeneous fluidized beds in the fluid-like region these contacts are absent, and the Richardson & Zaki parameters take on the expected fluid dynamic values denoted as n and u_t . In most of the stable interval of homogeneous expansion, nevertheless, gas-fluidized beds find themselves in the solid-like region, where enduring contacts among particles are present. We believe that these play a key role, their presence explaining why the values of the Richardson & Zaki parameters are larger than expected. We are now in a position to put this claim to the test. The model results provide, for any given superficial gas velocity, the axial profile of the solid volume fraction, and therefore of the void fraction as well. Using these profiles, we may determine the mean values of the void fraction through the bed as a function of the superficial gas velocity: these values are those that one measures in experiments on homogeneous fluidized beds and uses in the Richardson & Zaki correlation. To determine the n^* and u_t^* values theoretically, we operate as follows: from the profiles of solid volume fraction, we calculate the mean solid volume fraction $\bar{\phi}$ at each fluidizing velocity u in the stable interval of expansion, using the following relationship:

$$\bar{\phi} = \frac{1}{H} \int_0^H \phi(z) dz \quad (3.26)$$

By plotting u against $\bar{\phi}$ in the Richardson & Zaki form:

$$\log u = \log u_t^* + n^* \log(1 - \bar{\phi}) \quad (3.27)$$

we then obtain the theoretical values of n^* and u_t^* from the slope and intercept on the velocity axis of the function above, respectively. The logarithmic plot of u against $(1 - \bar{\phi})$ for Powder 1 is shown in Figure 3.19 for the bed with 10 cm diameter. Table 3.5 reports the theoretical and experimental values of n^* and u_t^* in beds of different diameters for Powders 1 and 2. The theoretical values of n^* and u_t^* obtained from our simulations show a reasonable agreement with the experimental results. In particular, the values of n^* are higher than the limiting values ascribed to n in the limit of inertial regime (discussed in Section 2). We also observe from Table 3.5 that the values of n^* and u_t^* increase as the bed diameter decreases; this is true for both

powders. This is due to the wall effects becoming more pronounced as the bed diameter reduces.

To further confirm our results, we ran simulations using powders investigated by Tsiontides & Jackson (1993) and Srivastava & Sundaresan (2002) – Powder 3 and 4, respectively. The physical properties of these powders are reported in Table 3.6. We adopt the same approach reported in the preceding paragraph to determine the values of n^* and u_t^* . The simulation results, alongside those obtained using Powder 1 and 2, are reported in Table 3.5. The results again show that the theoretical values of n^* and u_t^* agree fairly well with the empirical values.

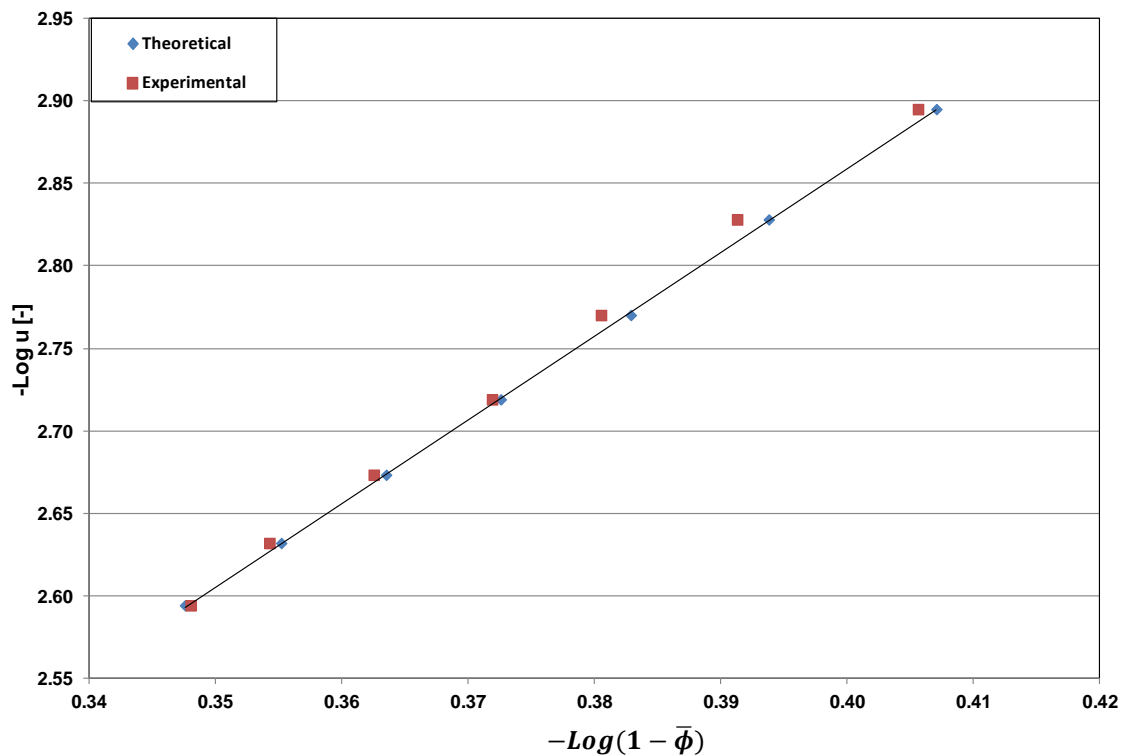


Figure 3.19: Logarithmic plot of velocity against bed voidage obtained theoretically. The points represent the theoretical data, while the solid line is the linear fit.

To investigate the role of enduring particle contacts in homogeneous fluidization, we reasoned as follows: if truly there were no particle-particle contacts in the fluidized bed, the particles floating freely in the fluid and the homogeneous expansion being dictated solely by fluid dynamic forces, as some authors argue, we would expect the values of n^* to be the same as the values used in our simulations to model the drag force (that is, the values of n). To explain this,

let us consider Eq. 3.13. The latter reduces to the Richardson & Zaki equation if we neglect the contribution of stress transmitted by enduring particle contacts. In this case, the equation merely expresses the fluid dynamic force balance (where the drag force on the particles balances their effective weight) which one would expect if the bed were to be uniformly fluidized; hence, the equation yields the hydrodynamic n and u_t values used as input in the model. However, as seen from the experiments, the values of n^* and u_t^* obtained for the powders are larger than the hydrodynamic ones (see Table 3.5). This reveals that by accounting for the stress transmitted via contacts among particles, we are able to capture the expansion profiles in the bed and to correctly predict the expansion parameters featuring in the Richardson & Zaki equation.

Table 3.5: Summary of Richardson & Zaki (1954) parameters

		Experimental		Theoretical		Hydrodynamic	
Powder 1							
<i>D</i> (cm)	n^*	u_t^* (m/s)	n^*	u_t^* (m/s)	n	u_t (m/s)	
10.0	5.36	0.183	5.04	0.144	4.6	0.10	
5.0	5.96	0.309	5.49	0.204	4.6	0.10	
2.5	6.62	0.587	6.35	0.437	4.6	0.10	
Powder 2							
<i>D</i> (cm)	n^*	u_t^* (m/s)	n^*	u_t^* (m/s)	n	u_t (m/s)	
10.0	5.03	0.437	4.94	0.417	4.3	0.25	
5.0	5.21	0.524	5.11	0.476	4.3	0.25	
2.5	6.21	1.156	6.13	1.081	4.3	0.25	
Powder 3							
<i>D</i> (cm)	n^*	u_t^* (m/s)	n^*	u_t^* (m/s)	n	u_t (m/s)	
5	5.01	0.224	5.10	0.189	4.5	0.12	
2.5	5.86	0.333	5.69	0.292	4.5	0.12	
Powder 4							
<i>D</i> (cm)	n^*	u_t^* (m/s)	n^*	u_t^* (m/s)	n	u_t (m/s)	
5	6.40	0.156	6.67	0.206	4.72	0.06	
2.5	7.43	0.331	7.61	0.374	4.72	0.06	

Table 3.6: Physical properties of Powders 3 and 4

	Powder 3	Powder 4
Mean particle diameter (μm)	50	75
Particle density, g/cm^3	2.35	1.44
Angle of internal friction, φ	13^0	30^0

3.9 Conclusions

We investigated the solid-like regime of homogeneous fluidization using both experimental and theoretical methods. We adopted a one-dimensional model to investigate the behaviour of gas-fluidized beds of fine particles in the homogeneous fluidization regime, accounting for enduring contacts among particles. These contacts, which are a manifestation of cohesiveness, strongly affect the expansion profiles of the beds. In particular, the values of the expansion parameters n and u_t of the Richardson & Zaki (1954) equation obtained when we accounted for stress transmitted through enduring particle contacts are higher than those obtained from purely fluid dynamic considerations. This agrees with what occurs in reality. We validated our numerical results by carrying out fluidization and defluidization experiments. The results indicate that fluid dynamic correlations for calculating the values of n and u_t , like those reported, for instance, in Gibilaro (2001), are unsuitable for describing the expansion profiles of gas-fluidized beds.

Chapter 4

Literature review on solid mixing in gas-fluidized beds

This chapter reviews the process of solid mixing in gas-fluidized beds.

1. We review the importance of solid mixing in gas-fluidized beds and the mechanism by which it proceeds.
2. We report on experimental and theoretical works carried out on lateral and axial solid mixing in gas-fluidized beds.
3. We discuss various methods adopted for measuring the rate of lateral solid mixing in gas-fluidized beds.
4. We report different empirical correlations developed for estimating lateral dispersion coefficients in gas-fluidized beds.

Parts of this chapter have been published:

Oke, O., Lettieri, P., Salatino, P., Mazzei, L. 2015. Eulerian modelling of lateral solid mixing in gas-fluidized suspensions, *Procedia Engineering*, 102, 1491 – 1499.

4.1 Introduction

Fluidized beds operate in different regimes depending on the superficial gas velocity. For most gas-fluidized beds, when the superficial gas velocity exceeds the minimum fluidization velocity, the bed enters the bubbling regime. This regime is characterized by the formation of bubbles, which cause vigorous mixing of solids in the bed. At higher gas flow rates agitation becomes more intense, and the movement of solids becomes more vigorous, creating violent mixing between the solid and gas phases. Intense mixing in the bed promotes extremely high surface contact between the fluid and the solid per unit volume of the bed, high heat and mass transfer and high relative velocity between the fluid and the dispersed solid phase.

Excellent mixing in fluidized beds allows them to find applications in many industrial operations. For instance good mixing in fluidized bed dryers promotes high intensity drying and high thermal efficiency with uniform and easily controllable temperature. This ensures that mixing is achieved quicker because of high rates of heat and mass transfer. Excellent mixing also allows easier maintenance and operation of the dryer and enhances greater adaptability to automation (Chandran et al., 1990).

In polymerization reactors good mixing is needed to achieve efficient operation and desired results (Naimer et al., 1982; Kim & Choi, 1999; McAuley et al., 1994). This ensures excellent gas-solid contact, minimal gas-bypassing and uniform temperature. The latter ensures that there are no hot spots in the bed. Hot spots are regions of maximum temperature in the bed, causing deleterious effects such as catalyst deactivation and undesirable reactions. In addition, the polymerization reaction is highly exothermic, generating significant amount of heat. Good mixing in the reactor allows the heat to be removed by fast flowing stream of fluidizing gas. Successful applications of fluidized beds to other highly exothermic and temperature sensitive processes has been achieved due to the excellent mixing that they provide.

Chemical synthesis in fluidized bed reactors relies on efficient mixing. Usually, the reactions in a chemical synthesis require strict temperature control. This is because the reaction may be

explosive outside a narrow temperature range. In addition, the yield of the desired products are sensitive to the temperature level of operations; hence, excellent solid mixing is needed for safety of operations and profitability.

Knowing how solids mix is also important in defining input parameters for modelling of fluidized bed reactors. Petersen & Werther (2005) developed a fluidized bed reactor model using lateral mixing data as an input parameter. They were able to investigate the distribution of volatiles (CH_4 , CO and H_2) in the region close to the feed point. Similarly, Wischniewski et al. (2010) simulated a 3-D industrial circulating fluidized bed (CFB) combustor, describing gas and solid mixing in the bed by using lateral solid mixing data. Similarly, Pallarès & Johnsson (2008) investigated fuel concentration at the bottom region of a fluidized bed combustor by developing a model which accounts for mixing patterns and fuel conversion in the bed. To use the model, lateral mixing data at the bottom part were necessary input parameters.

In a fluidized bed combustor the rate at which solid fuel mixes laterally has a strong influence on the performance of the plants. This is because it affects the combustion efficiency, the allocation of heat release and the formation of emissions (Gomez-Barea & Leckner, 2010). It is therefore crucial to ensure that fuel spreads homogeneously over the whole cross-section of the bed. To do this, fuel is usually fed at multiple entry points with the aid of a spreader. However, each added feed point increases the installation cost, making it crucial to minimize the feed entry points and, at the same time, maintain fuel burnout to achieve low emissions. These requirements make the knowledge of how fuel mixes laterally essential for optimal design of the fluidized bed combustor.

A good understanding of the mixing process is very important in the design of large-scale fluidized beds. Solid mixing studies combined with gas flow analysis and reaction mechanisms provide the basis for designing commercial fluidized bed reactors (Shen, et al. 1995). Therefore, several authors have examined the phenomenon of mixing in fluidized beds; on the one hand using experimental approaches to investigate the causes of mixing and the mechanisms by

which it proceeds, on the other hand using theoretical approaches to describe the process and predict it for design purposes.

The importance of solid mixing in fluidized beds has made researchers focus more on its study (Marshack & Gomezplata, 1965; Rowe, et al.1965; Partridge, 1965; Rowe & Widmer, 1973; Nguyen et al., 1977; Potter, 1971). Knowing the mechanism by which mixing occurs is crucial in designing efficient fluid bed reactors. This is because it affects important phenomena such as heat and mass transfer rates, which in turn can affect mechanical design of fluidized bed accessories such as the number and position of solids feed and withdrawal points (Mostoufi & Chaouki, 2001). Therefore, a better understanding of how mixing proceeds will significantly aid the design and operation of fluidized beds.

4.2 The mechanism of solid mixing in gas-fluidized beds

When granular materials are fluidized with a velocity that is at least equal to their minimum bubbling velocity, bubbles begin to form in the bed. These are regions of low solid density or voids rising in the bed. They are usually enveloped by a cloud of circulating gas and particles which is generally referred to as *bubble cloud*. The region below the bubble is the *wake region*. The latter is most likely formed because the pressure in the lower part of the bubble is less than in the nearby emulsion, drawing the gas into the bubble. This causes partial collapse of the bubble and creates turbulent mixing (Kunii & Levenspiel, 1991). The turbulent mixing causes solids to be drawn up behind the bubble, forming the wake region. As bubbles rise through the bed, they periodically shed the wake, leaking solids into the emulsion. This implies that there is exchange of solids between the wake and the emulsion.

Researchers believe that solid mixing in fluidized beds is caused mainly by the actions of the bubbles. The wakes of the bubbles carry solids from the bottom of the bed to the top. Along the way up, there is exchange of particles among the bubble wakes and the rest of the bed. This phenomenon is referred to as *wake shedding*. To balance the upward transport of solid particles,

there is a downward movement of solid particles in the bubble-free region, creating a global circulation of particles in the bed. This mechanism is illustrated in Figure 4.1.

Several authors (Sitnai & Whitehead, 1985; Lin et al., 1985; Yamazaki et al., 1986) studied the mixing mechanisms of different types of powders. They reported that mixing of Geldart B powders generally depends on the geometry of the bed and the fluidizing velocity. At low fluidizing velocities, and in beds of aspect ratio lower than unity, the emulsion phase moves upwards in the regions near the wall and downwards at the centre of the bed. At higher flow rates however there is a reversal of the flow; the emulsion now moves downwards in the regions close to the wall and upwards at the bed axis. In beds having aspect ratio greater than unity, two regions of solid circulation form in the bed: the first forms in the region close to the distributor and the second forms near the top of the bed. At higher gas flow rates, the latter region becomes more vigorous and dominates the entire solid mixing process.

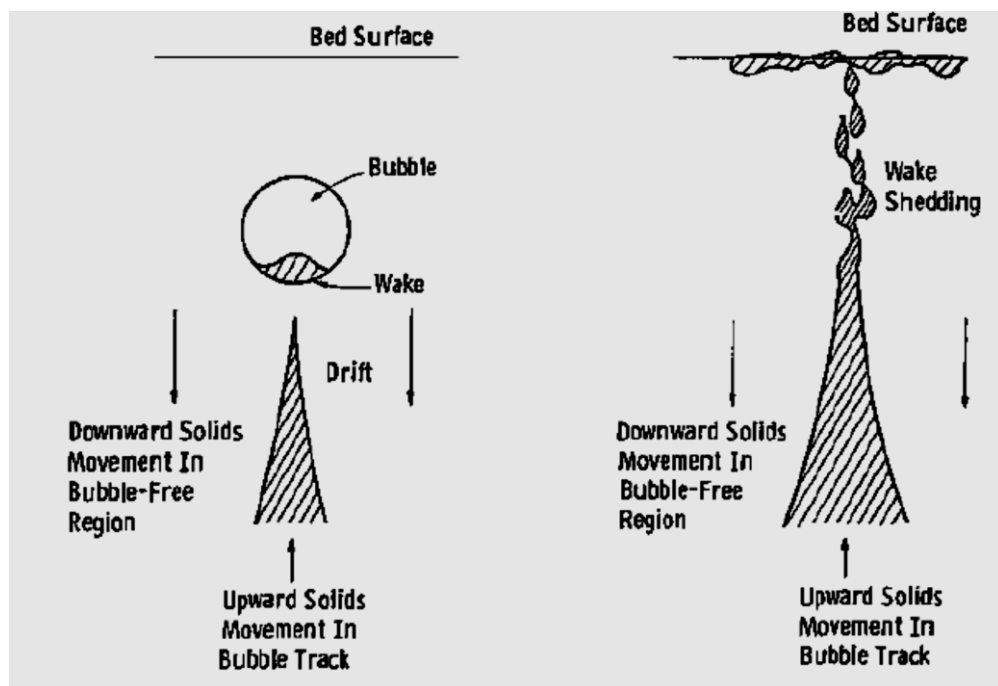


Figure 4.1: Solid mixing mechanism in fluidized beds (Yang, 2003)

The solid mixing pattern of Geldart A powders is more complex: there is both upflow and downflow of emulsion at the center of the bed (Tsutsui et al., 1979). Mixing of Geldart D

powders is characterized by elongated bubbles near the distributor plates which transform into spherical bubbles as they move up the bed (Fitzgerald, 1980). The bubbles grow rapidly and do not follow any specific path. This makes it difficult to establish a solid mixing pattern, as is the case for other classes of powders. Canada et al. (1978) reported that at higher superficial gas velocities, bubbles coalesce, forming large voids which produce large bed oscillations and cyclic movement of the bed surface.

Solid mixing in a freely bubbling bed is not only caused by vertical motion of bubbles, but also by bursting of bubbles at the bed surface. This induces lateral dispersion of parts of the wake's particles over a wide area, and the remaining particles are ejected into the freeboard (Shen, et al., 1995). Lateral mixing of particles is also improved by coalescence and lateral motion of bubbles, as well as gross particle circulation or the so-called 'Gulf Stream'.

4.3 Axial and lateral solid mixing in gas-fluidized beds

The importance of solid mixing has made researchers focus on its study. To do this, they investigated how solid mix axially (vertically) and laterally (horizontally) in fluidized beds. May (1959) was among the first to investigate the process of axial mixing. He measured axial mixing rate using the dispersal of radioactive particles injected at the bed surface, analysing the results using the diffusion equation:

$$\partial_t C = D_{sa} \partial_{yy}^2 C \quad (4.1)$$

where C represents the concentration of tracer particles, D_{sa} represents the axial dispersion coefficient and y is the axial spatial coordinate. He found reasonable agreement between the latter equation and experimental results for Geldart A powders fluidized in a bed of aspect ratio 24. However, when the experiments were carried out in a bed of aspect ratio 6.4 the model could not fit experimental results satisfactorily.

Similarly, Miyauchi et al. (1981) studied axial mixing of Geldart A powders in a turbulent bed, analysing the results using Eq. 4.1. They found that mixing data could be well represented by the latter. They derived the following equation for D_{sa} :

$$D_{sa} = 12u^{1/2}W^{0.9} \quad [cm^2/s] \quad (4.2)$$

where u is the superficial gas velocity and W is the vessel width. Avidan & Yerushalmi (1985) also found reasonable agreement between Eq. 4.1 and experimental data when they studied axial solid mixing in the turbulent regime, but their data fitted poorly when the bed was in the bubbling regime.

To explain why the experimental results of May (1959) did not satisfactorily fit the diffusion equation at low bed aspect ratio, Kunii & Levenspiel (1969) reported that low aspect ratios cause strong solid circulation; consequently, strong convective mixing (as a result of bulk movement of particles), rather than diffusive mixing (due to random fluctuations in particle velocity), prevails; so that their experimental data cannot satisfactorily fit the diffusion equation. Conversely, May (1959) obtained a reasonable fit in tall beds because there was mild solid circulation. Furthermore, when bubbling is vigorous, which is the case in the turbulent regime, convective mixing is less dominant, and hence experimental data are better fitted by the diffusion equation. This explains why Miyauchi et al. (1981) and Avidan & Yerushalmi (1985) obtained reasonable agreement between Eq. 4.1 and their experimental data.

Esin & Altun (1984) studied the rate of axial solid mixing using ion-exchange resins as tracer particles. They placed a known amount of particles in the bed and a uniform layer of accurately weighed tracer particles were placed on top. Then the bed was fluidized by air. After fluidizing the bed for a certain period, they switched off the air supply. Subsequently, they determined the concentration of tracer particles at different horizontal layers along the bed, analysing the results using the diffusion equation. They derived the following correlation for D_{sa} :

$$D_{sa} = 0.051 \frac{u}{u_m} (u - u_m)^{1.471} \quad [cm^2/s] \quad (4.3)$$

Following May (1959), Mostoufi & Chaouki (2000) adopted a radioactive particle tracking technique to investigate the mechanism of axial solid mixing. They fluidized FCC particles at different fluidization velocities, covering bubbling and turbulent regimes. They reported that upward movement of solids occurs by diffusive mechanism, while downward movement proceeds via convective transport. Their results showed that the upward motion was characterised by bubble-bubble and/or cluster-cluster interaction in the central part of the bed. On the other hand, solid clusters descend with very little interaction with other clusters, making the downward solid movement a convective process. Similar to foregoing authors, they quantified the rate of upward solid mixing using the diffusion equation.

Lee & Kim (1990) studied axial mixing of solids in a fluidized bed containing glass beads, but they focussed on mixing in the slugging and turbulent flow regimes. They used axial transport of heat at steady state to determine the mixing rate of solids, analysing their experimental results using the diffusion equation. Their results showed that effective axial mixing rates did not change appreciably in the slugging regime, but increased with an increase in gas velocity in the turbulent regime. Others (Geldart, 1973; Cranfield, 1978; Abrahimi & Resnick, 1974) also investigated axial mixing of solids in fluidized beds experimentally.

Experimental work on solid mixing is not only limited to axial mixing; researchers have investigated lateral mixing, focussing on the mechanism by which it proceeds and on how the lateral mixing rate can be quantified. HIRAMA *et al.* (1975) showed that bubble eruption at the bed surface contributes significantly to lateral solid dispersion. To demonstrate this, they installed lattice at the bed surface to restrict the movement of solids at the surface. They found that the lateral solid mixing rate was higher than when no lattice was installed on the surface of the bed, showing that the burst of bubbles at the bed surface substantially affects lateral solid mixing.

Similarly, Merry & Davidson (1973) investigated how solids mix laterally in fluidized beds. They reported that uneven distribution of fluidizing medium will promote lateral solid mixing,

stating that the process induces rapid mixing in the bed, and subsequent eruption of bubbles at the bed surface. The eruption of bubbles causes their solid contents to be ejected into the freeboard over a wide area. Kunii & Levenspiel (1991) provided more insight on the mechanisms of eruption of bubbles at the bed surface. They stated that the bubble pressure being higher than the pressure at the bed surface causes the bubble to “pop” on reaching the surface, spraying solids from the bubble roofs into the freeboard. In addition to this, bubbles may rise faster than the surrounding material, causing the solids in the wake of the bubble to be thrown as a clump into the bed surface. They further stated that the coalescence of bubbles as they emerge at the bed surface may result in strong ejection of wake solids into the freeboard, thus increasing lateral solid transport. In the same vein, Shi & Fan (1984) investigated the mechanism of lateral solid mixing using coloured particles as tracers. They reported that the lateral solid mixing mechanism consists of movement of bubbles through the bed, eruption of bubbles at the bed surface and gross particle circulation in the bed.

To further investigate the process of lateral solid mixing, Pallarès et al. (2007) carried out solid mixing studies in fluidized bed boilers. They showed that under operational conditions the flow pattern of fuel in the latter is highly convective and structured in horizontally aligned vertical vortices with alternating rotational directions. These are referred to as bubble paths. Each main bubble path is assumed to create a solid mixing cell around itself. In each cell, these three mechanisms for lateral dispersion occur: bubble wake mixing, emulsion drift sinking and bubble eruption of scattering at the bed surface. They reported that the net lateral dispersion is the result of solid exchange between different mixing cells.

Instead of studying axial and lateral solid mixing in separate experiments, some researchers concentrated on investigating both in the same experiments. Valenzuela & Glicksman (1984) carried out a qualitative study on solid mixing in a two-dimensional bubbling bed using glass bead particles of sizes between 600 and 850 μm , investigating axial and lateral mixing by using heated particles as tracers. They carried out two experiments: the first was by measuring the steady state temperature around a heated wire placed at the centre of the bed, while the second

was by measuring the transient temperature response of heated particles injected in the bed. Their results revealed that lateral solid mixing is partially due to mixing in the bubble wakes. They also reported that upward solid transport is characterized by a mixing length of the order of the bubble size, while downward solid transport is more uniform and at a much lower velocity.

Similarly, Shen & Zhang (1998) investigated the effect of particle size on both axial and lateral mixing of solids in fluidized beds using heated particles as tracers. The heated particles were injected pneumatically into the bed and the bed temperature was measured at different locations. The results of their experiments show that temperature fluctuations become more prominent as the particle size increases. Their results also revealed that convective axial mixing rates are higher than those for lateral mixing. They reported that lateral mixing of solid is composed of two components: the primary being the diffusive component generated by the random motion of solids, and the secondary being the convective component imparted by the motion of bubbles. They further interpreted their experimental results using a convection-diffusion model for solid mixing.

Schlichthaerle & Werther (2001) adopted a different approach to study both axial and lateral mixing in the bottom zone of circulating fluidized beds (CFB). They injected solid carbon dioxide into the bed and measured the temperature and gas concentration at different locations, analysing their results using the convection-diffusion equation. The experiment was carried out in a CFB riser with a rectangular cross-section and at operating conditions similar to those usually present in fluidized bed combustors. Their measurements showed a higher extent of mixing in the axial direction than in the horizontal direction, supporting the observations of Shen & Zhang (1998).

Most studies on solid mixing reported in the preceding paragraphs were analysed using either the diffusion equation or the diffusion-convection equation, but as the understanding of fluidized bed hydrodynamics grew, researchers began to study the process of solid mixing using

mechanistic models that would enable them to make fundamental measurements for the design of large-scale fluidized beds. The simplest version of these mechanistic models was introduced by van Deemter (1967). He developed a *counter-current solid circulation model* for mixing of solids in a bubbling fluidized bed. He then used the model to investigate axial mixing in a gas-fluidized bed. To develop this model, he divided the solid phase into two streams: one flowing upwards and another flowing downwards with exchange between the two streams. By taking a mass balance for the tracer injected into the bed, he derived a differential equation describing the axial mixing of the tracer. This reads:

$$f \frac{\partial c}{\partial t} + fv \frac{\partial c}{\partial x} + k_e(c - C) = 0; \quad \text{for the upward moving phase} \quad (4.4)$$

$$F \frac{\partial C}{\partial t} + FV \frac{\partial C}{\partial x} + k_e(C - c) = 0; \quad \text{for the downward moving phase} \quad (4.5)$$

where f and F , c and C , and v and V are the solid volume fractions, tracer volume fractions and phase velocities in the upward and downward moving phases respectively and k is the interchange mass transfer coefficient between the two phases.

Sitnai (1981) proposed a modified form of van Deemter's counter-current solid circulation model. The model is similar to that derived by the latter author, except in one aspect: he divided the bed into three regions instead of two. He assumed that there is a thick region of solids descending down the vessel wall, representing the third region. The governing equations therefore contain three partial differential equations of solid concentration. The model was employed to interpret mixing data, revealing that there is low circulation of solids and high solid exchange rate between phases. He reported that both processes affect heat and mass transfer rates in fluidized beds. The model however cannot predict random, short-term, disturbances near the bed surface.

Shen et al. (1995) adopted the procedure of Sitnai (1981) to develop a model for investigating axial and lateral mixing in fluidized beds. The model divided the solid mixing process in two

components: the first is the convection component between the upward moving bubble wakes and the down-flowing emulsion phase; the second is the diffusion in the emulsion phase. Their results also showed that the vertical mixing of solids is much faster than the lateral mixing. Several researchers (Gilliland & Mason, 1949; Leva & Grummer, 1952; May, 1959; Tailby & Cocquerel, 1961; Talmor & Benenati, 1963; Bailie, 1967; Potter, 1971) have developed theoretical models to study the mixing process in fluidized beds.

The key limitation of the counter-current solid circulation model is the lack of reliable equations for estimating the exchange coefficients appearing in the model. Researchers have employed different means to estimate these coefficients. For instance, Kunii & Levenspiel (1969), through their bubbling bed model, developed an expression for the interchange mass transfer coefficient. The model considered the bed as consisting of a continuous phase, called the emulsion, through which bubbles rise. The latter are surrounded by a cloud of rising gas and particles, called bubble cloud. The bubbling model bed indicates that the gas in a vigorous bubbling bed exists in three regions: bubbles surrounded by cloud gas, both rising through an emulsion gas. The model provides relationships among various quantities necessary for describing bubble conditions in the bed, in particular the interchange mass transfer coefficient k_e appearing in the counter-current solid circulation model:

$$k_e = \frac{3(1 - \varepsilon_{mf}) u_{mf}}{(1 - \delta)\varepsilon_{mf} d_b} \quad [s^{-1}] \quad (4.8)$$

where ε_{mf} is the minimum fluidization voidage, u_{mf} is the minimum fluidization velocity, δ is the bubble fraction and d_b is the bubble diameter.

The foregoing experimental and theoretical studies on axial and lateral solid mixing revealed their importance in ensuring efficient operation of fluidized bed processes. In recent times, researchers have concentrated more on the study of lateral mixing of solids in gas-fluidized beds. This is because of its importance in large scale fluidized beds. Grace (1981) emphasizes the importance of lateral solid mixing in shallow beds, stating that its knowledge is even more

important than that of axial mixing in assessing the performance of gas-solid fluidized beds. In the remaining part of this chapter, and in the next chapter, we focus on lateral solid mixing, reporting on various works that have been done on it and the methods employed for measuring the rate at which it occurs. To quantify the rate at which solids mix laterally in fluidized beds, researchers often resort to lateral dispersion coefficient, D_{sr} ; this, as we shall see in this study, is an *effective* diffusivity relating to the time that solids take to spread laterally over a given distance in the bed. Lateral dispersion coefficient is usually defined using the following equation:

$$\partial_t C = D_{sr} \partial_{xx}^2 C \quad (4.9)$$

where C represents the void-free solids concentration, D_{sr} represents the lateral dispersion coefficient and x is the horizontal spatial coordinate. This equation, as just said, should be regarded as a *definition* of such coefficient. We will now report various experimental methods adopted by researchers for estimating D_{sr} .

4.4 Estimating lateral dispersion coefficients in gas-fluidized beds

A pioneering attempt at estimating lateral dispersion coefficients was by Brotz (1956). He used a shallow rectangular bed, consisting of two solids which are similar in physical properties, but differ only in colour. He separated the solid with a removable partition plate which divided the bed into two equal parts. He fluidized the bed for a certain time and the partition was removed. By measuring the rate at which the two solids approach uniformity, he estimated the lateral dispersion coefficient.

Gabor (1964) used a similar experimental method to Brotz. Instead of using solids of different colours in his analysis, he used differences in magnetic property. In the experiment, he used copper and nickel having different magnetic behaviour but having the same density, size and shape. He placed the solids in a rectangular vessel separated by a partition placed at the centre. On removing the partition, mixing occurred on either side of the centre line. After a certain

mixing time, he turned off the fluidized gas and carried out sampling at known radial distances across the bed. From the sampling, he determined the concentration profiles across the bed. By employing the diffusion-type equation, he estimated the value of the lateral dispersion coefficient. He developed an empirical relationship for the dispersion coefficient D_{sr} as follows:

$$D_{sr} = D_p \left[\frac{(u - u_{mf})}{d_p \varepsilon} \right] (1.22 \times 10^{-6}) \quad [ft^2 s^{-1}] \quad (4.10)$$

Here D_p is the diameter of the fixed packing in ft , d_p is the particle diameter in ft , u is the superficial gas velocity in $ft./s$ and u_{mf} is the superficial gas velocity in $ft./s$.

Borodulya & Epanov (1982) employed a heated particle tracer to determine lateral solid dispersion coefficients in fluidized beds. They also divided the bed into two parts; the heating chamber and the working chamber with a movable barrier. They pre-heated a very small portion of the bed to a temperature of 400-600°C and poured it into the heating chamber. By measuring the time taken for thermocouples in different locations of the bed to show a variation in temperature, they estimated the dispersion coefficient. They proposed the following correlation for D_{sr} :

$$\frac{D_r}{(u - u_{mf})H_o} = 0.013 \left(\frac{D_c}{H_o} \right)^{0.5} Fr^{-0.15} \quad (4.11)$$

In Eq. 4.11, D_c is the equivalent diameter of the vessel, H_o is the bed height at rest, u is the superficial gas velocity, u_{mf} is the minimum fluidization velocity. Fr is the Froude number given by the following expression:

$$Fr = \frac{(u - u_{mf})^2}{gH_o} \quad (4.12)$$

Shi & Fan (1984) measured lateral dispersion of solids in a rectangular fluidized bed using a similar approach to that employed by Brotz (1959). They divided the bed equally into two parts using a removable partition inserted vertically in the bed. In the first half of the bed they put

dyed particles and in the other half they put undyed particles. Shi & Fan fluidized the particles at constant superficial gas velocity and quickly removed the partition when the stable state of fluidization was reached. After fluidizing the particles for a certain time, they took samples of mixed particles from different lateral positions of the bed. By washing a weighed sample with a known amount of water, they used spectrophotometer to determine the concentration of tracer particles in the sample. From series of experimental runs carried out, they obtained the following correlation for the lateral solid dispersion coefficient:

$$\frac{D_{sr}}{(u - u_{mf})h_{mf}} = 0.46 \left[\frac{(u - u_{mf})d_p\rho_f}{\mu_f} \right]^{-0.21} \left[\frac{h_{mf}}{d_p} \right]^{0.24} \left[\frac{\rho_p - \rho_f}{\rho_f} \right]^{-0.43} \quad (4.13)$$

Here ρ_p and ρ_f are the densities of particle and fluid respectively, μ_f is the fluid viscosity, d_p is the particle diameter and h_{mf} is the height at minimum fluidization.

Bellgart & Werther (1986) estimated the lateral solid dispersion in fluidized beds by using carbon dioxide pellets as a tracer. The sublimation of the latter is an endothermic process having a thermal effect on the bed and the formation of gaseous CO_2 can be used to locate the tracer. They measured the temperature gradient in the bed and the concentration of evaporated carbon dioxide on the surface of the bed. From their experimental measurements, they obtained the following correlations:

$$D_{sr} = D_0 + 0.023 \frac{1}{H} \int_0^H \frac{t_k}{1 - t_k} \sqrt{gd_b^3} dh \quad (4.14)$$

They determined the value of D_0 from the experiment to be $0.67 \times 10^{-3} m^2/s$, g is the acceleration of gravity, t_k is the thickness of the suspension layer around a bubble and H is the expanded bed height.

Berruti et al. (1986) determined the axial and lateral solid dispersion coefficient by continuously measuring solid tracer concentration at different locations in the bed. They inserted a tube filled with tracer up to a particular level in the centre of an empty reactor. Then, they charged sand

into the reactor to reach the same level as the tracer. They fluidized both the tracer and the sand for a certain time sufficient to reach stable fluidization, and the tube containing the tracer was subsequently removed to allow the sand and the tracer to mix. Samples were collected and analyzed. They obtained the following correlation:

$$\frac{D_{sr}}{(u - u_{mf})d_p} = 0.185 \times 10^{-4} \left[1 - \left(0.44 + 2.87 \frac{h}{h_{mf}} \right) \left(\frac{r}{R} \right)^5 \right] \times \left(\frac{(u - u_{mf})d_p \rho_f}{\mu_f} \right)^{-0.25} \left(\frac{h}{d_p} \right)^{1.45} \left(\frac{\rho_p - \rho_f}{\rho_f} \right)^{-0.43} \quad (4.15)$$

Here ρ_p and ρ_f are the densities of particle and fluid respectively, μ_f is the fluid viscosity, d_p is the particle diameter and h_{mf} is the height at minimum fluidization.

Du & Wei (2002) studied lateral mixing behaviour of FCC particles in fluidized beds using phosphor tracer techniques. They injected the tracer into the bed using pneumatic tracer injector. With the aid of an electric flash, the phosphor tracers were excited and gave out emissive light immediately. The intensity of light given out by the particles at various locations in the bed was measured using a detector. The tracer concentration is proportional to the emissive light strength of the particles. By performing the experiments under various operating conditions and particle properties, Du & Wei (2002) derived the following correlation for the lateral solid dispersion coefficient:

$$D_{sr} = 0.018 Re_p^{0.74} \exp[-19(1 - \varepsilon)] \left(\frac{d_p}{d_s} \right)^{-0.53} \left(\frac{\rho_p}{\rho_s} \right)^{-0.72} \phi^{2.32} \quad (4.16)$$

Here ϕ is the sphericity of the particles, Re_p is the particle Reynolds number, d_p is the diameter of tracer particles, ρ_s is the density of particles originally in the bed and ε is the void fraction.

Several other empirical methods, reported in Table 4.1, have been used by researchers to study the lateral dispersion of solids in fluidized beds. Kashyap & Gidaspow (2011) summarized these methods as saline (Rhodes et al., 1991), ferromagnetic (Avidan & Yerushalmi, 1995), thermal (Borodulya & Epanov, 1982), radioactive (Mostoufi & Chaouki, 2001), carbon (Winaya et al.,

2007) and phosphorescent tracers (Du et al., 2002). These empirical approaches to studying lateral solid mixing in fluidized beds have their limitations. For instance, in thermal tracking techniques the heat transferred to the fluid phase and walls makes it difficult to interpret the results. In radioactive tracing methods, safety of equipment and personnel are of great concern. In phosphorescence tracking, most successful applications are usually in dilute fluidized beds.

Table 4.1: Experimental results on lateral solid mixing in gas-fluidized beds

Author	Bed size (m)	Tracer particles	Range of D_{sr} (m^2/s)
Highley & Merrick (1971)	\varnothing 1.52	Radioactive	0.007 – 0.015
Borodulya et al. (1982)	\varnothing 0.70 0.60 × 0.20 0.40 × 0.25 0.50 × 0.05	Heated bed material	Not evident
Shi & Fan (1984)	0.30 × 0.05	Dyed bed material	0.0001 – 0.0008
Subbarao et al. (1985)	0.20 × 0.010	Heated bed material	0.0001 – 0.08
Bellgardt & Werther (1986)	2.0 × 0.3	Carbon dioxide ice	0.0007 – 0.0026
Berruti et al. (1986)	\varnothing 0.27	Potassium cyanide	0.0002 – 0.002
Xiang et al. (1987)	2.6 × 1.6	Coal particles	0.001 – 0.01
Salam et al. (1987)	0.90 × 0.15	Coal particles	0.0005 – 0.002
Yang & Kojima (1995)	0.30 × 0.05	Coal particles	0.0004 – 0.0016
Xiao et al. (1998)	Tapered[2.5 × 0.15	Mung bean	0.04 – 0.40
Schlichthaerle & Werther (2001)	1.0 × 0.3	Carbon dioxide ice particles	0.12

For all solid tracer techniques, the common limitation is that repeatable results are only guaranteed if numerous runs of experiments are carried out, which may not be practicable in real experiments. In addition to these, experiments with solid tracers are difficult to perform because of lack of continuous sampling and existence of residual tracers. Furthermore, the values of dispersion coefficients reported by these studies differ by up to four orders of magnitude making it difficult to generalize or scale up the results from these studies (Liu & Chen, 2010).

Despite previous experimental and theoretical investigations of the influence of geometry (Liu & Chen, 2010; Xiao et al., 1998), operating conditions (Bellgardt et al., 1985; Bellgardt & Werther, 1986; Chirone et al., 2004; Lim & Argarwal, 1994; Pallares et al., 2007) and particle properties (Pallares & Johnsson, 2006; salam et al., 1987; Xiang et al., 1987) on lateral mixing in fluidized beds, the understanding of how these parameters affect the dispersion coefficient is still limited. This is because the mechanisms governing solid mixing are quite complex. There are several disconnected values reported for lateral solid dispersion coefficients in the literature. We observed differences of about five orders of magnitude in their values (Gidaspow et al., 2004; Breault, 2006; Jiradilok, 2007). These differences are due to the fact that investigators used different definitions, theories, and approaches to determine them (Kashyap & Gidaspow, 2011).

More importantly, studies on lateral solid dispersion in fluidized beds using a computational approach are still scanty. This has hindered the advancement of knowledge on how various design and operating parameters affect the coefficient. The computational approach to studying lateral solid mixing in fluidized beds offers some distinct advantages: an accurate computational-based model that describes well the lateral mixing process can be useful for the design of fluidized bed reactors. This reduces time and eliminates the cost of constructing pilot plants. It also helps to avoid the risks inherent in pilot plant scale-up processes. Another

important advantage is that a fundamental model can help to shed light on the mechanisms of lateral mixing potentially allowing for considerably more insight. To the best of our knowledge, numerical works on lateral solid dispersion in fluidized beds have only been carried out by Liu and Chen (2010) and Farzaneh et al. (2011). Liu & Chen (2010) employed a hybrid model to determine lateral dispersion coefficient in large-scale fluidized beds. They used a combination of Eulerian-Granular simulation and fictitious particle tracing technique. This approach involves tracking massless fictitious tracer particles in the bed. They determined lateral dispersion coefficients using two methods; micro and macro methods. The latter is based on fitting the transient particle concentration profile by the Fickian-type diffusion equation, while the former is based on statistics of particles from the Lagrangian view. They used the Fickian-type method to study the distribution of fuel particles over the cross-section of a fluidized bed, assuming that the dispersion rate of fuel particles is the same as that of inert bed materials. However, the validity of their approach has been questioned by Farzaneh et al. (2011). They argued that the assumption that the dispersion rate of fuel particles and inert bed materials are the same is not convincing because they have substantially different size and density. Farzaneh et al. (2011) employed the Lagrangian modeling approach to determine lateral dispersion coefficients. They developed a multi-grid Lagrangian model to study the lateral dispersion of fuel particles in the inert bed materials. The approach was adopted to account for the size difference between the fuel particles and the inert particles. By using statistical methods, they determined the lateral dispersion coefficient in the bed. As with other Lagrangian-based approaches, the method is limited with respect to the number of particles that can be tracked.

In the next chapter, we employed the Eulerian-Eulerian modelling approach to determine lateral solid dispersion coefficients in fluidized beds, investigating how changes in operating parameters affect it. The approach describes both the solid and fluid phases as interpenetrating continua. The model consists of the continuity equations and linear momentum balance equation written for each phase. These equations are valid for any physical and chemical system, and therefore this approach does not introduce any assumption in the model, except for the

constitutive equations needed to render the equations mathematically closed. We follow an approach similar to that proposed by Brotz (1956). He used two solids of equal physical properties, but differing in colour. The solids were separated by a vertical partition plate which divided the bed into two equal parts. He fluidized the bed for a certain time and then removed the partition; by measuring the rate at which the two solids mix, he estimated the lateral dispersion coefficient. Following Brotz, we defined two solid phases, Solid-1 and Solid-2, with equal physical properties, differing only in the names assigned to them in the computational code. We then placed Solid-1 on the left and Solid-2 on the right of a removable partition. We fluidized the bed with air at ambient temperature, allowing it to reach pseudo-stationary conditions, and then removed the partition. From the radial concentration of the Solid-1 phase, we estimated the lateral solid dispersion coefficient at the assigned operating conditions.

4.5 Conclusions

Efficient mixing is crucial in many fluidized bed processes including combustion, drying, polymerization and granulation. To study the phenomenon of solid mixing, researchers often investigate how solids mix vertically (axially) and horizontally (laterally) in the bed. There has been considerable effort to investigate axial and lateral solid mixing experimentally. Researchers have adopted several approaches including radioactive, thermal, saline and phosphorescent tracing methods. In all these experimental techniques, the common limitation is that repeatable results are only guaranteed if numerous runs of experiments are carried out, which may not be practicable in real experiments. In addition to these, experiments with solid tracers are difficult to perform because of lack of continuous sampling and existence of residual tracers. More recently, computational fluid dynamics (CFD) simulations have proved to be effective in the study of fluidized beds. By using CFD, it is possible to simulate the behaviour of large-scale fluidized beds directly and gain insight into the fluid dynamic interactions in the bed.

In the next chapter we focus on lateral solid mixing. We use the CFD modelling approach to investigate it, examining the effects of operating conditions on it.

Chapter 5

2D CFD simulations of lateral solid mixing in gas-fluidized beds

This chapter is concerned with 2D CFD simulations of lateral solid mixing in gas-fluidized beds.

1. We describe lateral solid mixing using the Eulerian-Eulerian modelling approach.
2. We quantify mixing by means of a lateral dispersion coefficient.
3. We investigate the influence of design parameters and operating conditions on lateral dispersion coefficients.
4. We validate our numerical results with empirical correlations reported in the literature.
5. We investigate the influence of frictional stress models on our numerical results.

Parts of this chapter have been published:

Oke, O., Lettieri, P., Solimene, R., Salatino, P., Mazzei, L. 2014. *Numerical simulations of lateral solid mixing in gas-fluidized beds*. Chemical Engineering Science, 120, 117-129.

5.1 Introduction

In Chapter 4 we reported different experimental methods employed to investigate lateral solid mixing in gas-fluidized beds. We emphasized the dearth of computational approach to studying lateral solid mixing, stressing the need to further explore computational methods in investigating the latter. In the present chapter we employ the multiphase fluid dynamic equations, consisting of the continuity and linear momentum balance equations written for the fluid and the solid phases, to investigate lateral solid mixing. These equations are valid for any physical or chemical system, since they are essentially expressing the law of conservation of mass and linear momentum. Nonetheless, these equations are mathematically unclosed. They contain some indeterminate terms which must be closed in order to solve the governing equations numerically. These terms are the fluid-particle interaction force, particle-particle interaction force (this arises when there are more than one solid phases) and effective stress tensor. The various constitutive equations employed to close these indeterminate terms are reported. We then solve the governing equations along with their constitutive equations numerically. We investigate the influence of superficial gas velocity, bed height and bed width on lateral dispersion coefficients, validating the numerical results with experimental data. Subsequently, we examine how the constitutive equations used to model the frictional flow regime affect lateral dispersion coefficients. To begin, we report on how we define the lateral dispersion coefficient and the methodology we adopt to estimate it.

5.2 Lateral dispersion coefficient – Definition and estimation

Sometimes one might be interested in *estimating* how fast particles mix in a fluid bed at given operating conditions, without wanting to solve complex and numerically expensive models. One way of doing this is resorting to axial and lateral *dispersion coefficients*; these, as said, are *effective* diffusivities relating to the time that solids take to spread axially and laterally over a given distance in the bed. We are going to focus on the lateral dispersion coefficient; therefore, before going any further, let us clarify how the latter is defined. Most researchers (Brotz, 1956;

Borodulya & Epanov, 1982; Shi & Fan, 1984; Liu & Chen, 2010) define it through an equation analogous to Fick's law of molecular diffusion, writing:

$$\partial_t C = D_{sr} \partial_{xx}^2 C \quad (5.1)$$

where C represents the void-free solids concentration, D_{sr} represents the lateral dispersion coefficient and x is the horizontal spatial coordinate. This equation, as just said, should be regarded as a *definition* of such coefficient. Let us briefly comment on the applicability of Eq. 5.1 to the present investigation. One might wonder how the diffusion equation above can be relevant to the study of lateral solid mixing in fluidized beds. Lacey (1954) proposed a diffusion-like mechanism for solid mixing, arguing that particles spread through a surface in a manner similar to ordinary molecular or thermal diffusion. Each particle has equal chance of moving to either side of the surface, closely resembling the motion of molecules of a gas. Indeed, experimental data obtained by Carstensen and Patel (1977) revealed that mixing of binary particles can be well characterized by Eq. 5.1 as long as the mean diameter of the particles are identical, the coefficient D_{sr} appearing in the equation lumping together the effects of various mechanisms responsible for solid mixing such as wake transport, emulsion drifting, bubble coalescence and break-up. Therefore D_{sr} is affected by operational and design conditions such as superficial gas velocity, bed height, bed geometry, bed width, including material properties such as particle size and density. This makes D_{sr} different from the diffusion coefficient appearing in the original Fick's law which is constant for a given solute in a solvent. For shallow beds, particle ejection/fall-back in the freeboard upon bubble bursting at the bed surface may also be relevant.

Take a 2D bed (we consider two dimensions to simplify the description, but similar considerations hold in three dimensions) where the concentration of solids depends in general on both spatial coordinates, so that $c = c(x, y, t)$, with x and y denoting the horizontal and vertical coordinates, respectively. The concentration in Eq. 5.1 is averaged over the vertical direction, and hence is a function of the x coordinate only, so that $C = C(x, t)$. For a given

system, by matching the actual concentration function $C_e(x, t)$, which one can determine either experimentally or numerically, with the analytical solution of Eq. 5.1, one can find the lateral dispersion coefficient. We should bear in mind that, unlike molecular diffusion coefficients, D_{sr} is not just a function of the particle properties, but depends on the system geometry and on the operating conditions. Let us be more specific. Often, to determine the lateral dispersion coefficient, one considers a bed divided into two equal compartments; the particles occupying the compartments differ solely in colour (having in particular same size and density). For instance, one can have red particles in the left compartment and white particles in the other, as shown in Figure 5.1. The functions $c(x, y, t)$ and $C(x, t)$ represent the concentration of just one kind of particles, say the red ones, which are regarded as tracer particles. Hence, the initial conditions characterizing this particular setup are:

$$t = 0: \quad C = \bar{C} \quad \text{for} \quad 0 \leq x < \frac{L}{2} \quad \text{and} \quad C = 0 \quad \text{for} \quad \frac{L}{2} < x \leq L \quad (5.2)$$

The boundary conditions that one needs to assign to solve Eq. 5.1 are:

$$x = 0, \quad x = L; \quad \partial_x C = 0 \quad (5.3)$$

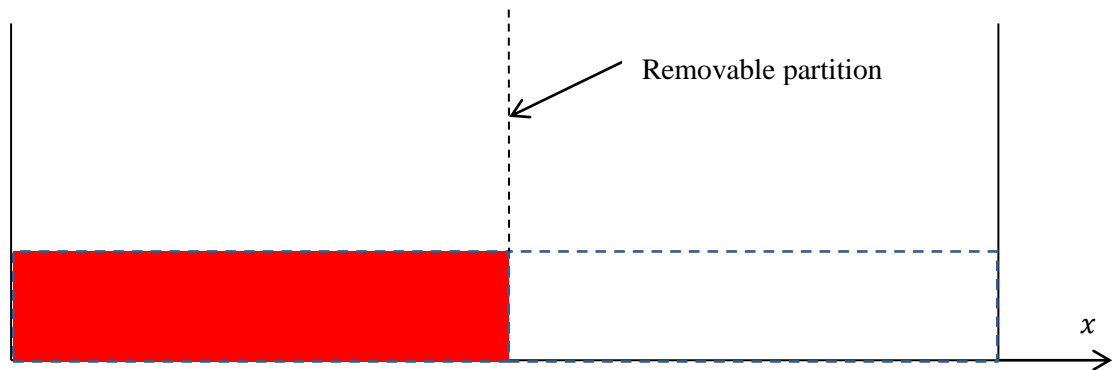


Figure 5.1: A set-up for estimating lateral dispersion coefficients

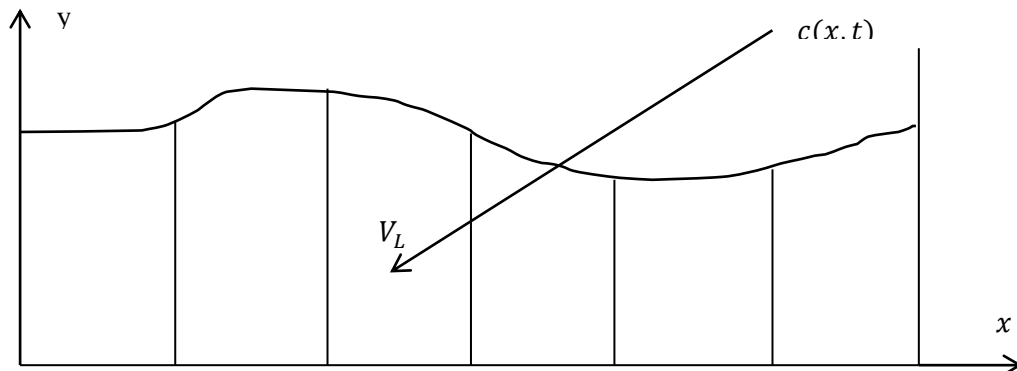


Figure 5.2: A set-up showing vertical layers for estimating lateral dispersion coefficients

In the real experiment (which may be numerical) the two compartments, as reported above, are separated by a removable wall. At time $t = 0$, one fluidizes the system, waiting for the latter to reach pseudo-stationary conditions. Then one removes the partition, letting the red and white particles spread through the bed. The void-free concentration of red particles, which one in theory could measure (or calculate numerically), is $c(x, y, t)$. One can then divide the bed in a given number of vertical layers, as shown in Figure 5.2, and calculate the value of C_e in each layer using the relation:

$$C_e(x, t) \equiv \frac{1}{V_L} \int_{V_L} c(x, y, t) dV \quad (5.4)$$

where V_L denotes the volume of each vertical layer. The next step is solving Eq. 5.1, using the conditions in Eq. 5.2 and 5.3. For this simple system an analytical solution is given by:

$$\frac{C(x, t; D_{sr})}{\bar{C}} = \frac{1}{2} + \frac{2}{\pi} \sum_{a=1}^{\infty} \frac{1}{a} \sin\left(\frac{a\pi}{2}\right) \cos\left(a\pi \frac{x}{L}\right) \exp\left(-a^2 \pi^2 \frac{t}{L^2/D_{sr}}\right) \quad (5.5)$$

Here we have reported explicitly the dependence of the analytical solution on the parameter D_{sr} . Then, to estimate D_{sr} we simply match the profiles $C_e(x, t)$ and $C(x, t; D_{sr})$. To do this, we define:

$$G \equiv [C(x, t; D_{sr}) - C_e(x, t)]^2 \quad (5.6)$$

The task of determining D_{sr} then reduces to finding the value of D_{sr} that minimizes G in Eq. 5.6. This value gives the lateral dispersion coefficient for the system under investigation. By repeating this procedure for many geometries and operating conditions, one can obtain a correlation of the form written in Eq. 5.7, which others can then use to estimate D_{sr} ; this reduces the need for solving complex models or conducting experiments each time one is interested in estimating D_{sr} .

$$\frac{D_{sr}}{(u - u_{mf})h_{mf}} = f\left(\frac{(u - u_{mf})d_p \rho_f}{\mu_f}, \frac{h_{mf}}{d_p}, \frac{\rho_p - \rho_f}{\rho_f}, \frac{L}{d_p}\right) \quad (5.7)$$

Here u is the superficial gas velocity, u_{mf} the minimum fluidization velocity, h_{mf} the height at minimum fluidization, ρ_p the particle density, ρ_f the fluid density, μ_f the fluid viscosity and L the bed width.

As said, one can use the lateral dispersion coefficient D_{sr} to roughly estimate the time τ that solids take to spread laterally over a distance L in the bed. To demonstrate this, we note that:

$$\frac{\partial C}{\partial t} \sim \frac{\bar{C}}{\tau} \quad ; \quad \frac{\partial C}{\partial x} \sim \frac{\bar{C}}{L} \quad ; \quad \frac{\partial}{\partial x} \left(\frac{\partial C}{\partial x} \right) \sim \frac{\bar{C}/L}{L} = \frac{\bar{C}}{L^2}$$

where \bar{C} represents the concentration scale (whose value does not affect τ , because Eq. 5.1 is linear in the concentration). Eq. 5.1 thus yields:

$$\tau \sim \frac{L^2}{D_{sr}} \quad (5.8)$$

So, if one knows the value of D_{sr} for a given design and set of operating conditions, one can estimate the time τ required for the solids to spread laterally over the length L in the bed.

We would like to emphasize that the parameter D_{sr} in Eq. 5.1 is different from the coefficient appearing in the original Fick's law. In the latter the parameter is molecular diffusivity, which is constant for a solute in a given solvent. Fick's law relates only to the diffusion of molecules generated by their random motion. The lateral dispersion coefficient, conversely, is affected by various competing mechanisms. These, as experimental evidence reveals, include bubble break-up at the upper bed surface and subsequent ejection of particles into the freeboard, wake transport, and drifting of emulsion owing to the passage of bubbles. Hence, the lateral dispersion coefficient is affected by several variables, among which we find bubble size and velocity, particle size and density as well as fluid density and viscosity. Shi & Fan (1984) reported that gross particle circulation also affects lateral mixing, this circulation in turn depending on bed height and superficial gas velocity. Determining D_{sr} is therefore quite challenging.

Another clarification is in order. As said, when calculating lateral dispersion coefficients, we operated in terms of concentrations averaged along the vertical direction of the bed, considering the function $C(x, t)$, defined through Eq. 5.5, in place of the function $c(x, y, t)$. In doing so, we lost information about vertical variations in concentration, which we expect to be present; these variations, nevertheless, are accounted for, inasmuch as they affect the value of $C(x, t)$ and in turn that of D_{sr} . We had to operate in terms of vertically-averaged concentrations, for we decided to define D_{sr} through Eq. 5.1, which is one-dimensional and accounts solely for variations along the horizontal space coordinate. We employed Eq. 5.1 to define D_{sr} because this is the relation usually used in the literature; in particular, the researchers cited in this article who measured D_{sr} experimentally - and whose results we used to validate our simulations - did adopt this definition and, as a consequence, operated in terms of vertically-averaged concentrations.

5.3 Multiphase fluid dynamic model

The governing equations in this work consist of balance equations for mass and linear momentum written for the fluid and the two solid phases:

Continuity equation – Fluid phase

$$\partial_t \varepsilon = - \nabla \cdot \varepsilon \mathbf{u}_f \quad (5.9)$$

Continuity equation – Solid phase i

$$\partial_t \phi_i = - \nabla \cdot \phi_i \mathbf{u}_i \quad (5.10)$$

Dynamical equation – Fluid phase

$$\partial_t (\varepsilon \rho_f \mathbf{u}_f) = - \nabla \cdot (\varepsilon \rho_e \mathbf{u}_f \mathbf{u}_f) + \nabla \cdot \mathbf{S}_f - n_1 \mathbf{f}_1 - n_2 \mathbf{f}_2 + \varepsilon \rho_e \mathbf{g} \quad (5.11)$$

Dynamical equation – Solid phase i

$$\partial_t (\phi_i \rho_i \mathbf{u}_i) = - \nabla \cdot (\phi_i \rho_i \mathbf{u}_i \mathbf{u}_i) + \nabla \cdot \mathbf{S}_i + n_i \mathbf{f}_i - n_i \mathbf{f}_{ik} + \phi_i \rho_i \mathbf{g} \quad (5.12)$$

Here i is a phase index, subscripts 1 and 2 identify the solid to the left and to the right of the partition, respectively (as reported in Section 5.2), ρ_e and ρ_i , ε and ϕ_i are the densities and volume fractions of the fluid and solid phases, respectively, while \mathbf{g} is the gravitational acceleration. Furthermore, \mathbf{u}_f , \mathbf{u}_i , \mathbf{S}_f , \mathbf{S}_i , \mathbf{f}_i , and \mathbf{f}_{ik} are the averaged velocities, effective stress tensors and interaction forces per unit particle exerted by the fluid and by the k th solid phase on the i th solid phase, respectively. The equations written above are unclosed; various terms need to be expressed constitutively.

5.3.1 Fluid-particle interaction forces

The main components of the fluid-particle interaction force are the buoyancy and drag forces. We neglect other contributions (Owoyemi et al., 2007); thus, we write $\mathbf{f}_i = \mathbf{f}_i^s + \mathbf{f}_i^d$. We define the buoyancy force as $n_i \mathbf{f}_i^s \equiv -\phi_i \nabla p_e$. We close the drag force using the expression of Mazzei & Lettieri (2007):

$$n_i \mathbf{f}_i^d \equiv \beta_i (\mathbf{u}_f - \mathbf{u}_i) \quad ; \quad \beta_i = \frac{3}{4} C_D(Re_i) \frac{\rho_e \|\mathbf{u}_f - \mathbf{u}_i\| \varepsilon \phi_i}{d_i} \varepsilon^{-\psi(\varepsilon, Re_i)} \quad (5.13)$$

$$\psi(\varepsilon, Re_i) \equiv -\frac{\ln \varphi(\varepsilon, Re_i)}{\ln \varepsilon} \quad ; \quad \varphi(\varepsilon, Re_i) \equiv \frac{C_D^*(\varepsilon, Re_i)}{C_D(Re_i)} \varepsilon^{2(1-n)}$$

$$C_D(Re_i) = (0.63 + 4.8 Re_i^{-\frac{1}{2}})^2 \quad ; \quad C_D^*(\varepsilon, Re_i^*) = (0.63 + 4.8 Re_i^{*\frac{-1}{2}})^2$$

$$Re_i \equiv \frac{\rho_f}{\mu_f} \varepsilon \|\mathbf{u}_f - \mathbf{u}_i\| d_i \quad ; \quad Re_i^*(\varepsilon, Re_i) \equiv \frac{Re_i}{\varepsilon^n} \quad ;$$

$$n(Re_i^*) = \frac{4.8 + 2.4 \cdot 0.175 Re_i^{*3/4}}{1 + 0.175 Re_i^{*3/4}} \quad (5.14)$$

Here d_i is the particle diameter of the i th solid phase, Re_i and Re_i^* are particle Reynolds numbers, while C_D and C_D^* are drag coefficients.

5.3.2 Particle-particle interaction force

We assume that the interaction force \mathbf{f}_{ik} exchanged between particles of different phases includes only a drag-like contribution. Therefore, it is proportional to the slip velocity between the phases. We use the constitutive equation developed by Syamlal (1987):

$$n_i \mathbf{f}_{ik} = \zeta_{ik} (\mathbf{u}_k - \mathbf{u}_i) ;$$

$$\zeta_{ik} = \frac{3}{4} (1 + e_{ik}) \left(1 + \frac{\pi}{4} F_{ik} \right) \frac{\rho_i \rho_k \phi_i \phi_k g_{ik} (d_i + d_k)^2}{\rho_i d_i^3 + \rho_k d_k^3} \|\mathbf{u}_k - \mathbf{u}_i\| \quad (5.15)$$

where e_{ik} is a coefficient of restitution equal to 0.90, F_{ik} is a coefficient of friction equal to 0.15 and g_{ik} is a radial distribution function that one obtains by combining the radial distribution functions g_i and g_k of the i th and k th particle phases, respectively. Their expressions are:

$$g_i = \frac{d_i}{2} \sum_{k=1}^2 \frac{\phi_k}{d_k} + \left[1 - \left(\frac{\phi}{\phi_{max}} \right)^{1/3} \right]^{-1} ; \quad g_{ik} = \frac{d_i g_k + d_k g_i}{d_i + d_k} \quad (5.16)$$

Here ϕ is the overall solid volume fraction, while ϕ_{max} is the maximum value that ϕ can attain.

5.3.3 Effective stress

We close the effective stress tensors using the Newtonian constitutive equations:

$$\mathbf{S}_f = -p_f \mathbf{I} + 2\mu_f \mathbf{D}_f + \left(\kappa_f - \frac{2}{3} \mu_f \right) (\text{tr} \mathbf{D}_f) \mathbf{I} \quad (5.17)$$

$$\mathbf{S}_i = -p_i \mathbf{I} + 2\mu_i \mathbf{D}_i + \left(\kappa_i - \frac{2}{3} \mu_i \right) (\text{tr} \mathbf{D}_i) \mathbf{I} \quad (5.18)$$

where p_f , p_i , μ_f , μ_i , κ_f and κ_i are the averaged pressures, viscosities and dilatational viscosities of the fluid and particle phases, respectively; \mathbf{I} is the identity tensor, while \mathbf{D}_f and \mathbf{D}_i are the rate of deformation tensors defined as:

$$\mathbf{D}_f \equiv \frac{1}{2}(\nabla \mathbf{u}_f + \nabla \mathbf{u}_f^T) ; \quad \mathbf{D}_i \equiv \frac{1}{2}(\nabla \mathbf{u}_i + \nabla \mathbf{u}_i^T) \quad (5.19)$$

Closing the effective stress tensors therefore reduces to finding constitutive expressions for the pressure, viscosity and dilatational viscosity of each phase. The fluid is regarded as incompressible and so the fluid pressure does not need a constitutive expression. The viscosity μ_f is assumed to be constant, while the dilatational viscosity κ_f is neglected. For the solid phases, we need constitutive expressions to model all these quantities.

The solid phase can be in two flow regimes: the *viscous regime* where particles undergo transient contacts and momentum transfer is translational and collisional, and the *frictional regime*, where particles are in enduring contacts and momentum transfer is mainly frictional. In both regimes, the solid phase is modelled as a continuum; in the viscous regime it is characterized by a viscous solid pressure p_i^v , viscosity μ_i^v and dilatational viscosity κ_i^v , while in the frictional flow regime it is characterized by a frictional solid pressure p_i^f , viscosity μ_i^f and dilatational viscosity κ_i^f .

We express p_i^v using the closure of Lun et al. (1984)

$$p_i^v = \left[1 + 2 \sum_{k=1}^2 \left(\frac{d_{ik}}{d_i} \right)^3 (1 + e_{ik}) \phi_k g_{ik} \right] \phi_i \rho_i \Theta_i ; \quad d_{ik} \equiv \frac{d_i + d_k}{2} \quad (5.20)$$

Here Θ_i is the granular temperature of the i th phase. In the present study, $d_i = d_k$, e_{ii} coincides with the restitution coefficient e_i and g_{ik} reduces to g_i . For the viscosity μ_i^v we adopt the closure of Gidaspow (1994):

$$\mu_i^v = \frac{10 \rho_i d_i \sqrt{\pi \Theta_i}}{96(1 + e_i) g_i} \left[1 + \frac{4}{5} (1 + e_i) \phi_i g_i \right]^2 + \frac{4}{5} \phi_i^2 \rho_i d_i g_i (1 + e_i) \left(\frac{\Theta_i}{\pi} \right)^{\frac{1}{2}} \quad (5.21)$$

For the dilatational viscosity κ_i^v we use the closure of Lun et al. (1984):

$$\kappa_i^v = \frac{4}{3} \phi_i^2 \rho_i d_i g_i (1 + e_i) \left(\frac{\Theta_i}{\pi} \right)^{\frac{1}{2}} \quad (5.22)$$

The granular temperatures are governed by balance equations for the pseudointernal energies related to the fluctuation velocities of the particles (Gidaspow, 1994; Syamlal et al., 1993). The equation reads:

$$\partial_t(\phi_i \rho_i U_i) = -\nabla \cdot (\phi_i \rho_i U_i \mathbf{u}_i) - \nabla \cdot \mathbf{q}_i + \mathbf{S}_i : \nabla \mathbf{u}_i + G_i^d - S_i^v - S_i^c \quad (5.23)$$

where S_i^c is a sink term representing losses of pseudointernal energy caused by inelastic collisions, G_i^d is a source term representing the generation of particle velocity fluctuations by fluctuating fluid-particle forces, while S_i^v is a sink term representing dampening of particle velocity fluctuations caused by viscous resistance to particle motion. The pseudointernal energy per unit particle mass is $U_i = \frac{3\Theta_i}{2}$, and \mathbf{q}_i is the pseudothermal heat flux. For the closures of \mathbf{q}_i , G_i^d , S_i^v and S_i^c we refer to Gidaspow (1994).

In the frictional flow regime, as reported earlier, particles interact largely through frictional enduring contacts. These are not accounted for by the kinetic theory of granular flow. Therefore, to model the flow properties in this regime, one needs to adopt the theories of plasticity and soil mechanics. Shaeffer (1987) developed a model that relates μ_i^f to p_i^f based on the principles of soil mechanics. The model reads:

$$\mu_i^f = \frac{p_i^f \sin \varphi}{2\sqrt{I_2}} \quad (5.24)$$

where φ is the angle of internal friction and I_2 is the second invariant of the rate of deformation tensor. The frictional solid pressure is often modelled by means of arbitrary functions that have no theoretical basis but correctly describe qualitatively how dense granular media behave (Syamlal et al., 1993). The prime feature that must be captured is that such materials cannot reach compactions that are unphysically high. A closure for the frictional solid pressure that some modellers use is:

$$p_i^f = \phi_i p^* \quad \text{where } p^* \equiv 10^A (\phi - \phi_{min})^B \quad (5.25)$$

where ϕ_{min} is the frictional packing limit, and A and B are coefficients having typical values of 25 and 10, respectively. This equation is extremely sensitive to the deviation of ϕ from ϕ_{min} and this could lead to big pressure fluctuations and violent numerical instabilities (Schaeffer, 1987). Eq. 5.25 is often employed with radial distribution functions that are bounded and so do not diverge positively when ϕ approaches ϕ_{max} . For instance, the model of Syamlal et al. (1993), used in the CFD code MFIx, adopts the expression of Lebowitz (1964):

$$g_i = \left(1 + \frac{3d_i}{2\varepsilon} \sum_{k=1}^2 \frac{\phi_k}{d_k} \right) \quad (5.26)$$

where, as opposed to Eq. 5.16, ϕ_{max} does not feature. As in Eq. 5.16 g_i diverges when ϕ approaches ϕ_{max} , the viscous solid pressure already prevents the mixture from overpacking; therefore, one can use the same equation used to model the viscous solid pressure, that is, Eq. 5.20, to model also the total solid pressure in the frictional regime (instead of summing to the viscous solid pressure an additional contribution modelled by means of an arbitrary divergent function, qualitatively sound but theoretically unfounded).

These considerations induced us to employ the so-called KTGF-based model, a frictional model partly based on the kinetic theory of granular flows (KTGF) which accounts only for the frictional viscosity μ_i^f neglecting the frictional solid pressure p_i^f and the frictional dilatational viscosity κ_i^f . When ϕ exceeds ϕ_f , the model keeps on using the viscous closure for the solid pressure, Eq. 5.20, but increases the solid viscosity by adding to the viscous contribution, Eq. 5.21, the frictional one given by Eq. 5.24. As a consequence, the solid viscosity becomes:

$$\mu_i = \mu_i^f + \mu_i^v \quad (5.27)$$

In Eq. 5.24 the pressure used in the calculation is the viscous solid pressure (which, as said, coincides with the total solid pressure, since the frictional solid pressure is not considered).

5.4 Boundary and initial conditions

The computational grid (uniform, with square cells of 5 mm side) is two dimensional; hence the front and back wall effects are neglected. On the left, right and middle walls, no-slip boundary conditions apply. At the bottom of the bed, a uniform inlet fluid velocity u is specified. The fluid is ambient air. At the upper boundary, the pressure is set to $10^5 Pa$. On all the boundaries, the solid mass fluxes are set to zero.

Initially, the bed is fixed and consists of two equal and adjacent compartments partitioned by a removable wall. Each compartment consists of solids having the same size and density. The voidage is set to 0.4 everywhere in the bed. We fluidize the solids in each compartment with the same superficial gas velocity for about three seconds until they reach stable fluidization, and then we remove the partition. To obtain the horizontal solid volume fraction profiles in the bed, we divide the bed into twenty equal vertical layers evenly distributed over the horizontal direction and we compute the void-free solid volume fraction in each layer following the procedure reported in Section 5.2.

5.5 Results

We considered two sets of powders: Powder 1 was used by Shi & Fan (1984) in their experimental study of lateral mixing of solids in batch fluidized beds, and Powder 2 was investigated by Mori & Nakamura (1965). The parameters used to simulate these powders, in particular the geometry and the bed height, are chosen to replicate the experimental work of these authors. We report in Table 5.1 the parameters employed in the simulations of Powder 1; those for Powder 2 are reported in Table 5.2.

Table 5.1: Simulation parameters for Powder 1

Parameters	Value
Vessel height	0.35 <i>m</i>
Bed Width	0.20 - 1.00 <i>m</i>
Superficial gas velocity	0.87 – 1.17 <i>m/s</i>
Particle diameter	491 μm
Particle density	2620 kg/m^3
Minimum fluidization velocity	0.20 <i>m/s</i>
Bed height	0.05 – 0.11 <i>m</i>
Computational cell	0.005 <i>m</i>
Time-step	0.001 <i>s</i>

As said in Section 5.2, we fluidized the bed, divided it into two equal parts by a removable partition, for a certain period, allowing them to reach pseudo-stationary conditions, and then removed the partition. We ran preliminary simulations, removing the partition after running simulations for three and five seconds, and comparing the void-free concentration profiles obtained in the two cases, as shown in Figures 5.3 – 5.6. The figures show the void-free concentration profiles at different times measured after the partition was removed. We observed that there was no significant difference between the two; consequently, in subsequent simulations, we removed the partition after three seconds.

Table 5.2: Simulation parameters for Powder 2

Parameters	Value
Vessel height	0.30 <i>m</i>
Bed Width	0.90 <i>m</i>
Superficial gas velocity	0.45 – 0.75 <i>m/s</i>
Particle diameter	595 μm
Particle density	1400 kg/m^3
Minimum fluidization velocity	0.25 <i>m/s</i>
Bed height	0.17 – 0.23 <i>m</i>
Computational cell	0.005 <i>m</i>
Time-step	0.001 <i>s</i>

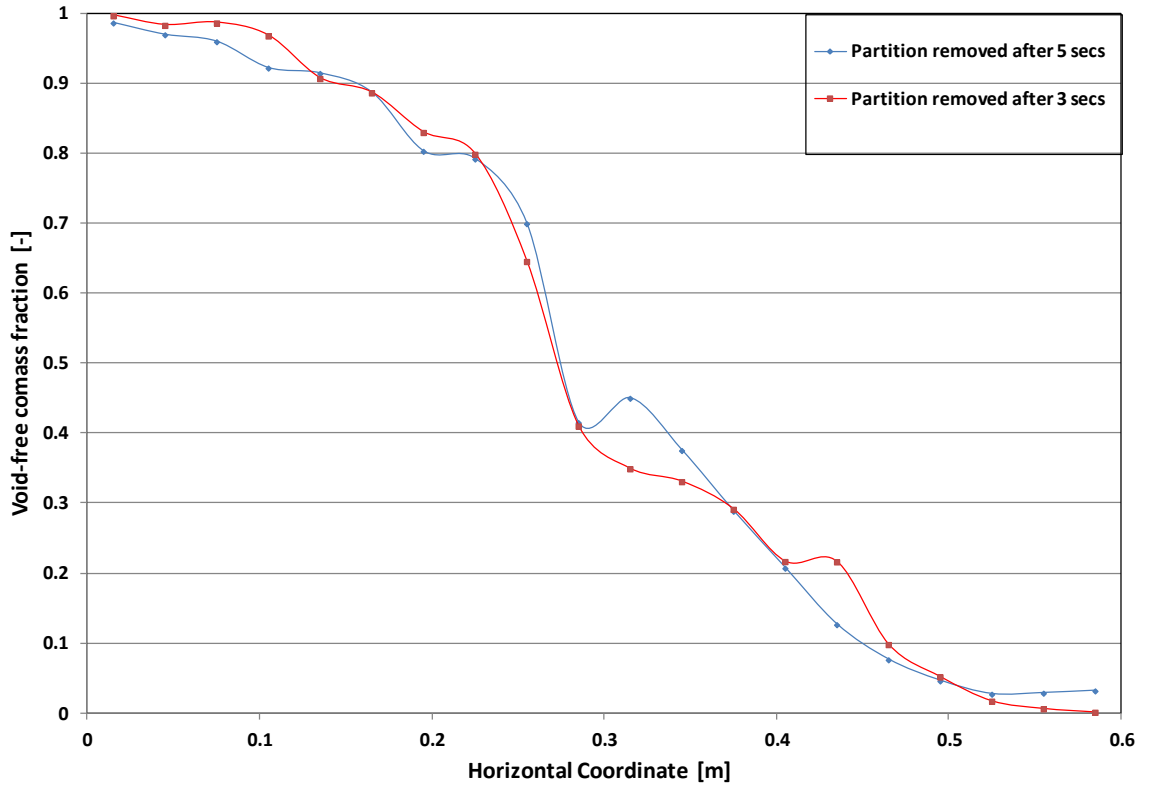


Figure 5.3: Void-free mass fraction profiles at $t = 1.0$ second after removing the partition.

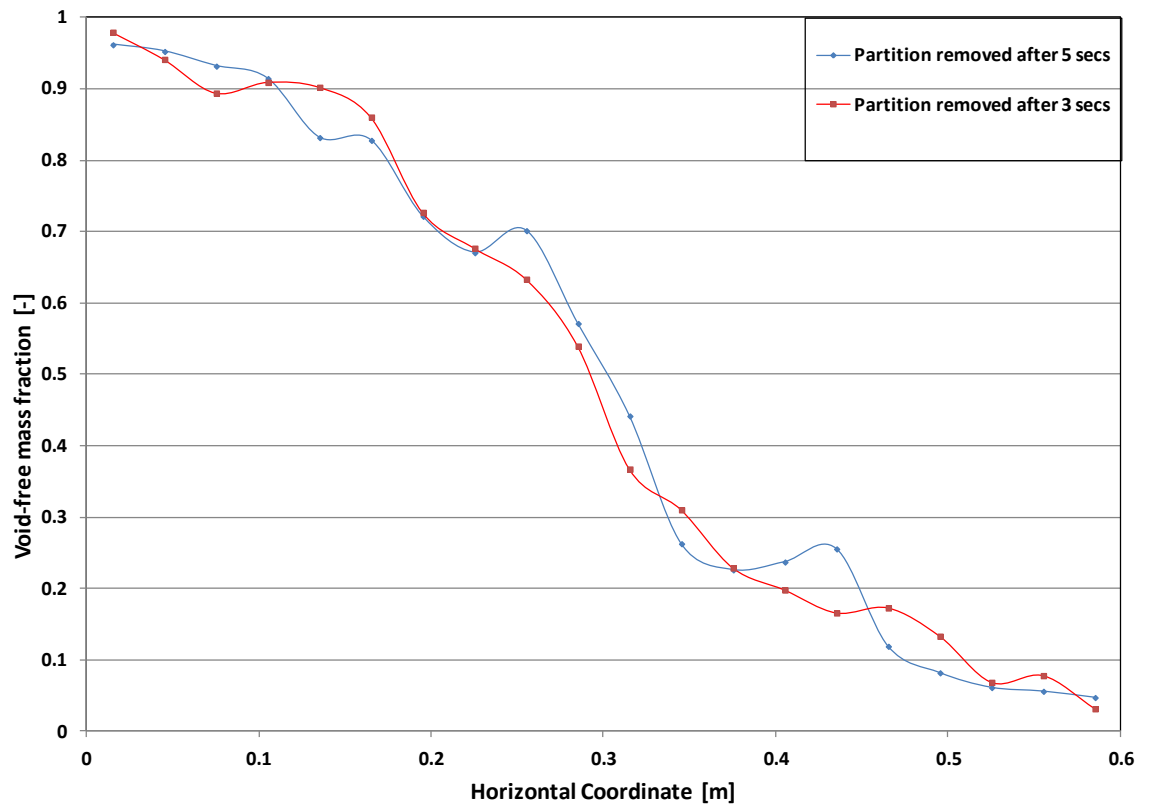


Figure 5.4: Void-free mass fraction profiles at $t = 2.0$ seconds after removing the partition.

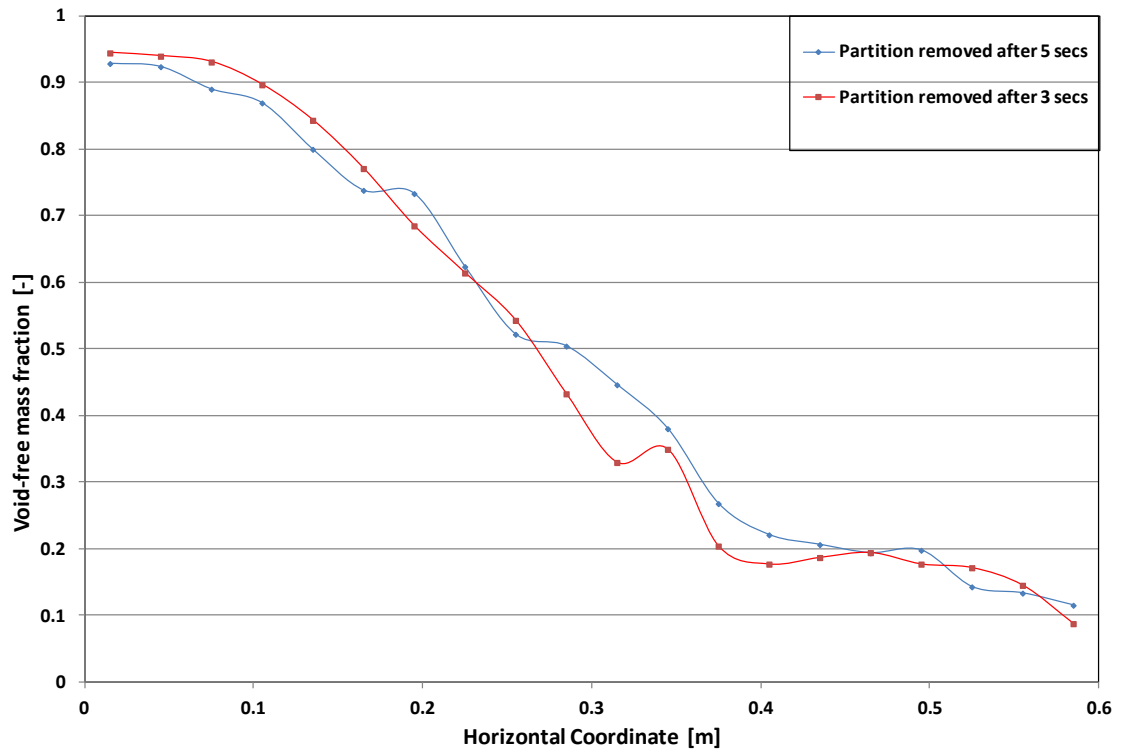


Figure 5.5: Void-free mass fraction profiles at $t = 4.0$ seconds after removing the partition.

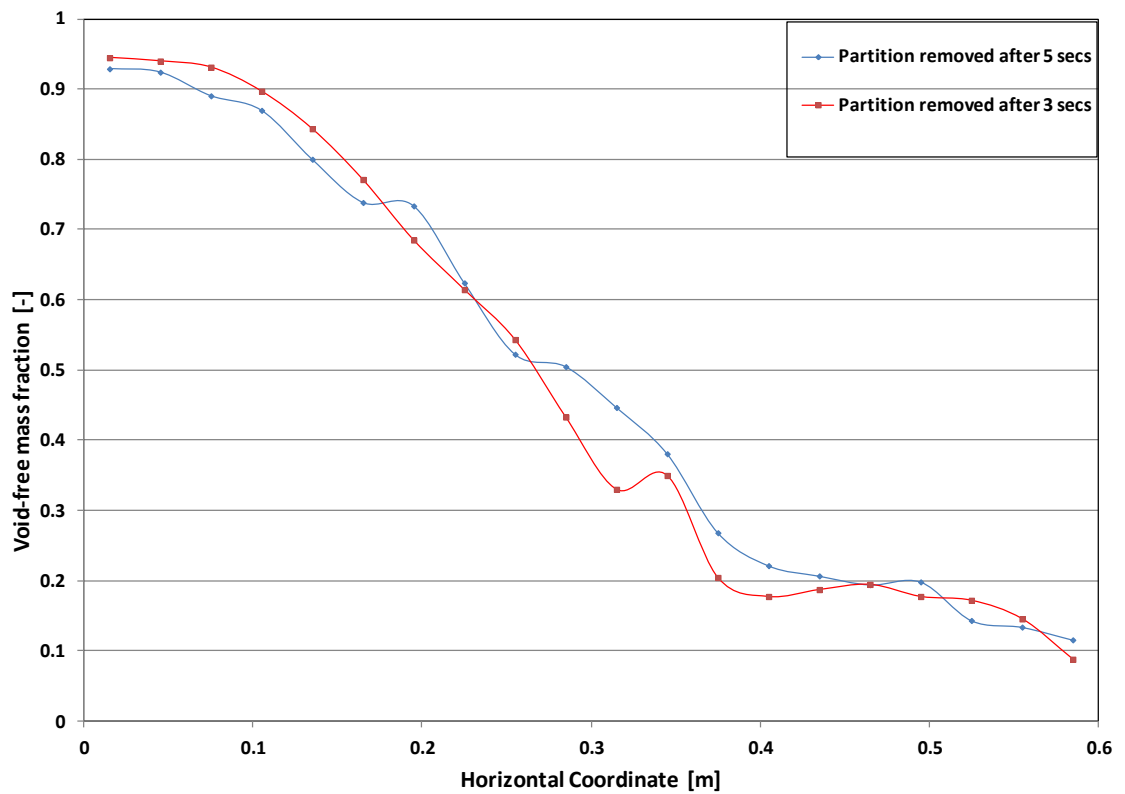


Figure 5.6: Void-free mass fraction profiles at $t = 5.0$ seconds after removing the partition.

5.5.1 Effect of superficial gas velocity

From the solid volume fraction profiles obtained numerically, we calculated the void-free mass fraction $\hat{\phi}_i$ of solid phase i in each layer:

$$\hat{\phi}_i \equiv \frac{\phi_i}{\phi_1 + \phi_2} \quad (5.28)$$

We ran the simulations at various superficial gas velocities (starting from 0.87 m/s, which is the minimum velocity investigated experimentally by Shi & Fan, 1984, up to 1.17 m/s, with increments of 0.10 m/s), keeping the minimum fluidization bed height at 5.23 cm (which is the maximum bed height at minimum fluidization conditions investigated by Shi & Fan, 1984) and the bed width at 0.6 m (which is the single bed width investigated by Shi & Fan, 1984). We fitted the void-free mass fraction profiles obtained from our simulations with those obtained from the analytical solution of Fick's law, using the least square regression method, as reported in Section 5.2. In Figures 5.7 and 5.8 we report the profiles of void-free mass fraction obtained from the Fick's equation (Eq. 5.1) and those obtained numerically at $t = 5.0$ s for superficial gas velocities of 0.87 and 1.07 m/s respectively. Similar profiles are found at other times, but we have chosen 5.0 s as representative time. We obtained a reasonable fit, as Figures 5.7 and 5.8 show. Figure 5.9 shows the values of dispersion coefficients calculated at different times for different superficial gas velocities. We observe an initial, sudden, increase in D_{sr} in the first two seconds. Subsequently, the values of D_{sr} remain approximately stable.

Figure 5.10 reports the snapshots of particle concentrations obtained from the simulations at a superficial gas velocity of 0.87 m/s (4.35 times u_{mf}). The figure shows how particles placed at the left of the removable partition spread to the right. We observe from Figure 5.10 that the spread of the particles proceeds in a manner similar to what one would observe in, for instance, the molecular diffusion of ink in water; even though in this case the spread of particles is induced primarily by bubbles. This diffusion-like spread of particles explains why we obtained a reasonable fit between our numerical results and those obtained from the Fick's equation.

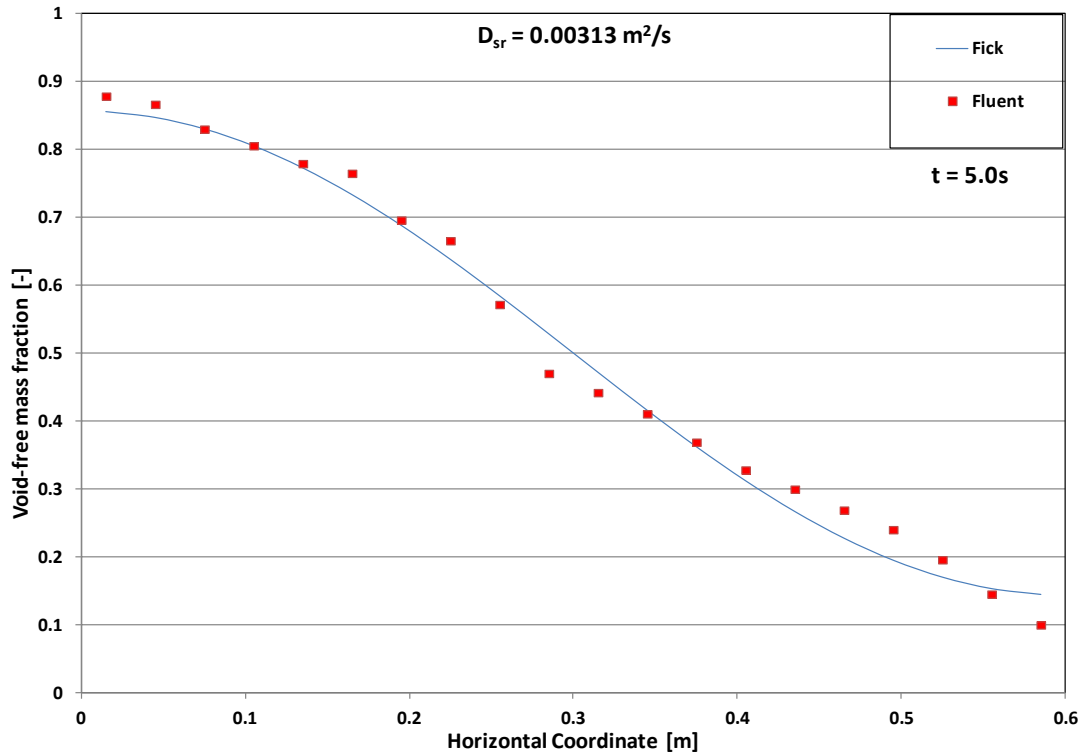


Figure 5.7: Solid 1 void-free vertically-averaged mass fraction horizontal profiles for a superficial fluid velocity of 0.87 m/s for Powder 1. The 'Fick' profile is that obtained from the analytical solution of the Fick's law, while the 'Fluent' profile is that obtained numerically.

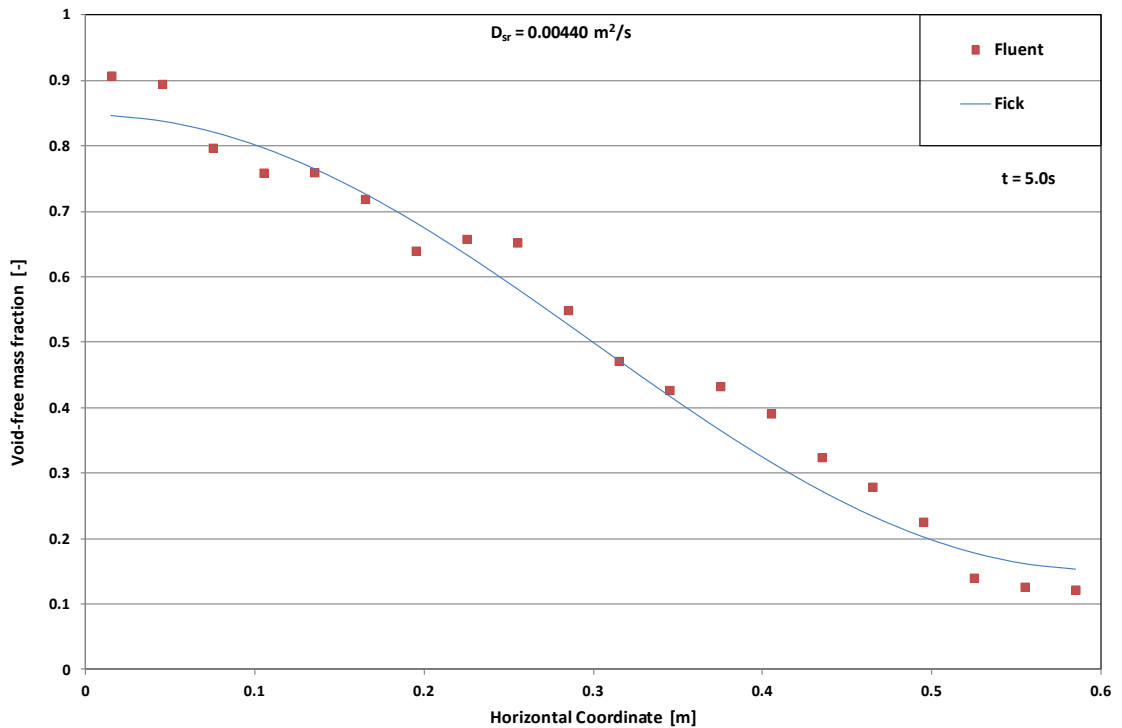


Figure 5.8: Solid 1 void-free vertically-averaged mass fraction horizontal profiles for a superficial fluid velocity of 1.07 m/s for Powder 1. The 'Fick' profile is that obtained from the analytical solution of the Fick's law, while the 'Fluent' profile is that obtained numerically.

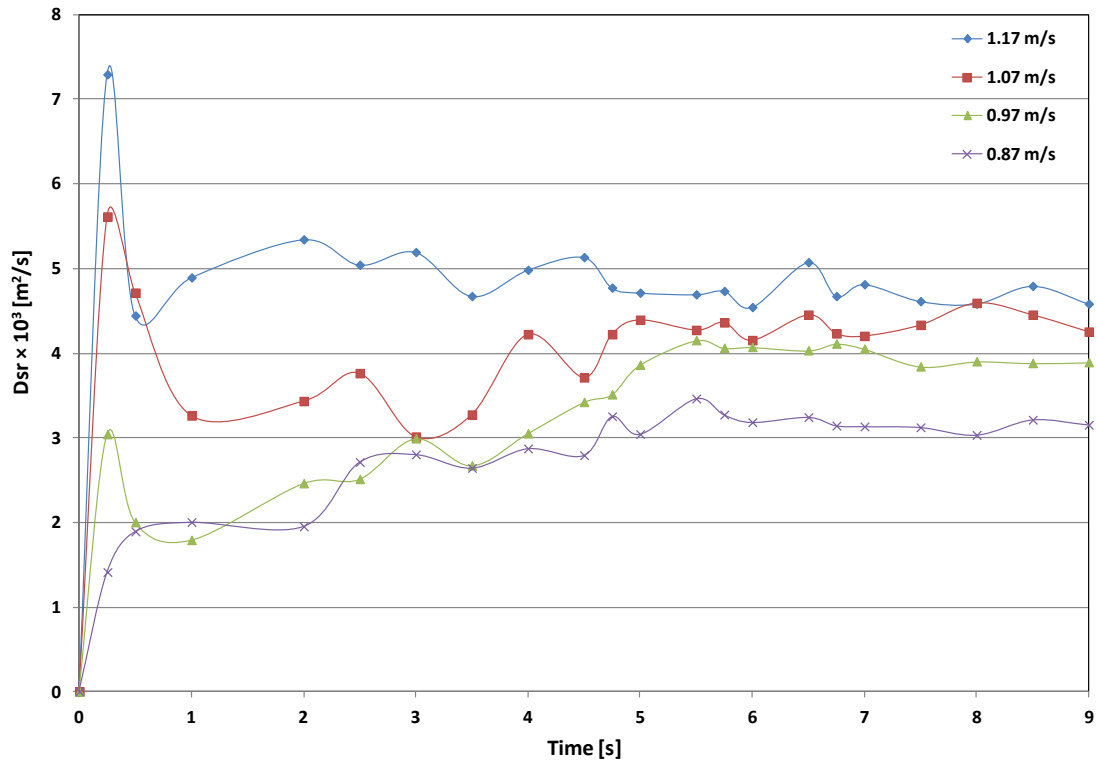


Figure 5.9: Lateral dispersion coefficients at different superficial gas velocities for Powder 1

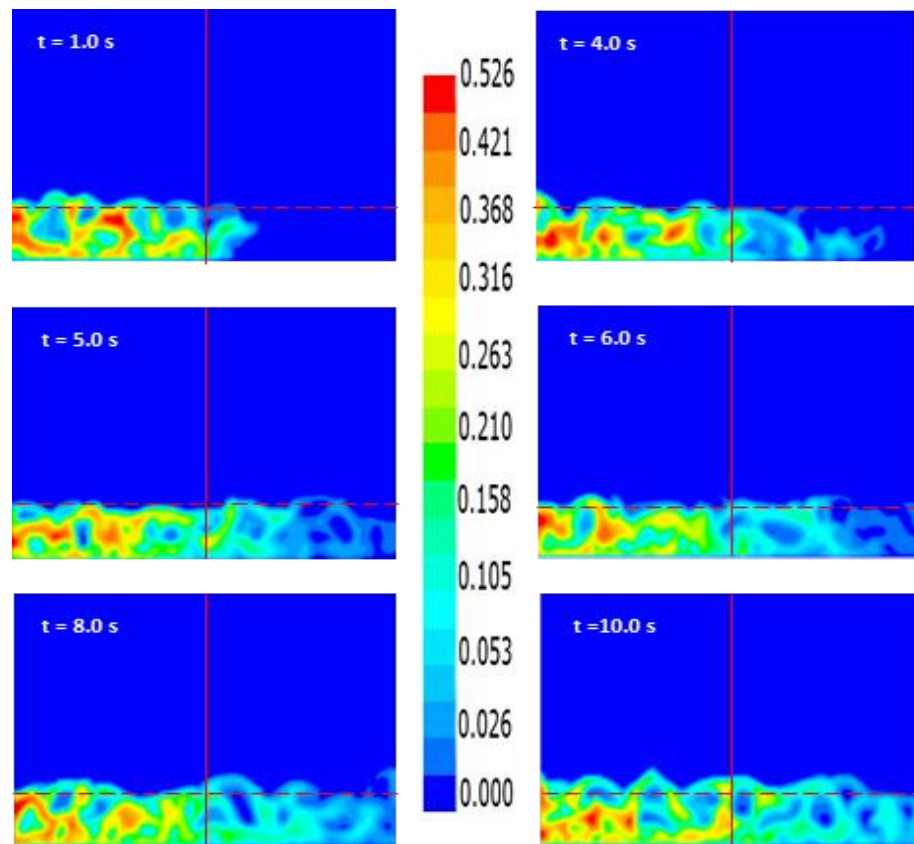


Figure 5.10: Solid 1 volume fraction profiles at different times for superficial fluid velocity of 0.87 m/s for Powder 1. The minimum fluidization bed height is 5.23 cm, while the bed width is 0.60 m. The horizontal dashed line indicates where the bed ends and the freeboard begins.

The snapshots showing the contours of particle concentrations at superficial gas velocity of 1.17 m/s (5.85 times u_{mf}) are reported in Figure 5.11. It is interesting to observe that the contours of solid volume fraction shown in this figure are partly different from those in Figure 5.10, even though the snapshots were taken at the same computational times. In Figure 5.11 we observe streams of particles transported into the freeboard in a region close to the bed surface. This is caused by the burst of bubbles and subsequent ejection of their solid content into the freeboard. As reported by Davidson & Harrison (1971), particles are carried up through the bed in the bubble wakes, and when bubbles burst, part of them spreads over the surface of the bed. This kind of solid transport is absent in Figure 5.10. This additional mechanism, observed when the superficial gas velocity is larger, contributes to the higher value of D_{sr} obtained at this velocity, as reported in Figure 5.12.

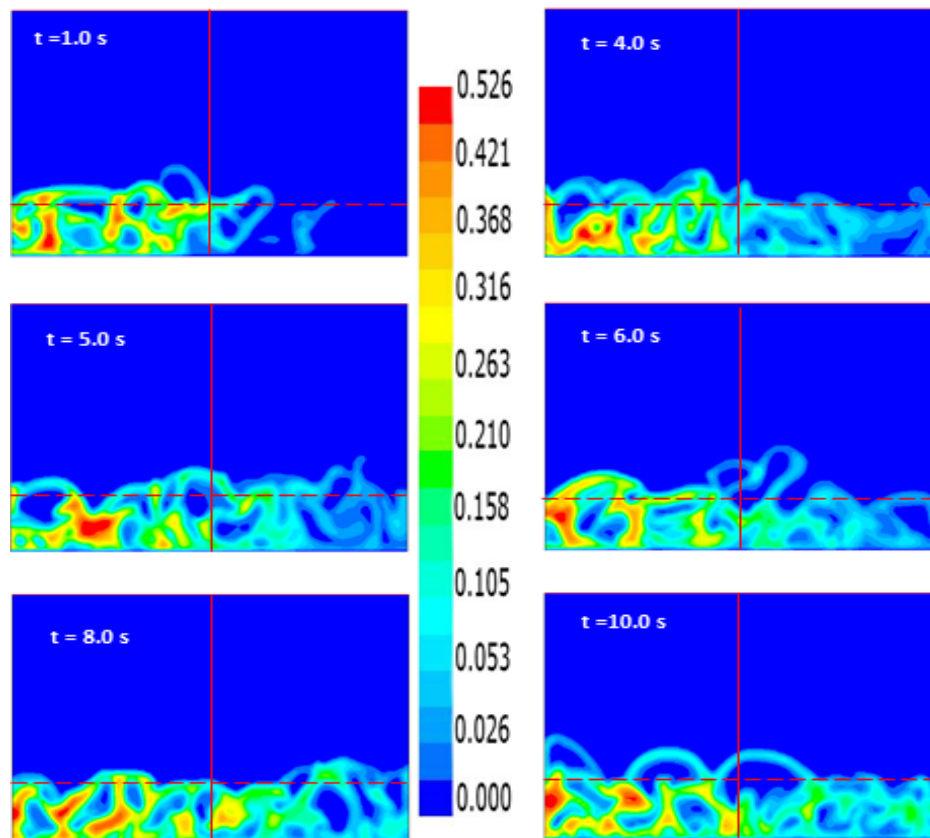


Figure 5.11: Solid 1 volume fraction profiles at different times for superficial fluid velocity of 1.17 m/s for Powder 1. The minimum fluidization bed height is 5.23 cm, while the bed width is 0.60 m. The horizontal dashed line indicates where the bed ends and the freeboard begins.

In Figure 5.12 we plot D_{sr} against the superficial gas velocity, comparing our simulation results with those obtained from empirical correlations available in the literature. We observe that the value of the dispersion coefficient increases as the superficial gas velocity increases. This is expected, because an increase in velocity induces more vigorous mixing in the bed, rendering solid circulation more intense and enhancing lateral solid transport. As said, at higher superficial gas velocities an additional mechanism affects lateral mixing; this is the solid transport across the bed surface caused by bubble eruption. These observations were also reported by Kunii & Levenspiel (1989). Figure 5.12 also shows that the numerical values of the dispersion coefficient have the same order of magnitude as those given by the empirical correlations, but in all cases overestimate the latter. We will later address the reason for the overestimation.

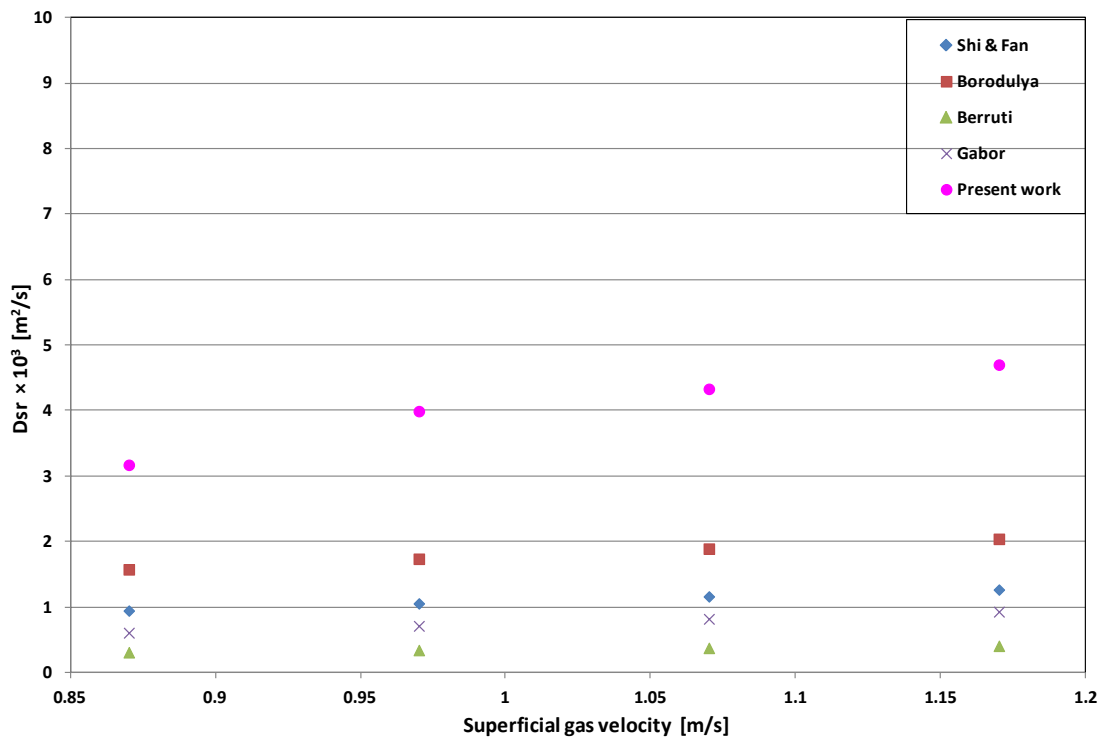


Figure 5.12: Dispersion coefficient values at different superficial fluid velocities for Powder 1. The minimum fluidization bed height is 5.23 cm, while the bed width is 0.60 m. The values are compared with those obtained from empirical correlations in the literature.

5.5.2 Effect of bed height

We investigated the effect of bed height on lateral dispersion coefficients. To do this, we ran simulations at different minimum fluidization bed heights (spanning the range between 5.23 cm

and 11.23 cm), fixing the superficial gas velocity at 1.07 m/s (5.35 times u_{mf}) and the bed width at 0.6 m. Following the same procedure outlined above, we obtained the void-free horizontal mass fraction profiles in the bed. We report in Figure 5.13 and 5.14 the profiles when the bed height is 7.23 and 9.23 cm, respectively. The numerical profiles fit reasonably well the analytical ones obtained from the Fick's law. As shown in Figure 5.15, we observe an increase in dispersion coefficient as the bed height is increased. This is because as the bed height increases, bubbles grow in size causing more recirculation and more particles to be drawn into their wakes. As bubbles erupt at the bed surface, they eject more particles into the freeboard, enhancing the lateral transport of solids. These effects are observed in the snapshots of solid volume fraction reported in Figure 5.16 for different bed heights at $t = 5.0$ s.

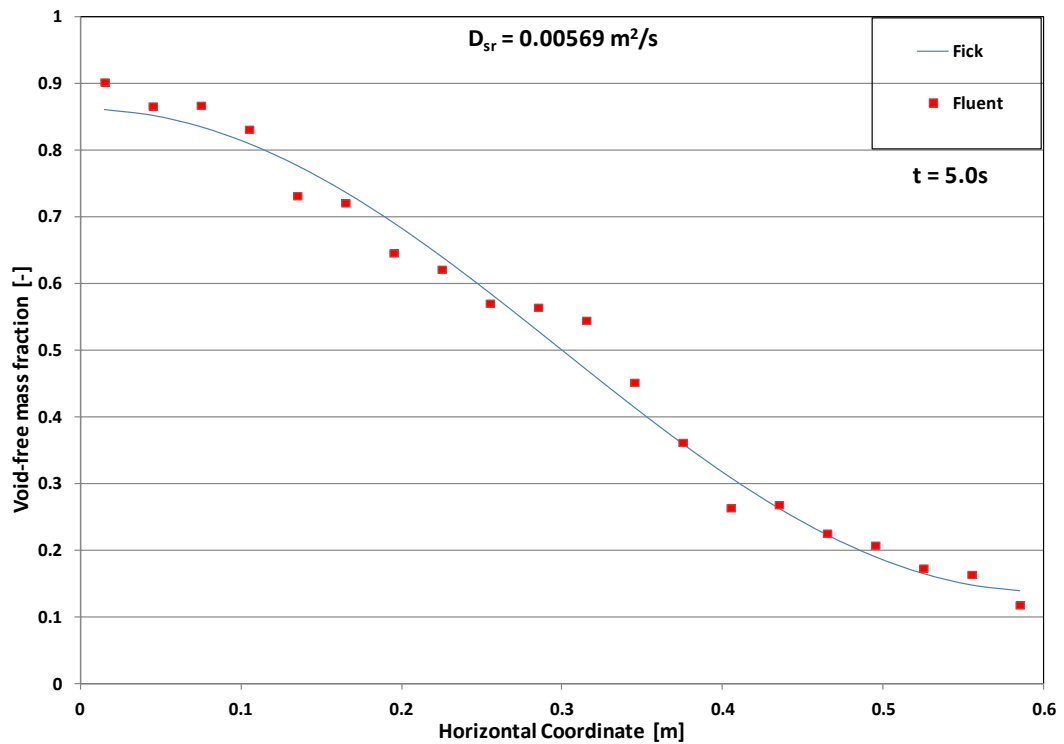


Figure 5.13: Solid 1 void-free vertically-averaged mass fraction horizontal profiles for a minimum fluidization bed height of 7.23 cm for Powder 1. The superficial fluid velocity is 1.07 m/s, while the bed width is 0.60 m. The 'Fick' profile is that obtained from the analytical solution of the Fick's law, while the 'Fluent' profile is that obtained numerically.

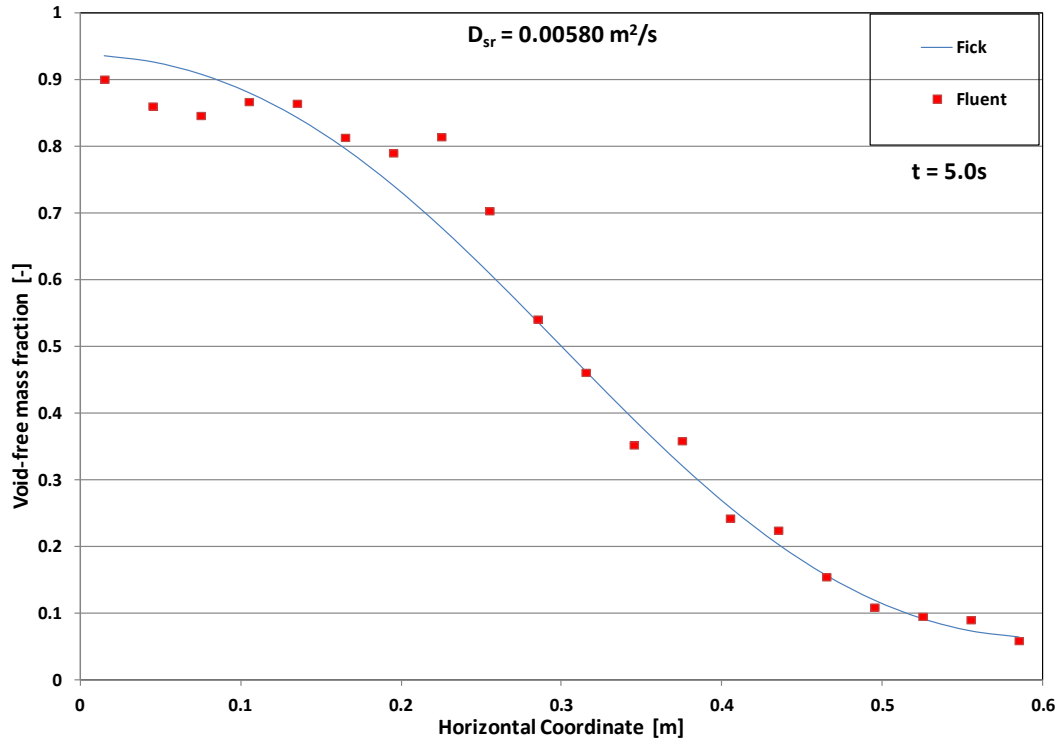


Figure 5.14: Solid 1 void-free vertically-averaged mass fraction horizontal profiles for a minimum fluidization bed height of 9.23 cm for Powder 1. The superficial fluid velocity is 1.07 m/s, while the bed width is 0.60 m. The 'Fick' profile is that obtained from the analytical solution of the Fick's law, while the 'Fluent' profile is that obtained numerically.

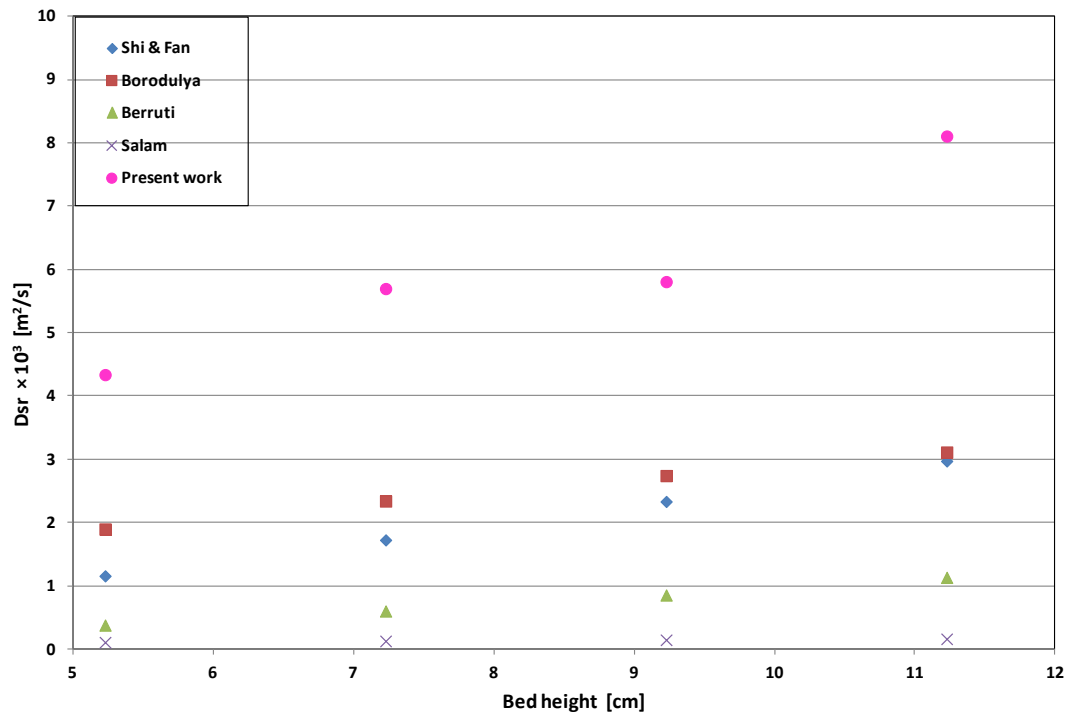


Figure 5.15: Dispersion coefficient values at different minimum fluidization bed heights for Powder 1. The superficial fluid velocity is 1.07 m/s, while the bed width is 0.60 m. The values are compared with those obtained from empirical correlations in the literature.

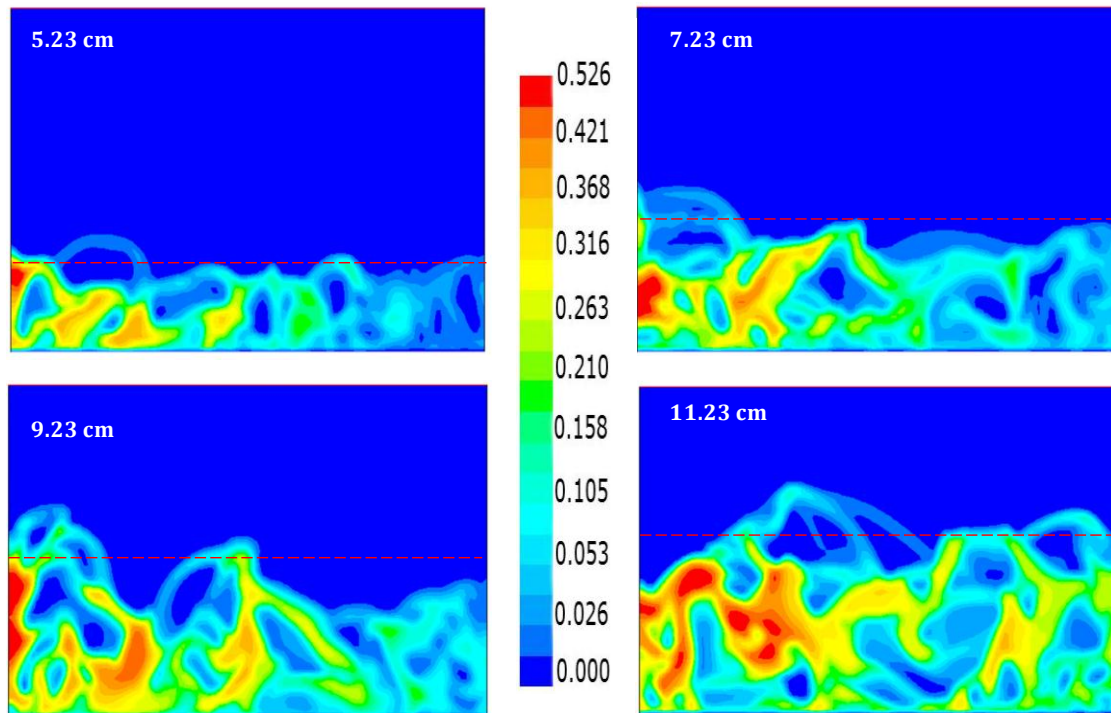


Figure 5.16: Solid 1 volume fraction profiles at minimum fluidization bed heights of 5.23 cm, 7.23 cm, 9.23 cm and 11.23 cm for Powder 1. The superficial fluid velocity is 1.07 m/s, while the bed width is 0.60 m. The horizontal dashed line indicates where the bed ends and the freeboard begins.

As the bed height increases, the size of the bubbles increases, implying that greater volume of emulsion can be driven aside. This leads to more intense mixing, and hence increases solid lateral transport. We also compared the simulation results with empirical correlations available in the literature, as shown in Figure 5.15. The values of dispersion coefficients obtained from the simulations have the same order of magnitude as those given by the empirical correlations; again, however, the numerical results overestimate the empirical ones.

5.5.3 Effect of bed width

Most researchers investigating lateral solid dispersion in fluidized beds often neglect the influence of bed width. For instance, Shi & Fan (1984) in their experimental work on lateral solid mixing in batch gas-fluidized beds summarized the mechanisms governing lateral solid mixing as: *bubble movement through the bed*, *bubble burst at the surface*, and *gross particle circulation in the bed*. In summarizing the parameters on which these mechanisms depend, they did not include bed width. Several other authors (Berruti et al., 1986; Bellgardt & Werther,

1986; Salam et al., 1987; Xiang et al., 1987; Winaya et al., 2007) who have developed empirical correlations for lateral dispersion coefficients also ignore bed width as a parameter that might affect it. We believe that bed geometry should influence lateral mixing, and hence the coefficient quantifying it, D_{sr} . This is because bed geometry plays a crucial role in gross particle circulation, which is an important mechanism responsible for lateral solid mixing.

To investigate the influence of bed width on lateral solid dispersion, we considered beds of different widths, ranging from 0.2 to 1.0 m. We fluidized these beds, maintaining the superficial gas velocity at 1.07 m/s and the minimum fluidization bed height at 5.23 cm. We then determined the lateral dispersion coefficient at each value of bed width, using the approach described previously. In Figure 5.17, we report the values of the dispersion coefficient at different bed widths. The figure shows that the coefficient increases rapidly as the bed width increases from 0.2 to 0.4 m, afterwards increases slowly and finally becomes approximately constant.

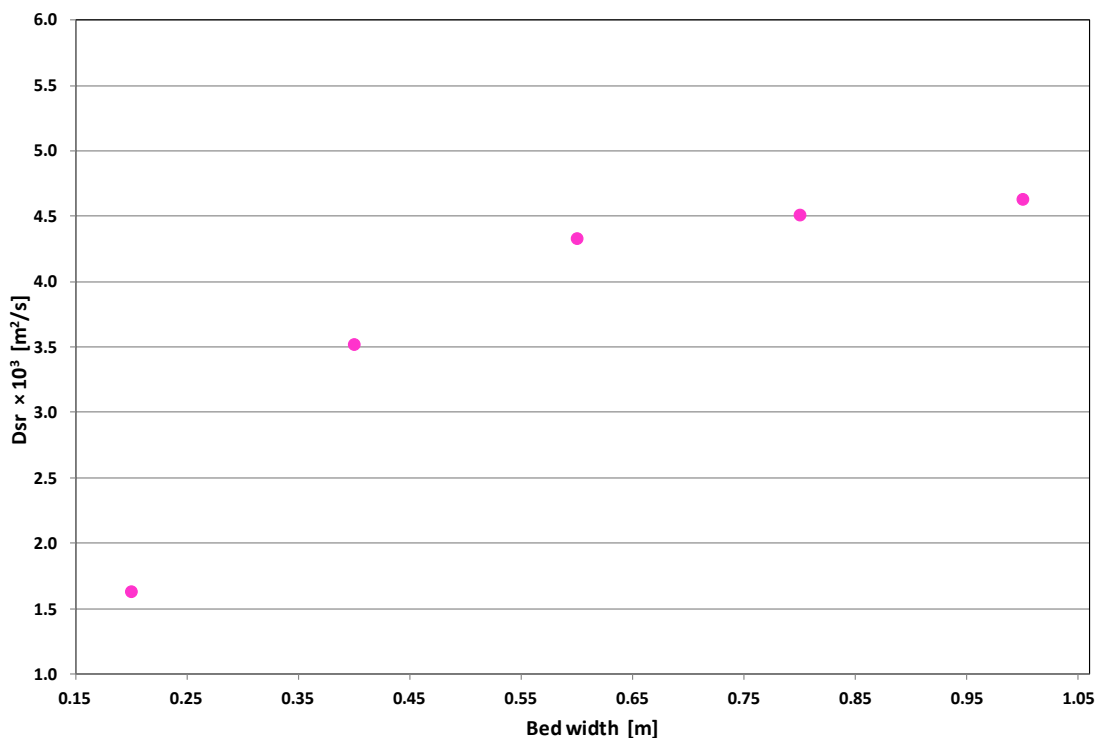


Figure 5.17: Dispersion coefficient values at different bed widths for Powder 1. The superficial fluid velocity is 1.07 m/s, while the minimum fluidization bed height is 5.23 cm.

To explain this trend, let us briefly report on the observation by Pallarès et al. (2007) regarding the mechanisms of lateral solid mixing. They reported that lateral solid mixing is due to horizontally aligned vertical vortices, rotating in alternate directions (these vortices are referred to as mixing cells). In these mixing cells, the following mechanisms for solid mixing take place: *bubble wake mixing*, *drifting aside of emulsion* and *bubble eruption at the bed surface*. The net lateral solid transport in the bed results from the exchange of solids in the mixing cells and is determined by the integral length scale of macroscopic solids circulation patterns. It is likely that the integral length scale of solids circulation be constrained by bed width for comparatively narrow beds. For wide beds the integral length scale of solids circulation, hence lateral solid transport, should rather be dictated by bed height.

5.6 Discussion

It is clear from the results presented above that the values of D_{sr} obtained from our simulations are larger than those predicted by empirical correlations, albeit the order of magnitude of the coefficient is correctly captured. We believe that this overestimation has two main causes. The first relates to how the frictional stress of the solid phase is modeled constitutively; we address this aspect in the next section. The second has to do with the dimensionality of our simulations. Our simulations are 2D (a choice often found in the literature, in our case dictated by our computational resources, the real-time duration of each simulation and the number of simulations that our analysis requires). In actual fluidized beds the lateral motion of the solid has, we might say, two degrees of freedom (bubble-induced particle lateral motion develops in a horizontal plane), while in 2D fluidized beds only one degree of freedom is present (particle lateral motion can only develop along a horizontal line). Hence, when comparing lateral solid dispersion coefficients obtained numerically by means of 2D simulations with those estimated using empirical correlations, one needs to account for the 2D nature of the simulations. As discussed by Norouzi et al. (2011), omitting one dimension in the simulations significantly affects the value of the coefficient. The latter, in particular, is overestimated, as we have also observed in our work. We shall address this aspect later.

5.7 Influence of hydrodynamic models

The Eulerian equations of motion adopted in this work, as said in section 5.1, contain indeterminate terms that need to be expressed constitutively. Such terms are the fluid-particle and particle-particle interaction forces and the fluid and solid stress tensors. To close the stress tensors, one usually regards the phases as Newtonian continua; therefore, the closure relationships take the form reported in Eq. 5.17 and 5.18. So, the problem of closure reduces to finding constitutive expressions for the pressure, viscosity and dilatational viscosity for each phase. For the solid phases one needs to model these parameters constitutively.

To model the solid stress, one usually adopts the kinetic theory of granular flows (KTGF). This assumes that particles are smooth and spherical, that collisions are binary and instantaneous and that the powder is far from the frictional packing limit. Thus, the kinetic and collisional momentum transfer arising from the particle velocity fluctuations and the particle collisions are modelled following the Enskog theory for dense gases (Chapman and Cowling, 1970). Nevertheless, in several fluidized bed applications, like the one investigated in this work, particles interact largely through frictional enduring contacts, and the kinetic theory of granular flows does not take into account these important interactions. Hence, using the kinetic theory to model the solid stress in dense systems is inadequate and creates problems. We will now discuss in detail these problems.

In regions of high solid volume fraction, particles interact with multiple neighbours and the mechanism for stress generation is not just due to kinetic and (particularly) collisional contributions, but also to sustained contacts among particles. These contacts make particles dissipate a lot of energy, making them form very dense regions in the bed. This increases the ability of the granular assembly to resist shearing, because tangential frictional forces at contact points are now present. Consequently, the frictional viscosity of the bed is larger than that predicted by the granular kinetic theory model, insofar as this does not account for frictional

interactions. So, using the kinetic theory alone to model dense fluidized beds underpredicts the solid viscosity, overestimating in turn the extent of particle mixing.

Enduring particle contacts in dense regions of fluidized beds do not only affect the viscosity of the solid phase, but also its pressure. The latter has a more pronounced effect on the fluid dynamics of the bed than the former, for the solid pressure influences significantly the formation and the size of the bubbles. Let us explain why. The two-phase theory by Toomey & Johnstone (1952) suggests that the void fraction around the bubbles and that in the emulsion phase are equal, for the theory assumes that all the gas in excess of that required to just fluidize the bed results in the formation of bubbles, the emulsion phase remaining at minimum fluidization conditions with uniform void fraction. However, local measurements of bed porosity by Lockett et al. (1967), done via capacitance probes, revealed that the void fraction around the bubbles is not uniform. This was observed experimentally by many other authors (Nguyen et al., 1973; Collins, 1989; Fan et al., 1990). Experimental investigations of voidage distributions around bubbles by Yates et al. (1994), and numerical simulations by Patil et al. (2005), confirmed this, showing that the void fraction decreases exponentially from the bubble interface to the bulk of the emulsion phase. Figure 5.18 reports the void fraction distribution around a bubble, as revealed by experimental and numerical studies (Patil et al., 2005); regions A, B and C represent the bubble, the bubble boundary and the bulk of the emulsion phase, respectively. A question that one may want to ask is how the void fraction distribution around the bubbles and the frictional interactions among the particles affect the size of the bubbles. Answering this question will allow us to highlight the role of frictional stress on the dynamics of bubbling beds.

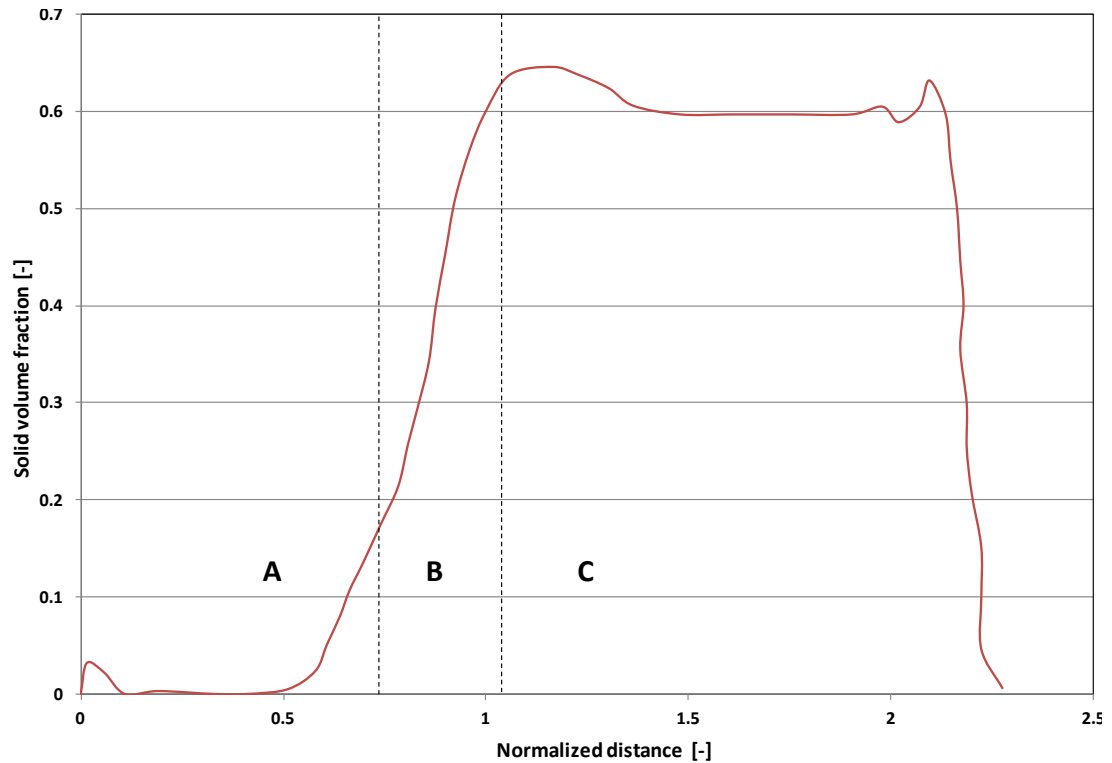


Figure 5.18: Solid volume fraction profile vs. normalized distance from the bubble centre (d_i/D_b). d_i is the distance from bubble centre and D_b is the bubble diameter.

The bubble size is affected by the resistance that the gas finds to cross the bubble boundary and reach the emulsion phase. The larger the resistance, the less leaky the bubble boundary is and, in consequence, the larger the bubble results. The resistance through the bubble boundary depends on the drag experienced by the gas. This decreases when the void fraction around the bubbles increases. The frictional solid pressure strongly influences the void fraction distribution around the bubbles by reducing the compaction of solids around their interface, which increases the gas flow through the bubble boundary into the emulsion phase, thereby leading to smaller bubbles. Hence, if one employs the kinetic theory to model the solid pressure, without accounting for frictional stress, the solid pressure and in turn the void fraction around the bubbles are underestimated. This increases the drag experienced by the gas around the bubble boundaries and in turn reduces the gas leakage from the latter. This makes numerical simulations overestimate the sizes of the bubbles and the extent of particle mixing.

To overcome this problem, Johnson & Jackson (1987) proposed that the frictional stress should be added to the viscous stress modeled by the granular kinetic theory. The latter, as said,

captures the flow regime in which the solid pressure is dictated mainly by kinetic and collisional contributions, whilst the former captures the flow regime in which enduring contacts are present among the particles. Even if the physical basis of adding the two stress contributions might be argued, the approach captures well the two extremes of granular flow. The frictional stress is usually modeled as follows:

$$\boldsymbol{\sigma}_i^f = -p_i^f \mathbf{I} + \mu_i^f (\nabla \mathbf{u}_i + \nabla \mathbf{u}_i^T) \quad (5.29)$$

where p_i^f is the frictional pressure and μ_i^f is the frictional viscosity (the dilatational viscosity is usually neglected). When the solid volume fraction exceeds a threshold value ϕ_{min} , the frictional contribution to the solid pressure and viscosity are added to the viscous contribution:

$$p_i = p_i^v + p_i^f \quad ; \quad \mu_i = \mu_i^v + \mu_i^f \quad (5.30)$$

Johnson & Jackson (1987) proposed the following constitutive equation for the frictional pressure:

$$p_i^f = \begin{cases} F \frac{(\phi - \phi_{min})^a}{(\phi_{max} - \phi)^b}, & \phi \geq \phi_{min} \\ 0 & \phi < \phi_{min} \end{cases} \quad (5.31)$$

Here F , a and b are empirical constants, ϕ_{min} is the minimum solid volume fraction at which particles start generating stress through enduring contacts, while ϕ_{max} is the maximum volume fraction that the particles can attain. The frictional viscosity is then related to the frictional pressure by the Coulomb (1776) friction law:

$$\mu_i^f = p_i^f \sin \varphi \quad (5.32)$$

where φ is the angle of internal friction of the granular material.

Another approach to modelling frictional stress was proposed by Shaeffer (1987) based on the principles of soil mechanics. The frictional pressure is given by:

$$p_i^f = 10^{25} (\phi - \phi_{min})^{10} \quad (5.33)$$

While the frictional viscosity is modelled by:

$$\mu_i^f = \frac{p_i^f \sin\varphi}{2\sqrt{I_2}} \quad (5.34)$$

where I_2 is the second invariant of the rate of deformation tensor.

Following the reasoning of Johnson & Jackson (1987), Srivastava & Sundaresan (2003) employed an additive approach to describe the solid stress, using Eq. 5.31 to model the frictional pressure. To model the frictional viscosity, they adopted a modified form of Shaeffer's model:

$$\mu_i^f = \frac{p_i^f \sin\varphi}{2\sqrt{I_2 + \frac{\Theta_i}{d_p^2}}} \quad (5.35)$$

where Θ_i is the granular temperature and d_p is the particle diameter. The additional term Θ_i/d_p^2 ensures that numerical singularity is avoided in regions where I_2 approaches zero, provided that in such regions the granular temperature does not vanish. They used this hybrid model to simulate the rise of a bubble in a fluid bed. To highlight the role of frictional stress on the bed dynamics, they ran another simulation without accounting for it. The results of their simulations revealed that frictional stress influences the bed dynamics significantly, affecting the shape and size of the bubbles. Passalacqua & Marmo (2009) employed the model of Srivastava & Sundaresan (2003) to investigate the influence of frictional stress on bubble growth in fluidized beds. They reported that it affects significantly the size of the bubbles: with frictional stress accounted for, the predicted bubble size was significantly lower than that observed in simulations with no frictional stress implemented. They also showed that the value ascribed to ϕ_{min} , appearing in Eq. 5.31, plays a key role: the size of the bubbles predicted with lower values of ϕ_{min} are smaller than those obtained with higher values of the parameter. This is expected, for the lower the value of ϕ_{min} , the sooner frictional stress is accounted for (in the simulations) and the more particle compaction reduces around the bubbles; this in turn makes

the latter leakier, reducing their sizes. This effect, as we shall see, affects significantly lateral dispersion. In light of this, we conclude that the way in which frictional stress is modelled affects significantly the fluid dynamic behaviour of fluidized beds; particularly in bubbling beds, where the latter is dictated mainly by the action of bubbles. In this section, we intend to investigate the role of frictional stress modelling on lateral solid mixing. These significantly influence bubble size and shape, which in turn affect how quickly the solid spreads throughout the bed. To investigate this aspect, we ran simulations using the operational conditions reported in Table 5.1 and considering the different cases outlined in Table 5.3. We tested different frictional pressure and viscosity models, changing the solid volume fraction at which the bed enters the frictional flow regime (ϕ_{min}) and observing the effects of these variations on lateral dispersion.

Table 5.3: Summary of simulation cases.

Cases	Frictional Pressure Model		Frictional Viscosity Model		Frictional Packing Limit	
	KTGF	J & J	Schaffer	J & J	0.50	0.61
1	X		X			X
2	X		X		X	
3	X			X		X
4	X			X	X	
5		X		X	X	

Figure 5.19 shows the plot of the lateral dispersion coefficient against the superficial gas velocity for Cases 1 and 2. These cases are identical; except that in Case 2 frictional stress is introduced earlier (the value chosen for ϕ_{min} is lower). Figure 5.19 shows that D_{sr} is predicted better in Case 2, its values being lower and closer to those found empirically. The same is observed for Cases 3 and 4, which are also identical, except that in Case 4 frictional stress is introduced earlier, as shown in Figure 5.20.

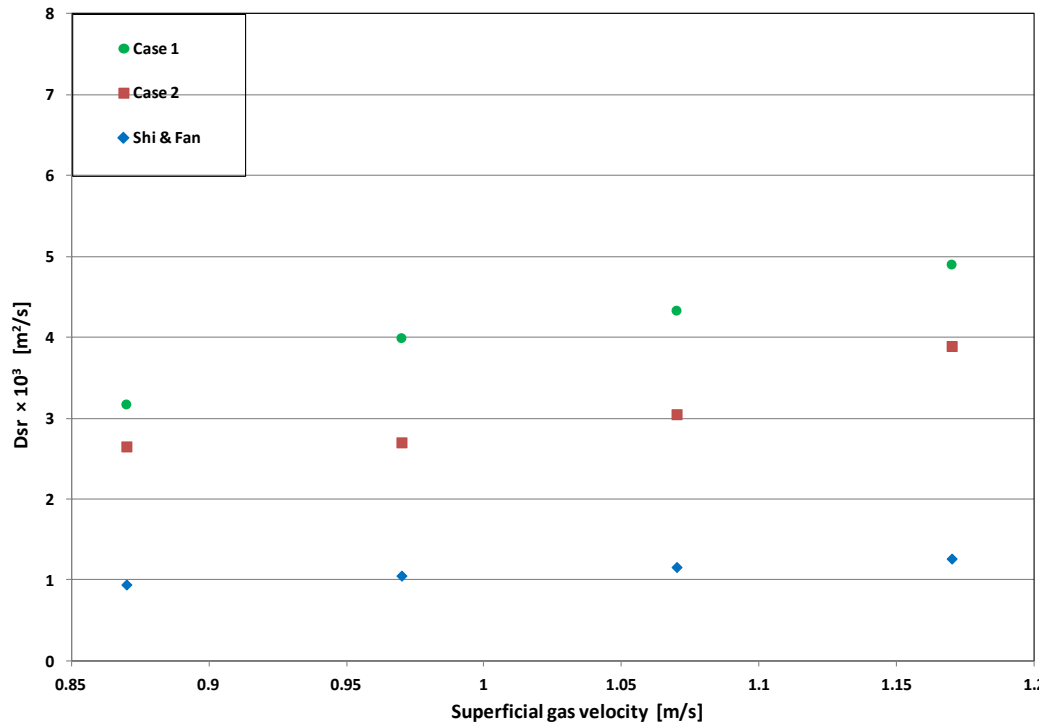


Figure 5.19: Dispersion coefficient values at different superficial fluid velocities for different simulation cases. The minimum fluidization bed height is 5.23 cm, while the bed width is 0.60 m. The details of the cases are reported in Table 5.3.

Figure 5.20 shows that the values of D_{sr} in Case 4 are lower than those in Case 3. This is because frictional stress is introduced earlier. The effect of this, as said in the preceding paragraphs, is that the voidage around the bubbles increases, reducing the compaction of the particles and lowering the drag experienced by the fluid. Consequently, the leakage of gas through the bubble boundary increases, leading to bubbles of smaller size compared with cases where the introduction of the frictional stress is delayed. To illustrate this, we determined a statistical distribution of the bubble diameters by dividing the diameter range into classes, as shown in Figure 5.21.

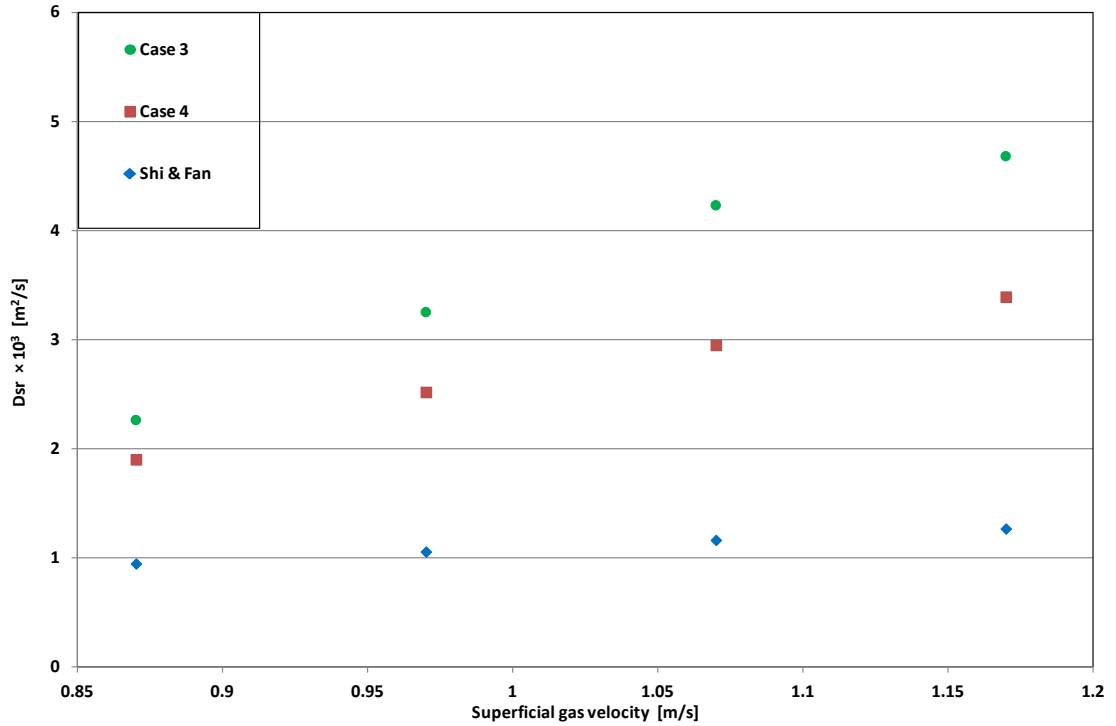


Figure 5.20: Dispersion coefficient values at different superficial fluid velocities for different simulation cases. The minimum fluidization bed height is 5.23 cm, while the bed width is 0.60 m. The details of the cases are reported in Table 5.3.

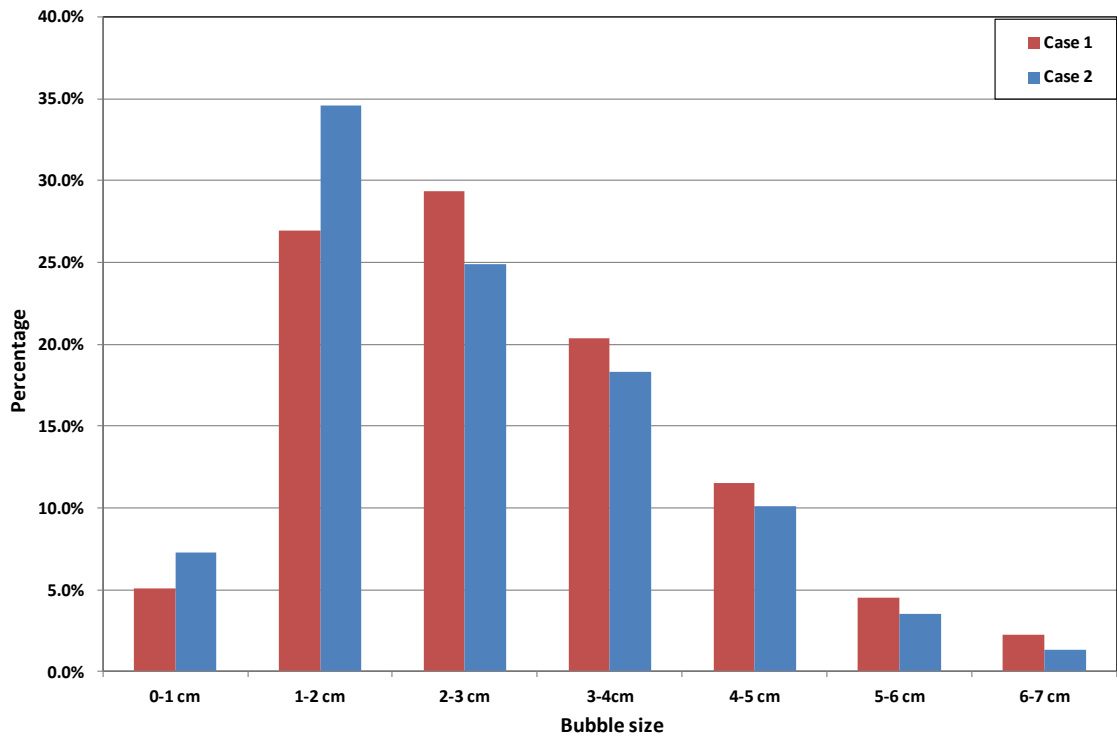


Figure 5.21: Comparison of bubble size distributions for Cases 1 and 2 for Powder 1. The superficial fluid velocity is 1.07 m/s, the minimum fluidization bed height is 5.23 cm, while the bed width is 0.60 m. The details of the cases are reported in Table 5.3.

Although there is no general consensus on how the equivalent bubble diameter should be defined, we took it to be the diameter of a circle having the same area (we are working in two dimensions) as the bubble. Thus, the equivalent bubble diameter is calculated as follows:

$$D_{eq} = \sqrt{\frac{4A}{\pi}} \quad (5.36)$$

where A denotes the area of the bubble. We used image analysis software to process the simulation results and compute the area of the bubbles. To do this, we assumed that bubbles are continuous regions in which the void fraction is larger than 0.85. By establishing a colour contrast between these regions and the other parts of the bed, the software allows to determine the number of bubbles and their areas. Figure 5.21 shows that Case 2, where we introduced the action of frictional stress earlier, predicts the largest percentage of small-sized bubbles, which belong to diameter classes [0cm, 1cm] and [1cm, 2cm]. Conversely, Case 1 predicts higher percentages for greater bubble diameter classes. The reduction in bubble size observed in Case 2 reduces the extent of lateral mixing, causing D_{sr} to have lower values.

To investigate the effects of frictional viscosity models on particle mixing, we compare Cases 1 and 3. In the first we adopted the model of Schaeffer (1987), while in the second that of Johnson & Jackson (1987). In both we used the same value for ϕ_{min} . As Figure 5.22 shows, Case 3 gives lower values for D_{sr} . This is because the model of Johnson & Jackson (1987) gives larger values of the frictional viscosity than those predicted by the model of Schaeffer (1987) (Passalacqua & Marmo, 2009). The larger the solid viscosity is, the more the granular assembly is able to resist shearing; this effect reduces the extent to which particles mix laterally, leading to lower values of the dispersion coefficient.

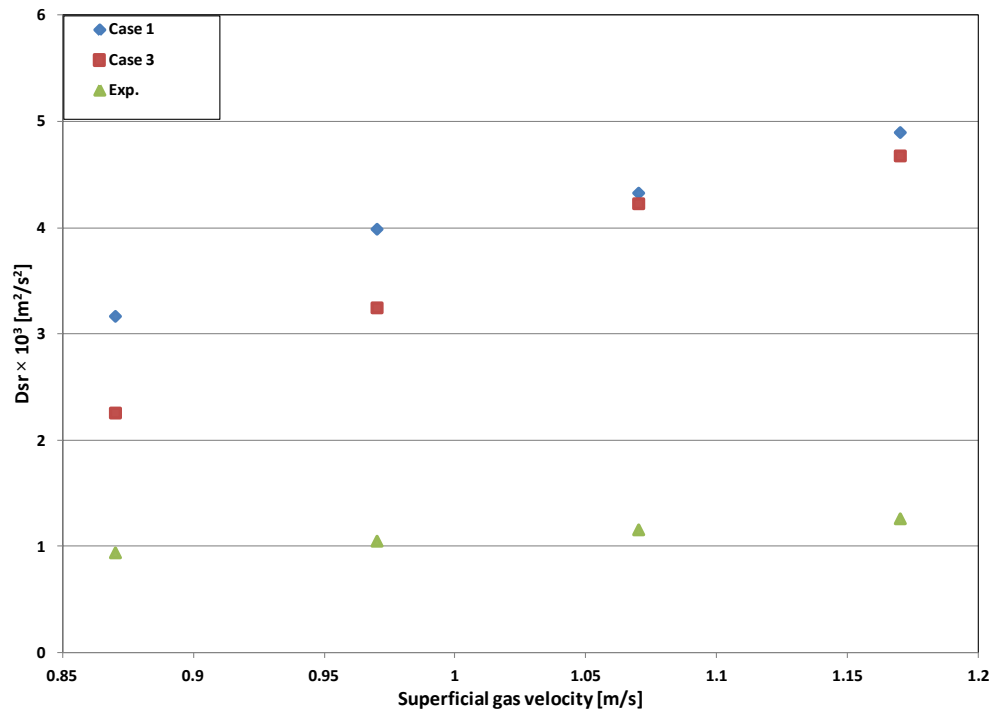


Figure 5.22: Dispersion coefficient values at different superficial fluid velocities for Cases 1 and 3. The minimum fluidization bed height is 5.23 cm, while the bed width is 0.60 m. The details of the cases are reported in Table 5.3.

In the cases investigated, we highlighted the influence of frictional viscosity on lateral mixing, modelling the frictional pressure by means of the kinetic theory while varying the frictional viscosity model and the frictional packing limit. The simulation results revealed that increasing the effective viscosity of the solid slows down the bed dynamics, making the particles less able to mix, thereby reducing D_{sr} . We think that we can further improve the simulation results by changing the frictional pressure model. Thus, instead of modeling the frictional pressure using the kinetic theory, we used the semi-empirical model proposed by Johnson & Jackson (1987). The simulation set-up is shown in Table 5.3, Case 5. In Figure 5.23 we compare the results obtained from Cases 4 and 5. In the latter we obtained lower D_{sr} values than in the former for all values of the superficial gas velocity. This is expected because the frictional pressure predicted by the model of Johnson & Jackson, used in Case 5, is higher than that predicted by the kinetic theory model, used in Case 4 (for a quantitative comparison between these pressure models, we refer to Passalacqua & Marmo, 2009). The higher frictional pressure is, the higher the void fraction around the bubbles is, and the leakier the latter become. Consequently, Case 5

predicts smaller bubbles than Case 4. To confirm this, we carried out a statistical analysis of the bubble size distributions on these cases, as we did previously. This is reported in Figure 5.24.

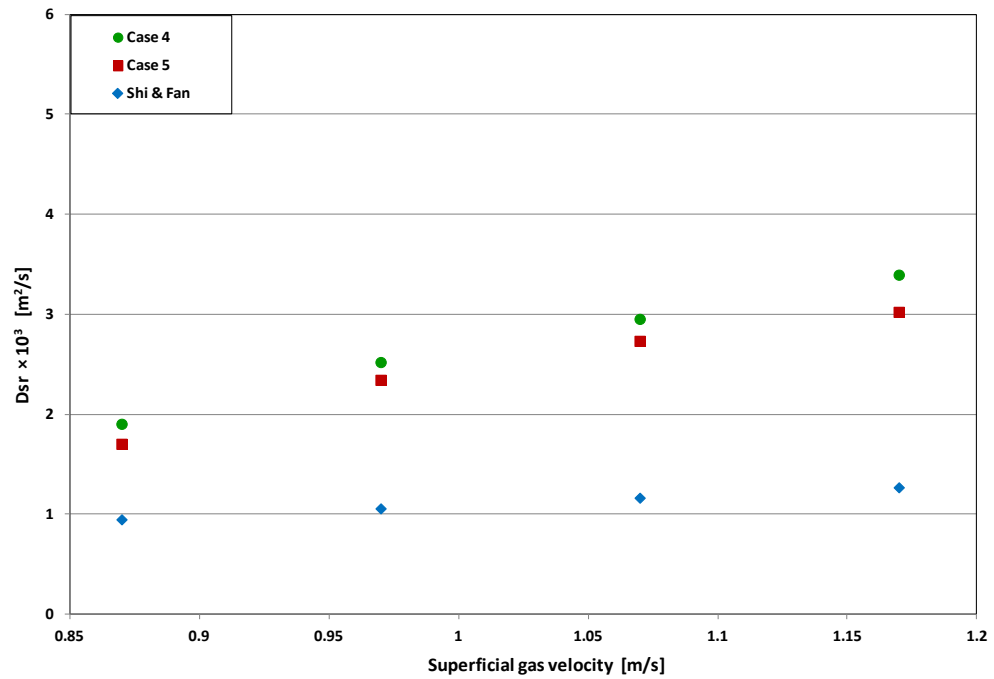


Figure 5.23: Dispersion coefficient values at different superficial fluid velocities for Cases 4 and 5. The minimum fluidization bed height is 5.23 cm, while the bed width is 0.60 m.

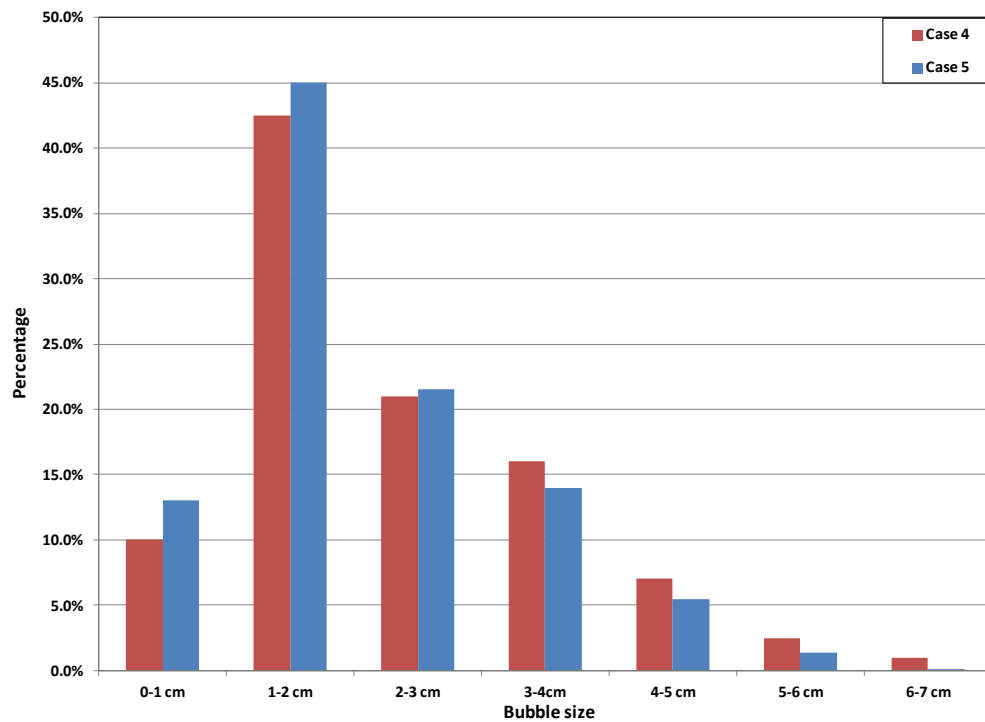


Figure 5.24: Comparison of bubble size distributions for Cases 4 and 5. The superficial fluid velocity is 1.07 m/s, the minimum fluidization bed height is 5.23 cm, while the bed width is 0.60 m.

In Figure 5.24, we observe that Case 5 has a higher proportion of small bubbles in the size range [0, 1cm], [1cm, 2cm] and [2cm, 3cm]. The results obtained revealed that Case 5 gives the best set-up for predicting D_{sr} out of all the cases considered. To confirm this, we used the set-up in Case 5 to investigate Powder 2. The properties of this powder are reported in Table 5.2. We compared the results with those obtained using the set-up in Case 1 (which is the default in Fluent). We began by investigating the influence of the superficial gas velocity on the dispersion coefficient. To do this, we kept the minimum fluidization bed height at 0.17 m and the bed width at 0.9 m, we fluidized the bed at different superficial gas velocities and we calculated the values of the dispersion coefficient. The results are reported in Figure 5.25. The trends observed are similar to what we reported for Powder 1: the dispersion coefficient increases with the superficial gas velocity, and Case 5 gives better predictions than Case 1.

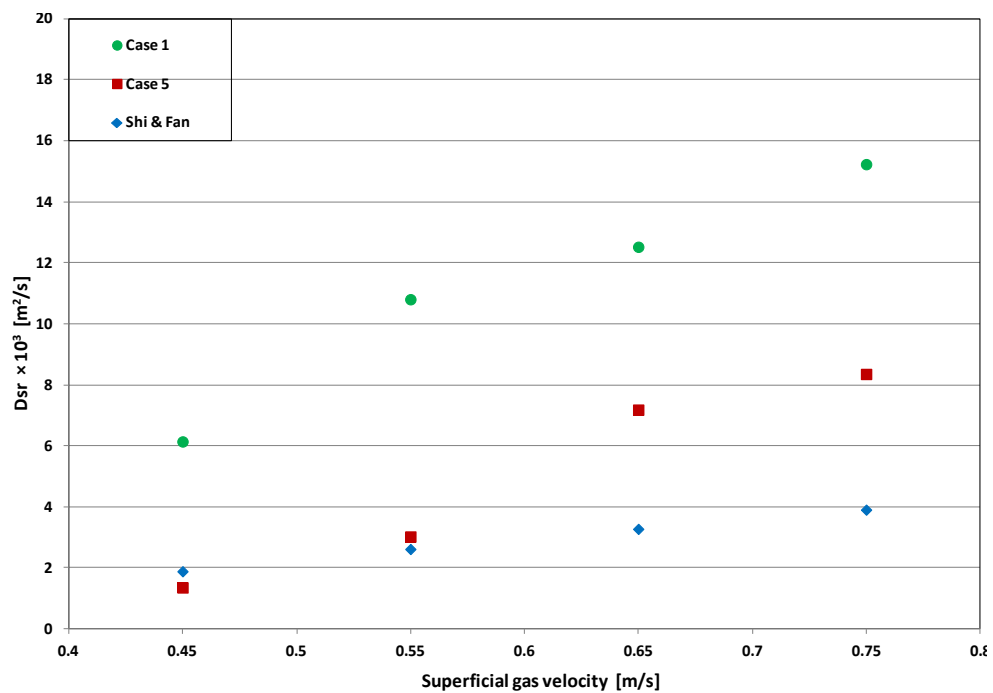


Figure 5.25: Dispersion coefficient values at different superficial fluid velocities for Cases 1 and 5 for Powder 2. The minimum fluidization bed height is 17.0 cm, while the bed width is 0.90 m. The details of the cases are reported in Table 5.3.

Figures 5.26 and 5.27 show the snapshots of solid volume fraction of solid-1 at 0.45 m/s (1.8 times u_{mf}) and 0.75 m/s (3 times u_{mf}), respectively.

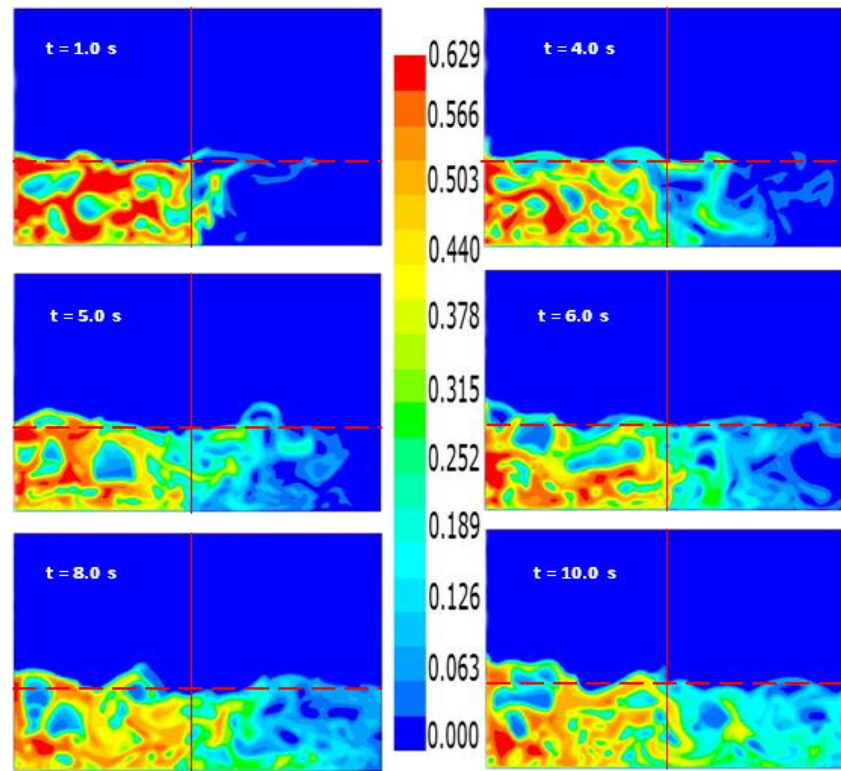


Figure 5.26: Solid 1 volume fraction profiles at different times for superficial fluid velocity of 0.45 m/s for Powder 2. The minimum fluidization bed height is 0.17 m, while the bed width is 0.90 m. The horizontal dashed line indicates where the bed ends and the freeboard begins.

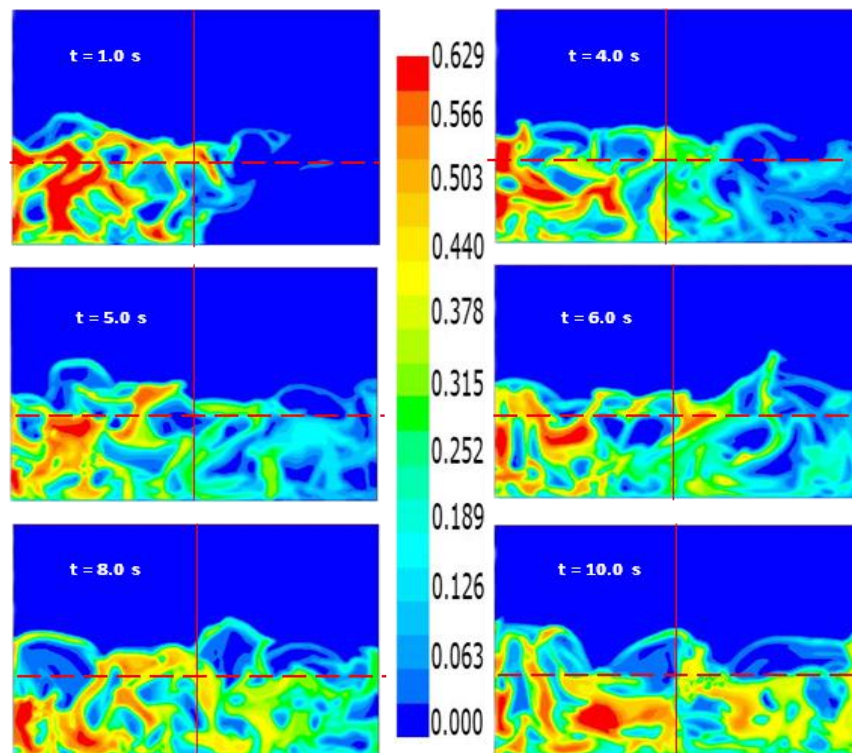


Figure 5.27: Solid 1 volume fraction profiles at different times for superficial fluid velocity of 0.75 m/s for Powder 2. The minimum fluidization bed height is 0.17m, while the bed width is 0.90 m. The horizontal dashed line indicates where the bed ends and the freeboard begins.

We also ran simulations changing the bed height and keeping the superficial gas velocity and bed width at 0.65 m/s (2.6 times u_{mf}) and 0.9 m, respectively. Figure 5.28 shows that the dispersion coefficient increases with bed height, and that Case 5 predicts better results than Case 1.

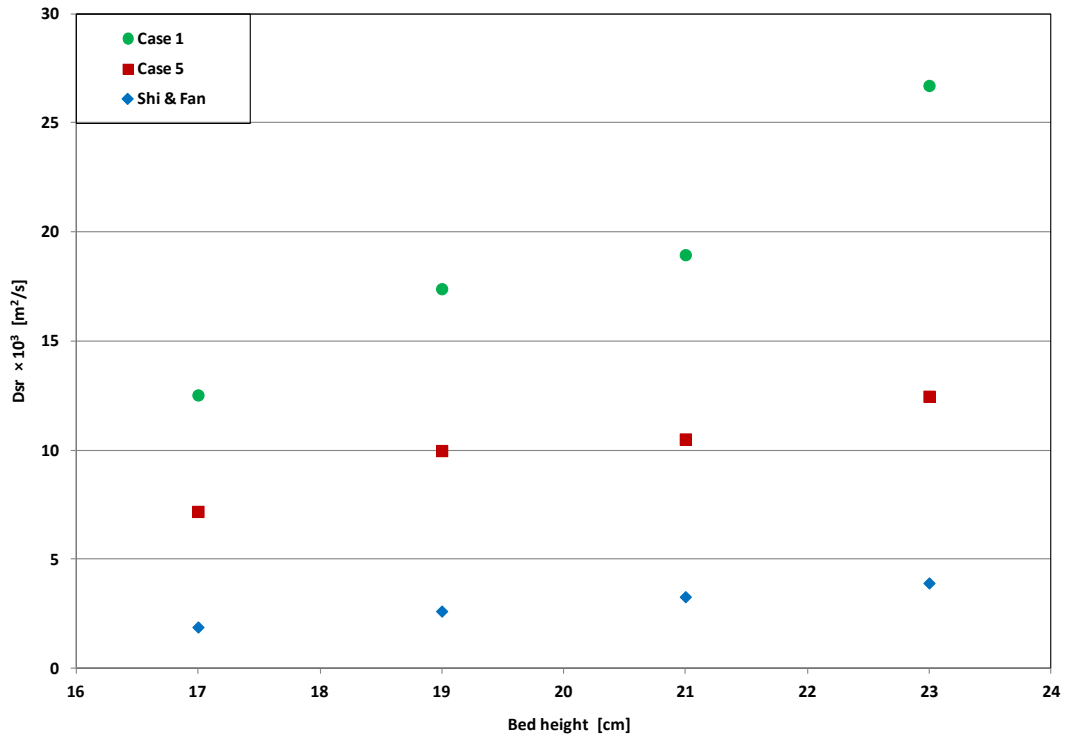


Figure 5.28: Dispersion coefficient values at different minimum fluidization bed heights for Cases 1 and 5 for Powder 2. The superficial fluid velocity is 0.65 m/s, while the bed width is 0.90 m. The details of the cases are reported in Table 5.3.

5.8 Effect of simulation dimensionality

As mentioned in Section 5.6, the overestimation of D_{sr} is partly due to the 2D nature of our simulations, which reduces the degrees of freedom of lateral solid motion. To assess how the dimensionality of our simulations affects the numerical results, we scaled down the numerical values obtained for D_{sr} by a factor α , to account for the dimensionality difference between the 2D domain used in our simulations and the 3D nature of the fluidized beds to which the empirical correlations used for validation refer. So, the dispersion coefficient values found empirically were no longer compared with the values D_{sr} found numerically, but rather with the scaled values D_{sr}/α . To a first approximation, it was speculatively assumed that scaling could

be accomplished by accounting for the degree of freedom lost when passing from a 3D to a 2D case, hence $\alpha = 2$. Figure 5.30 reports, for Case 1, the original and scaled-down values of the dispersion coefficient obtained numerically and those obtained from the empirical correlations. The scaled values of D_{sr} compare fairly well with predictions of Borodulya et al. (1982), but are still larger than the values yielded by the other empirical correlations. Altogether, it may be concluded that values of D_{sr} of reasonable accuracy can be obtained from 2D simulations with proper consideration of particle frictional stress combined with scaling to account for simulation dimensionality. This aspect is further investigated in Chapter 6.

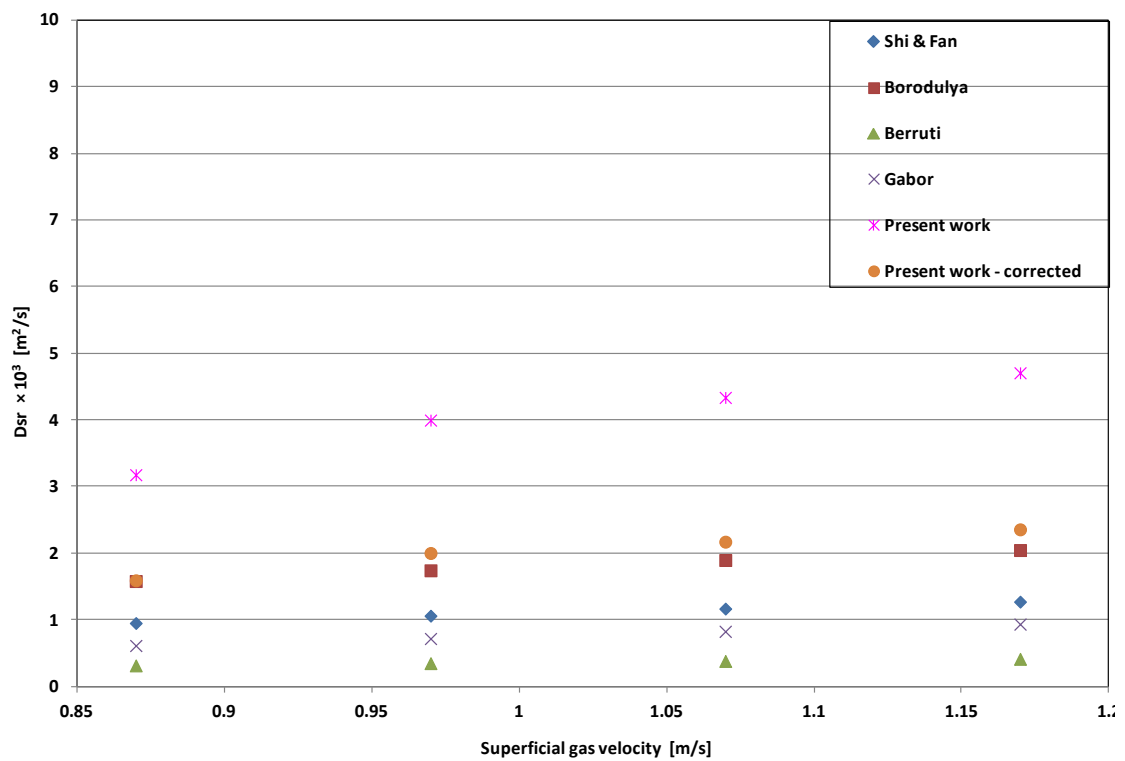


Figure 5.29: Comparison of dispersion coefficient values obtained by scaling down the original results in Case 1. The details of the cases are reported in Table 5.3. The values are compared with those obtained from empirical correlations in the literature.

5.9 Conclusions

In this chapter we investigated lateral solid mixing in fluidized beds using the Eulerian-Eulerian modeling approach. We defined the lateral dispersion coefficient D_{sr} using an equation analogous to the Fick's law of molecular diffusion. We examined the influence of design

parameters and operational conditions on the values of D_{sr} , considering how the latter is affected by the constitutive equations used to model the frictional solid stress. The simulation results show that D_{sr} increases with the superficial gas velocity and bed height. We also observed that D_{sr} increases rapidly at low values of bed width, but as this increases, D_{sr} rises slowly and then remains approximately constant. Furthermore, we investigated the influence of the fluid-dynamic model used in the simulations on the numerical results. To do so, we ran simulations with different frictional pressure and viscosity models, changing the solid volume fraction at which the bed is assumed to enter the frictional flow regime. The results showed that the model choice significantly affects the numerical results. Bubble size distributions in the bed show that early introduction of frictional solid stress results in the formation of smaller bubbles, leading to lower values of D_{sr} . We confirmed such findings by running simulations with another powder. For the two sets of powders, we obtained similar trends in D_{sr} values. Finally, we examined the influence that the 2D dimensionality of our simulations has on the numerical results obtained. The overestimation found is partly due to this dimensionality issue. A simple scaling rule based on the consideration of the loss of degree of freedom of lateral particle motion when passing from a 3D to a 2D domain was effective to largely reconcile simulated and empirical values of D_{sr} . This aspect is investigated in greater detail in Chapter 6.

Chapter 6

3D numerical simulations of lateral solid mixing in gas-fluidized beds: CFD and DEM studies

This chapter is concerned with the numerical simulations of lateral solid mixing using both the Eulerian-Eulerian and the Eulerian-Lagrangian modelling approaches:

1. We investigate the effects of simulation dimensionality on the numerical results presented in Chapter 5.
2. We run 2D and 3D simulations, comparing their numerical results.
3. We use the Discrete Element Modelling (DEM) approach to investigate the process of lateral solid mixing.
5. We carry out a parametric study to examine the influence of collision parameters on the accuracy of DEM simulations.
6. We compare the numerical results obtained from the CFD and DEM simulations.

Parts of this chapter have been submitted for publication:

Oke, O., Lettieri, P., van Wachem, B.G.M., Mazzei, L. 2015. *Lateral solid mixing in gas-fluidized beds: CFD and DEM studies*. *Chemical Engineering Research & Design*. Submitted for publication.

6.1 Introduction

In Chapter 5 we adopted the Eulerian-Eulerian approach to investigate lateral solid mixing in gas-fluidized beds. We investigated the influence of design and operational conditions on lateral dispersion coefficients, D_{sr} . For all the cases considered numerical results overestimated the empirical values of the latter, but within the same order of magnitude. We identified two possible causes for the overestimation. The first relates to the two-dimensional nature of our simulations; in actual fluidized beds the lateral motion of the solid has, we may say, two degrees of freedom (bubble-induced particle lateral motion develops in a horizontal plane), while in 2D fluidized beds solely one degree of freedom is present (particle lateral motion can only develop along a horizontal line). Thus, lateral dispersion coefficients obtained in 2D simulations should be expected to overestimate empirical results. This observation was also reported by Norouzi et al. (2011). To address the dimensionality issue, we proposed a simple scaling rule based on the consideration of the loss of a degree of freedom of lateral particle motion when passing from a 3D to a 2D domain. The overprediction, nevertheless, was not eliminated. The second overestimation cause that we identified relates to how the solid-phase frictional stress is modelled constitutively. We attempted to investigate this aspect by using different frictional stress models, and changing the solid volume fraction value ϕ_{min} at which the bed was assumed to enter the frictional flow regime. We obtained improved results with this, but numerical results were still higher than the empirical ones.

The present chapter intends to address these problems. We believe that the issue of simulation dimensionality can be investigated by running 3D simulations. Thus, we ran 3D simulations, considering the same powder, the same computational setup and the same simulation cases employed in our former 2D simulations. This permitted us to see how simulation dimensionality affects the numerical results. Furthermore, we attempted to investigate the frictional stress modelling issue by using DEM simulations. These offer a simpler way of describing the rheology of the solid phase. This is because we no longer need to model the solid stress, since the solid is no longer modelled as a continuum. As we shall see later, in the DEM model the

mechanisms responsible for particle-particle interaction are well captured by just three parameters: *spring constant*, *damping coefficient* and *friction coefficient*. Finally, we compared the results of the Eulerian-Eulerian and Eulerian-Lagrangian simulations.

To estimate lateral dispersion coefficients, we follow an approach similar to that proposed by Brotz (1956), reported in Chapter 5. We briefly summarise the approach again for clarity: He used two solids having the same physical properties, but differing in colour. The solids were separated by a vertical partition plate which divided the bed into two equal parts. He fluidized the bed for a certain time and then removed the partition; by measuring the rate at which the two solids mix, he estimated the lateral dispersion coefficient. Following Brotz, we placed two types of solids (for example, red and blue particles) with the same physical properties, but differing in colour, in a 3D rectangular bed. We placed the red particles on one side and the blue particles on the other side of a removable partition. We fluidized the bed with air at ambient temperature, allowing it to reach pseudo-stationary conditions, and then removed the partition. The solution of the Eulerian-Lagrangian model provides the position of each particle at a given point in time, and this can be used to calculate the spatial concentration profile of the particles after the partition is removed. Similarly, the solution of the Eulerian-Eulerian models provides the radial solid concentration profiles which can be used to estimate the rate of lateral solid mixing. We divide this chapter into two parts: the first part is concerned with 3D Eulerian-Eulerian simulations and the second part is about the Eulerian-Lagrangian (DEM) simulations of lateral solid mixing.

6.2 2D versus 3D simulations of gas-fluidized beds

Until recently, many numerical simulations of dense fluidized beds were two-dimensional (2D) (Gidaspow & Ettehadieh, 1983; Ettehadieh et al., 1984; Lyczkowski et al., 1987; Bouillard et al., 1989; Ding & Gidaspow, 1990; Tsuo & Gidaspow, 1990; Ding & Lyczkowski, 1992; Kuipers et al., 1992; Wang & Bouillard, 1993; Gamwo et al., 1995; Nieuwland et al., 1996; Boemer et al., 1995; Blazer et al., 1995; Enwald et al., 1997). This is because three-dimensional

(3D) simulations are computationally expensive due to memory capacity and processor speed of available computers. To date, even with available computational resources, 3D simulations are still very expensive because the governing equations have to be integrated over a longer period of time to compute the inherently chaotic dynamics of the fluidization process (Xie et al., 2008).

Many experimental works aimed at gaining fundamental insights into the dynamics of fluidized beds are also carried out using 2D beds (often referred to as pseudo-2D beds because there are no beds that are truly two-dimensional; the latter is generally understood to mean rectangular equipment having a small depth compared to their width and height). The use of 2D beds for experimentation has many advantages, especially when studying the growth, velocity and coalescence of bubbles: it allows bubbles to be readily seen and photographed; it is relatively easy to modify the distributor plates; a 2D bed and its ancillary equipment, when compared to a 3D bed of the same width, is cheaper to fabricate (Geldart, 1970). Thus, 2D beds have helped researchers to understand the behaviour of fluidized beds better.

Researchers have obtained satisfactory results from 2D simulations of gas-fluidized beds. Many of these simulations were carried out for systems where the fluid dynamics are inherently two-dimensional; in such systems the variation of fluid dynamic properties in space and time can be neglected in the third dimension. For example, Johanssen et al. (2006) performed 2D simulations of a rectangular fluidized bed, validating their numerical results with experimental data from a pseudo-2D bed. In the latter, particle motion in the depth direction is suppressed and the fluid dynamics can be assumed to be two-dimensional. Their numerical results showed good agreement with experimental data. Other researchers (Boemer et al., 1998; Goldschmidt et al., 2001; Goldschmidt et al., 2004; Chiesa et al., 2005; Sun et al., 2006) have also employed 2D simulations to investigate pseudo-2D bed and reported considerable success.

Despite the success of 2D simulations in understanding and predicting the dynamic behaviour of fluidized beds, significant differences between 2D and 3D simulations have been reported. Pyle & Harrison (1967) compared the rise velocities of bubbles in 2D and 3D beds. They reported

that bubbles in 2D beds have lower rise velocities than those in 3D beds. Similarly, Geldart & Kelsey (1968) compared bed expansion in 2D and 3D beds. They reported that, under the same condition of superficial gas velocity, particle properties and bed height, 2D beds have higher bed expansion than 3D beds. This is expected, since in the former bed solid flow is completely restrained in the third dimension.

Peirano et al. (2001) performed numerical simulations of a rectangular bubbling bed using the Eulerian-Eulerian (E-E) modelling approach. They compared their numerical results with experimental values of pressure fluctuations and bed height fluctuations. They observed significant differences between 2D and 3D simulations; in particular only the 3D simulations could predict correctly the experimental data. They concluded that 2D simulations should be used with caution. Similarly, Cammarata et al. (2003) studied bubbling behaviour of fluidized beds in rectangular apparatus using 2D and 3D simulations. They compared the bed expansion and bubble size obtained from their simulations with the predictions from Darton's (1977) equation. They reported that a more physically realistic behaviour was obtained in 3D simulations. They concluded, like Peirano et al. (2001), that 3D simulations should be preferably used, except in situations where the system is 2D by nature.

Xie et al. (2008) presented a slightly contrary view to the authors in the preceding paragraph. They reported that 2D E-E simulations are still applicable for studying the behaviour of fluidized beds, but within a certain range of operating conditions. They performed 2D simulations of cylindrical and rectangular beds, investigating the bubbling, slugging and turbulent regime of fluidization. Their results showed that 2D simulations can accurately predict the behaviour of the bubbling regime where the superficial gas velocity is close to the minimum bubbling velocity. However, like Peirano et al. (2001), they emphasized that caution must be taken when employing 2D simulations in other fluidization regimes.

Similarly, Reuge et al. (2008) investigated the expansion and bed height fluctuations of Geldart B particles using E-E simulations. They carried out both 2D and 3D simulations of the bed.

Their results showed that 2D simulations overestimated the bed expansion, while 3D simulations correctly predicted them. They concluded that 3D simulations are necessary to correctly predict the behaviour of fluidized beds. Significant quantitative differences between 2D and 3D simulations were also reported by Li et al. (2010) in their CFD simulations of gas mixing in fluidized beds. They reported that bed expansion, solid concentration, gas and solid velocities were different in 2D and 3D simulations. Accordingly Li et al. (2010) concluded that 2D simulations cannot be used to accurately simulate a 3D system.

Quite recently, Li et al. (2014) evaluated the difference between 2D and 3D simulations of circulating fluidized beds. They compared the axial pressure gradient and radial void-fraction profiles obtained from 2D and 3D simulations with those obtained experimentally. Their results showed that, unlike 3D simulations, 2D simulations could not satisfactorily predict experimental data.

The works reported in the preceding paragraphs show that there are significant differences between the dynamics of 2D and 3D beds. We believe that better agreement between our numerical simulations and experimental data may be achieved if simulations are performed in 3D. Accordingly, we ran simulations in 3D, using *the same* powder and *the same* computational set-up used in the 2D simulations, and considering all the simulation cases investigated for the latter. The results of our simulations are now reported in the following sections.

6.2.1 Results and discussion on 3D Eulerian-Eulerian simulations

The governing equations, initial and boundary conditions are the same as those used in Chapter 5 for our 2D simulations. The geometry employed is also the same, except that the present geometry is 3D. The computational domain is shown in Figure 6.1, while Table 6.1 reports the simulation parameters employed in the present simulations.

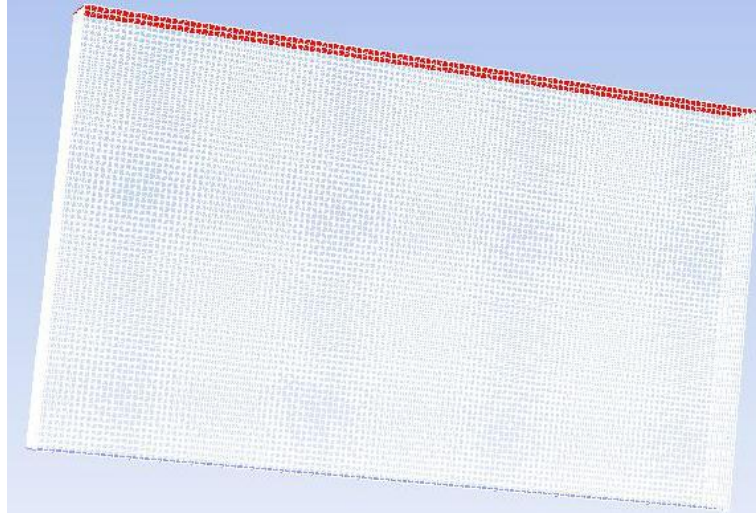


Figure 6.1: Computational grid of our 3D simulations

Table 6.1: Simulation parameters for 3D E-E simulations of Powder 1

Parameters	Value
Vessel height	0.35 m
Bed depth (thickness)	0.05 m
Bed Width	0.60 m
Superficial gas velocity	0.87 – 1.17 m/s
Particle diameter	491 μm
Particle density	2620 kg/m ³
Minimum fluidization velocity	0.20 m/s
Bed height	0.05 m
Computational cell	0.005 m
Time-step	0.001 s

From the solid volume fraction profiles obtained numerically, we calculated the void-free mass fraction $\hat{\phi}_i$ of solid phase i in each layer:

$$\hat{\phi}_i \equiv \frac{\phi_i}{\phi_1 + \phi_2} \quad (6.1)$$

We ran the simulations at various superficial gas velocities, keeping the minimum fluidization bed height at 5.23 cm, the bed width at 0.6 m and the bed depth at 5 cm. We fitted the void-free mass fraction profiles obtained from our simulations with those obtained from the Fick's law using the least square regression method, as did previously. In Figure 6.2 we report the profiles of void-free mass fraction obtained from the Fick's law and those obtained numerically at $t = 5.0$ s at superficial gas velocities 0.87 m/s, for both 2D and 3D simulations. Similar profiles are found at other times, but we have chosen 5.0 s as representative time. We obtained a good match between the theoretical and numerical profiles.

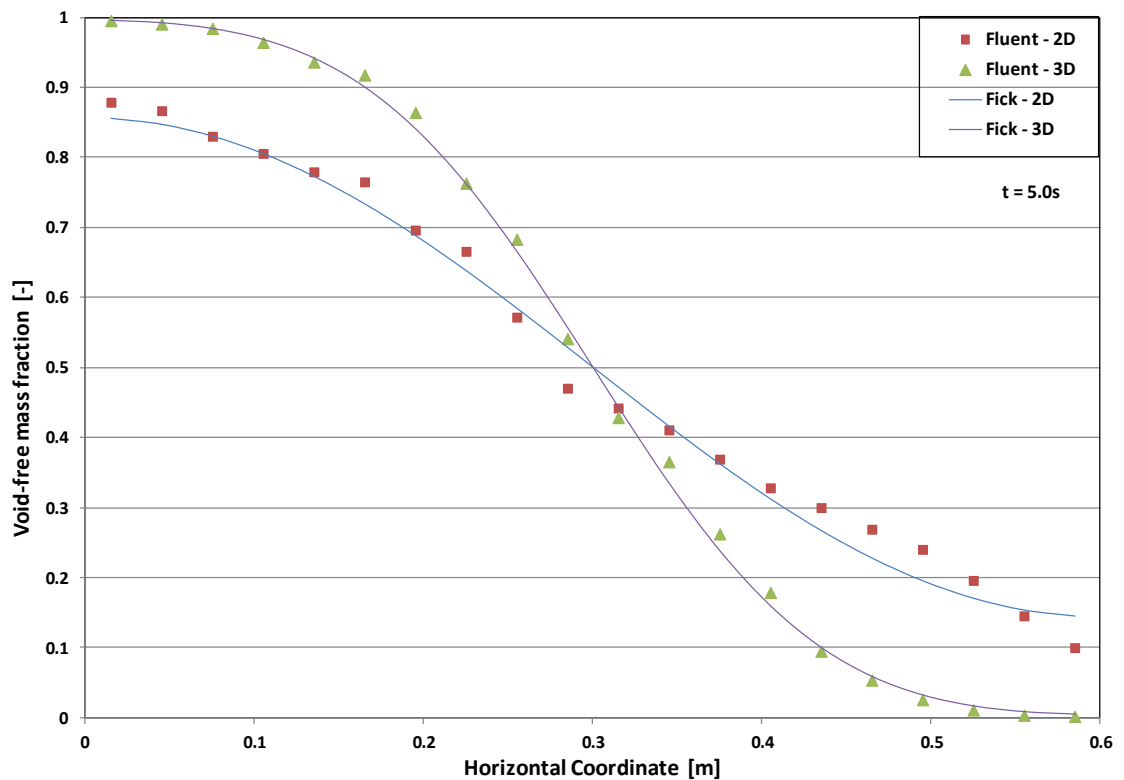


Figure 6.2: Solid 1 void-free vertically-averaged mass fraction horizontal profiles for a superficial fluid velocity of 0.87 m/s/. The 'Fick' profile is that obtained from the analytical solution of the Fick's law, while the 'Fluent' profile is that obtained numerically.

We observe that concentration falls faster in time in the 2D simulations compared to the 3D simulations. This is expected because in the latter simulations there movement of solid and gas is restrained by the front and back walls. Consequently the lateral movement of solid is slower in 3D simulations. This is confirmed by the snapshots of solid-1 concentration reported in

Figures 6.3A and 6.3B, which refer to the 2D and 3D simulations, respectively, and to a superficial gas velocity of 0.87 m/s. The figures show how the tracer particles placed at the left of the removable partition wall spread to the right. We observe that the movement of solids in the 2D simulation is faster than that in the 3D simulation. This, as mentioned, is consistent with the profiles reported in Figure 6.2.

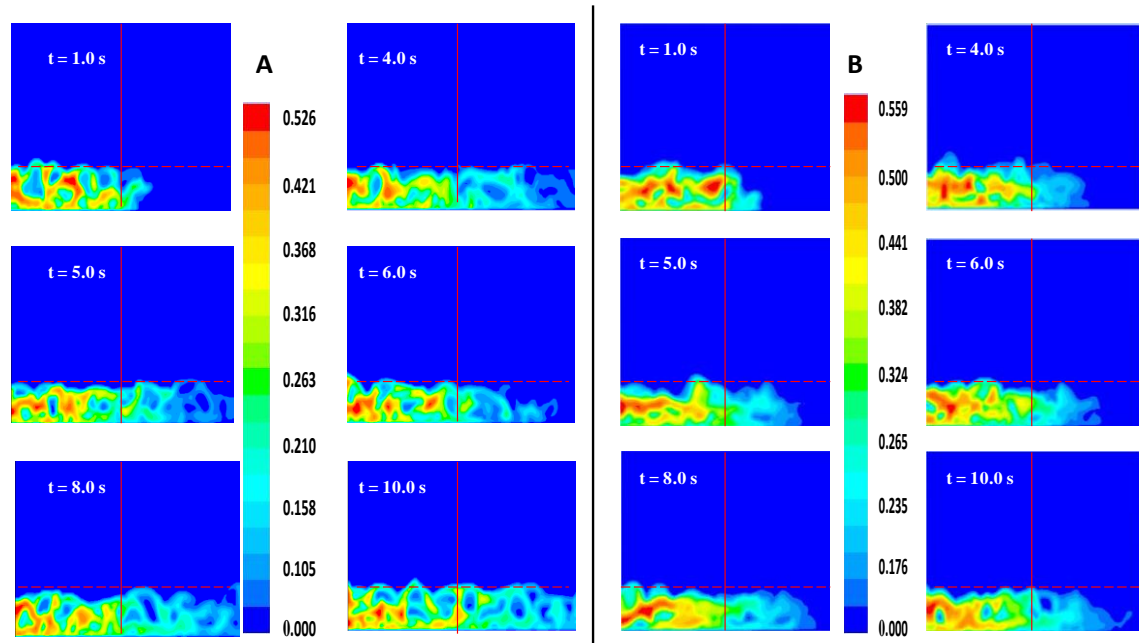


Figure 6.3: Solid-1 volume fraction profiles at different times for superficial fluid velocity of 0.87 m/s. (A) 2D simulations (B) 3D simulations. The minimum fluidization bed height is 5.23 cm, while the bed width is 0.60 m. The horizontal dashed line indicates where the bed ends and the freeboard begins.

Table 6.2: Simulation cases for E-E simulations

Cases	Frictional Pressure Model		Frictional Viscosity Model		Frictional Packing Limit	
	KTGF	J & J	Schaffer	J & J	0.50	0.61
1	X		X			X
2	X		X		X	
3	X			X		X
4	X			X	X	
5		X		X	X	

We ran simulations considering the different cases reported in Table 6.2, using the same operational conditions reported in Table 6.1, as we did in Chapter 5. We tested different frictional pressure and viscosity models, changing the solid volume fraction at which the bed enters the frictional flow regime (ϕ_{min}) and observing the effects of these variations on lateral dispersion.

Figures 6.4 - 6.8 show the variation of lateral dispersion coefficient with superficial gas velocity for cases 1 – 5. The values of D_{sr} are compared with the empirical data of Shi & Fan (1984). We observe an increase in D_{sr} as the superficial gas velocity is increased. This is true for both 2D and 3D simulations. Nevertheless, in all the cases considered, 2D simulations clearly overestimate D_{sr} values, and their values are higher than those of 3D simulations. Bègis & Balzer (1997) and Bègis et al., (1998) have reported significant difference between fluidization dynamics predicted by 2D and 3D simulations. To explain this, Xie et al. (2008) carried out a budget analysis of the governing partial differential equations, evaluating each term appearing in the latter. Their analysis revealed that the difference between 2D and 3D simulation results is due to the additional terms appearing in the three dimensional equations of change. The difference, according to Xie et al. (2008), increases as the superficial gas velocity increases. This possibly explains why, in Figures 6.4 – 6.8, the difference between D_{sr} values obtained in 2D simulations and 3D simulations increases as the superficial gas velocity increases. We observe in Figures 6.4 – 6.8 that 3D simulations results agree reasonably well with empirical data in all cases than the 2D simulations.

Figures 6.4 - 6.8 show that the results of the 2D simulations are appreciably affected by the model used for the frictional solid stress (frictional pressure and frictional shear viscosity) and by the value ascribed to ϕ_{min} . The reasons for this were discussed in Chapter 5 and so will not be repeated here. The results of the 3D simulations are far less sensitive to the frictional solid stress model. In both 2D and 3D simulations, we see that lowering the value of ϕ_{min} or using the constitutive model of Johnson & Jackson (1987) instead of the kinetic theory of granular

flow (KTGF) model for the frictional pressure results into lower values of the lateral dispersion coefficient. As explained in Passalacqua & Marmo (2009), this is because the model of Johnson & Jackson (1987) yields larger solid pressure than the KTGF model, given the same solid concentration, whilst lowering the value of ϕ_{min} introduces this effect sooner, that is to say, at lower power compaction. Larger solid pressures in turn result into smaller bubbles, reduced solid recirculation and reduced solid dispersion. This trend is found also in the 3D simulations, but the effect is less significant. For instance, for a fluid velocity of 1.17 m/s, the difference in the D_{sr} value between Cases 1 and 5 is $1.9 \text{ E-3 m}^2/\text{s}$ for the 2D simulations, while it reduces to $0.3 \text{ E-3 m}^2/\text{s}$ for the 3D simulations.

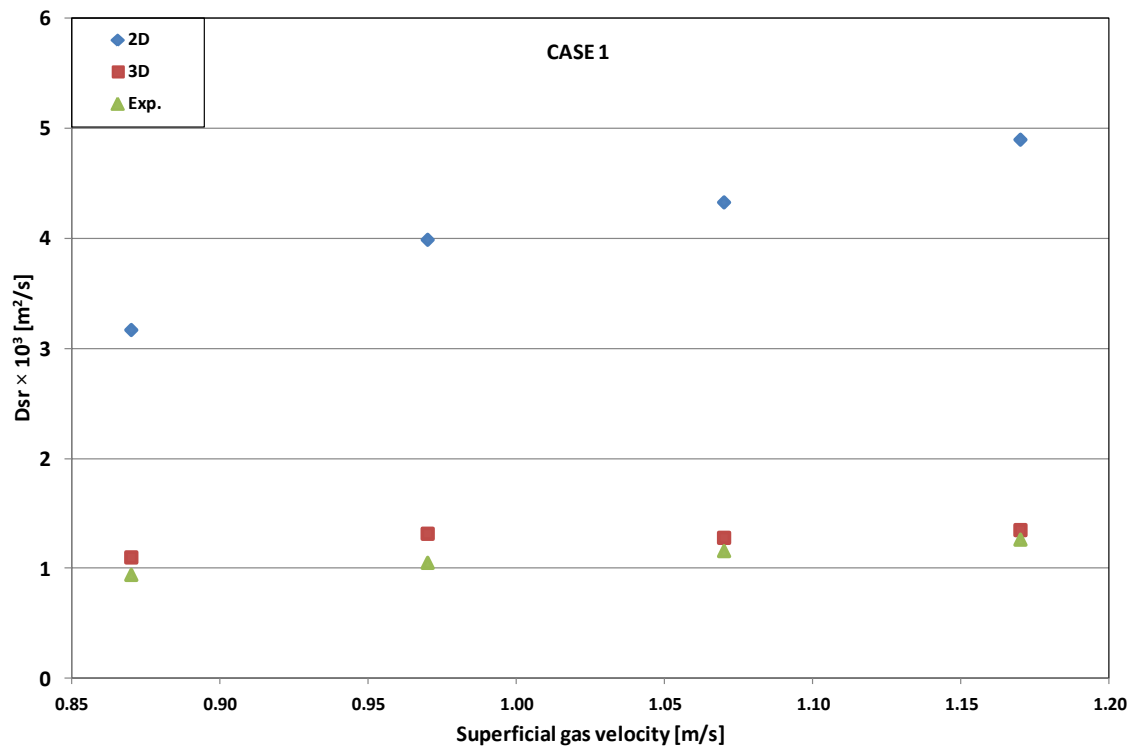


Figure 6.4: Dispersion coefficient values at different superficial fluid velocities for Case 1. The values are compared with those obtained from empirical data of Shi & Fan (1984).

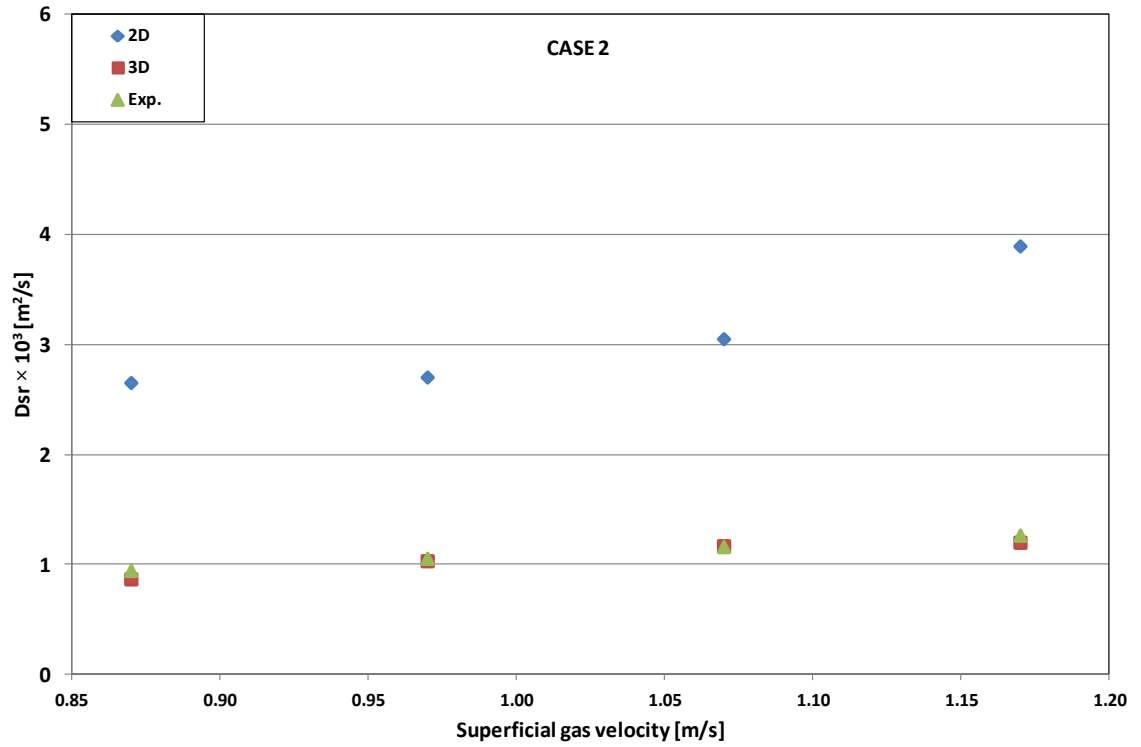


Figure 6.5: Dispersion coefficient values at different superficial fluid velocities for Case 2. The values are compared with those obtained from empirical data of Shi & Fan (1984).

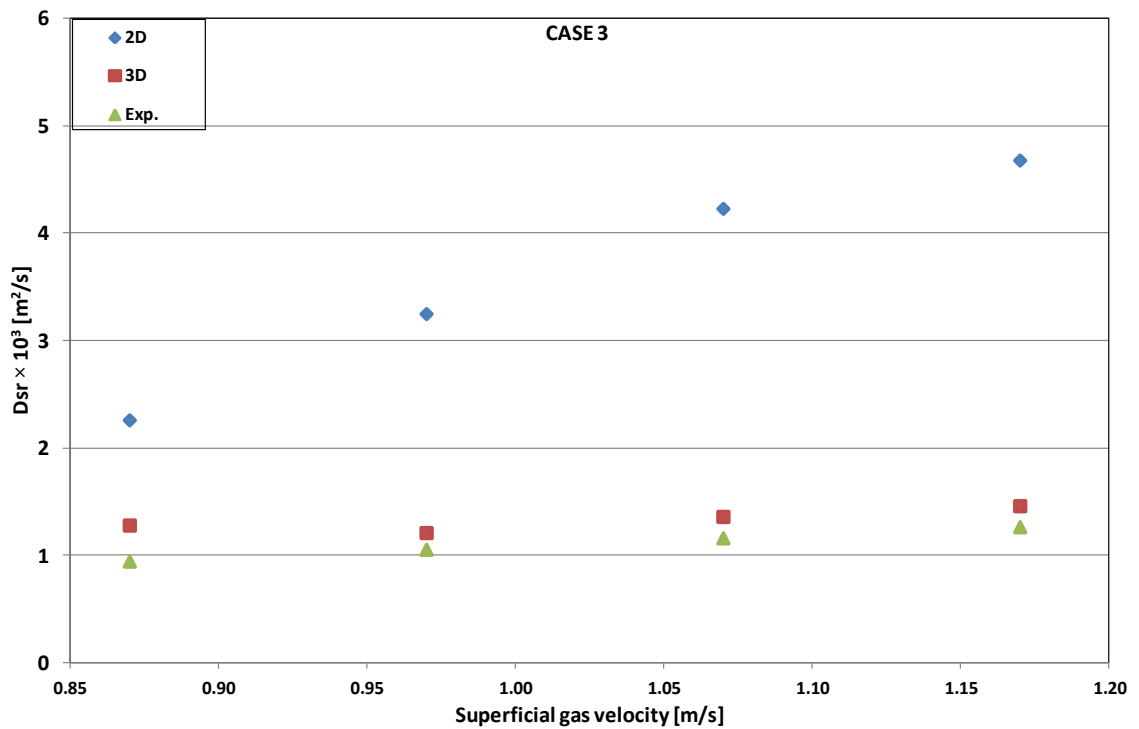


Figure 6.6: Dispersion coefficient values at different superficial fluid velocities for Case 3. The values are compared with those obtained from empirical data of Shi & Fan (1984).

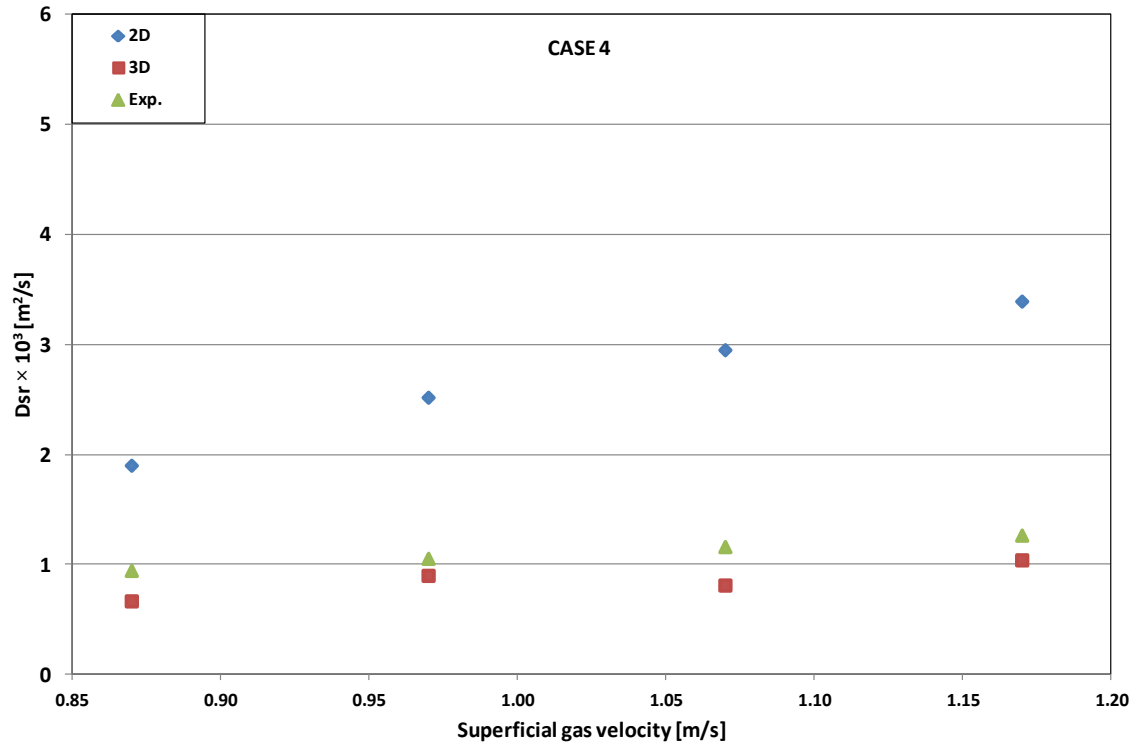


Figure 6.7: Dispersion coefficient values at different superficial fluid velocities for Case 4. The values are compared with those obtained from empirical data of Shi & Fan (1984).

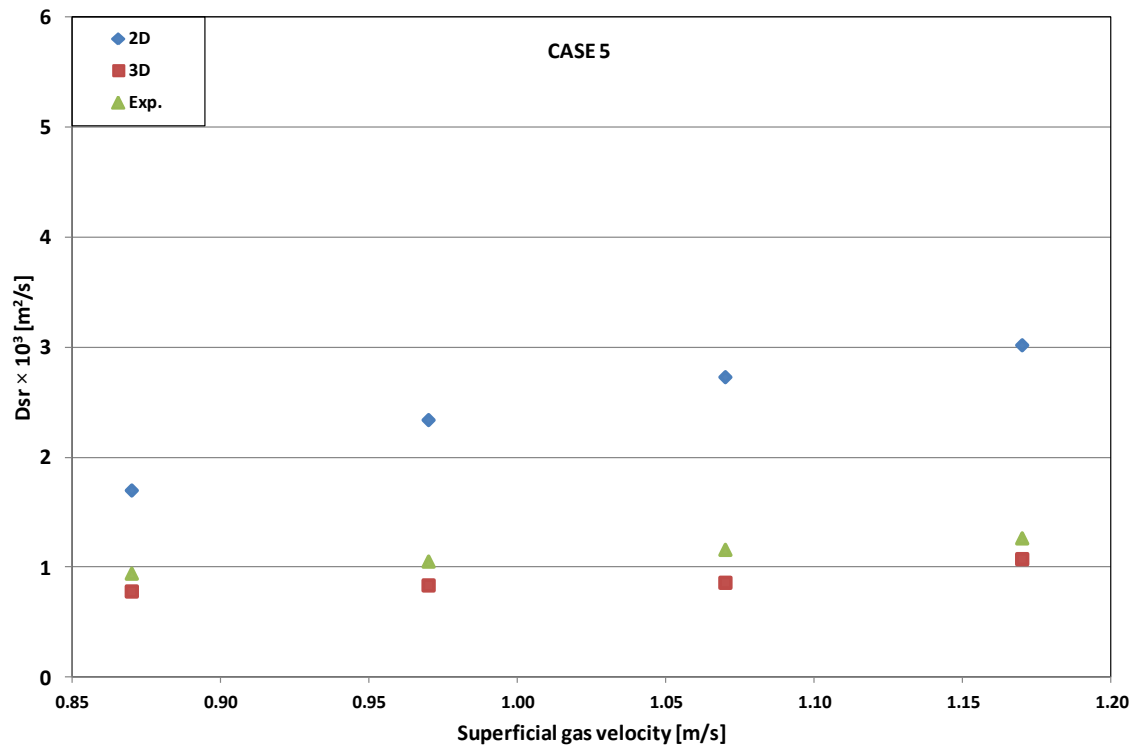


Figure 6.8: Dispersion coefficient values at different superficial fluid velocities for Case 5. The values are compared with those obtained from empirical data of Shi & Fan (1984).

6.3 Eulerian-Lagrangian (DEM) Simulations

Before advancing further let us briefly recap one of the main goals of this chapter. The Eulerian-Eulerian models employed in Chapter 5 overestimated the values of D_{sr} . We identified two possible causes for the overestimation: the first relates to the 2D nature of our simulations and the second has to do with how we modelled the frictional solid stress appearing in the Eulerian-Eulerian models. We investigated these issues in Section 6.2. It is clear from the results presented in the latter that the major cause for the overestimation is largely the 2D nature of our previous simulations. This section investigates the capability of the Eulerian-Lagrangian (E-L) modelling approach to estimate lateral dispersion coefficients with the intent of comparing the simulation results with those obtained using the Eulerian-Eulerian models. The E-L approach used in this work is the Discrete Element Method (DEM). In the latter, we track the motion of each particle individually, and the fluid phase is described using the averaged equations of motion. The particle-particle interaction can be modelled either by using a soft sphere or a hard sphere approach. The following sections summarize these approaches, commenting on their relative advantages and disadvantages.

6.3.1 Hard-sphere approach

In the hard-sphere approach, collisions between particles are assumed to be binary and instantaneous. Collisions are processed one by one according to the order in which the events occur. The approach uses the conservation equations of linear and angular momenta to calculate the velocities of particles emerging from collisions. The model equations for this approach are reported below. These are based on the hard-sphere model developed by Hoomans et al. (1996, 2000, 2001).

Consider two colliding spheres i and j with position vectors \mathbf{r}_i and \mathbf{r}_j , diameters d_i and d_j , and masses m_i and m_j , respectively. The normal and tangential unit vectors are defined respectively as:

$$\mathbf{n}_{ij} = \frac{(\mathbf{r}_i - \mathbf{r}_j)}{|\mathbf{r}_i - \mathbf{r}_j|}; \quad \mathbf{t}_{ij} = \frac{\mathbf{v}_{ij}}{|\mathbf{v}_{ij}|} \quad (6.2)$$

where \mathbf{v}_{ij} can be expressed as:

$$\mathbf{v}_{ij} = (\mathbf{v}_i - \mathbf{v}_j) - \left(\frac{1}{2}d_i\boldsymbol{\omega}_i + \frac{1}{2}d_j\boldsymbol{\omega}_j \right) \times \mathbf{n}_{ij} \quad (6.3)$$

\mathbf{v}_i and \mathbf{v}_j denote the linear velocities of the spheres and $\boldsymbol{\omega}_i$ and $\boldsymbol{\omega}_j$ their angular velocities before collisions, and the corresponding velocities after collisions are denoted by primes. The impulse \mathbf{J} exerted on sphere i by sphere j is given by:

$$m_i(\mathbf{v}_i' - \mathbf{v}_i) = -m_j(\mathbf{v}_j' - \mathbf{v}_j) = \mathbf{J} \quad (6.4)$$

and

$$\frac{2I_i}{d_i}(\boldsymbol{\omega}_i' - \boldsymbol{\omega}_i) = \frac{2I_j}{d_j}(\boldsymbol{\omega}_j' - \boldsymbol{\omega}_j) = -\mathbf{n}_{ij} \times \mathbf{J} \quad (6.5)$$

where I is the moment of inertia about the centre of a sphere given by:

$$I = md^2/10 \quad (6.6)$$

where m is the mass of the sphere and d is its diameter. The relative velocity at the point of contact is expressed as:

Eq. 6.4 and 6.5 can be combined to obtain:

$$\mathbf{v}_{ij}' - \mathbf{v}_{ij} = \frac{7}{2} \left(\frac{1}{m_i} + \frac{1}{m_j} \right) \mathbf{J} - \frac{5}{2} \left(\frac{1}{m_i} + \frac{1}{m_j} \right) \mathbf{n}_{ij} (\mathbf{J} \cdot \mathbf{n}_{ij}) \quad (6.7)$$

To determine the velocities of particles after collision, we need to calculate the impulse \mathbf{J} . Therefore we use the following closure models. First, we express the coefficient of normal restitution e characterising the normal component of \mathbf{v}_{ij} as:

$$\mathbf{n}_{ij} \cdot \mathbf{v}_{ij}' = -e(\mathbf{n}_{ij} \cdot \mathbf{v}_{ij}) \quad (6.8)$$

where $0 \leq e \leq 1$. The coefficient of dynamic friction ($\mu \geq 0$) is written as:

$$|\mathbf{n}_{ij} \times \mathbf{J}| = \mu(\mathbf{n}_{ij} \cdot \mathbf{J}) \quad (6.9)$$

and the coefficient of tangential restitution ($0 \leq \beta \leq 1$) is given by:

$$\mathbf{n}_{ij} \times \mathbf{v}_{ij}' = -\beta(\mathbf{n}_{ij} \times \mathbf{v}_{ij}) \quad (6.10)$$

If we combine Eq. 6.7 and 6.8, we obtain the normal component of the impulse vector:

$$\mathbf{J}_n = \frac{-(1+e)(\mathbf{v}_{ij} \cdot \mathbf{n}_{ij})}{\frac{1}{m_i} + \frac{1}{m_j}} \quad (6.11)$$

For the tangential component of \mathbf{J} , two types of collisions are possible: sticking or sliding.

According to Lu et al. (2005), if

$$\mu < \frac{(1+\beta)m_i m_j}{3.5(m_i + m_j)J_n} (\mathbf{v}_{ij} \cdot \mathbf{t}_{ij}) \quad (6.12)$$

then, the collision involves sliding, and

$$\mathbf{J}_t = -\mu \mathbf{J}_n \quad (6.13)$$

If collision involves sticking,

$$\mu \geq \frac{(1+\beta)m_i m_j}{3.5(m_i + m_j)J_n} (\mathbf{v}_{ij} \cdot \mathbf{t}_{ij}) \quad (6.14)$$

then,

$$\mathbf{J}_t = \frac{(1+\beta)m_i m_j}{3.5(m_i + m_j)} (\mathbf{v}_{ij} \cdot \mathbf{t}_{ij}) \quad (6.15)$$

Given the definitions of \mathbf{J} in Eq. 6.11, 6.13 and 6.15, the velocities of particles after collision can be calculated from Eq. 6.4 and 6.5.

When the hard-sphere model is used for simulations of dilute systems, they are much faster than soft-sphere simulations, since the former approach does not take into account multiple collisions at the same instant. Campbell & Brennen (1985) were the first to use the hard-sphere model to investigate granular systems. Subsequently, it has been employed to study a wide range of

complex system. Hoomans et al. (1996) used the hard-sphere approach, together with CFD conservation equations for the fluid phase, to study gas-solid flow in fluidized beds. Through this approach, they investigated the influence of particle-particle interaction on bubble formation. Later, they used the approach to examine segregation caused by density and size difference in fluidized beds (Hooman et al., 2000). Other researchers (Goldschmidt et al., 2001; Li & Kuipers, 2002; Helland et al., 1999; Lun, 2000; Zhou et al., 2004) have also employed the hard-sphere approach to investigate various aspects of fluidized beds, including high pressure fluidization, circulating fluidized beds and gas turbulence. Nevertheless, the approach becomes useless when particle concentration is high, such as those encountered in dense fluidized systems, because it does not consider multiple contacts of particles. When this happens, the soft-sphere approach becomes the plausible alternative.

6.3.2 Soft-sphere Model

The soft-sphere model was developed originally by Cundall & Strack (1979). In this method, particles are allowed to overlap slightly at the point of collisions, and the forces at the point of contacts are calculated from the deformation history of the contacts. The physical motivation for the soft-sphere model is that collisions of particles are accompanied by deformation at the point of contact. The deformation, described by the overlap displacement of two particles, is the driving force of the soft-sphere model (van Wachem, 2003). The greater the overlap, the greater the repulsive force between the colliding particles. The soft-sphere model allows for multiple overlap; the net contact force is calculated as the addition of all pair-wise interactions. Tsuji et al. (1993) were the first authors to use the soft-sphere approach to simulate the dynamics of fluidized beds. Based on the model developed by Tsuji et al. (1993), Iwadate & Horio (1998) introduced van der Waals forces to simulate the fluidization of cohesive particles. The soft-sphere model has also been employed in other applications such as heat transfer (Li & Mason, 2000) and coal combustion (Zhou et al., 2003).

In the soft-sphere models, the motion of particles is described individually by applying Newton's equation of motion.

6.3.2.1 Equations of motion

The linear motion of a particle i , assumed to be spherical, with mass m_i and centre coordinate \mathbf{r}_i , can be modelled using the Newton's second law of motion:

$$m_i \frac{d^2 \mathbf{r}_i}{dt^2} = \mathbf{F}_{c,i} + \mathbf{F}_{ext,i} + \mathbf{F}_{s,i} \quad (6.16)$$

Here $\mathbf{F}_{c,i}$ is the total contact force. The latter is the addition of individual contact forces exerted by all other particles in contact with particle i . $\mathbf{F}_{c,i}$ has normal and tangential components:

$$\mathbf{F}_{c,i} = \sum_j (\mathbf{F}_{ij,n} + \mathbf{F}_{ij,t}) \quad (6.17)$$

where $\mathbf{F}_{ij,n}$ and $\mathbf{F}_{ij,t}$ are the normal and tangential components of \mathbf{F}_{ij} , respectively, where \mathbf{F}_{ij} represents the contact force exerted by particle j on particle i . $\mathbf{F}_{ext,i}$ is the total external force acting on particle i . This can be decomposed into the following forces:

$$\mathbf{F}_{ext,i} = \mathbf{F}_{g,i} + \mathbf{F}_{d,i} + \mathbf{F}_{p,i} \quad (6.18)$$

here $\mathbf{F}_{g,i}$, $\mathbf{F}_{d,i}$, and $\mathbf{F}_{p,i}$ are the gravitational, drag and pressure forces respectively. Other contributions to $\mathbf{F}_{ext,i}$ such as the virtual mass, lift, Faxen and Basset forces are neglected. Lastly, $\mathbf{F}_{s,i}$ is the sum of all other particle-particle forces, which can include electrostatic and van der waals forces. In this work, we do not consider these particle-particle forces.

The rotational motion of particle i is given by:

$$I_i \frac{d\boldsymbol{\omega}_i}{dt} = \mathbf{T}_i \quad (6.19)$$

where I_i is the moment of inertia, $\boldsymbol{\omega}_i$ is the angular velocity and \mathbf{T}_i is the torque of particle i .

The torque depends only on the tangential component of individual contact forces, thus:

$$\mathbf{T}_i = \sum_j (R_i \mathbf{n}_{ij} \times \mathbf{F}_{ij,t}) \quad (6.20)$$

where \mathbf{n}_{ij} is the unit vector from the centre of particle i to that of particle j , R_i is the radius of particle i . We should note that although the total force acting on particle i is given by the sum of the forces on the right hand side of Eq. 6.16, only the tangential component of the contact force exerted by particle j on particle i is used in Eq. 6.20 to calculate \mathbf{T}_i . According to Xu & Yu (1997), the total external force (the fluid-particle interaction force and the gravity) acts on the centre of mass of the particle, hence it has no contribution to the rotational motion of the latter. Conversely, the interparticle forces (the total contact force and the particle-particle interaction force) act on the contact point between particle i and j , generating a torque which causes particle i to rotate. The only interparticle force acting between particle i and j is \mathbf{F}_{ij} (since the contribution of $\mathbf{F}_{s,i}$ has been neglected). The tangential component $\mathbf{F}_{ij,t}$ of the latter is therefore responsible for the effective torque on particle i . As said in the preceding paragraphs, the translational and rotational motions of particles are described Eqs. 6.16 and 6.19. By integrating these equations, we obtain the evolution in time of particle positions and velocities.

6.3.2.2 External force

The gravitational force $\mathbf{F}_{g,i}$ on particle i is expressed as:

$$\mathbf{F}_{g,i} = m_i \mathbf{g} \quad (6.21)$$

The drag force $\mathbf{F}_{d,i}$ that the fluid exerts on particle i is given by:

$$\mathbf{F}_{d,i} = (V_i/\phi_i)\beta(\mathbf{u}_f - \mathbf{v}_i) \quad (6.22)$$

Here \mathbf{v}_i and V_i are the linear velocity and volume of particle i , respectively, while β denotes the drag coefficient, whose constitutive expression has been reported in Chapter 5.

The pressure force $\mathbf{F}_{p,i}$ on particle i is expressed as:

$$\mathbf{F}_{p,i} = -V_i \nabla p_f \quad (6.23)$$

where p_f represents the volume-averaged fluid pressure. This force may be regarded as the buoyancy force acting on particle i . The expression that we selected for the drag coefficient β is consistent with this choice of buoyancy force.

We will now describe the contact force scheme employed in the soft-sphere approach.

6.3.2.3 Contact force

The most widely used contact force model in DEM simulations, which is also employed in this work, is the *spring, slider and dash-pot model*, proposed by Cundall & Strack (1978). The diagram representing this model is reported in Figure 6.11.

The Cundall & Strack (1978) contact force model considers three mechanisms of particle-particle interactions. These mechanisms are captured by three mechanical elements in the model – *spring, dash-pot and slider*. The spring simulates the deformation following collision of particles. The dash-pot models the energy dissipation due to particle-particle interaction, and the slider simulates the frictional force arising when particles slide on each other under the application of a normal force. The effects of these mechanisms on particle motion are captured by the following parameters: the *spring stiffness* K , the *damping coefficient* η and the *coefficient of friction* μ . This is represented in Figure 6.11.

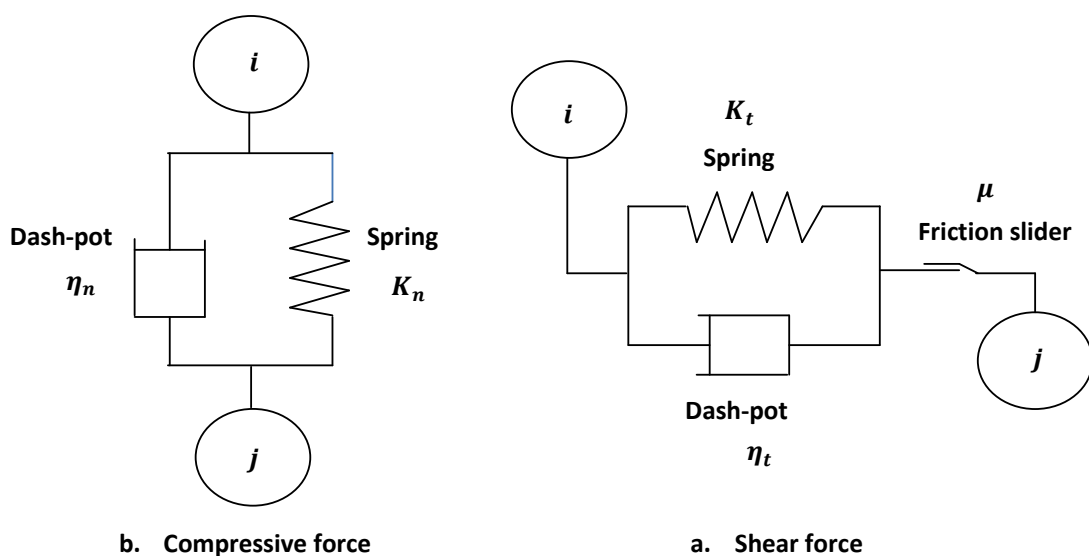


Figure 6.11: Graphical representation of spring/dashpot model (Tsuji et al., 1992).

When particle i is in contact with particle j , the contact force $\mathbf{F}_{ij,n}$ acting on particle i is given by the sum of the forces due to the spring and the dashpot:

$$\mathbf{F}_{ij,n} = - [K_n \delta_n^{3/2} + \eta_n (\mathbf{v}_{ij} \cdot \mathbf{n}_{ij})] \mathbf{n}_{ij} \quad (6.24)$$

With Tsuji (1992), we used the Hertzian contact theory to model the relationship between the normal spring force and the normal displacement; the relationship between the two is non-linear. In Eq. 6.24, K_n is the normal spring stiffness, δ_n is the normal displacement or overlap, η_n is the normal damping coefficient and \mathbf{v}_{ij} is the relative velocity between particles i and j , given by:

$$\mathbf{v}_{ij} = (\mathbf{v}_i - \mathbf{v}_j) + (R_i \boldsymbol{\omega}_i + R_j \boldsymbol{\omega}_j) \times \mathbf{n}_{ij} \quad (6.25)$$

The normal vector \mathbf{n}_{ij} and the overlap δ_n are given by:

$$\mathbf{n}_{ij} = \frac{\mathbf{r}_i - \mathbf{r}_j}{|\mathbf{r}_i - \mathbf{r}_j|} \quad ; \quad \delta_n = (R_i + R_j) - |\mathbf{r}_i - \mathbf{r}_j| \quad (6.26)$$

The expression for the tangential component of the contact force depends on whether particles i and j slide on each other (kinetic friction) or not (static friction). If they do not, the force is given by:

$$\mathbf{F}_{ij,t} = - [K_t \delta_t + \eta_t (\mathbf{v}_{ij} \cdot \mathbf{t}_{ij})] \mathbf{t}_{ij} \quad (6.27)$$

where K_t , δ_t , η_t and \mathbf{t}_{ij} are the spring stiffness, the displacement, the damping coefficient and the unit vector in the tangential direction. The vector \mathbf{t}_{ij} and the tangential displacement δ_t are found by adding the displacement vectors through subsequent time-steps of collision (van Wachem et al. 2015). If the following relation is satisfied:

$$\mathbf{F}_{ij,t} > \mu |\mathbf{F}_{ij,n}| \quad (6.28)$$

particles i and j slide. Then, Eq. 6.27 no longer holds and must be replaced by:

$$\mathbf{F}_{ij,t} = -\mu \left| \mathbf{F}_{ij,n} \right| \mathbf{t}_{ij} \quad (6.29)$$

The next step is determining the values of the normal and tangential spring constants and damping coefficients. We address this in the following sections.

6.3.2.4 Spring stiffness

For two spheres of equal size, Tsuji (1992) suggested the following expression to calculate the normal spring stiffness:

$$K_n = \frac{\sqrt{2R_i E_i}}{3(1 - \sigma_i^2)} \quad (6.30)$$

where E_i is the Young modulus and σ_i is the Poisson ratio of particle i . In the case of contact between a sphere and a wall, K_n is given by:

$$K_n = \frac{\frac{4\sqrt{R_i}}{3}}{\frac{1 - \sigma_i^2}{E_i} + \frac{1 - \sigma_w^2}{E_w}} \quad (6.31)$$

where E_w and σ_w are the Young modulus and Poisson ratio of the wall, respectively.

The relation for calculating the tangential spring stiffness was derived by Mindlin (1949) and Mindlin & Deresiewicz (1953) and reads:

$$K_t = \frac{2\sqrt{2R_i G_i}}{2 - \sigma_i} \delta_n^{1/2} \quad (6.32)$$

where G_i is the shear modulus of particle i . This is related to the Young modulus E_i and to the Poisson ratio σ_i as follows:

$$G_i = \frac{E_i}{2(1 + \sigma_i)} \quad (6.33)$$

For the case of contact between a particle and the wall, Tsuji (1992) provides the following expression for calculating the tangential spring stiffness:

$$K_t = \frac{8\sqrt{R_i G_i}}{2 - \sigma_i} \delta_n^{1/2} \quad (6.34)$$

6.3.2.5 Damping coefficient

Following van Wachem et al. (2010), we use the following expressions for the damping coefficients:

$$\eta_n = \alpha \sqrt{MK_n} \delta_n^{1/4} ; \eta_t = \alpha \sqrt{MK_t} \delta_t^{1/4} \quad (6.35)$$

For collisions between particle i and j , it is:

$$M = \frac{m_i m_j}{(m_i + m_j)} \quad (6.36)$$

For collisions between particle i and the wall, $M = m_i$. where α is a parameter that depends on the coefficient of restitution e . This dependence is well defined by Tsuji et al. (1992), as reported in Figure 6.12.

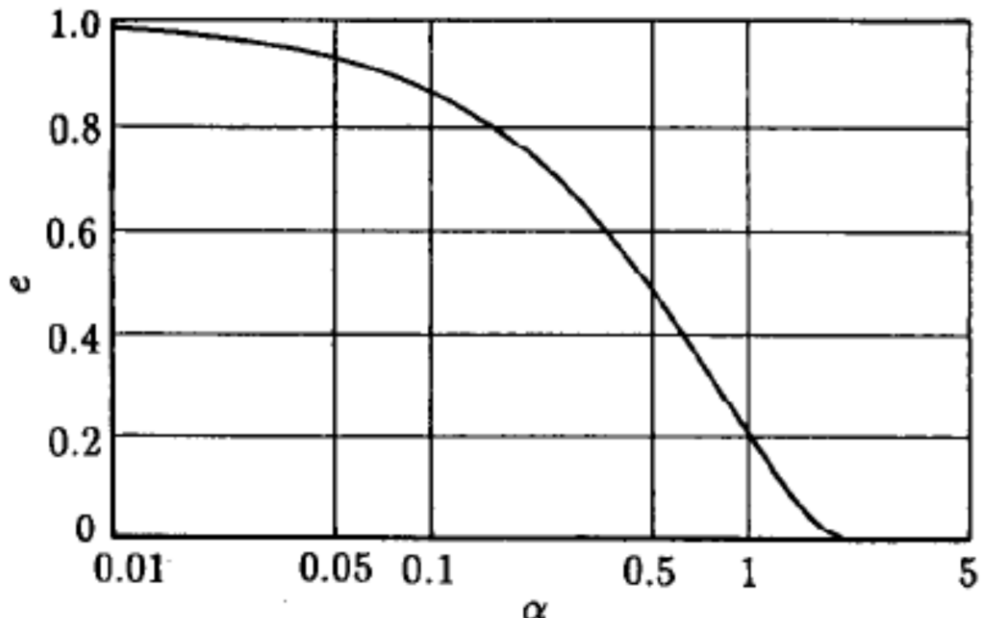


Figure 6.12: Relationship between parameter α and restitution coefficient e (Tsuji et al., 1992)

We would like to point out that although the values of K_n and K_t can be obtained from Eq. 6.30, 6.31, 6.32 and 6.34, in practice the values assigned to these parameters are smaller than those

obtained from these equations (which are based on the material properties, that is, the Young modulus and Poisson ratio); this is because otherwise the integration time step required in the simulation becomes impractically small. So, when assigning the values of K_n and K_t , one takes into account computational efficiency as much as material properties (Gera et al., 1998; Kawaguchi et al., 1998; Mikami et al., 1998; Kaneko et al., 1999; Rong et al., 1999; Rhodes et al., 2001; Tian et al., 2007). Extra care has to be taken when choosing the stiffness values, for too small values can lead to unrealistic overlap between the colliding particles, rendering the results inaccurate, whereas too large values can render the computational time exceedingly high. Tsuji et al. (1993) suggested a normal stiffness value of 800 N/m. This value has been widely used by researchers, producing acceptable results (refer, for instance, to Gera et al., 1998; Kawaguchi et al., 1998; Mikami et al., 1998; Kaneko et al., 1999; Rong et al., 1999; Rhodes et al., 2001). Albeit this value reduces the computational effort considerably, there is a risk that the accuracy of the simulation results might be affected (Di Maio & Di Renzo, 2004). All these aspects will be examined in this chapter.

6.3.3 Comparison between hard-sphere and soft-sphere approaches

Although numerical simulations of fluidized beds have been carried out using both hard-sphere and soft-sphere models, each approach has distinct features which make it suitable in some applications and unsuitable in others. In soft-sphere models, slight deformation is allowed at contact points of particles and multiple contacts among particles are permitted. This is not possible in hard-sphere models where collisions are binary and instantaneous. Similarly, it is quite straightforward to incorporate cohesive forces into soft-sphere models. This is because collisions among particles are described using the Newton's equations of motion of individual particles. In hard-sphere models, doing this is quite challenging because the model equations are not in terms of forces; they are derived via momentum exchange at the point of contact (Van der Hoef et al., 2006). However, soft-sphere models, when compared to their hard-sphere counterpart, present some difficulties when dealing with particles of different sizes. In soft-

sphere models, one needs to use different values of spring constants to model contact forces between particles of different sizes. Doing this is quite challenging.

Table 6.3: Comparison between hard and soft-sphere models. (YY) – Good; (Y) – Normal; (N) – Not suitable (Van der Hoef et al., 2006).

	Hard-sphere	Soft-sphere
Computing efficiency	YY	Y
Multiple contacts	N	YY
Dense systems	N	YY
Incorporation of cohesive force	Y	YY
Energy conservation during collisions	YY	Y
Multiple particle sizes	YY	Y

Furthermore, hard-sphere models are more straightforward and require less complicated constitutive equations than soft-sphere models. In the latter, we need to derive closure equations for the contact force, damping coefficient and stiffness. Some of these equations rely on the physical properties of particles which, in some cases, have to be determined experimentally. We briefly summarize the comparison between hard and soft-sphere models in Table 6.3. In this work, we employ the soft-sphere approach.

6.3.4 DEM simulation results and discussion

This section investigates the capability of the Eulerian-Lagrangian (DEM) modelling approach to estimating lateral dispersion coefficients with the intent of comparing their simulation results with those obtained using the Eulerian-Eulerian models. In the former approach, as said, we solve relatively less complicated models; in particular, closure problems for frictional solid stress no longer arise, since we do not solve average equations.

Setting up DEM simulations

The DEM simulations code (MultiFlow) employed in this code was provided by Professor Berend Van Wachem at Imperial College London. Setting up simulations in MultiFlow requires selecting the files that describe the simulation. This include selecting the options file *case.mf* containing the simulation set-up, a *mesh.geo* file containing the computational mesh and a *compileoptions.h* file including specific options at compile time and a script for running

MultiFlow. Additionally, the user needs to select the *USERinit.c* file for describing the initial conditions, *USERBoundary.c* file for describing the boundary conditions. It is important to note that appropriate values should be used in the above files and if changes are made to any of the files, one needs to recompile MultiFlow. A detailed description of how MultiFlow works, including the step-by-step guide of how to use the codes are reported in Appendix A.

Discussion

It is important to point out that the powder and the bed geometry used in Section 6.2 for our Eulerian-Eulerian simulations are different from those used in the DEM simulations. This is consequence of the limitations imposed by this modelling approach. The simulations required to treat the same geometry and powder considered in the previous CFD simulations are far too expensive for our computational resources, requiring about 13 million more particles than those used in the DEM simulations that we were able to run. Since our aim is to compare the performance of the Eulerian-Eulerian and Eulerian-Lagrangian modelling approaches, we simulated a new geometry and powder. We used the powder investigated experimentally by Grakhovskii (1968), which has a bigger mean size than those employed previously in Section 6.2. The parameters used in our simulations, in particular the bed height and the superficial gas velocities, were chosen to replicate the work of the author. However, the bed depth and width used in our simulations are smaller than those of Grakhovskii (1968) (He used a bed of depth 100 mm and width 1000 mm). This is again because of the huge computational cost we will incur if we employed the bed dimensions of the former author. In Table 6.4 we summarize the powder properties and the bed dimensions employed in our simulations.

Table 6.4: DEM simulation parameters for Powder 2

Conditions of particle	
Particle shape	Spherical
Diameter	3 mm
Density	1000 kg/m ³
Stiffness	40,9772 N/m ^{3/2}
Restitution coefficient	0.90
Friction coefficient	0.1 – 0.4
Poisson ratio	0.33
Minimum fluidization velocity	0.76 m/s
Number	29,470
Conditions of gas	
Density	1.2 kg/ m ³
Viscosity	1.7 × 10 ⁻⁵ Ns / m ³
Simulation conditions	
Bed height	60 mm
Bed width	200 mm
Bed depth	60 mm
Superficial gas velocity	1.9 – 2.66 m/s

To estimate the D_{sr} values, we used the same procedure as in the Eulerian-Eulerian simulations. The results of DEM simulations provide the position of each particle at any given time. This allowed us to determine the radial void-free concentration profiles in the bed. By matching these profiles with those obtained analytically from the Fick's equation, we calculated the D_{sr} values at different operational conditions. We report in Figure 6.13 the concentration profiles for a superficial gas velocity of 1.9 m/s; the values of the other parameters are those shown in Table 6.4. The profile given by the CFD simulation is also included for completeness. We observe a good agreement between the numerical and analytical profiles. These refer to a time $t = 2.0$ s, but similar results were obtained at other times and superficial gas velocities.

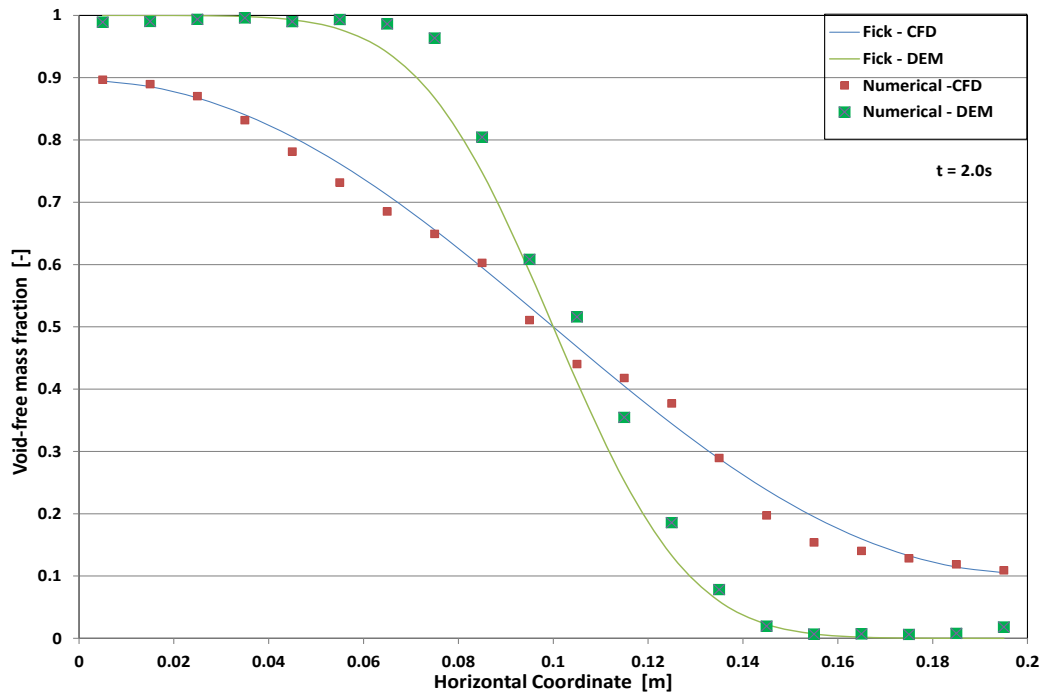


Figure 6.13: Void-free concentration profiles obtained in DEM and CFD simulations at superficial gas velocity of 1.9 m/s.

We should notice that the accuracy of the simulations depends strongly on the values assigned to the parameters appearing in the model (i.e., *restitution coefficient*, *particle-particle friction coefficient* and *stiffness* or *spring constant*); hence, extra care has to be taken when choosing them. The coefficient of restitution accounts for the kinetic energy dissipated when particles collide. The energy that is lost is accounted for by the contact damping force included in the DEM model through the dashpot model. It is customary to base the damping coefficient on the collisional properties of the particles, in particular the restitution coefficient e . Nevertheless, we should notice that the latter is neither a material property nor a constant, but it depends, among other parameters, on the relative impact velocity of the colliding particles (Kuwabara & Kono, 1987). However, the variation of the restitution coefficient is negligible, except at very high impact velocities (usually 10 m/s and above) (Labous et al., 1997). So, the value of e is normally taken to be constant in DEM simulations. The typical value employed in the literature is 0.90, and therefore in the present work we employed this value. Unlike the coefficient of restitution, the friction coefficient and spring constants depend on the material properties. The friction coefficient is an empirical parameter whose value depends on many factors, including

particle shape, particle size and surface texture, whilst the spring constants depend on the Young's modulus and Poisson's ratio of the material. Since we do not have the empirical values for these parameters (even if we did, we could not have used them, insofar as the simulations would have been too expensive computationally), we performed a parametric study to determine how the values assigned to them influence the numerical results of our simulations.

To investigate how friction coefficient and stiffness affect our numerical predictions of D_{sr} , we carried out sensitivity analyses on them using the values of parameters reported in Table 6.4 as a reference case. We begin by considering the effect of friction coefficient. The latter is a key parameter that can significantly affect the fluid bed dynamics in DEM simulations. Cleary et al. (1998) carried out a sensitivity analysis of friction coefficient on solid mixing rate in a ball mill using DEM simulations. They reported that the mixing rate increased as the friction coefficient was reduced. To investigate the influence of friction coefficient on lateral solid mixing, we performed simulations using different values of μ in the range commonly employed in DEM simulations of fluidized beds, keeping the normal spring stiffness K_n at $40977 \text{ N/m}^{3/2}$, the restitution coefficient at 0.9 and the superficial gas velocity at 2.66 m/s (3.5 umf)(an intermediate value in the range investigated experimentally by Grakhovskii (1968)). The snapshots of the bed, obtained using the reference conditions in Table 6.4 at a superficial gas velocity of 2.66 m/s, at different computational times are reported in Figure 6.14. The latter shows the lateral spread of particles past the removable wall partition. This is similar to what we observe in CFD simulations in the previous section. Figure 6.15 shows that D_{sr} reduces as the friction coefficient increases. This is consistent with the findings of Cleary et al. (1998) and had to be expected, because when the friction force increases, sustained interaction among particles increases, inhibiting the motion of the solid and thereby reducing D_{sr} ; nevertheless, the order of magnitude of D_{sr} remains the same.

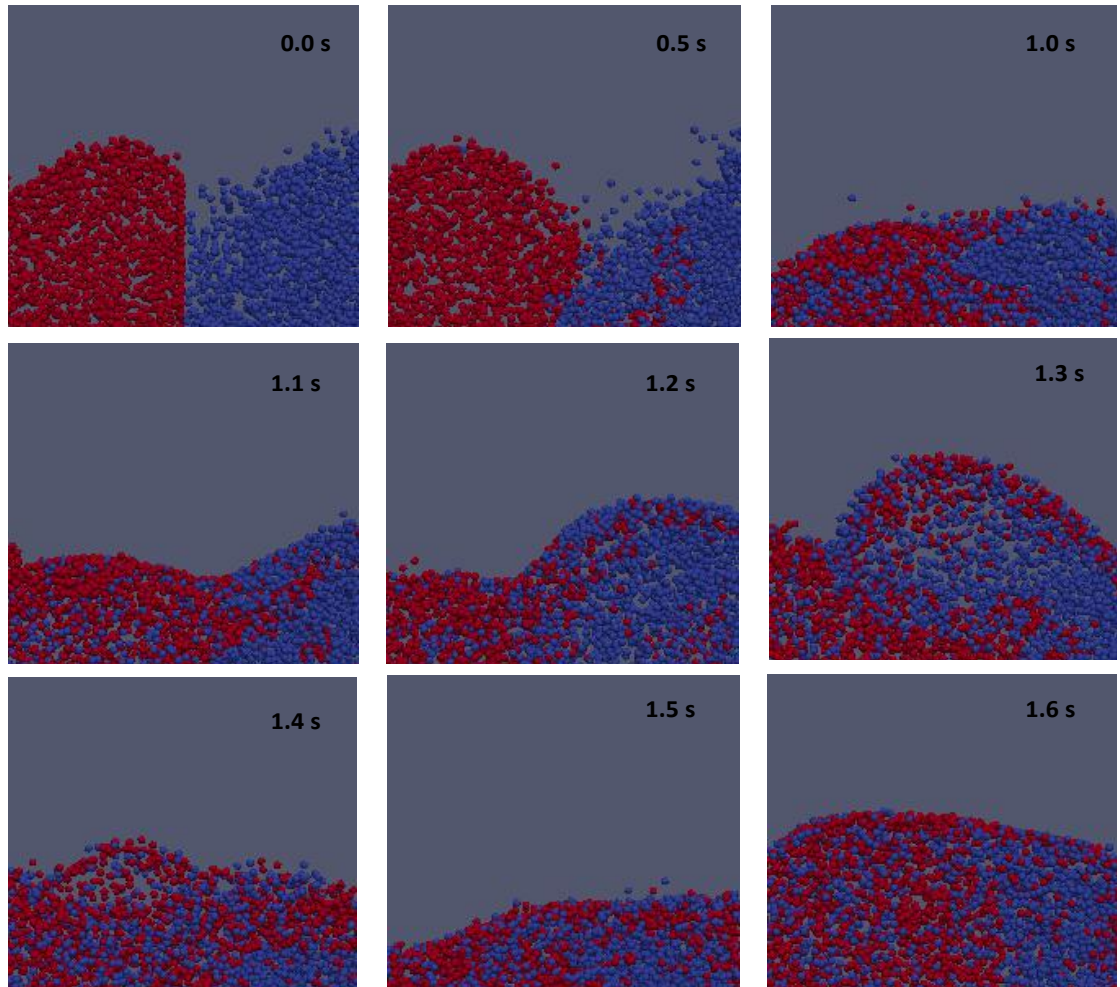


Figure 6.14: Snapshots of the bed at different computational times obtained at a superficial gas velocity of 2.66 m/s.

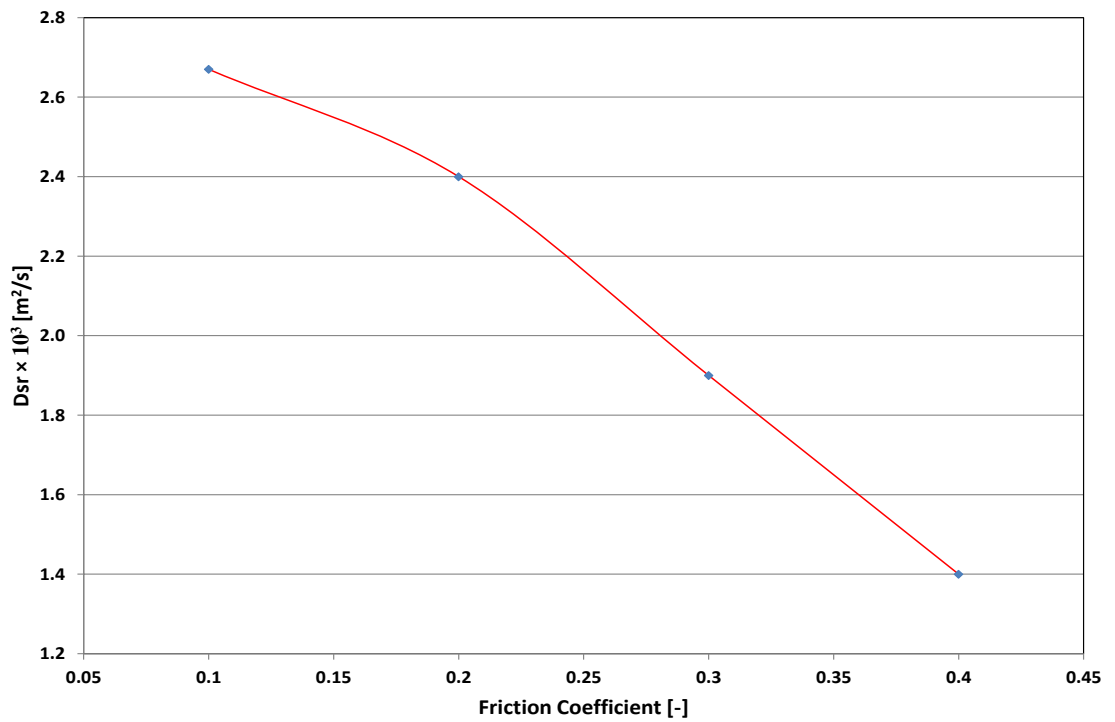


Figure 6.15: Lateral dispersion coefficient vs. friction coefficient.

Generally, the value of the stiffness should as well be carefully chosen, since it affects the integration time-step significantly: the higher the stiffness, the smaller the necessary integration time-step. This is because higher stiffness results in shorter collision times. Stiffness also influences interparticle overlap during collisions; generally, small stiffness leads to large interparticle overlap. Stiffness values must be chosen in such a way as to attain a balance between accuracy and computational efficiency. A large stiffness value, albeit it may yield more accurate results, does reduce the computational efficiency dramatically. On the other hand, when stiffness values are impractically small, the accuracy of the simulations could be compromised. Therefore, it requires careful judgement on the modeller's part to strike a reasonable balance between accuracy and efficiency. To investigate the effect of stiffness on the lateral dispersion coefficient, we conducted a sensitivity analysis on it, using the parameters reported in Table 6.4 as a reference case. We ran simulations at different stiffness values, keeping the coefficient of restitution at 0.90, the friction coefficient at 0.20 and the superficial gas velocity at 2.66 m/s. Figure 6.16 reports how D_{sr} changes with stiffness. We can see that D_{sr} decreases slowly initially, and then more rapidly, as stiffness increases. However, the order of magnitude of D_{sr} remains unchanged.

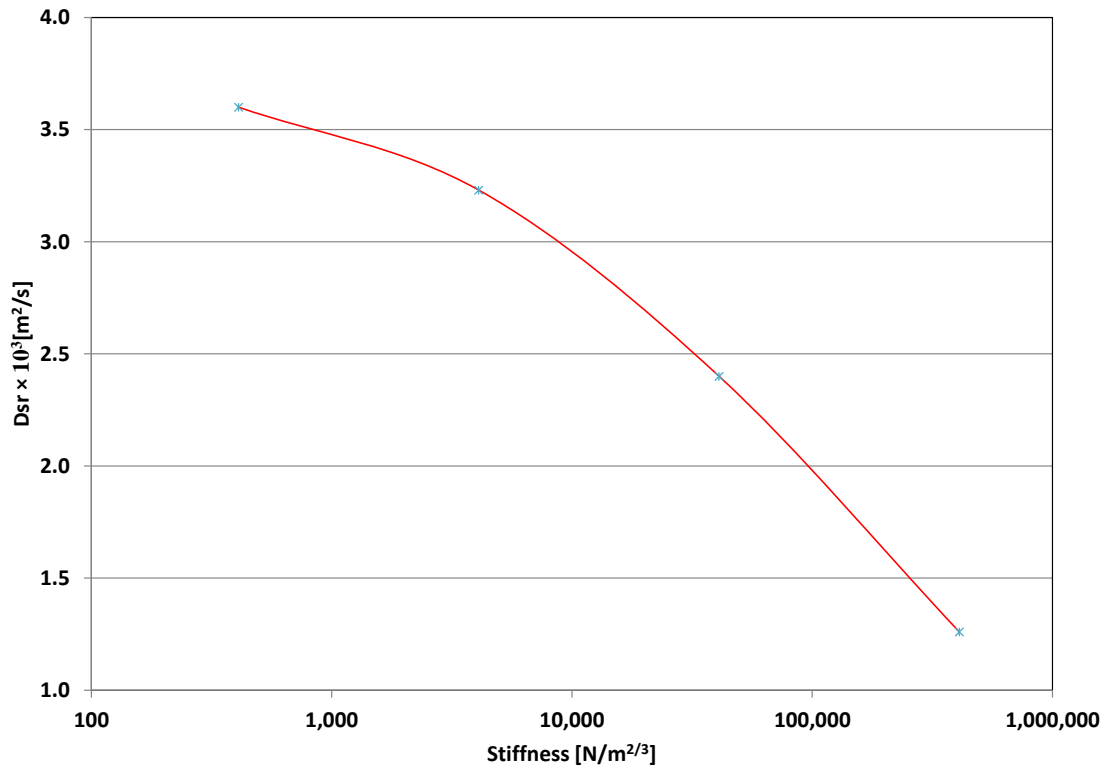


Figure 6.16: Lateral dispersion coefficients at different stiffness values.

We investigated how the bed thickness (i.e. the bed depth in the z -direction) influences the D_{sr} values, because we could not simulate directly the experimental system, adopting the real value of bed depth (100 mm), owing to the enormous computational resources required. Hence, we decided to investigate how the choice of bed depth value affects the numerical prediction of D_{sr} . In the literature, the effect of the bed thickness has mainly been studied with respect to the minimum fluidization velocity. It was observed that the latter increases as the bed thickness decreases (Kathuria & Saxena, 1987; Saxena & Vadivel, 1988; Caicedo et al., 2002; Sanchez-Delgado et al., 2011). This is because, as the bed depth reduces, the effect of wall friction becomes more pronounced, limiting the movement of the particles. For this same reason, we believed that the bed thickness would affect our numerical results. Indeed, studies have shown that bed thickness does affect bubble size, shape, velocity and expansion (Geldart, 1970; Geldart & Cranfield, 1972; Rowe & Everett, 1972; Cranfield & Geldart, 1974; Glicksman & McAndrews, 1985); these are important parameters that strongly influence solid mixing in fluid beds. To investigate the effect of bed thickness, we ran simulations at different superficial fluid

velocities, using geometries of depths $10 dp$ and $20 dp$, where dp is the particle diameter, and (in a third case) periodic walls (imposing periodic boundary conditions at the front and back walls of the vessel). The values of the simulation parameters were those shown in Table 6.4. Figure 6.17 reports how D_{sr} changes with the superficial gas velocity for the various bed depths examined. We note that D_{sr} reduces as the depth of the bed is decreased, as expected. The simulations run with periodic boundary condition give higher values of D_{sr} than those with rigid walls, because the walls do not constrain the bed dynamics. Since the depth of the bed considerably affects solid dispersion, in the simulations one should employ the correct dimension (the same as that of the real system investigated experimentally). If doing so is not feasible (for instance because the number of particles to be tracked would be too large), then one has to keep in mind that simulating a narrower bed may affect the simulation results, leading to lower dispersion coefficient values, as seen in Figure 6.17.

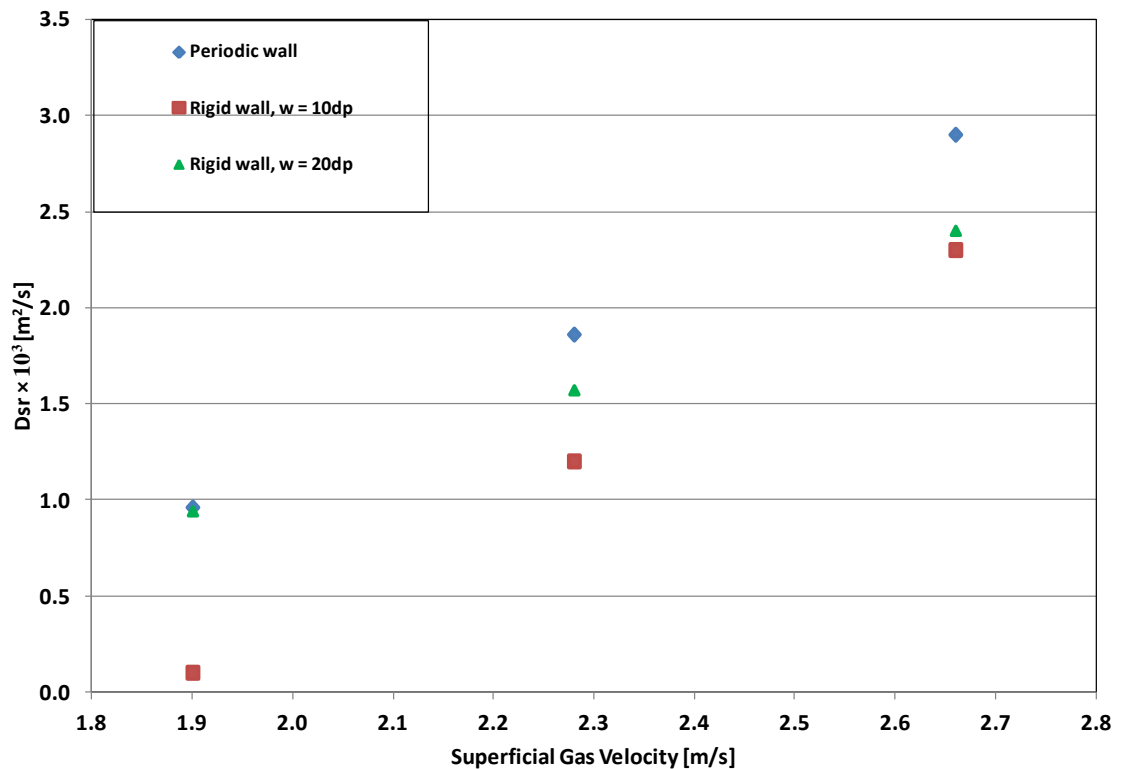


Figure 6.17: Dispersion coefficient values for different superficial gas velocities and bed depths. The minimum fluidization bed height is 6 cm, while the bed width is 0.20 m. ‘dp’ is the particle diameter.

The results presented in these paragraphs reveal that DEM simulations are able to estimate the rate of lateral solid mixing in fluidized beds, but the accuracy of this modelling approach, as we

have seen, depends largely on the values chosen for the simulation parameters. So, even if we are not faced with the problem of constitutively expressing the frictional solid stress, as we are in the Eulerian-Eulerian simulations, we are still faced with the challenge of assigning appropriate values to the simulation parameters. To overcome this issue, one needs to estimate the parameters experimentally, but doing so is extremely time-consuming, and, as pointed out in Section 6.3.2, employing the empirical values in the simulations would require enormous computational resources; this, in particular, is true for the spring constants. In the next section, we compare the DEM simulation results with the experimental ones and those obtained from the Eulerian-Eulerian simulations.

6.4 DEM vs. CFD simulations

We ran simulations in CFD using the same powder, geometry and operational conditions employed in the DEM simulations. Table 6.5 reports the simulation parameters and the powder properties used in the CFD simulations. In the DEM ones, we considered two stiffness values: $40,977 \text{ N/m}^{3/2}$ and $409,772 \text{ N/m}^{3/2}$. For each, we ran simulations at various superficial gas velocities, keeping the other parameters constant (the values are those reported in Table 6.4). Figure 6.18 reports how D_{sr} changes with superficial gas velocity. We observe that D_{sr} increases with superficial gas velocity; this is expected because an increase in the latter induces more bubbling, which makes the rate of lateral solid mixing rise. The D_{sr} values calculated at $40,977 \text{ N/m}^{3/2}$ are larger than those calculated at $409,772 \text{ N/m}^{3/2}$. This is true for all the superficial gas velocities considered and agrees with what Figure 6.16 reports.

In the CFD simulations we considered Cases 1 and 5 reported in Table 6.2. The void-free mass fraction profile for Case 1 obtained at a superficial gas velocity of 1.9 m/s is reported in Figure 6.13. In Figure 6.18, it is interesting to note that the D_{sr} values obtained in Case 5 are lower than those obtained in Case 1. The trend is the same as that observed in Section 6.2. The figure also shows that the CFD simulations predict the D_{sr} values better than the DEM simulations, although the empirical data are still slightly overestimated. The predictions of the DEM

simulations are fairly accurate, the order of magnitude of the results matching that of the empirical data. This reveals that DEM simulations are equally capable of estimating D_{sr} accurately, provided one assigns appropriate values to the collision parameters.

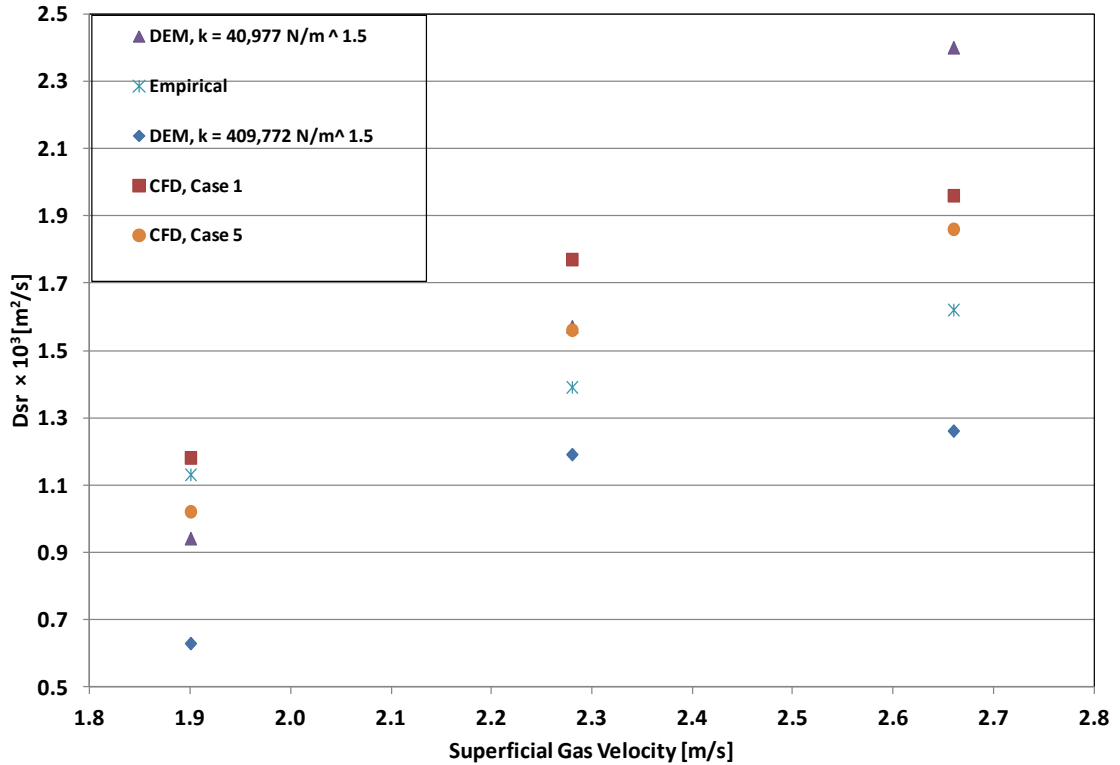


Figure 6.18: Dispersion coefficient values for different superficial gas velocities for DEM and CFD simulations. The minimum fluidization bed height is 6 cm, the bed width is 0.20 m and the bed depth is 6 cm.

Table 6.5: Simulation parameters for Powder 2

Conditions of particle	
Diameter	3 mm
Density	1000 kg/m ³
Minimum fluidization velocity	0.76 m/s
Conditions of gas	
Density	1.2 kg/ m ³
Viscosity	1.7 × 10 ⁻⁵ Ns / m ³
Simulation conditions	
Bed height	60 mm
Bed width	200 mm
Bed depth	60 mm
Superficial gas velocity	1.9 – 2.66 m/s

6.5 Conclusions

We investigated lateral solid mixing in gas-fluidized beds using the Eulerian-Eulerian (CFD) and the Eulerian-Lagrangian (DEM) modelling approaches. The former approach describes both the solid and fluid phases as interpenetrating continua, while the latter tracks the motion of each particle and solves the average equations of motion only for the continuous phase. We examined the influence of simulation dimensionality on our CFD results. To do this, we ran simulations in 3D at different superficial gas velocities. Our results showed that as the latter increases as D_{sr} increases. We compared our 3D simulation results with those previously obtained in 2D. We observed that 3D simulations predict D_{sr} better. Subsequently, we ran 3D DEM simulations, adopting the same methodology used in CFD to estimate D_{sr} . The results obtained agreed reasonably well with empirical results. DEM simulation results revealed that the accuracy of numerical predictions depends on the choice of collision parameters; in particular, the restitution coefficient, the friction coefficients and the stiffness. Both DEM and CFD modelling approaches provided a reasonably good prediction for D_{sr} . Nevertheless, CFD simulations yield slightly better results than DEM simulations.

Chapter 7

Conclusions and future work

Fluidization is a winning technology employed in various industrial processes such as drying, coating, granulation, food freezing, oil cracking and oil reforming, to cite just a few. Designing a fluidized bed is very challenging because of the complex interrelationships among the particles and between the solid and fluid phases. For many years, and partly today, process engineers have always relied on pilot plant and scale-up relationships to design fluidized beds. This approach is by no means efficient; a satisfactory performance of the bed on a pilot plant scale does not guarantee an efficient performance on a commercial scale. This makes the scale-up method risky and uncertain. Computational fluid dynamics offers an attractive alternative that can significantly contribute to designing fluidized beds more efficiently. CFD can directly simulate commercial size beds and permits to investigate the influence of design and process conditions on its performance. We must however emphasize that the accuracy of CFD simulation results depends on the accuracy of models employed. To develop accurate models, it is important that we understand the complex fluid dynamic behaviour of fluidized beds.

The behaviour of gas-fluidized beds depends, among other things, on the superficial gas velocity. The latter determines the fluid dynamic regime in which the bed operates. Typically, when the superficial gas velocity exceeds the minimum fluidization velocity, pockets of gas,

referred to as bubbles, are seen rising through the bed and the bed behaves like a boiling liquid. This fluid dynamic regime is known as the bubbling regime. As the superficial gas velocity increases, the bed may operate in other regimes including turbulent, fast fluidization and pneumatic transport. However, for powders belonging to Group A of Geldart (1973) classification, there exists an interval of stable expansion before they transit to the bubbling regime. Thus, for this class of powder, when the superficial gas velocity exceeds the minimum fluidization velocity, the suspension does not bubble; rather, it expands homogeneously over a certain range of superficial gas velocity.

The origin of stability of Group A powder has been a subject of controversy among researchers. Some researchers argued that the stability of Group A powder is solely due to the fluid dynamic forces in the bed, some maintained that it is due to the existence of interparticle forces, while others attribute the stability to the existence of both fluid dynamic and interparticle forces in the bed. In Chapter 2, we reviewed this lingering controversy on the origin of stability of this class of powders, drawing from both theoretical and experimental evidence. We reported on the experimental discovery by Valverde (1998) which harmonized the differing ideas on the stability of gas-fluidized beds, revealing that the homogeneous regime of gas-fluidized beds consists of two distinct regimes of solid-like and fluid-like behaviours. The solid-like regime is characterized by the existence of enduring contacts among particles, which are manifestations of interparticle contact forces. In the fluid-like regime, however, enduring particle-particle contacts are absent and the particles are freely suspended in the fluid.

In Chapter 3, we investigated the homogeneous regime more closely, using theoretical and experimental methods. We modelled the stable interval of expansion, accounting for enduring particle contacts and wall effects. One of the crucial input parameters to the model is the yield locus of the powders. This features five independent parameters which must be determined experimentally. The experimental results provided the compressive strength values at different solid volume fractions at the bottom of the bed, which were then fitted to the yield locus

expression of Johnson et al. (1990). This allowed us to determine the five independent parameters in the yield locus expression which were used as inputs into the model. We solved the model numerically to obtain the expansion profiles in the bed at different fluidization velocities in the interval of stable bed expansion, back-calculating from them the values of expansion parameter n appearing in the model. For all the cases considered, we observed that the values of n are higher than those obtained by purely fluid dynamic correlations, such as those advanced by Richardson & Zaki and Rowe (1987). This effect was more pronounced in beds of smaller diameter. To validate our model, we carried out fluidization and defluidization experiments. This involved measuring the pressure drop and bed height at different superficial gas velocities in the interval of stable bed expansion. Because our fluidizing vessels were made of stainless steel, we used a pulsed x-rays facility at UCL to enable us to see through the bed in order to measure the bed height. We analysed our results by means of the Richardson & Zaki equation, determining the parameters n and u_t appearing in the latter. We obtained a reasonable agreement between numerical and experimental findings. The results revealed that enduring contacts among particles, which are manifestations of cohesiveness, plays a crucial role in the homogeneous expansion of gas-fluidized beds. In a liquid-fluidized bed such particle-particle contacts are absent, and one can confidently use the fluid dynamic correlations commonly found in the literature to analyze their expansion profiles.

The results presented in Chapter 3 revealed that sustained frictional contacts among particles exist even in the homogeneous gas-fluidized state of fine powders. We confirmed this from our theoretical and experimental analyses. The numerical solution of linear momentum balance equation for homogeneous fluidized beds shows that solid volume fraction profiles develop along the bed axis which is a consequence of enduring particle contacts. The back-calculated values of Richardson & Zaki parameters, obtained theoretically and experimentally, also reveal that enduring contacts do play a role in the homogeneous expansion of gas-fluidized beds. The results presented in this work thus support the view that interparticle forces are likely the dominant mechanism responsible for the homogeneous expansion of gas-fluidized beds. This is

contrary to the ideas of some authors, reported in Chapter 2, that fluid dynamic forces play a major role.

In Chapter 4, we examined the phenomenon of solid mixing in the bubbling regime of gas-fluidized beds. We reviewed the importance of solid mixing in the latter, highlighting the mechanisms by which it proceeds. We reported on the processes of axial and lateral solid mixing, emphasizing their importance in the design and efficient operation of large-scale fluid beds. We then discussed various experimental methods employed in the literature for measuring the rate of lateral solid mixing and the empirical correlations available for its estimation.

In Chapter 5, we used the Eulerian-Eulerian modelling approach to investigate the phenomenon of lateral solid mixing in gas-fluidized beds. We quantified the rate of lateral solid mixing by means of a lateral dispersion coefficient D_{sr} . The latter was defined using an equation analogous to the Fick's law of molecular diffusion. We solved the Eulerian-Eulerian models in CFD codes to obtain the void-free solid volume fraction profiles in bed. By matching void-free solid volume fraction profile obtained numerically with those obtained analytically from the Fick's equation, we determined the values of D_{sr} at different operational conditions. The results of our simulations revealed that D_{sr} increases with the superficial gas velocity and bed height, while it initially increases with bed width, but then remains approximately constant. In all the simulation cases, our numerical results overestimated the empirical ones, but the order of magnitude was predicted correctly.

We provided a two-fold explanation for the overestimation: on one side, it reflects the different dimensionality of simulations (2D) as compared with real fluidized beds (3D), which affects the degrees of freedom of particle lateral motion. On the other, it is related to the way frictional solid stress was modelled: we employed the kinetic theory of granular flow model for the frictional solid pressure and the model of Schaeffer (1987) for the frictional solid viscosity. To investigate how sensitive the numerical results are on the constitutive model adopted for the frictional stress, we ran the simulations again using different frictional models and changing the

solid volume fraction at which the bed is assumed to enter the frictional flow regime (ϕ_{min}). We observed that D_{sr} is quite sensitive to the latter. We obtained the best prediction when $\phi_{min} = 0.50$. Nevertheless, numerical results still overestimated the empirical ones. To investigate the effect of simulation dimensionality on our results, we proposed a simple scaling rule, based on the loss of degree of freedom when passing from a 3D to a 2D domain. The overprediction, nevertheless, was not eliminated.

In Chapter 6, we focussed on the problem of overestimation reported in Chapter 5, using both CFD and DEM approaches. In the former, we ran 3D simulations using the same powder, the same operational conditions and the same computational setup as in the previous 2D simulations reported in Chapter 5. We observed that the frictional stress model, and in particular the value of solid volume fraction at which the bed is assumed to enter the frictional regime, plays a role in the numerical simulations of lateral solid mixing. This was also observed in our 2D simulations, but in the 3D case the effect is less pronounced. The 3D simulations predicted D_{sr} more accurately than the 2D simulations, the simulation dimensionality appearing to be the most important factor.

To analyse further the role of frictional stress models, we ran 3D DEM simulations, employing the soft-sphere approach in order to model the particle-particle contact forces. This approach, when compared to its CFD counterpart, offers a relatively simpler alternative for describing the rheology of the solid phase, since we no longer model the solid stress. To run the DEM simulations, we carried out a sensitivity analysis on some collision parameters employed. The simulation results revealed that the accuracy of numerical predictions depends on the values assigned to the collision parameters; in particular, the friction coefficients and the stiffness. Our simulation results showed that D_{sr} decreases with both friction coefficient and stiffness. We compared the numerical results obtained from DEM simulations with those from CFD simulations. We observed that both modelling approaches predicted D_{sr} fairly accurately. Nevertheless, CFD simulations yielded slightly better results.

7.1 Future work

In Chapter 2 we reported the ongoing controversy on the origin of stability of gas-fluidized particles. Some researchers attributed the stability to the existence of interparticle forces in the bed, while some argued that the stability arises from the fluid dynamic forces, and some others maintained that both forces are responsible. To gain deeper insight into this problem, it will be interesting to investigate the fluidization of Geldart A powders using the DEM approach. The latter offers a flexible way to incorporate interparticle forces and to vary their magnitude. Thus, one can run two sets of simulations: the first set will account for interparticle forces and the other will not. This study will allow us to further highlight the role of interparticle forces on the homogeneous fluidization of Geldart A powders.

We reported in Chapter 2 that the granular Bond number is an important parameter that determines the fluidization behaviour of powders. For Geldart B powders $B_n < 1$, hence they bubble as soon as they are fluidized; for Geldart A powders $B_n \cong 1$, so they exhibit smooth expansion over a range of superficial gas velocity as soon as they are fluidized. It is worth investigating whether Geldart B powders can be fluidized homogeneously by increasing their granular Bond number to unity. This can be achieved by imposing interparticle forces on them. If they do fluidize homogeneously, do they fluidize in the solid-like or fluid-like regime?

In Chapter 3, we modelled the stable expansion of gas-fluidized beds and we estimated the expansion parameter n . We observed that the values of the latter are higher than those obtained from purely fluid dynamic correlations, signifying that enduring particle contacts, and indeed interparticle forces, do play a role in the homogeneous expansion. It is necessary to investigate how changes in the magnitude of interparticle forces will affect the value of the expansion parameter n . By imposing varying magnitudes of interparticle forces and back-calculating the latter, one can further gain useful insights into the relationship between parameter n and interparticle forces.

In Chapters 4 to 6, we investigated the process of lateral solid mixing in bubbling gas-fluidized beds, emphasizing its importance in the efficient operation of large-scale fluidized beds, such as fluidized bed combustors. In our analyses, we considered particles similar in physical properties, but differing only in the names assigned to them in the computational codes. This approach, even though enabled us to investigate the influence of operational conditions on lateral solid mixing, presented a simplistic view of fluidized bed combustion processes. In actual combustors, the fuel and inert bed materials differ substantially in size and density. In the future, it would be necessary to account for this difference.

Furthermore, in our simulations we considered a batch process, where the particles are charged into the reactor at once and then fluidized for given length of time. This is the usual method commonly employed by most researchers studying solid mixing process in fluidized beds. Nevertheless, many physical and chemical processes are carried out in fluidized beds with continuous flow of solids. To design and operate these processes, it is crucial to know the residence time distribution of particles in the bed which can be used to characterize the mixing process. The methodology adopted in this work can be employed to incorporate continuous flow of solids into the bed. This, however, will require using a definition of D_{sr} which is different from those used in this work and assigning appropriate boundary and initial conditions.

APPENDIX A

Set-up procedures for the Eulerian-Lagrangian simulations

A.1 Preliminaries

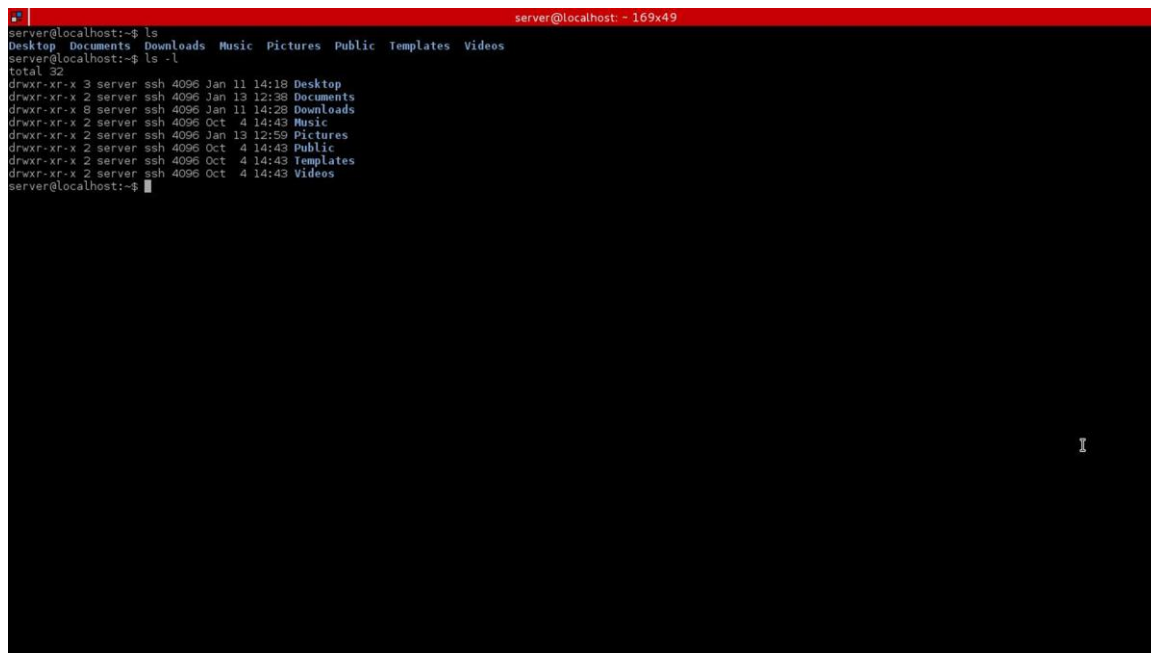
This section provides a basic guide for setting the Eulerian-Lagrangian simulations.

1. Log in to the computer with the following **username** and **password**:

Username: luca

Password: gbzv4321

2. The MultiFlow software runs on linux operating system. When you login, open a terminal. To do this, click on a black square icon at the bottom right corner of the screen. An interface appears as shown in the figure below:

A terminal window screenshot with a red title bar. The title bar contains the text 'server@localhost: - 169x49'. The terminal content shows a user at the 'server@localhost' prompt running 'ls' and 'ls -l'. The output of 'ls' lists directories: Desktop, Documents, Downloads, Music, Pictures, Public, Templates, Videos. The output of 'ls -l' shows a list of files with permissions, owner, group, size, date, and filename. The files listed are Desktop, Documents, Downloads, Music, Pictures, Public, Templates, and Videos, each with permissions 'drwxr-xr-x', owner 'server', group 'ssh', size '4096', and various dates and times. The prompt returns to 'server@localhost:~\$'.

3. Type **eclipse** inside the interface and press enter on the keyboard. This takes the user to eclipse workspace which contains the programme for the MultiFlow simulations.
4. In the eclipse workspace, there are three major project directories: MFTL, MultiDoc and MultiFlow. The latter is the most relevant for setting up and running multiflow simulations.
5. Double click on **MultiFlow**. This brings out a number of sub-directories.
6. Double click on **examples**. Again, this contains many sub-directories. Double click on **Eullag**, and then click on **FluidizedBed**.
7. Then, double click on **Delft-FluidizedBed**; a number of files appear. The most relevant ones are: **run**, **run-mf**, **USERBoundary.c** and **USERinit.c**.

A.2 Setting up simulations

8. Double click on **USERBoundary.c** file. This is where you set the boundary conditions, in particular the inlet superficial gas velocity. You can set this value on the line **110** and **114** of the programme. The **USERBoundary.c** is as shown below, with the line number omitted. Line 110 and 114 are written in bold letters in the programme below.

```

/*****
*
* This file
*
* Is intended to specify the boundary conditions on all the
outer
* boundaries, or inner thin walls, by setting A, B, and C.
*
* The routine will be called for every boundary and for
every variable.
*
* Creation date: 05-09-2003
* Author (C) Berend van Wachem
*
*****/

#include <string.h>

```

```

#include "cfdmesh.h"
#include "constants.h"
#include "petsc.h"
#include "general.h"

int USERBoundary(char *varname, char *typename, char
*boundname, int direction, int Istart, int Jstart, int Kstart,
int Iend,
    int Jend, int Kend, int blocknumber, int Ilen, int Jlen,
int Klen, double *A, double *B, double *C, struct CFDMesh
*Mesh)
{

    int i, j, k;
    int index = 0;
    double *XC, *YC, *ZC;
    int bladdress;
    int ierr;
    Vec *VFRAC;
    double *vfrac;
    int OwnThisBlock = MF_NO;
    int OwnThisPoint = MF_NO;
    int HaveVolumeFraction = MF_NO;
    int lblock;
    int li, lj, lk;
    int Ireal, Jreal, Kreal;

    /*****
    *****/
    /* Find out if current processor owns this block number
    */

    /*****
    *****/
    if ((lblock = FindBlock(Mesh->NMyBlocks, Mesh->CFDBlocks,
blocknumber)) >= 0)
    {
        OwnThisBlock = MF_YES;

        ierr = VecGetArray(Mesh->CFDBlocks[lblock].CC.X,
&XC);CHKERRQ(ierr);
        ierr = VecGetArray(Mesh->CFDBlocks[lblock].CC.Y,
&YC);CHKERRQ(ierr);
        ierr = VecGetArray(Mesh->CFDBlocks[lblock].CC.Z,
&ZC);CHKERRQ(ierr);
    }

    if (FindDataListofLocalVectors(Mesh->BLCC, "VFracL",
&VFRAC))
    {
        HaveVolumeFraction = MF_YES;
    }

    if (HaveVolumeFraction && OwnThisBlock)
    {
        ierr = VecGetArray(VFRAC[lblock], &vfrac);CHKERRQ(ierr);
    }
}

```

```

}

/* Loop over boundary */

for (k = Kstart; k < Kend + 1; k++)
{
  for (j = Jstart; j < Jend + 1; j++)
  {
    for (i = Istart; i < Iend + 1; i++)
    {
      index = (i - Istart) + (j - Jstart) * (Iend - Istart +
1) + (k - Kstart) * (Iend - Istart + 1) * (Jend - Jstart + 1);

      if (OwnThisBlock)
      {
        Ireal = (i - Mesh->CFDBlocks[lblock].IGs + Mesh-
>CFDBlocks[lblock].IDs - 1);
        Jreal = (j - Mesh->CFDBlocks[lblock].JGs + Mesh-
>CFDBlocks[lblock].JDs - 1);
        Kreal = k - Mesh->CFDBlocks[lblock].KGs + Mesh-
>CFDBlocks[lblock].KDs - 1;

        bladdress = (Ireal - Mesh->CFDBlocks[lblock].IGs) +
(Jreal - Mesh->CFDBlocks[lblock].JGs) * Mesh-
>CFDBlocks[lblock].IGe
          + (Kreal - Mesh->CFDBlocks[lblock].KGs) * Mesh-
>CFDBlocks[lblock].IGe * Mesh->CFDBlocks[lblock].JGe;

        if (OwnGlobalPoint(Ireal, Jreal, Kreal, Mesh-
>CFDBlocks[lblock].Is, Mesh->CFDBlocks[lblock].Js,
          Mesh->CFDBlocks[lblock].Ks, Mesh-
>CFDBlocks[lblock].Ie, Mesh->CFDBlocks[lblock].Je, Mesh-
>CFDBlocks[lblock].Ke,
          Mesh->CFDBlocks[lblock].IGs, Mesh-
>CFDBlocks[lblock].JGs, Mesh->CFDBlocks[lblock].KGs, Mesh-
>CFDBlocks[lblock].IGe,
          Mesh->CFDBlocks[lblock].JGe, Mesh-
>CFDBlocks[lblock].KGe, &li, &lj, &lk))
        {
          OwnThisPoint = MF_YES;
        }
        else
        {
          OwnThisPoint = MF_NO;
        }
      }
    }
  }

  if (memcmp(boundname, "INLET", 5) == 0)
  {
    if (memcmp(varname, "Pressure", 5) == 0)
    {
      A[index] = 0.0;
      B[index] = 0.0;
      C[index] = MF_FLOW_EXTRAPOLATE;
    }
    else if (memcmp(varname, "UVelocity", 5) == 0)

```

```

    {
      A[index] = 1.0;
      B[index] = 0.0;
      if (HaveVolumeFraction && OwnThisPoint &&
OwnThisBlock)
      {
        C[index] = 5.02 / vfrac[bladdress];
      }
      else
      {
        C[index] = 5.02;
      }
    }
    else if (memcmp(varname, "VVelocity", 5) == 0)
    {
      A[index] = 1.0;
      B[index] = 0.0;
      C[index] = 0.0;
    }
    else if (memcmp(varname, "WVelocity", 5) == 0)
    {
      A[index] = 1.0;
      B[index] = 0.0;
      C[index] = 0.0;
    }
    else if (memcmp(varname, "TEMPERATURE", 5) == 0)
    {
      A[index] = 1.0;
      B[index] = 0.0;
      C[index] = 100.0;
    }
    else if (memcmp(varname, "VFrac", 4) == 0)
    {
      A[index] = 0.0;
      B[index] = 1.0;
      C[index] = 0.0;
    }
    else
    {
      A[index] = 0.0;
      B[index] = 1.0;
      C[index] = 0.0;
    }
  }
  else if ((memcmp(boundname, "PRESS", 5) == 0) ||
(memcmp(boundname, "OUT", 3) == 0))
  {
    if (memcmp(varname, "Pressure", 5) == 0)
    {
      A[index] = 1.0;
      B[index] = 0.0;
      C[index] = 0.0;
    }
    else if (memcmp(varname, "UVelocity", 5) == 0)
    {

```

```

        A[index] = 0.0;
        B[index] = 1.0;
        C[index] = 0.0;
    }
    else if (memcmp(varname, "VVelocity", 5) == 0)
    {
        A[index] = 0.0;
        B[index] = 1.0;
        C[index] = 0.0;
    }
    else if (memcmp(varname, "WVelocity", 5) == 0)
    {
        A[index] = 0.0;
        B[index] = 1.0;
        C[index] = 0.0;
    }
    else if (memcmp(varname, "VFrac", 4) == 0)
    {
        A[index] = 0.0;
        B[index] = 1.0;
        C[index] = 0.0;
    }
    else
    {
        A[index] = 0.0;
        B[index] = 1.0;
        C[index] = 0.0;
    }
}
else if ((memcmp(boundname, "WALL", 4) == 0) ||
(memcmp(boundname, "SIDEWALL", 8) == 0))
{
    if (memcmp(varname, "Pressure", 5) == 0)
    {
        A[index] = 0.0;
        B[index] = 1.0;
        C[index] = 0.0;
    }
    else if (memcmp(varname, "UVelocity", 5) == 0)
    {
        A[index] = 1.0;
        B[index] = 0.0;
        C[index] = 0.0;
    }
    else if (memcmp(varname, "VVelocity", 5) == 0)
    {
        A[index] = 1.0;
        B[index] = 0.0;
        C[index] = 0.0;
    }
    else if (memcmp(varname, "WVelocity", 5) == 0)
    {
        A[index] = 1.0;
        B[index] = 0.0;
        C[index] = 0.0;
    }
}

```



```

else if (memcmp(varname, "TEMPERATURE", 5) == 0)
{
    A[index] = 1.0;
    B[index] = 0.0;
    C[index] = -100.0;
}
else if (memcmp(varname, "VFrac", 4) == 0)
{
    A[index] = 0.0;
    B[index] = 1.0;
    C[index] = 0.0;
}
else
{
    A[index] = 0.0;
    B[index] = 1.0;
    C[index] = 0.0;
}
}
else
{
    A[index] = 0.0;
    B[index] = 1.0;
    C[index] = 0.0;
}
}
} /* End looping over K */
}
// ierr = VecRestoreArray(Mesh->CFDBlocks[lblock].CC.X,
&X);
// CHKERRQ(ierr);
// ierr = VecRestoreArray(Mesh->CFDBlocks[lblock].CC.Y,
&Y);
// CHKERRQ(ierr);
//
// if (Mesh->ThreeD)
// {
//     ierr = VecRestoreArray(Mesh-
>CFDBlocks[lblock].CC.Z, &Z);
//     CHKERRQ(ierr);
// }

if (HaveVolumeFraction && OwnThisBlock)
{
    ierr = VecRestoreArray(VFRAC[lblock],
&vfrac);CHKERRQ(ierr);
}

if (OwnThisBlock)
{
    ierr = VecRestoreArray(Mesh->CFDBlocks[lblock].CC.X,
&XC);CHKERRQ(ierr);
    ierr = VecRestoreArray(Mesh->CFDBlocks[lblock].CC.Y,
&YC);CHKERRQ(ierr);
}

```

```

    ierr = VecRestoreArray(Mesh->CFDBlocks[lblock].CC.Z,
&ZC);CHKERRQ(ierr);
}

return (0);
}

```

9. Double click on **USERinit.c** file to set the initial conditions for the primary cell.

Usually you do not need to change anything here. The file is shown below:

```

/*****
*****
*   This file
*
*! Is intended to specify all initial conditions for
the primary cell
*! centered variables.
*
*   This routine is called only once, in the beginning
of a non restart run
*
*   Creation date: 18-11-2003
*   Author (C) Berend van Wachem
*
*   File $Id:USERinit.c 6 2007-03-20 20:52:28Z berend $
*   Last modified by: $Author:berend $
*   On: $Date:2007-03-20 21:52:28 +0100 (Tue, 20 Mar
2007) $
*
*****
*****/

#include <string.h>
#include "cfdmesh.h"
#include "constants.h"
#include <stdlib.h>
#include "general.h"
#include "io.h"
#include "petsc.h"
#include "options.h"

int USERInit(char *varname, double *varray, int Istart,
int Jstart, int Kstart, int Iend, int Jend,
int Kend, int blocknum, struct CFDMesh *Mesh, struct
MFOptions *Options)
{
    int ierr;
    int i, j, k, address;
    double *X, *Y, *Z;
    int bladdress;

```

```

double x0 = 1.5e-2;
double y0 = 4.5e-2;
double r0 = 4e-3;

/* Open up Mesh->CFDBlocks[blocknum].X, Y and Z */
ierr = VecGetArray(Mesh->CFDBlocks[blocknum].CC.X,
&X);
CHKERRQ(ierr);
ierr = VecGetArray(Mesh->CFDBlocks[blocknum].CC.Y,
&Y);
CHKERRQ(ierr);

if (Mesh->ThreeD)
{
ierr = VecGetArray(Mesh->CFDBlocks[blocknum].CC.Z,
&Z);
CHKERRQ(ierr);
}

/* Loop over boundary */
for (i = Istart; i < Iend + Istart; i++)
{
for (j = Jstart; j < Jend + Jstart; j++)
{
for (k = Kstart; k < Kend + Kstart; k++)
{
/* Calculate address */
address = (i - Istart) + (j - Jstart) * Iend +
(k - Kstart) * Iend * Jend;

bladdress = (i - Mesh->CFDBlocks[blocknum].IGs)
+ (j - Mesh->CFDBlocks[blocknum].JGs)
* Mesh->CFDBlocks[blocknum].IGe+ (k - Mesh-
>CFDBlocks[blocknum].KGs)
* Mesh->CFDBlocks[blocknum].IGe* Mesh-
>CFDBlocks[blocknum].JGe;

if (memcmp(varname, "Pressure", 5) == 0)
{
varray[address] = (double) 0.0;
}
else if (memcmp(varname, "UVelocity", 5) == 0)
{
varray[address] = (double) 2.0000;
}
else if (memcmp(varname, "VVelocity", 5) == 0)
{
varray[address] = (double) 0.0000;
}
else if (memcmp(varname, "WVelocity", 5) == 0)
{
varray[address] = (double) 0.0;
}
else if (memcmp(varname, "TEMPERATURE", 5) == 0)
{
varray[address] = (double) 1.00;
}
}
}
}
}
}

```

```

    }
    else if (memcmp(varname, "VFrac", 5) == 0)
    {
        if (X[bladdress] <= 0.7)
        {
            varray[address] = 1.0;
        }
        else
        {
            varray[address] = 1.0;
        }
    }
    else if (memcmp(varname, "Density", 5) == 0)
    {
        varray[address] = Options->Phase[0].density;
    }
    }
}
}

ierr = VecRestoreArray(Mesh->CFDBlocks[blocknum].CC.X,
&X);
CHKERRQ(ierr);
ierr = VecRestoreArray(Mesh->CFDBlocks[blocknum].CC.Y,
&Y);
CHKERRQ(ierr);

if (Mesh->ThreeD)
{
    ierr = VecRestoreArray(Mesh-
>CFDBlocks[blocknum].CC.Z, &Z);
    CHKERRQ(ierr);
}

return (0);
}

```

10. Next, double click on the **run file**. It is a script to run the simulations.
11. Double click on the **run.mf** file. This contains really the set-up of the simulations. The file is quite self-explanatory (**Please note that the particle box number in the file below should be kept in the range 1.01 – 1.4**. This number affects the fluid volume fraction in the bed; if you choose a number that is too large, the volume fraction may be unrealistically small). Here we set the conditions for the fluid and the particles. The run.mf file is shown below:

```
#####
MultiFlow Options File
#####
# All options need to be specified,
# or set to "DEFAULT".
# If an option is NOT specified, MultiFlow will ask
# to do so.

# debugging options
# these can only be yes or no

#
# Information about the phases to be solved in the
system
#
PHASE 01
  Fluid
  Eulerian
  Incompressible
  Density 1.280
  Viscosity 1.7e-5
  AutoMesh 70 2 120 0.0 0.0 0.0 3.5e-1 1.0e-3 6.0e-1
  GravityVector -9.81 0.0 0.0
END

PHASE 02
  Solid
  Lagrangian
  TimeStep 1.0e-3
  CollisionModel Tsuji
  AutoTimeStep
  MinCollisionStep 040
  WallYoungsMod 1.0e+6
  WallPoissonRatio 0.33
  WallFriction 0.35
  WallRestCoef 0.9
# ParticleType <NUM> <DIAM> <DENSITY> <YOUNGS>
<POISSON> <FRICT> <REST COEF>
ParticleType 01 4.9e-04 2620.0 1.0e+6 0.33 0.35 0.9
ParticleType 02 4.9e-04 2620.0 1.0e+6 0.33 0.35 0.9
ParticleType 03 0.02 0500 1.0e+7 0.35 0.1 0.06
ParticleType 04 0.03 1000 1.0e+7 0.35 0.1 0.06
# InitBlockParticles 01 0.0 0.0 0.0 90.0e-3 8e-03
115.0e-03 1.8e-4
InitBlockParticles 01 0.0 0.0 0.0 -5.0e-2 1.0e-03 2.99e-
1 1.0e-4
InitBlockParticles 02 0.0 0.0 3.01e-1 5.0e-2 1.0e-03 -
6.0e-1 1.0e-4
# InjectParticles <PNUM> <Point> <Velocity> <StartTime>
<EndTime> <interval> <randomness>
ParticleBox 1.2
# PSDFileName <PNUM> <FILENAME>
# PSDFileName 01 examples/Eullag/FluidizedBed/Delft-
FluidizedBed/psd
# ParticleOutlet OUTLET
  GravityVector -9.81 0.0 0.0
```

```
END
#
# Executing, timesteps, filenames
#
EXECUTE
#Restart NO
Restart YES
  ResDirectory wallresults1
  ResTime Last
  TimeSteps 10 1.0e-3
  OutputFrequency 10
  OutputFileName results.mfo
END

#
# Convergence criteria
#
CONVERGENCE
  Mass 1.0e-6
  Maxiter 500
END

NUMERICS
  AdvScheme UPWIND
END
```

12. Then you can compile the simulation set-up. To do this, click on the **project** icon at the top of the screen. A number of options appear from which you have to click on **build project**. For every modification you make in the simulation set-up, remember to re-compile the simulation before going to step 13.

13. To run the simulation, open another terminal (black square icon at the bottom right corner of the screen). Then type the following command

```
cd src/eclipseworkspace/MultiFlow/
```

then press enter. This takes you to the MultiFlow directory.

14. The next step is to run the simulations. To do this, type the following command in the terminal:

```
examples/EulLag/FluidizedBed/Delft-FluidizedBed/run
```

now you are running the script called 'run' in the Delft-FluidizedBed directory.

A.3 Visualization and post-processing

15. The results of the simulations are created in a directory (assume this directory is called results). You will go to the paraview directory and translate the results from the native MultiFlow format to a format that can be read in paraview (paraview is a software for post processing and visualization of simulation results). To do this, type the following commands in the terminal

```
cd paraview
```

this takes you to the paraview directory.

16. To translate the results, use the following command

```
mftovtk -d ../results; ptovtk -d ../results; collection -d ../results
```

then press enter.

17. To go to the paraview software for visualization, type **paraview** in the terminal and press enter.

The following additional steps are needed if you run a simulation with partition and you intend to remove the partition.

18. The programme that adds and removes partition to the geometry is the **createparticlebox.c** file which you can find in the MultiFlow directory. The programme line 1573 adds or removes a partition from the geometry. If the line is deactivated, by adding double backslash (//) before the text on this line, the partition is removed, otherwise the partition is present in the geometry. If you intend to run simulations with a partition, you need to define two types of particles, one on each side of the partition, in the **run.mf** file in step 10 above; you will also need to specify the location of the partition in the geometry. This is also done in the **createparticlebox.c file**. For instance, if you intend to insert a partition at the middle of a geometry having a width of 0.6, in the **createparticlebox.c** file you will set the **zwallv = 0.3**. Remember also to specify the values of other spatial coordinates; these should be the same as the depth and height of your geometry. Another important parameter that needs to be specified in the **createparticlebox.c**

file is the **xdims** and **ydims** values. The latter is approximately the number of particles that fit in the y direction divided by the particle box number (step 11 above), while the **xdims** is approximately the number of particles that fit in the x direction divided by the particle box number.

19. To remove the partition when the simulation is completed, you need to move the simulation results to a new directory, for example let us assume that the name of the new directory is **wallresults**. To do this, type the following commands inside the terminal (you may not need to open another terminal for this, you can type the command inside the same terminal where you ran the simulations):

mv results wallresults

20. Then remove the partition by following the steps in 18.
21. After this, in the **run.mf** file remove the ash symbol (#) before the **RESTART YES**, and put it before the **RESTART NO** option. Recompile the simulations (step 12) and start running the simulations (following the steps from 13).

APPENDIX B

Creating geometries in ANSYS Workbench

B.1 Procedures

The following is a step-by-step guide on how to create geometries in ANSYS workbench.

1. Open Workbench.
2. Create a new project by double clicking on mesh icon at the left hand side of the screen.
A box comes up in the project schematic containing three icons – 1.mesh 2. Geometry
3. Mesh.
3. Double click on the geometry option. This takes you to the design modeller which enables you to create the geometry.
4. In the design modeller, select the unit of distance you would like to work with, usually the S.I. unit is preferred – meters.
5. In the tree outline, select the XY plane.
6. Click on the sketch icon at the top of the page – a blue icon with a star on top. This brings out the option of sketch 1 in the tree outline.
7. Then click on sketching at the bottom of the tree outline. This brings out the sketching toolbox.

8. Select rectangle and draw, from the origin, the rectangle of your choice in the XY plane. You can adjust the dimensions of the rectangle by clicking on dimension below the sketching toolbox. Then click on the side whose dimension you wish to modify. Then in the detailed view write the dimension of your choice. When you are happy with the sketch, click on generate at the top of the screen.
9. If you intend to have geometry separated by a partition, repeat steps 6 – 8. You will then have two sketches in the tree outline – Sketch 1 and Sketch 2.
10. Select the Sketch 1 in the tree outline. Then, on top of the page, click on concept, then surfaces from sketches. On the details view (below the page) click on operations and select add frozen. Still on the details view, set the value of thickness to 0.0001m.
11. Repeat Step 10 for Sketch 2.
12. In the tree outline, click on 2 parts 2 bodies. When you do this, you have two surface bodies appearing below the 2 parts 2 bodies. Click on the first surface body, then in the details view select fluid option. Repeat this for the other surface body.
13. Save the project by clicking on the save icon at the top left of the screen.
14. Go back to the workbench page (the original page that came up when you opened the Workbench). Double click on mesh (3). The geometry you have created comes up in a separate window.
15. Right click on mesh (at the left side of the screen), and then click on insert and the mapped face meshing, select the geometry (the sketch you have created) and then click on apply in the box below.
16. Mapped face meshing option appears on the left hand side of the screen. Right click on mapped face meshing and then insert and then sizing. A box appears at the bottom left of the screen. Using the mouse, click on the face of the sketch you intend to ‘mesh’. Then click on apply (in the geometry option) inside the box. In the latter, the type of the mesh should be element size, then in the element size (below the ‘type’ option) specify the dimension of your element (grid size). THEN click on update at the top of the

screen. This generates the mesh for the face you selected. If you have more than one face, repeat step 16.

17. The next step is to name the edges. To do this, click on the second box at the top of the screen, have an edge highlighted in green. Then, select each edge by right clicking. Then, you have an option –create named selection. Click on the latter and name the edge as you wish. Do this for all the edges, except the partition (If you are dealing with geometry having partition).
18. You also need to name the faces. To do this, click on the third box at the top of the screen, having a face highlighted in green, then select the face and right click. Click on create named selection and name the face as you wish. If you have two faces, do this for the other face.
19. Export the file as .msh file. To do this click on file, and export as .msh file.

B.2 Loading the mesh in Fluent

20. Load the mesh you have created in workbench into Fluent. Go to cell zone condition, change the solid type to fluid. Below the mesh you loaded in Fluent, there is a typing interface. Type mesh, then press enter on the keyboard.
21. Then type modify-zones, and press enter again.
22. Type fuse-face-zones and press enter again. This procedure is necessary for the following reasons: We created two rectangles in workbench and we joined them together. Essentially we have two edges at the middle of the rectangles which must be fused together to make one partition; hence the reason for this step.
23. Type the ID number of surface_body_face1. To know the ID go to boundary conditions, then click on surface_body_face1. The ID comes out. Do this also for surface_body_face1 (if applicable). Press enter three times. Once this has been done, a fuse zone is created named interior-4 in the list of the boundary conditions. This interior-4 has to be changed to wall boundary condition. You can do this by selecting

the interior-4, and changing the boundary condition to a wall in the box below the list of boundary conditions. A message comes up asking you to confirm if you wish to change the interior-4 to wall. Click on Yes. Then an interface comes up where you can select the condition of the wall you wish. Usually, we use a stationary wall with a no-slip boundary condition. Click Ok. This completes the task.

B.3 Creating a 3D geometry

24. Follow steps 1-9 above.
25. Then extrude the geometry. To do this, select the sketches you have created (by clicking on it in the tree outline) and click on the extrude icon at the top of the page. Down the page, you will see the detailed view box. Click on add material and select add frozen option. You can specify the depth of the extrusion in the detailed view box by changing the FDI depth value to the value of your choice. Then click on generate. Do this for all the sketches in the tree outline if you have more than one sketch.
26. Click on 2parts 2bodies (depending on the number of bodies you joined together). Click on solid. In the detailed view box below, change the option to fluid. Do this for the two solids (if applicable). Then click save.
27. Go back to the workbench click on mesh (step 14 above). A graphical interface comes up which brings out the geometry you have created.
28. In the outline at the left side of the screen, right click on mesh and select the option generate mesh.
29. You can modify the mesh by clicking on sizing in the box below and adjusting the element size to the value of your choice and click on update.
30. The next step is to name the faces of the geometry. To do this click on the third box at the top, having a face highlighted in green. Then select each of the faces by clicking on them, then right click and create a named selection and name them accordingly. Do this for all the faces, except for the partition.

31. Then you need to name the bodies (If you have joined two or more bodies together). To do this, click on fourth box on top of the page – having all the faces green. Then select the body by clicking on it, right click and create a named selection. This enables you to assign names to the body or bodies.
32. Save and export the mesh as .msh file.

In Fluent

33. Load the geometry in Fluent. Again, we need to fuse the partition together.
34. To do this, follow steps 20 – 23. The only difference here is that instead of fusing surface_body_face1 and surface_body_face2, we fuse instead wall_zone1_body and wall_zone2_body. This completes the task.

APPENDIX C

Setting up simulations in ANSYS FLUENT

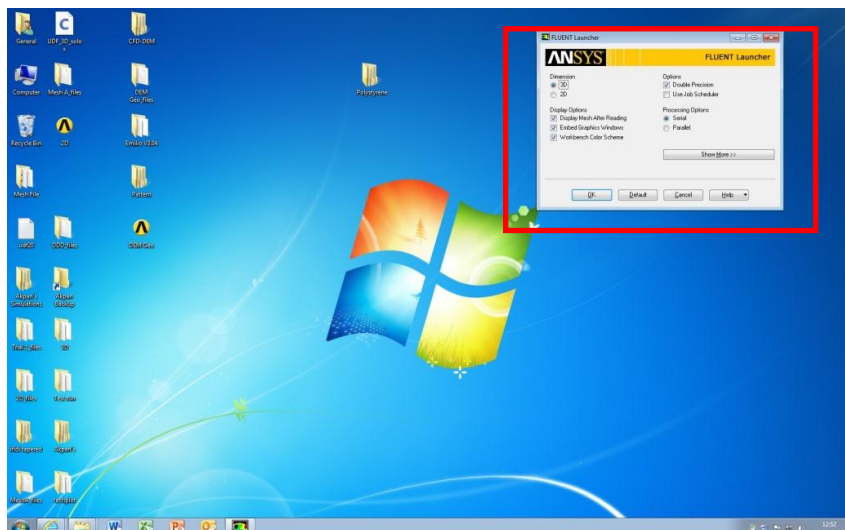
C.1 Introduction

This section provides a guide on how to set up Eulerian-Eulerian simulations in ANSYS FLUENT 12.1. The procedures given in this section are based on the simulation cases considered in our research, but users can easily adapt the procedures to suit their purpose.

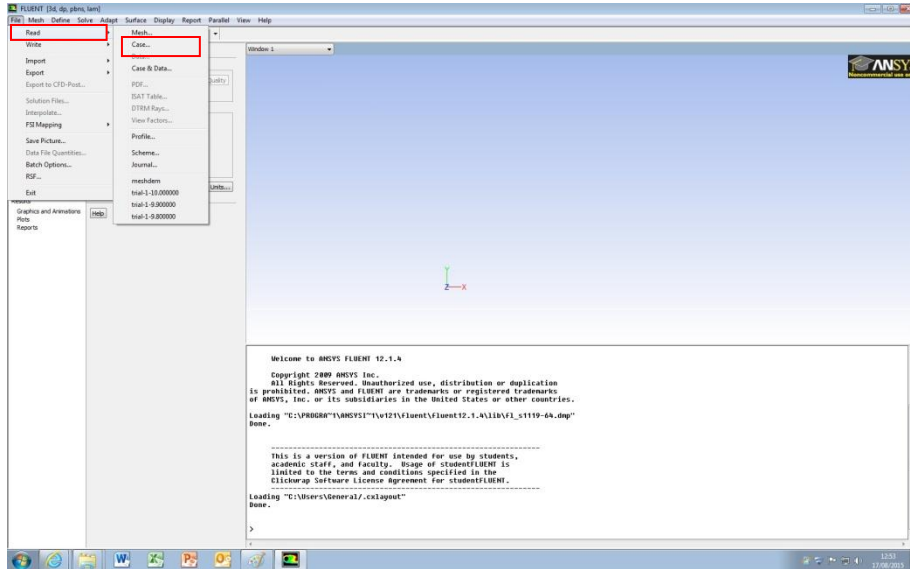
C.2 Procedures

The following gives the outline of how to set-up the simulations

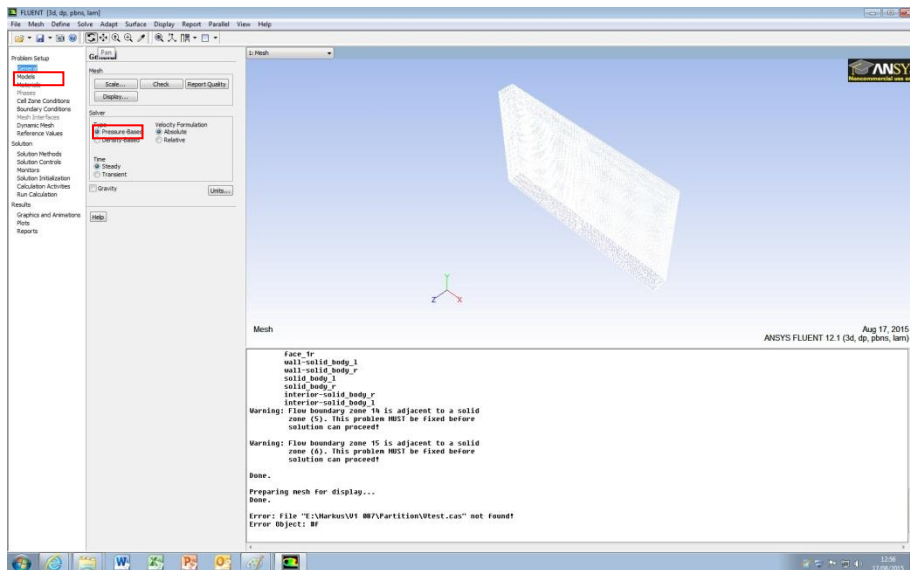
1. Open Fluent. An interface, inside the red box in the screenshot below, comes up. Here you can select the dimension of the simulations you intend to run. Select **double precision**, and **serial**. Then click **Ok**.



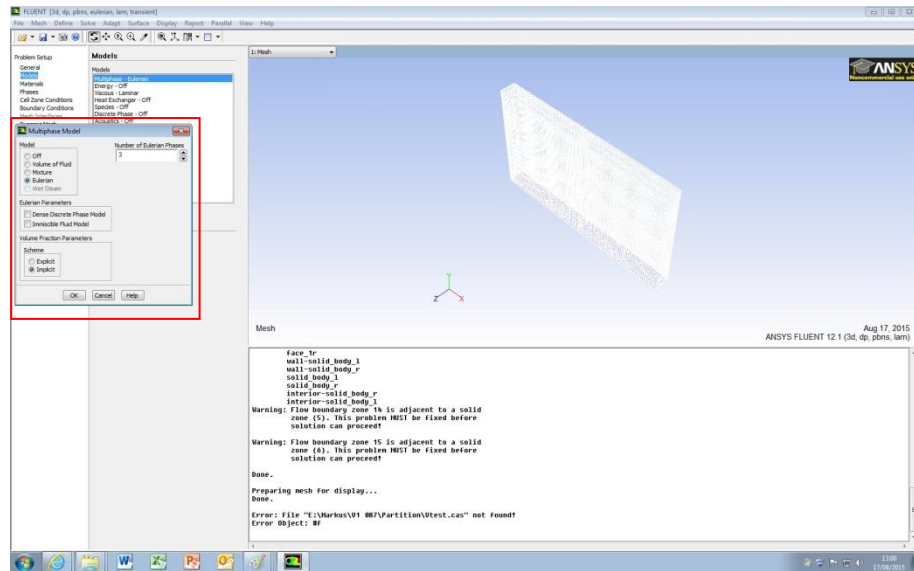
- Next, load the mesh. To do this, click on **file** at the top of the page. Select **read**, then select **case**. Navigate to the folder where you have saved your mesh and UDFs. Select the mesh and click Ok. Refer to the screenshot below.



- Click on **General** at the left side of the screen. The under solver select pressure-based, absolute, transient/steady (this depend on the type of simulations you intend to run, but generally we choose transient).

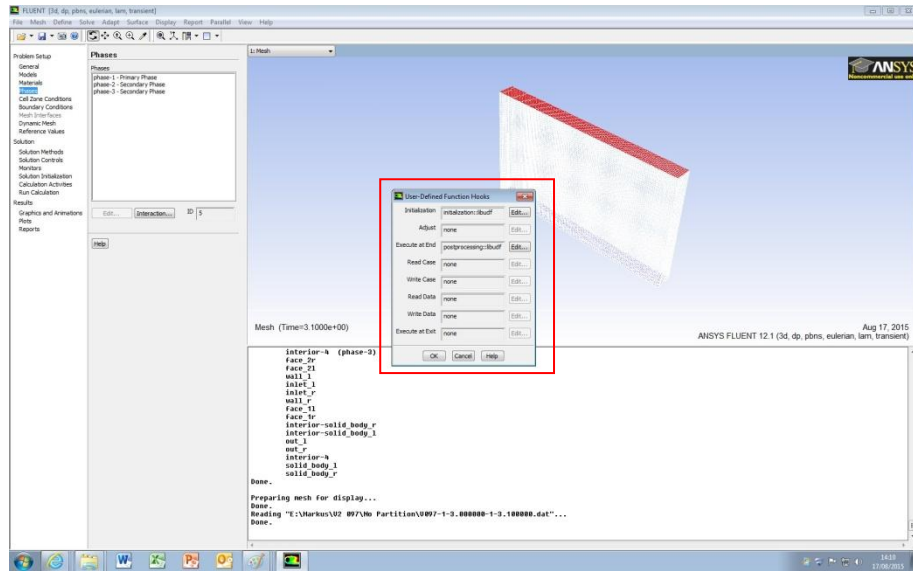


- Next, select **model** at the left side of the screen. Then click on multiphase, select Eulerian. Next, specify the number of phases. The screenshot for this step is shown below. In our simulations we used 3 Eulerian phases because we have two solid phases and one fluid phase.

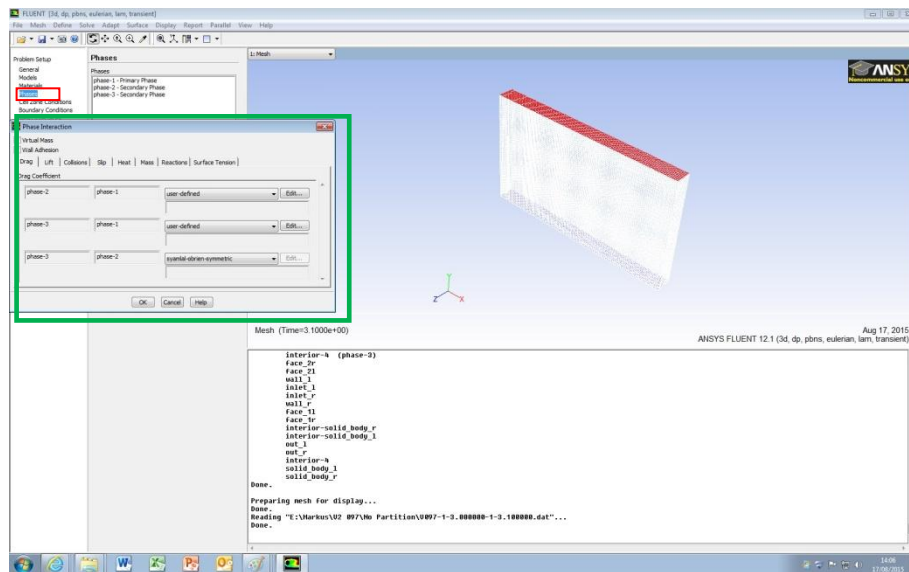


- Click on **material** under the problem setup. Then click on **fluid** (Usually, this is the default. You can either leave it or modify the fluid properties to suit your purpose). Once you are happy with the fluid properties, write the name of the first solid phase, for example you can name it solid-1. Then input its density and viscosity. For the latter, choose a very small value; we suggest 10^{-6} . Then click on **change/create**. A message pops up asking you if you want to overwrite air, click **No**. If you have more than one solid phase, repeat the same thing you did for solid-1.
- The next step is to load the UDF. To do this, click on **Define** (at the top of the page), then **user-defined**, then click **function**, then click **compiled**. A box comes up as shown below. Click **add**, then navigate to the UDF folder. Click on **build**, then **Ok**. Then click on load. This loads the UDF.

7. Next, click on **Define**, then **user-defined**, then **function hook**. A box comes up as shown in the screenshot below. In the box, click **edit** for the **initialization**, another box pops up, select initialization and click Ok. Do the same for the **post-processing**.



8. Next, we need to specify the number of memories. To do this, click on **Define**, then **user-defined**, then click **memory**. You can now specify the number of memories you want. This will depend on your UDF.
9. Next, click on **phases** under problem set-up group. If you have three phases, like we had, you have one primary phase and two secondary phases, as shown in the screenshot below. Select the first secondary phase, then click edit.

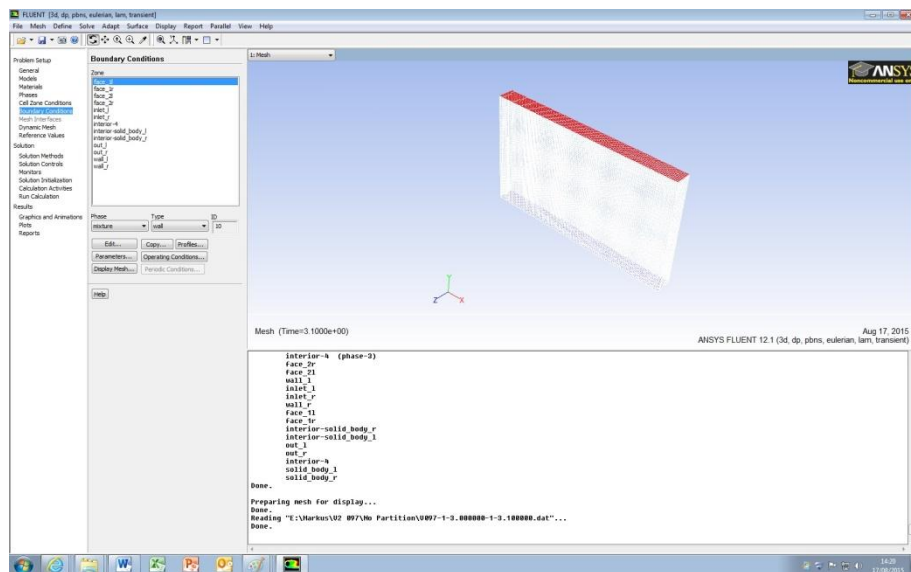


A box comes up. Select **phase material**, select **granular** under granular temperature model. Select **phase property**. Then input the diameter of the particle. For the following options, we suggest you make your selections as shown below, but you can modify them to suit your purpose.

Granular viscosity	Gidaspow
Granular bulk viscosity	Lun et al.
Frictional viscosity	KTGF
Angle of internal friction	Default
Frictional pressure	KTGF
Frictional modulus	Derived
Frictional packing limit	Default
Granular temperature	Algebraic
Solid pressure	Lun et al.
Radial distribution	Lun et al.
Elasticity modulus	Derived
Packing limit	Default

Next, click on **interaction**. A box, with green boundary in the screenshot above, comes up. Here, you select the drag coefficient of your choice; in our case, we used the user-defined drag. To select the drag coefficient, you have to click on **edit**.

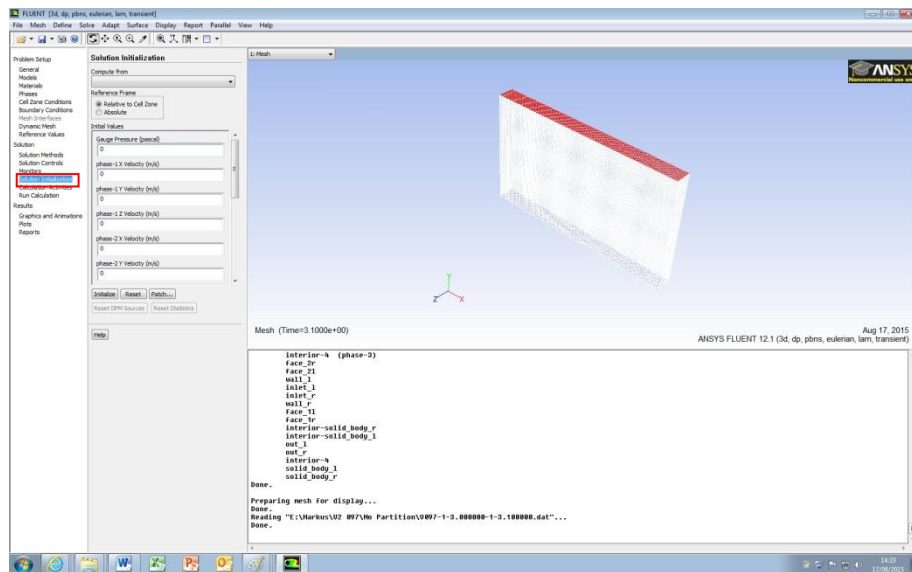
- Next, click on boundary conditions in the problem setup group. A box comes up as shown in the screenshot below. Select each zone and choose the appropriate boundary condition from the **type**. For faces that are walls, select wall; for outlet, select pressure outlet; for inlet, select velocity inlet. For the velocity inlet, here you need to specify the magnitude of the superficial gas velocity. To do this, you select phase-1 by clicking on phase, select phase-1 in the drop-down menu and click edit.



- Click on solution methods. We suggest that you make the following selections; of course you can make selections to suit your purpose.

Scheme	multiphase couples
Gradient	Green-Gauss cell based
Momentum	Second order upwind
Volume fraction	Quick

- Click on **solution initialization** in the problem setup group. Then click **initialize** again.



13. In the problem setup group, click on **calculation activities**. Then select how you would like the solutions to be saved (we suggest saving every 100 time steps). Next, click edit, an autosave box comes up, select everytime. Click Ok.
14. Next, click on display at the top of the page. Then click on residuals. A box comes up where you can modify the absolute criteria; we suggest you change the absolute criteria to 10^{-5} .
15. Next, click on **run calculations** in the problem setup group. Here you input the time step (we suggest a value of 0.001 s), the number of time steps (this depends on how long you want your simulations to run), maximum iteration/time step (we suggest 250), reporting interval (use the default value of 1), profile update interval (we suggest the default value of 1). If you are satisfied with the simulation setup, then click on **calculate** to start your simulations.

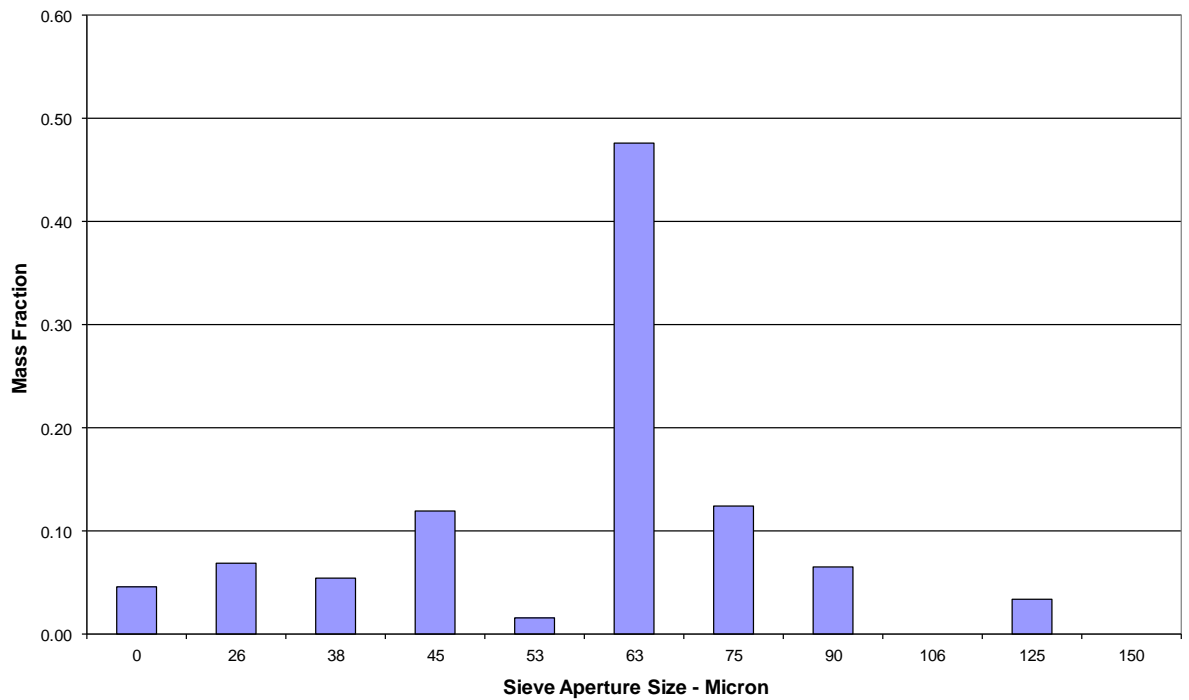
You may want to display your setup before starting the simulations or during the simulations. To do this, click on **display** at the top of the page. Then graphics and animations, then click contours. Then you can display the contours of any parameter you like.

APPENDIX D

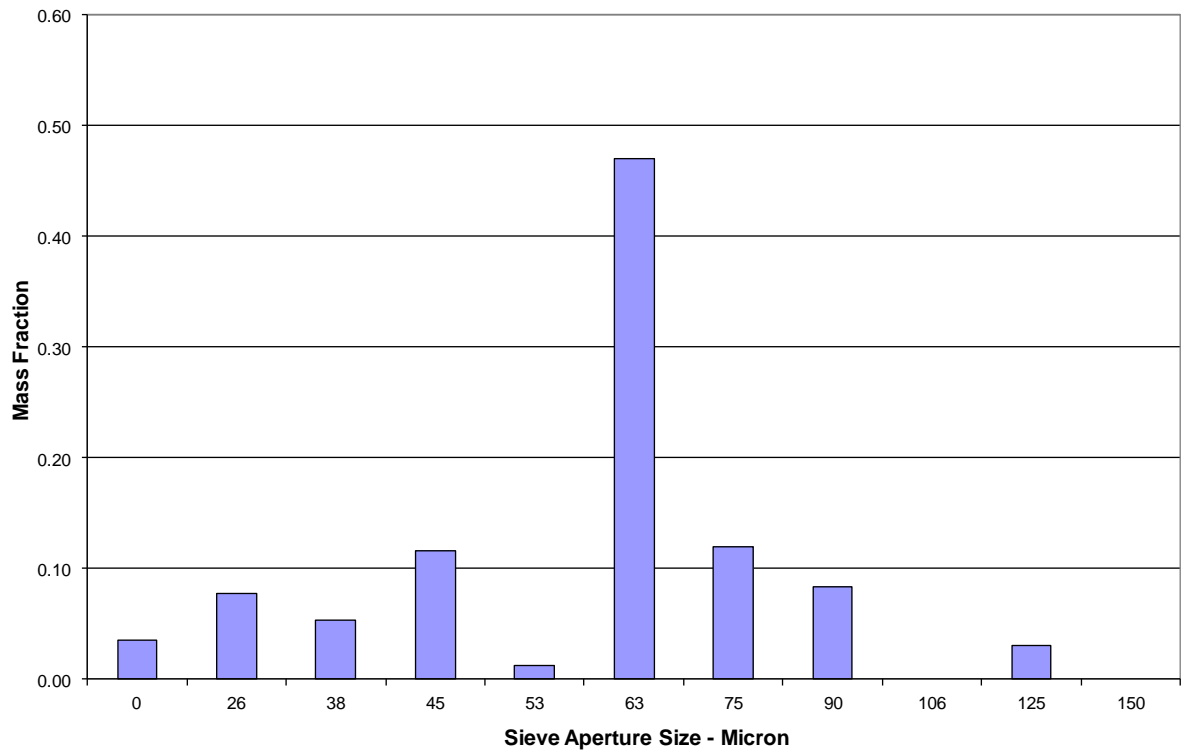
Experimental Results

D.1 Particle size distributions for Powder 1(Alumina)

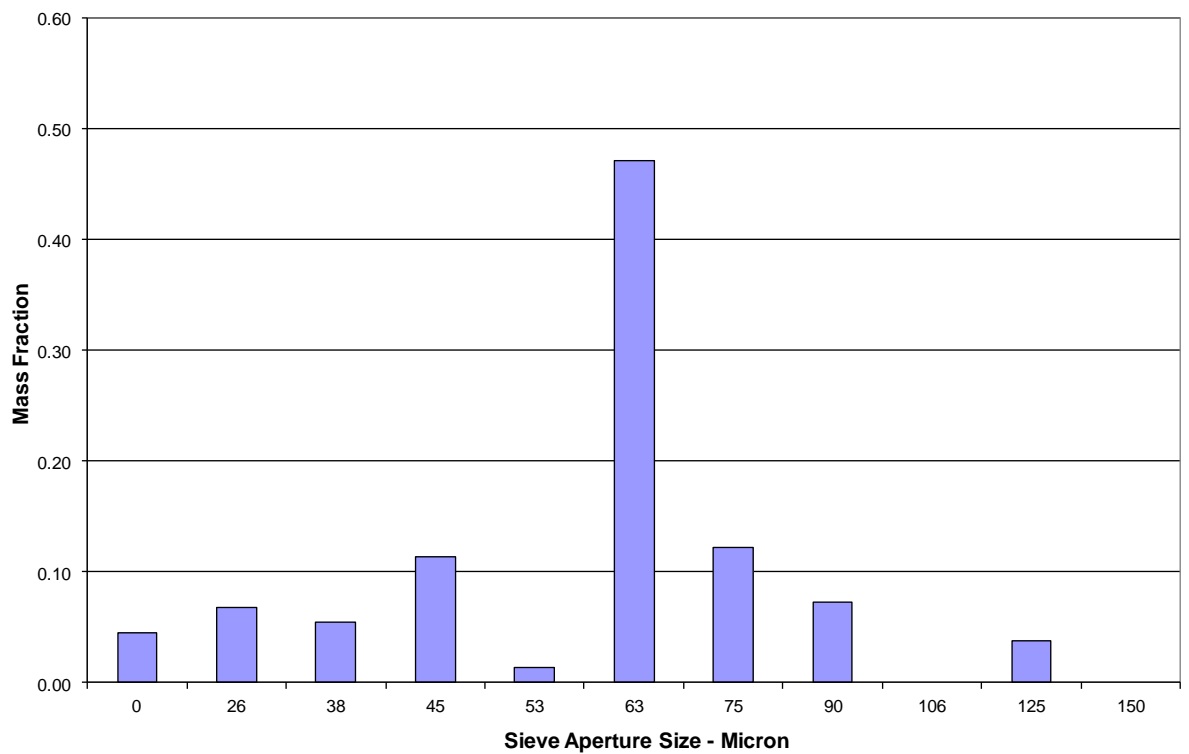
This section reports the particle size distribution of powders used for fluidization and defluidization experiments.



D1. 1 Experimental run 1

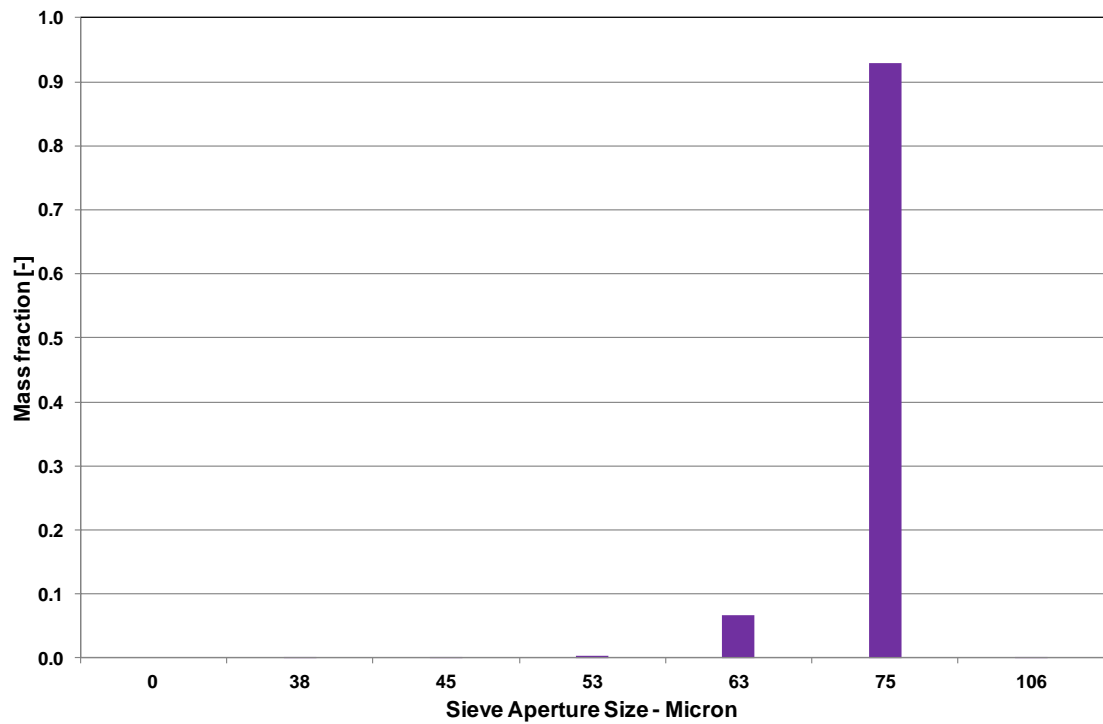


D1. 2 Experimental run 2

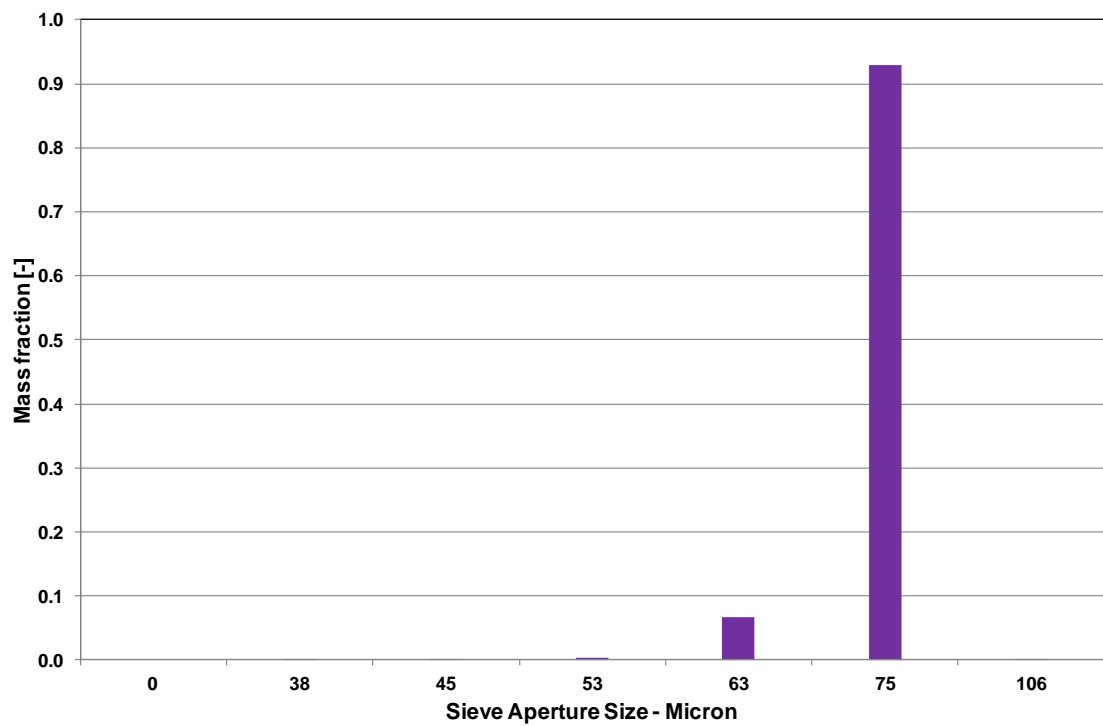


D1. 3 Experimental run 3

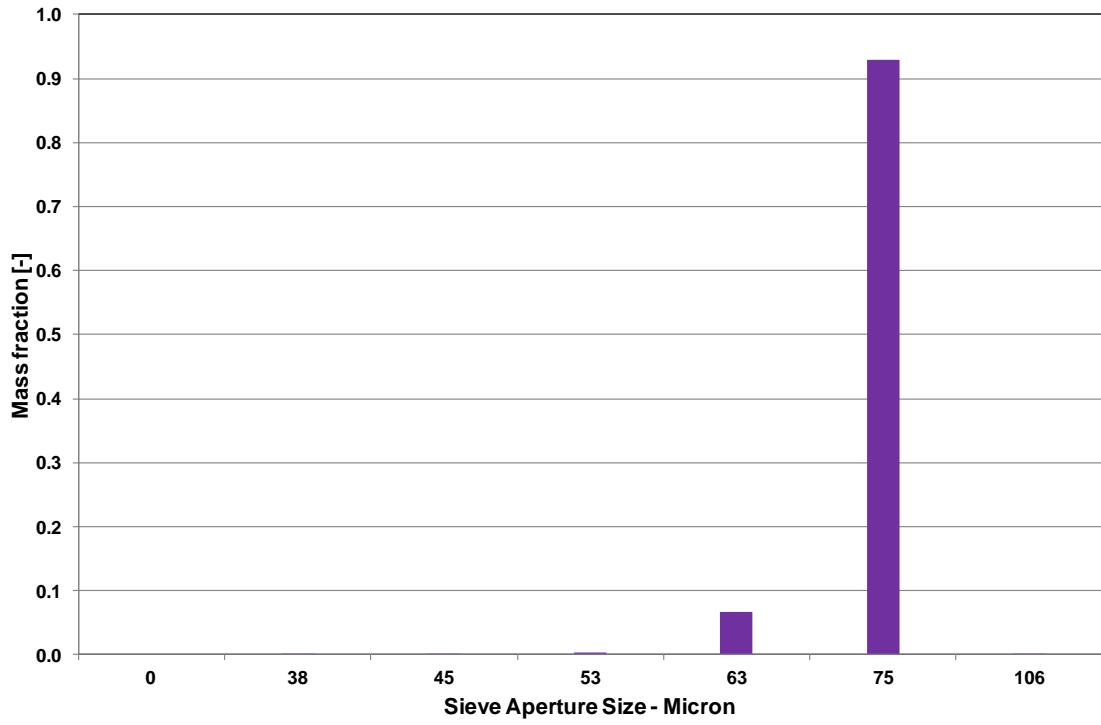
D.2 Particle size distributions for Powder 2(Ballotini)



D2. 1 Experimental run 1

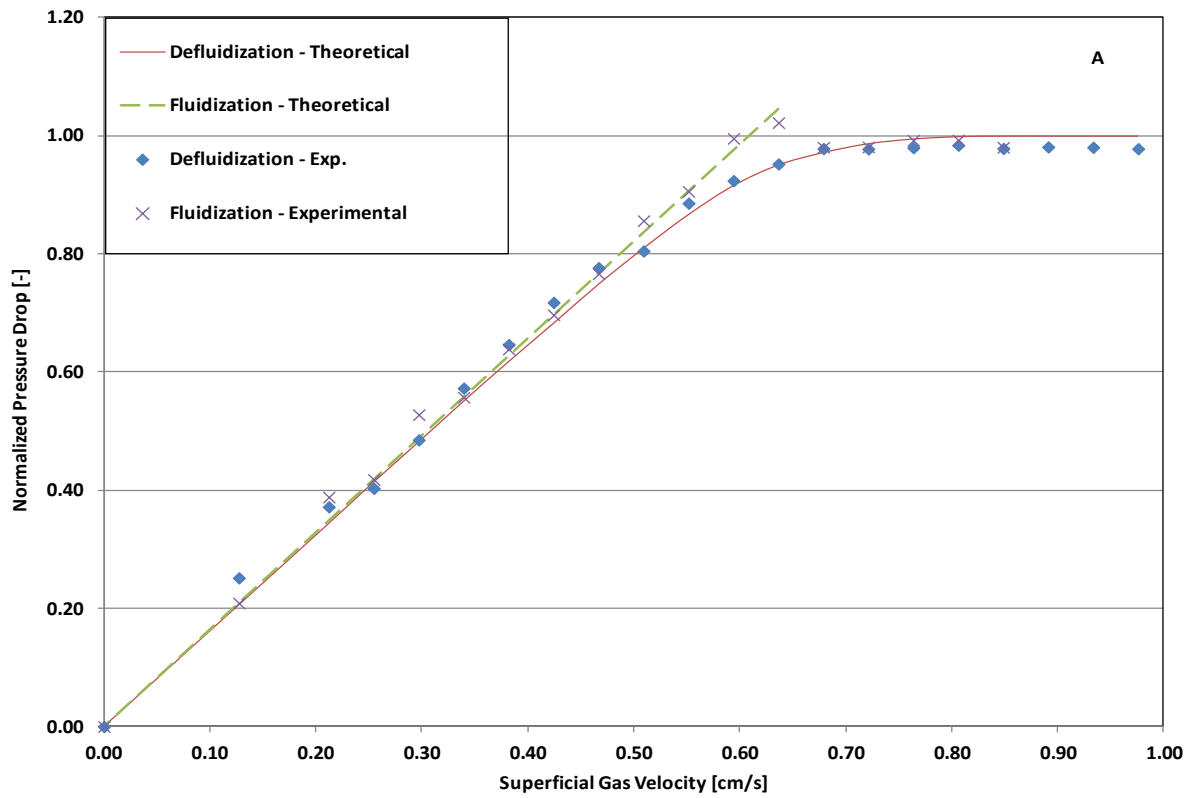


D2. 2 Experimental run 2

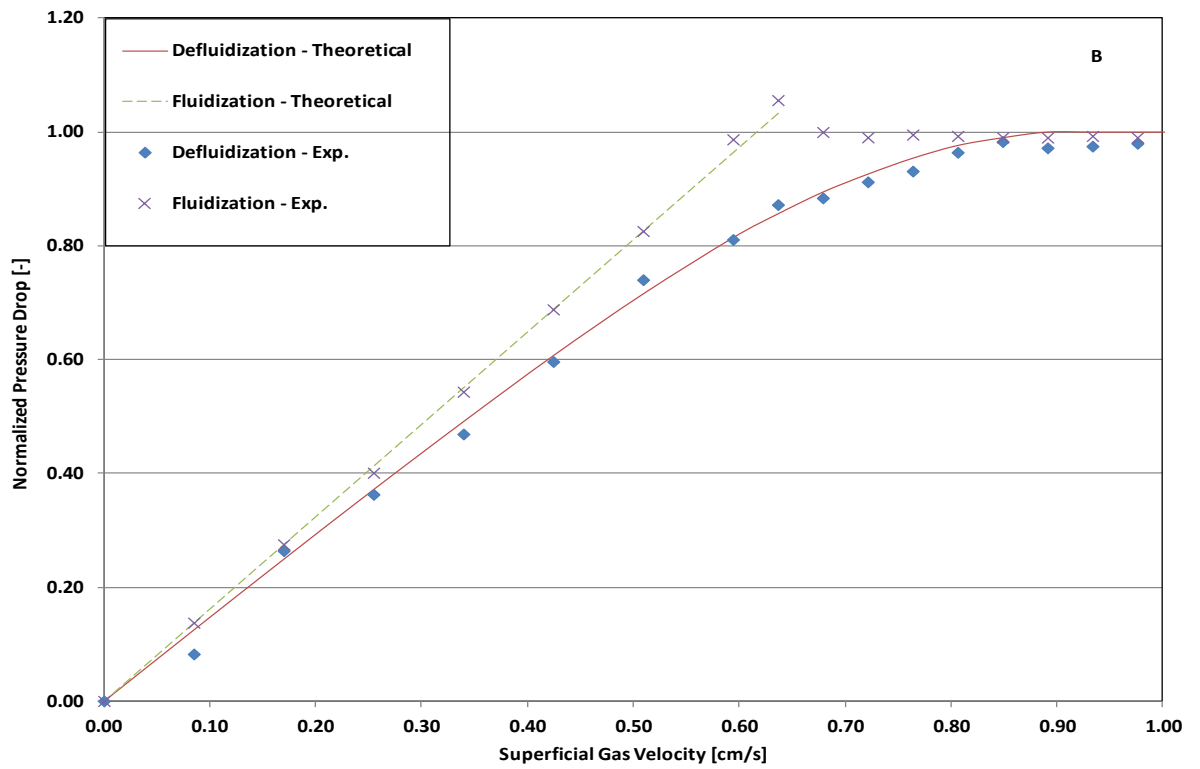


D2. 3 Experimental run 3

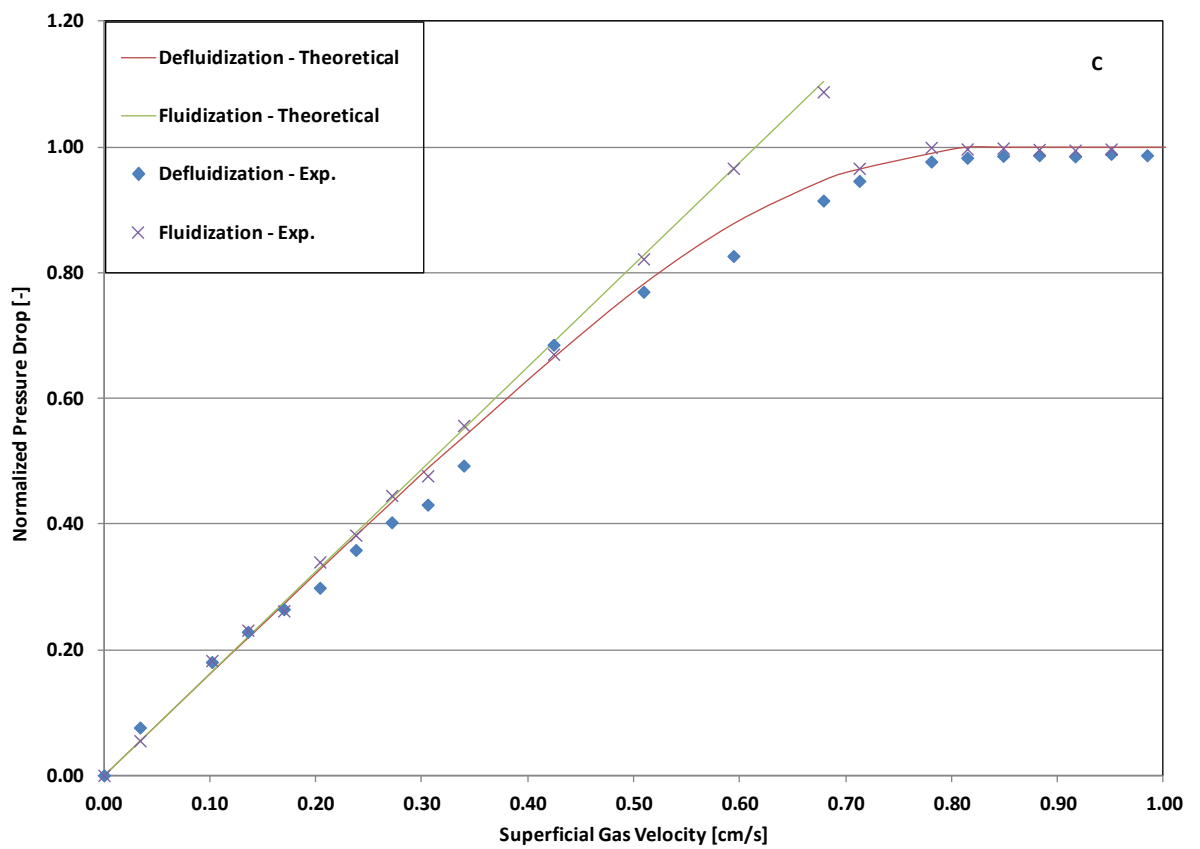
D.3 Pressure drop curves for fluidization and defluidization (Powder 2)



D3. 1 Normalized pressure drop (mg/A). Tube diameter – 10.0 cm.

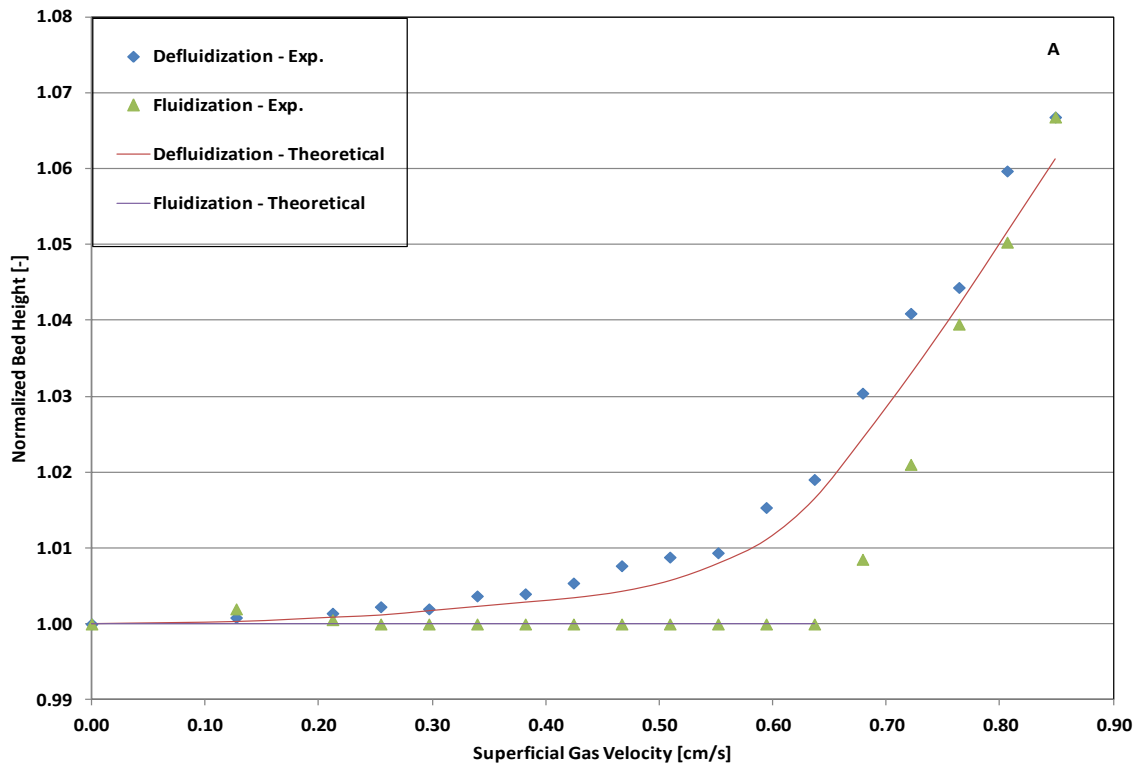


D3. 2 Normalized pressure drop (mg/A). Tube diameter – 5.0 cm.

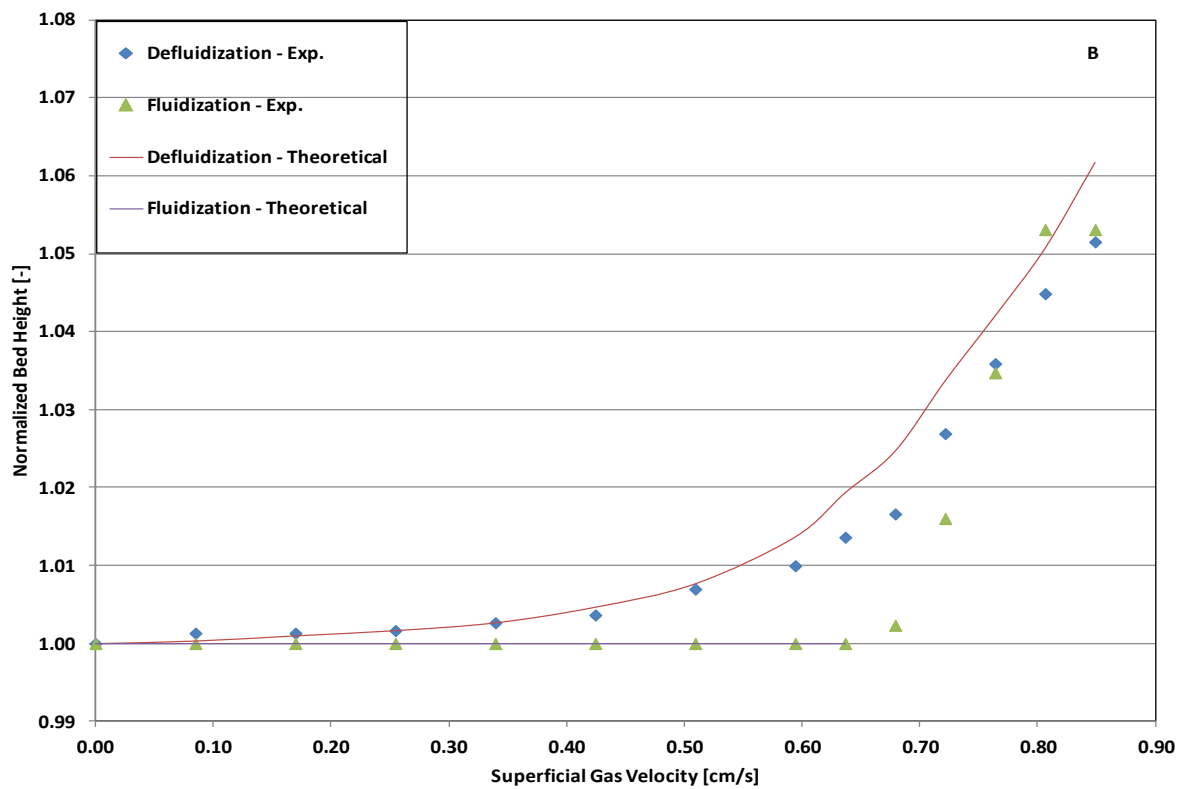


D3. 2 Normalized pressure drop (mg/A). Tube diameter – 2.5 cm.

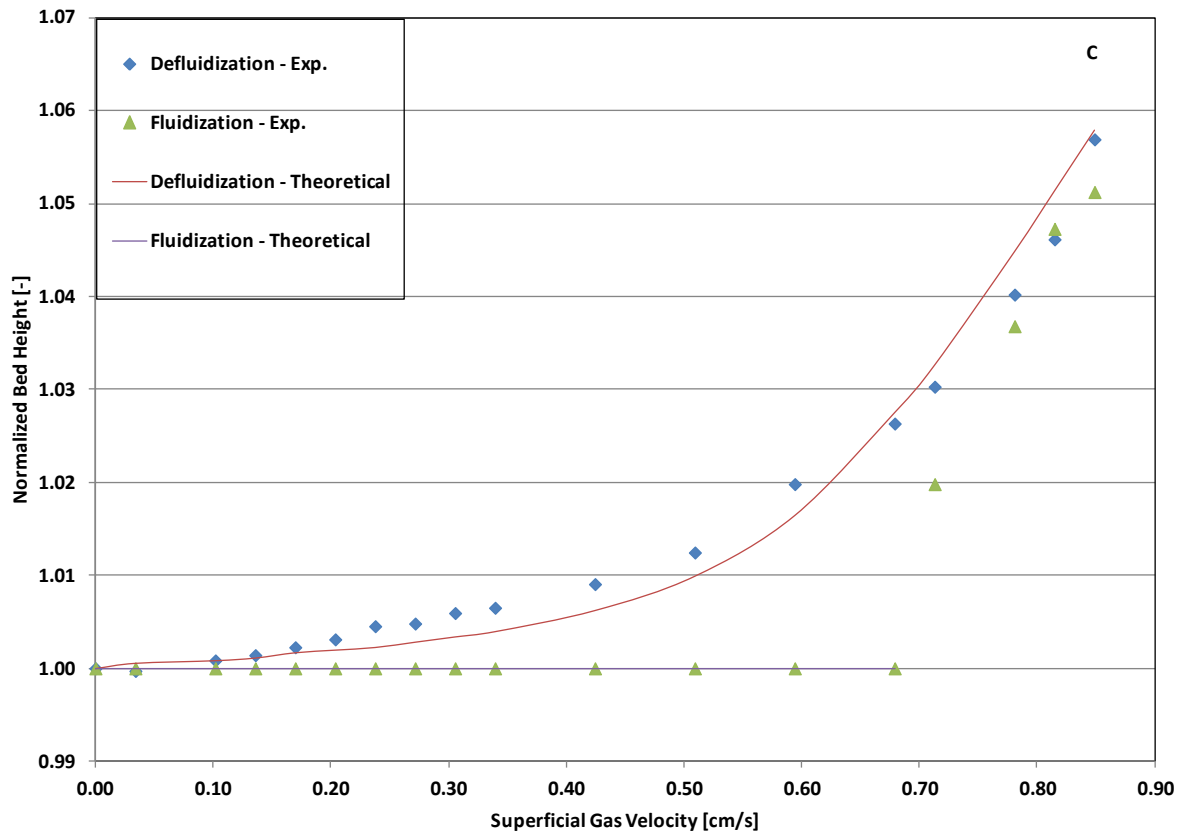
D.4 Bed height curves for fluidization and defluidization (Powder 2)



D4.1 Normalized bed height (H/H_0) against superficial gas velocity – Tube diameter 10 cm



D4.2 Normalized bed height (H/H_0) against superficial gas velocity – Tube diameter 5cm



D4.3 Normalized bed height (H/H_0) against superficial gas velocity – Tube diameter 2.5cm

Bibliography

- Abrahami, S. N., Resnick, W. 1974. Fluidised bed behaviour near incipient fluidization in a three-dimensional bed. *Transactions of the Institution of Chemical Engineers*, 80, 80.
- Ajbar, A., Alhumazi, K., Asif, M. 2005. Improvement of the Fluidizability of Cohesive Powders through Mixing with Small Proportions of Group A Particles. *Canadian Journal of Chemical Engineering*, 83.
- Ajbar, A., Bakhbaki, Y., Ali, S., Asif, M. 2011. Fluidization of nanopowders: Effect of sound vibration and pre-mixing with group A particles. *Powder Technology*, 206, 327-337.
- Anderson, T. B. & Jackson, R. 1967. A fluid mechanical description of fluidized beds. Equations of motion. *Industrial & Engineering Chemistry Fundamentals*, 6, 527.
- Anderson, T.B, Jackson R. 1969. Fluid mechanical description of fluidized beds. Comparison of theory and experiments. *Industrial & Engineering Chemistry Fundamentals*, 8,137-44.
- Anderson, K, Sundaresan, S., Jackson, R. 1995. Instabilities and the formation of bubbles in fluidized beds. *Journal of Fluid Mechanics*, 303, 327-66.
- Bailie, R. C. 1967. Double transport model for particle movement in a fluidized bed. In *Proceedings International Symposium on Fluidization*, Eindhoven, 322-333.
- Batchelor, G.K. 1988. A new theory of the instability of a uniformly fluidized bed. *Journal of Fluid Mechanics*, 193, 75 – 110.
- Bégis, J., Flour, I., Peirano, E. 1998. Modélisation numérique d'un distributeur d'air appliqué aux lits fluidisés de l'Université de Chalmers. Tech. Rep. HE/44/98/017/A.
- Bégis, J., Balzer, G. 1997. Modélisation numérique 2D et 3D de lit fluidisé circulant: application a la réalisation du diagramme des régimes. Tech. Rep. HE/44/97/001A.
- Bellgardt, D., Schoessler, M., Werther, J. 1985. An investigation into the lateral mixing of feed particles in atmospheric fluidized-bed combustors. *International Conference on Fluidized-Bed Combustion*, 115-129.

Bibliography

Bellgardt, D., Schoessler, M.; Werther, J. 1987. Lateral Nonuniformities of Solids and Gas Concentrations in Fluidized Bed Reactors. *Powder Technology* 53, 205-216.

Berruti, F., Scott, D. S., Rhodes, E., 1986. Measuring and modelling lateral solid mixing in a three dimensional batch gas-solid fluidized bed reactor. *Canadian Journal of Chemical Engineering* 64, 48-56.

Bicknell, J.A., Whitmore, R. L. 1967. Particle forces in fluidized beds. *Proceedings of the International Symposium on Fluidisation (Edited by A.A.H. Drinkenburg)*, Netherland University Press, Amsterdam. 31-38.

Blazer, G., Simonin, Q., Boelle, A., Lavieville, J. 1996. A unifying modelling approach for the numerical prediction of dilute and dense gas—solid two-phase flow. *Proceedings of 5th International Conference on Circulating Fluidized Beds*, May, Beijing, China.

Boemer, A., Qi, H., Renz, U., Vasquez, S., Boysan, F. 1995. Eulerian computation of fluidized bed hydrodynamics - A comparison of physical models. In *13th International Conference on Fluidized Bed Combustion*.

Boemer, A., Qi, H., Renz, U. 1998. Verification of Eulerian simulation of spontaneous bubble formation in a fluidized bed. *Chemical Engineering Science*, 53, 1835-1846.

Borodulya, V.A., Epanov, Y.G., Teplitskii, Y.S., 1982. Horizontal particle mixing in a free fluidized bed. *Journal of Engineering Physics* 42, 528-533.

Bouillard, J. X., Lyczkowski, R. W., Gidaspow, D. 1989. Porosity distributions in a fluidized bed with an immersed obstacle. *AIChE Journal*, 35, 908-922.;

Breault, R. W. 2006. A review of gas—solid dispersion and mass transfer coefficient correlations in circulating fluidized beds. *Powder technology*, 163, 9-17.

Brereton, C., Chaouki, J., Grace, J. R., Legros, R., Yeung, J. 1987. Hydrodynamic behaviour of a silica aerogel powder in a circulating fluidized bed. *37th Canadian Chemical Engineering Conference*, Montreal, Canada.

Brinkman, H. C. 1947. A calculation of the viscous force exerted by a flowing fluid on a dense swarm of particles. *Applied Scientific Research*, A1, 27-34.

Brotz, W., 1956. Untersuchungen über Transportvorgänge in durchströmtem, gekömtem Gut. *Chemie Ingenieur Technik* 28, 165-174.

Caicedo, G. R., Ruiz, M. G., Marques, J. J. P., & Soler, J. G. 2002. Minimum fluidization velocities for gas—solid 2D beds. *Chemical Engineering and Processing*, 41, 761–764.

Cairns, E. J. and Prausnitz, J. M., 1960, Macroscopic mixing in fluidization. *A.I.ChE Journal*, 6, 554-560.

Cammarata, L., Lettieri, P., Micale, G. D., Colman, D. 2003. 2D and 3D CFD simulations of bubbling fluidized beds using Eulerian-Eulerian models. *International Journal of Chemical Reactor Engineering*, 1(1).

Bibliography

- Campbell, C. S., Brennen, C. E. 1985. Computer simulation of granular shear flows. *Journal of Fluid Mechanics*, 151, 167-188.
- Canada, G.S., McLaughlin, M.H., Staub, F.N. 1978. Flow regimes and void fraction distribution in gas fluidization of large particles in beds without tube banks. *AIChE Symposium Series*, 74, 14 - 26.
- Carstensen, J.T., Patel, M.R., 1977. Blending of irregularly shaped particles. *Powder Technology* 17, 273-282.
- Castellanos, A., Valverde, J. M., Quintanilla, M. A. S. 2005. Physics of Compaction of Fine Cohesive Particles. *Physical Review Letter*, 94, 075501.
- Chandran, A. N., Rao, S. S. Varma, Y. B. G. 1990. Fluidized bed drying of solids. *AIChE Journal*, 36, 29-38.
- Chaouki, J., Chavarie, C., Klvana, D., Pajonk, G. 1985. Effect of interparticle forces on the hydrodynamic behaviour of fluidized aerogels. *Powder Technology*, 43, 117-125.
- Chapman, S., Cowling, T. G. 1970. *The Mathematical Theory of Non-Uniform Gases*. Cambridge University Press.
- Cherntongchai, P., Brandani, S. 2013. Prediction ability of a new minimum bubbling criterion. *Advanced Powder Technology*, 24, 1-13.
- Chiesa, M., Mathiesen, V., Melheim, J.A., Halvorsen, B. 2005. Numerical simulation of particulate flow by the eulerian-lagrangian and the eulerian-eulerian approach with application to a fluidized bed. *Computers and Chemical Engineering*, 29, 291.
- Chirone, R., Massimilla, L., Russo, S. 1992. Bubbling fluidization of a cohesive powder in an acoustic field. *Fluidization VII*, 545-553.
- Chirone, R., Massimilla, L., Russo, S. 1993. Bubble-free fluidization of a cohesive powder in an acoustic field. *Chemical Engineering Science*, 48, 41 - 52.
- Chirone, R., Miccio, F., Scala, F. 2004. On the relevance of axial and transversal fuel segregation during the FB combustion of a biomass. *Energy and fuels*, 18, 1108-1117.
- Cleary, P.W., Metcalfe, G., Liffman, K. 1998. How well do discrete element granular flow models capture the essentials of mixing processes? *Applied Mathematical Modelling*, 22(12), 995-1008.
- Cleary, P. W. 2000. DEM simulation of industrial particle flows: Case studies of dragline excavators, mixing in tumblers and centrifugal mills. *Powder Technology*, 109, 83-104.
- Cody, G.D., Goldfarb, D.J., Storch, G.V. J., Norris, A.N. 1996. Particle granular temperature in gas-fluidized beds. *Powder Technology*, 87, 211 - 232.
- Collins, R., 1989. A model for the effects of the voidage distribution around a fluidization bubble. *Chemical Engineering Science* 44, 1481-1487.
- Coulomb, C. A., 1776. Essai sur une application des règles de maximis et minimis à quelques problèmes de statique, relatifs à l'architecture. *Academie Royale Des Sciences* 7, 343-382.

Bibliography

- Cranfield, R. R., Geldart, D. 1974. Large particle fluidisation. *Chemical Engineering Science*, 29, 935–947.
- Cranfield, R. R. 1978. Solids mixing in fluidized beds of large particles. *AIChE Symposium Series*, 74, 54-59.
- Cui, H., Mostoufi, N., Chaouki, J. 2000. Characterization of dynamic gas–solid distribution in fluidized beds. *Chemical Engineering Journal*, 79, 133-143.
- Cundall, P. A., Strack, O. D. L. 1979. A discrete numerical model for granular assemblies. *Geotechnique*, 29, 47–65.
- Cundall, P. A., Strack, O. D. L. 1978. BALL-A program to model granular media using the distinct element method. Technical Note Advanced Technology Group.
- Darton, R. C. 1977. Bubble growth due to coalescence in fluidised beds. *Transactions of the Institution of Chemical Engineers*, 55, 274.
- Davidson, J.F., Harrison, D. 1971. *Fluidization*. Academic press, London.
- Davidson, D. 2002. The role of computational fluid dynamics in process industries. *The Bridge*, 32, 4.
- Didwania, A. K., Homsy, G. M. 1981a. Flow regimes and flow transitions in liquid fluidized beds. *International Journal of Multiphase Flow*, 7, 563 – 580.
- Di Renzo, A., Di Maio, F. P. 2004. Comparison of contact-force models for the simulation of collisions in DEM-based granular flow codes. *Chemical Engineering Science*, 59, 525–541.
- Ding, J., Gidaspo, D. 1990. A bubbling fluidization model using kinetic theory of granular flow. *AIChE Journal*, 36, 523-538.
- Ding, J., Lyczkowski, R. W. 1992. Three-dimensional kinetic theory modelling of hydrodynamics and erosion in fluidized beds. *Powder Technology*, 73, 127-138.
- Donsi, G., Massimilla, L., 1973. Bubble-free expansion of gas-fluidized beds of fine particles. *AIChE Journal*, 19, 1104-1110.
- Dorgelo, E. A. H., van der Meer, A. P., Wesselingh, J. A. 1985. Measurement of the axial dispersion of particles in a liquid fluidized bed applying a random walk method. *Chemical Engineering Science*, 40, 2105 – 2111.
- Du, B., Fan, L.S., Wei, F., Warsito, W. 2002. Gas and solids mixing in a turbulent fluidized bed. *AIChE Journal*, 48, 1896–1909.
- Du, B., Wei, F. 2002. Lateral solids mixing behaviour of different particles in a riser with FCC particles as fluidized material. *Chemical Engineering and Processing: Process Intensification*, 41, 329-335.
- Duru, P., Guazzelli, É. 2002. Experimental investigation on the secondary instability of liquid-fluidized beds and the formation of bubbles. *Journal of Fluid Mechanics*, 470, 359-382.

Bibliography

- Dutta, A., Dullea, L. V. 1991. Effects of external vibration and the addition of fibers on the fluidization of a fine powder, *AIChE Symposium Series*, 87, 38–46.
- El-Kaissy, M. M., Homsy, G. M. 1973. A theoretical study of pressure drop and transport in packed beds at intermediate Reynolds numbers. *Industrial & Engineering Chemistry Fundamentals*, 12, 82 – 90.
- Enwald, H., Peirano, E., & Almstedt, A. E. (1996). Eulerian two-phase flow theory applied to fluidization. *International Journal of Multiphase Flow*, 22, 21-66.
- Esin, A., Altun, M. 1984. Correlation of axial mixing of solids in fluidized beds by a dispersion coefficient. *Powder technology*, 39, 241-244
- Espin, M.J., Valverde, J.M., Quintanilla, M.A.S., Castellanos, A. 2011. Stabilization of gas-fluidized beds of magnetic powders by a cross-flow magnetic field. *Journal of Fluid Mechanics*, 680, 80 - 113.
- Ettehadieh, B., Gidaspow, D., Lyczkowski, R. W. 1984. Hydrodynamics of fluidization in a semicircular bed with a jet. *AIChE journal*, 30, 529-536.
- Fan, Z., Chen, G. T., Chen, B. C., Yuan, H, 1990. Analysis of pressure fluctuations in a 2-D fluidized bed. *Powder Technology* 62, 139-145.
- Fan, L. S., Zhu, C. 1998. *Principles of Gas–Solid Flows*. Cambridge University Press.
- Fanucci. B., Ness, N., Yen, R. 1979. On the formation of bubbles in gas-particulate fluidized beds. *Journal of Fluid Mechanics*, 94, 353 – 367.
- Farzaneh, M., Sasic, S., Almstedt, A., Johnsson, F., Pallarès, D. 2011. A novel multigrid technique for lagrangian modelling of fuel mixing in fluidized beds. *Chemical Engineering Science*, 66, 5628-5637.
- Fitzgerald, T. J. 1980. Cold modeling of fluidized-bed combustors. EPRI CS-1476.
- Fortes, A.F., Caldas, P., Gallo, J.V., 1998. Particle aggregation and the van der Waals forces in gas-solid fluidization. *Powder Technology*, 98, 201-208.
- Foscolo, P. U., Gibilaro, L. G., Waldram, S. P. 1983. A unified model for particulate expansion of fluidized beds and flow in fixed porous media. *Chemical Engineering Science*, 38, 1251 – 1260.
- Foscolo, P.U., Gibilaro, L.G.1984. A fully predictive criterion for transition between particulate and aggregative fluidization, *Chemical Engineering Science*, 39, 1667-1675.
- Gabor, J. D. 1964. Lateral solids mixing in fluidized-packed beds. *AIChE Journal*, 10, 345-350.
- Gamwo, I. K., Gidaspow, D., Lyczkowski, R. W., Soong, Y. 1995. Three-dimensional hydrodynamic modeling of a bubbling fluidized bed. *Proceedings of the 13th International Conference on Fluidized Bed Combustion*, Orlando, 297-303.
- Ganser, G. H., Drew, D. A. 1990. Nonlinear stability analysis of a uniformly fluidized bed. *International journal of multiphase flow*, 16, 447-460.

Bibliography

- Garside, J., Al-Dibouni, M. R. 1973. Behaviour of liquid fluidized beds containing a wide size distribution of solids. Proceedings International Symposium Fluidization and its Application, Toulouse, 53-62.
- Garside, J., Al-Dibouni, M. R. 1977. Velocity-voidage relationships for fluidization and sedimentation in solid-liquid systems. Industrial and Engineering Chemistry Process Design and Development, 16, 206-213.
- Geldart, D., Kelsey, J. R. 1968. The influence of the gas distributor on the bed expansion, bubble size and the bubble frequency in the fluidized beds. Chemical Engineering Symposium Series, 114-125.
- Geldart, D. (1970). The size and frequency of bubbles in two- and three-dimensional gas-fluidised beds. Powder Technology, 4, 41-55.
- Geldart, D., Cranfield, R. R. 1972. The gas fluidization of large particles. The Chemical Engineering Journal, 3, 211-231.
- Geldart, D., 1973. Types of gas fluidization. Powder Technology, 7, 285-292.
- Geldart, D., Wong, A.C.Y. 1984. Fluidization of powders showing degree of cohesiveness-I. Bed expansion. Chemical Engineering Science 39, 1481-1488.
- Geldart, D., Wong, A.C.Y. 1985. Fluidization of powders showing degrees of cohesiveness—II. Experiments on rates of de-aeration. Chemical Engineering Science, 40, 653-661.
- Gera, D., Gautam, M., Tsuji, Y., Kawaguchi, T., Tanaka, T. 1998. Computer simulation of bubbles in large-particle fluidized beds. Powder Technology 98, 38-47.
- Gibilaro, L.G. 2001. Fluidization-Dynamics. Butterworth Heinemann.
- Gidaspow, D., Ettehadieh, B. 1983. Fluidization in two-dimensional beds with a jet. Part 2. Hydrodynamic modelling. Industrial & Engineering Chemistry Fundamentals, 22, 193-201.
- Gidaspow, D., Syamlal, M. & Seo, Y. C. 1986. Hydrodynamics of fluidization: supercomputer generated vs. experimental bubbles. Journal of Powder and Bulk Solids Technology. 10, 19.
- Gidaspow, D. 1994. Multiphase Flow and Fluidization. Academic Press.
- Gidaspow, D., Jung, J., & Singh, R. K. 2004. Hydrodynamics of fluidization using kinetic theory: an emerging paradigm: 2002 Flour-Daniel lecture. Powder Technology, 148, 123-141.
- Gilbertson, M.A., Yates, J.G. 1996. The tilting fluidized bed: A re-examination. Powder Technology, 89, 29-36.
- Gilliland, E. R., Mason, E. A. 1949. Gas and solid mixing in fluidized beds. Industrial and Engineering Chemistry, 41, 1191-1196.
- Glasser, B.J, Kevrekidis, I.G, Sundaresan, S. 1997. Fully developed travelling wave solutions and bubble formation in fluidized beds. Journal of Fluid Mechanics, 334, 157.

Bibliography

- Glicksman, L. R., McAndrews, G. 1985. The effect of bed width on the hydrodynamics of large particle fluidized beds. *Powder Technology*, 42, 159–167.
- Godard, K.M.S. & Richardson, J.F., 1968. The behaviour of bubble-free fluidized beds. I. *Chemical Engineering Symposium Series* 30, 126.
- Goldshtein, A. & Shapiro, M. 1995. Mechanics of collisional motion of granular materials. Part I. General hydrodynamic equations. *Journal of Fluid Mechanics*, 282, 75.
- Goldschmidt, M.J.V., Kuipers, J.A.M., van Swaaij, W.P., 2001. Hydrodynamic modelling of dense gas-fluidised beds using the kinetic theory of granular flow: effect of coefficient of restitution on bed dynamics. *Chemical Engineering Science*, 56, 571–578.
- Goldschmidt, M.J.V., Beetstra, R., Kuipers, J.A.M., 2004. Hydrodynamic modelling of dense gas-fluidised beds: comparison and validation of 3D discrete particle and continuum models. *Powder Technology*, 142, 23–47.
- Gómez-Barea, A., Leckner, B. 2010. Modeling of biomass gasification in fluidized bed. *Progress in Energy and Combustion Science*, 36, 444-509.
- Grace, J. R. 1981. Fluidized bed reactor modelling: an overview. *American Chemical Society*, 168, 3 -18.
- Grakhovskii, B.M. 1968. Particle mixing and residence time in a fluidized bed: High temperature endothermal processes in a fluidized bed (in Russian), *Metallurgiya*, Moscow, 70 – 75.
- Guo, Q., Wang, M., Li, Y., Yang, C. 2005. Fluidization of Ultrafine Particles in a Bubbling Fluidized Bed with Sound Assistance. *Chemical Engineering Technology*, 28, 1117-1124.
- Guo, Q., Liu, H., Shen, W., Yan, X., Jia, R. 2006. Influence of sound wave characteristics on fluidization behaviors of ultrafine particles. *Chemical Engineering Journal*, 119, 1-9.
- Haff, P. K. 1983. Grain flow as a fluid mechanical phenomenon. *Journal of Fluid Mechanics*, 134, 401.
- Ham, J.M., Thomas, S., Guazzelli, E., Homsy, G.M, Anselmet, M.C. 1990. An experimental study of the stability of liquid-fluidized beds. *International Journal of Multiphase Flow*, 16, 171.
- Hanratty, T. J., Bandukwala, A. 1957. Fluidization and sedimentation of spherical particles. *A.I.ChE Journal*, 3,293-296.
- Happel, J. 1958. Viscous flow in multiparticle systems: Slow motion of fluids relative to beds of spherical particles and particulate fluidization and sedimentation of spheres. *AIChE Journal*, 4, 197 – 201.
- Harris, A. T. 2008. On the vibration assisted fluidisation of silica nanoparticles. *International Journal of Nanotechnology*, 5,179-194.
- Harrison, D., Davidson, J. F., de Kock, J. W. 1961. On the nature of aggregative and particulate fluidisation. *Transactions of the Institution of Chemical Engineers*, 39, 202 - 211.

Bibliography

- Hassett, N. J. 1961a. Flow patterns in particle beds. *Nature*, 189, 997 - 998.
- Hassett, N. J., 1961b. The mechanics of fluidization. *British Chemical Engineering*, 19, 777 – 780.
- Hawksley, P. G. W. 1951. Some aspects of fluid flow. Paper 7, Institute of Physics and E. Arnold, London.
- Helland, E., Occelli, R., Tadriss, L., 1999. Numerical study of cohesive powders in a dense fluidized bed. *Comptes Rendus de l'Academie de Sciences—Serie IIB: Mecanique, Physique, Chimie, Astronomie* 327 (14), 1397–1403.
- Highley, J., & Merrick, D. 1971. Effect of the spacing between solid feed points on the performance of a large fluidized bed reactor. *AIChE Symposium Series*, 67, 116.
- Hirama, T., Ishida, M., Shirai, T. 1975. The lateral dispersion of solid particles in fluidized beds. *Kagaku Kogaku Ronbunshu*, 1, 272-276.
- Hirata, A., Bulos, F. B. 1990. Predicting bed voidage in solid-liquid fluidization. *Journal of Chemical Engineering of Japan*, 599-604.
- Homsy, G.M. 1998. Nonlinear waves and the origin of bubbles in fluidized beds. *Applied Scientific Research*, 58, 251.
- Hoomans, B. P. B., Kuipers, J. A. M., Briels, W. J., Van Swaaij, W. P. M. 1996. Discrete particle simulation of bubble and slug formation in a two-dimensional gas-fluidised bed: a hard-sphere approach. *Chemical Engineering Science*, 51, 99-118.
- Hoomans, B. P. B., Kuipers, J. A. M., Van Swaaij, W. P. M. 2000. Granular dynamics simulation of segregation phenomena in bubbling gas-fluidised beds. *Powder Technology*, 109, 41-48.
- Hoomans, B.P.B., Kuipers, J. A. M., Salleh, M. M., Stein, M., Seville, J. P. K. 2001. Experimental validation of granular dynamics simulations of gas-fluidised beds with homogenous in-flow conditions using positron emission particle tracking. *Powder Technology*, 116, 166-177.
- Iwodate, M., Horio, M. 1998. Agglomerating fluidization of wet powders and group C powders: a numerical analysis. *Fluidization IX*, Engineering Foundation, Durango, USA.
- Jackson, R. 1963. The mechanics of fluidized beds: Part I. The stability of the state of uniform fluidization. *Transactions of the Institution of Chemical Engineers*, 41, 13.
- Jackson, R., 2000. *The dynamics of fluidized particles*. Cambridge University Press.
- Jamialahmadi, M., Müller-Steinhagen, H. 1992. Bed voidage in annular solid—liquid fluidized beds. *Chemical Engineering and Processing: Process Intensification*, 31, 221-227.
- Jenkins, J. T., Savage, S. B. 1983. A theory for the rapid flow of identical, smooth, nearly elastic spherical particles. *Journal of Fluid Mechanics*, 130,187.
- Jenkins, J. T. 1987. Rapid flows of granular materials. In *Non-Classical Continuum Mechanics*.

Bibliography

Cambridge University Press.

Jiradilok, V., Gidaspow, D., & Breault, R. W. 2007. Computation of gas and solid dispersion coefficients in turbulent risers and bubbling beds. *Chemical Engineering Science*, 62, 3397-3409.

Johansson, K., van Wachem, B.G.M., Almstedt, A.E. 2006. Experimental validation of CFD models for fluidized beds: influence of particle stress models, gas phase compressibility and air flow models. *Chemical Engineering Science*, 61, 1705 – 1717.

Johnson, P.C., Jackson, R., 1987. Frictional-collisional constitutive relations for granular materials, with application to plane shearing. *Journal of Fluid Mechanics* 176, 76-93.

Johnson, P.C., Nott, P., Jackson, R., 1990. Frictional-collisional equations of motion for particulate flows and their application to chutes. *Journal of Fluid Mechanics* 210, 501–535

Jottrand, R. 1952. An experimental study of the mechanism of fluidization. *Journal of Applied Chemistry*, 2, 17-22.

Kafui, K. D., Thornton, C., Adams, M. J. 2002. Discrete particle-continuum fluid modelling of gas-solid fluidized beds. *Chemical Engineering Science*, 57, 2395.

Kaliyaperumal, S., Barghi, S., Briens, L., Rohani, S., Zhu, J. 2011. Fluidization of nano and sub-micron powders using mechanical vibration. *Particuology*, 9,279-287.

Kaneko, Y., Shiojima, T., Horio, M. 1999. DEM simulation of fluidized beds for gas-phase olefin polymerization. *Chemical Engineering Science* 54, 5809–5821.

Kashyap, M., Gidaspow, D., Tsai, T. W. 2006. Effect of electric field on the hydrodynamics of nanoparticles in a rectangular fluidized bed. *AIChE Annual Meeting*, San Francisco, CA, US.

Kashyap, M., Gidaspow, D., Driscoll, M. 2008. Effect of electric field on the hydrodynamics of fluidized nanoparticles. *Powder Technology*, 183, 441-453.

Kashyap, M., Gidaspow, D. 2011. Measurement of dispersion coefficients for FCC particles in a free board. *Industrial and Engineering Chemistry Research*, 50, 7549-7565.

Kathuria, D. G., Saxena, S. C. 1987. A variable-thickness two-dimensional bed for investigating gas–solid fluidized bed hydrodynamics. *Powder Technology*, 53, 91–96.

Katz, H., & Sears, J.T., 1969. Electric field phenomena in fluidized and fixed bed. *Canadian Journal of Chemical Engineering* 47, 50–53.

Kawaguchi, T., Tanaka, T., Tsuji, Y. 1998. Numerical simulation of two-dimensional fluidized beds using the discrete element method (comparison between the two- and the three-dimensional models). *Powder Technology* 96, 129–138.

Kelly, V. P., 1961, Hydraulic studies for the fluid-bed reactor. *Nuclear Science and Engineering*, 10, 40 – 44.

Bibliography

- Kenche, V., Feng, Y., Ying, D., Solnordal, C., Lim, S., Witt, P. J. 2013. Numerical investigation of solid mixing in a fluidized bed coating process. Proceedings of the 7th International Conference on Micromechanics of Granular Media, 1542, 1270-1273.
- Khan, A.R. & Richardson, J.F., 1989. Fluid-particle interactions and flow characteristics of fluidized beds and settling suspensions of spherical particles. Chemical Engineering Communication 78, 111.
- Kim, J.Y., Choi, K. Y. 1999. Polymer particle mixing and segregation in a gas phase olefin polymerization reactor. AIChE Symposium Series, 95, 77–82
- Kmiec, A. 1982. Equilibrium of forces in a fluidized bed - experimental verification. Chemical Engineering Journal, 23, 133 – 136.
- Koch, D.L., Sangani, A.S. 1999. Particle pressure and marginal stability limits for a homogeneous monodisperse gas-fluidized bed: Kinetic theory and numerical simulations. Journal of Fluid Mechanics, 400, 229 – 263.
- Kriebitzsch, S. H. L., van der Hoef, M. A., Kuipers, J. A. M. 2013. Fully resolved simulation of a gas-fluidized bed: A critical test of DEM models. Chemical Engineering Science, 91, 1-4.
- Krupp, H. 1967. Particle Adhesion. Advances in Colloids and Interface Science, 1, 111.
- Kuipers, J. A. M., Van Duin, K. J., Van Beckum, F. P. H., Van Swaaij, W. P. M. 1992. A numerical model of gas-fluidized beds. Chemical Engineering Science, 47, 1913-1924.
- Kunii, D. 1972. Levenspiel, O. 1969. Fluidization Engineering.
- Kunii, D., Levenspiel, O. 1991. Fluidization Engineering. Butterworth-Heinemann.
- Kuwabara, G., Kono, K. 1987. Restitution coefficient in a collision between 2 spheres. Japanese Journal of Applied Physics, 26(8), 1230–1233.
- Kwauk, M. 1973. Particulate fluidization in chemical metallurgy. Scientia Sinica, 16, 407-430.
- Labous, L., Rosato, A. D., & Dave, R. N. 1997. Measurements of collisional properties of spheres using high-speed video analysis. Physical Review, 56, 5717–5725.
- Lacey, P.M.C., 1954. Developments in theory of particle mixing. Journal of Applied Chemistry, 257-268.
- Laux H., 1998. Modelling of dilute and dense dispersed fluid-particle flow. PhD Thesis, NTNU, Trondheim, Norway.
- Lebowitz, J. L. 1964. Exact solution of generalised Percus-Yevick equation for a mixture of hard spheres. Physical Review 133, 895-899.
- Lee, W.K. 1983. The rheology of magnetically stabilized fluidized solids. AIChE Symposium Series. 79, 87–96.
- Lee, G.S., Kim, S.D. 1990. Axial mixing of solids in turbulent fluidized beds. Chemical Engineering Journal, 44, 1–9

Bibliography

- Lepek, D., Valverde, J. M., Pfeffer, R., Dave, R. N. 2010. Enhanced nanofluidization by alternating electric fields. *AIChE Journal*, 56, 54-65.
- Letan, R. 1974. On vertical dispersion two-phase flow. *Chemical Engineering Science*, 29, 621 – 624.
- Lettieri, P., Newton, D., Yates, J.G., 2002. Homogeneous bed expansion of FCC catalysts, influence of temperature on the parameters of the Richardson-Zaki equation. *Powder Technology* 123, 221-231.
- Lettieri, P., Mazzei, L. 2009. Challenges and issues on the CFD modeling of fluidized beds: a review. *Journal of Computational Multiphase Flows* 1, 83-131.
- Leva, M., Grummer, M. 1952. A correlation of solids turnover in fluidized systems-its relation to heat transfer. *Chemical Engineering Progress*, 48, 307-313.
- Levy, E. K., Shnitzer, T. Masaki, J. Salmento. 1997. Effect of an acoustic field on bubbling in a gas-fluidized bed. *Powder Technology*, 90, 53-57.
- Levy, E. K., Celeste, B. 2006. Combined effects of mechanical and acoustic vibrations on fluidization of cohesive powders. *Powder Technology*, 163, 41-50.
- Lewis, W. K., Gilliland, E. R., Bauer, W. 1949. Characteristics of fluidized particles. *Industrial and Engineering Chemistry*, 1104- 1117.
- Lewis, E. W., Bowerman, E. W. 1952. Fluidization of Solid Particles in Liquids. *Chemical Engineering Progress*, 48, 603 – 611.
- Lewis, W. K., Gilliland, E. R., Girouard, H., 1962. Heat transfer and solids mixing in a bed of fluidized solids. *Chemical Engineering Progress Symposium*, 58, 87–97.
- Li, T., Grace, J. R., Bi, X. 2010. Study of wall boundary condition in numerical simulations of bubbling fluidized beds. *Powder Technology*, 203, 447–457.
- Li, T., Pannala, S., Shahnam, M. 2014. CFD simulations of circulating fluidized bed risers, part II, evaluation of differences between 2D and 3D simulations. *Powder Technology*, 254, 115-124.
- Li, J., Kuipers, J. A. M. 2002. Effect of pressure on gas–solid flow behaviour in dense gas-fluidized beds: a discrete particle simulation study. *Powder Technology*, 127, 173-184.
- Li, J., Mason, D.J. 2000. A computational investigation of transient heat transfer in pneumatic transport of granular particles. *Powder Technology*, 112, 273.
- Lian, G., Thornton, C., Adams, M. J. 1993. A Theoretical Study of the Liquid Bridge Forces between Two Rigid Spherical Bodies. *Journal of Colloids and Interface Science*, 161, 138-147.
- Liang-wan, R., Zhan, J. 2010. Improved DEM-CFD model and validation: A conical-base spouted bed simulation study. *Journal of Hydrodynamics*, 22, 351-359.
- Lighthill, M. J., Whitham, G.B. 1955. On Kinematic Waves: a Theory of Traffic Flow on Long Crowded Roads. *Proc. of the Royal Society, Series A*, 229, 317-345.

Bibliography

- Lim, K. S., Agarwal, P. K. 1994. Circulatory motion of a large and lighter sphere in a bubbling fluidized bed of smaller and heavier particles. *Chemical Engineering Science*, 49, 421-424.
- Lin, J. S., Chen, M. M., Chao, B. T. 1985. A novel radioactive particle tracking facility for measurement of solids motion in gas-fluidized beds. *AIChE Journal*, 31, 465-473.
- Liu, D., Chen, X. 2010. Lateral solid dispersion in large scale fluidized beds. *Combustion and Flame* 157, 2116-2124.
- Liu, J.T.C.1982. Note on a wave-hierarchy interpretation of fluidized bed instabilities. *Proceedings of the Royal Society of London A: Mathematical, Physical and Engineering Sciences*, 380, 229-239.
- Lockett, M. J., Davidson, J. F., Harrison, D. 1967. On the two-phase theory of fluidisation. *Chemical Engineering Science*, 22, 1059-1066.
- Loezos, P.N., Costamagna, P., Sundaresan, S. 2002. The role of contact stresses and wall friction on fluidization. *Chemical Engineering Science*, 57, 5123-5141.
- Lu, X., Li, H. 2000. Fluidization of CaCO_3 and Fe_2O_3 particle mixtures in a transverse rotating magnetic field. *Powder Technology*, 10, 66-78.
- Lu, H., Wang, S., Zhao, Y., Yang, L., Gidaspow, D., Ding, J. 2005. Prediction of particle motion in a two-dimensional bubbling fluidized bed using hard-sphere model. *Chemical Engineering Science*, 60, 3217.
- Lun, C. K. K., Savage, S. B., Jeffrey, D. J., Chepurny, N. 1984. Kinetic theories for granular flow: Inelastic particles in Couette flow and slightly inelastic particles in a general flow field. *Journal of Fluid Mechanics*, 140, 223.
- Lun, C. K. K. 1991. Kinetic theory for granular flow of dense, slightly inelastic, slightly rough spheres. *Journal of Fluid Mechanics*, 223, 539.
- Lun, C.K.K. 2000. Numerical simulation of dilute turbulent gas–solid flows. *International Journal of Multiphase Flow*, 26, 1707–1736.
- Lyczkowski, R. W., Bouillard, J. X., Berry, G. F., Gidaspow, D. 1987. Erosion calculations in a two-dimensional fluidized bed (No. CONF-870540-2). Argonne National Lab., IL (USA); Illinois Institute of Technology, Chicago (USA).
- Mabrouk, R., Chaouki, J., Guy, C., 2008. Wall surface effects on particle-wall friction factor in upward gas-solid flows. *Powder Technology* 186, 80 – 88.
- Makkawi, Y., Ocone, R. 2006. A model for gas-solid flow in a horizontal duct with a smooth merge of rapid-intermediate-dense flows. *Chemical Engineering Science*, 61, 4271.
- Mallouppas, G.,van Wachem. B.G.M. 2013.Large Eddy Simulations of turbulent particle-laden channel flow. *International Journal of Multiphase Flow*, 54, 65-75.

Bibliography

- Marring, E., Hoffmann, A. C., Janssen, L. P. B. M. 1994. The effect of vibration on the fluidization behaviour of some cohesive powders. *Powder Technology*, 79, 1-10.
- Marzocchella, A., Salatino, P. 2000. Fluidization of solids with CO₂ at pressures from ambient to supercritical. *AIChE Journal*, 46, 901 – 910.
- Marsheck, R. M., Gomezplata, A. 1965. Particle flow patterns in a fluidized bed. *AIChE Journal*, 11, 167-173.
- Massimilla, L., Donsì, G. 1976. Cohesive forces between particles of fluid-bed catalysts. *Powder Technology*, 15 , 253-260.
- Matsen, J.M. 1996. Scale-up of fluidized bed processes: principles and practice. *Powder Technology*, 88, 237-244.
- Mawatari, Y., Koide, T., Tatemoto, Y., Uchida, S., Noda, K. 2002. Effect of particle diameter on fluidization under vibration. *Powder Technology*, 123, 69-74.
- May, W.G. 1959. Fluidized-bed reactor studies. *Chemical Engineering Progress*, 55, 49–56.
- Mazzei, L., Lettieri, P., 2007. A drag force closure for uniformly-dispersed fluidized suspensions. *Chemical Engineering Science* 62, 6129-6142.
- Mazzei, L. 2008. Eulerian modelling and computational fluid dynamics simulation of mono and polydisperse fluidized suspensions, Ph.D. Dissertation, Department of Chemical Engineering, University College London.
- Mazzei, L., Casillo, A., Lettieri, P., Salatino, P. 2010. CFD simulations of segregating fluidized binary mixtures of particles differing in size. *Chemical Engineering Journal* 156, 432-445.
- McAuley, K. B., Talbot, J. P., Harris, T. J. 1994. A comparison of two-phase and well-mixed models for fluidized-bed polyethylene reactors. *Chemical Engineering Science*, 49, 2035-2045.
- Menon, N., Durian, D.J. 1997. Diffusing wave spectroscopy of dynamics in a three-dimensional granular flow. *Science*, 275, 1920-1922.
- Merry, J. M. D., Davidson, J. F. 1973. Gulf stream circulation in shallow fluidized beds. *Transactions of the Institution Chemical Engineers*, 51, 361-368.
- Mikami, T., Kamiya, H., Horio, M. 1998. Numerical simulation of cohesive powder behaviour in a fluidized bed. *Chemical Engineering Science* 53, 1927–1940.
- Mindlin, R.D. 1949. Compliance of elastic bodies in contact, *Journal of Applied Mechanics*. 16, 259.
- Mindlin, R. D. and Deresiewicz, H. 1953. Elastic spheres in contact under varying oblique forces. *Journal of Applied Mechanics* , 20, 327.
- Milburn, R. J., Naylor, M. A., Smith, A. J., Leaper, M. C., Good, K., Swift, M. R., King, P. J. 2005. Faraday tilting of water-immersed granular beds. *Physical Review*, 71(1), 011308.
- Miyauchi, T., Furusaki, S., Morooka, S., Ikeda, Y. 1981. Transport phenomena and reaction in fluidized catalyst beds. *Advances in Chemical Engineering*, 11, 275-448.

Bibliography

Molerus, O. 1982. Interpretation of Geldart's Type A, B, C and D Powders Taking into Account Interparticle Cohesion Forces. *Powder Technology*, 33, 81 – 87.

Moreno-Atanasio, R., Xu, B. H., Ghadiri, M. 2007. Computer simulation of the effect of contact stiffness and adhesion on the fluidization behaviour of powders. *Chemical Engineering Science*, 62, 184–194.

Mori, S., Yamamoto, A., Iwata, S., Harahan, T., Yamada, I. 1990. Vibrofluidization of Group C particles and its industrial applications, *AIChE Symposium Series*, 1990, 88–94.

Morse, R.D. 1955. Sonic Energy in Granular Solid Fluidization. *Industrial & Engineering Chemistry Research*, 47, 1170-1175.

Mostoufi, N., Chaouki, J. 2001. Local solid mixing in gas–solid fluidized beds. *Powder Technology*, 114, 23-31.

Mutsers, S.M.P., Reitema, K. 1977a. The effect of inter-particle forces on the expansion of a homogeneous gas-fluidized bed. *Powder Technology*, 18, 239-248.

Mutsers, S.M.P., Reitema, K. 1977b. Gas-solids fluids fluidization in a centrifugal field. The effect of gravity upon bed expansion, *Powder Technology*, 18, 249-256.

Naimer, N. S., Chiba, T., Nienow, A. W. 1982. Parameter estimation for a solids mixing| segregation model for gas fluidised beds. *Chemical Engineering Science*, 37, 1047-1057.

Needham, D. J., Merkin, J. H. 1983. The propagation of a voidage disturbance in a uniformly fluidized bed. *Journal of Fluid Mechanics*, 131, 427-454.

Nguyen, X. T., Leung, L. S., Weiland, R. H., 1973. On void fractions around a bubble in a two-dimensional fluidized bed. *Proceedings of the International Congress on Fluidization and its Applications*, Toulouse (Edited by H. Angelino, J. P. Couderc, H. Gilbert and C. Laguerie), 230-239. Societe de Chemie Industrielle, Paris.

Nguyen, H. V., Whitehead, A. B., Potter, O. E. 1977. Gas backmixing, solids movement, and bubble activities in large scale fluidized beds. *AIChE Journal*, 23, 913.

Nieuwland, J. J., Sint Annaland, M. V., Kuipers, J. A. M., Swaij, W. V. 1996. Hydrodynamic modelling of gas-particle flows in riser reactors. *AIChE Journal*, 42, 1569-1582.

Noda, K., Mawatari, Y., Uchida, S. 1998. Flow patterns of fine particles in a vibrated fluidized bed under atmospheric or reduced pressure. *Powder Technology*, 99, 11-14.

Norouzi, H.R., Mostoufi, N., Mansourpour, Z., Sotudeh-Gharebagh, R., Chaouki, J., 2011. Characterization of solids mixing patterns in bubbling fluidized beds. *Chemical Engineering Research & Design* 89, 817-826.

Ocone, R., Sundaresan, S., Jackson, R., 1993. Gas–particle flow in a duct of arbitrary inclination with particle–particle interactions. *AIChE Journal*, 39, 1261–1271.

Oke, O., Lettieri, P., Solimene, R., Salatino, P., Mazzei, L. 2014. Numerical simulations of lateral solid mixing in gas-fluidized beds. *Chemical Engineering Science*, 120, 117-129.

Bibliography

- Oke, O., Lettieri, P., Mazzei, L. 2015. An investigation on the mechanics of homogeneous expansion in gas-fluidized beds. *Chemical Engineering Science*, 127, 95-105.
- Oke, O., Lettieri, P., Salatino, P., Mazzei, L. 2015. Eulerian modelling of lateral solid mixing in gas-fluidized suspensions, *Procedia Engineering*, 102, 1491 – 1499.
- Oliver, D. R., 1961. The sedimentation of suspensions of closely sized spherical particles. *Chemical Engineering Science*, 15, 230 – 242.
- Ouyang, J., Li, J. 1999. Discrete simulations of heterogeneous structure and dynamic behavior in gas–solid fluidization. *Chemical Engineering Science*, 54, 5427-5440.
- Owoyemi, O., Mazzei, L., Lettieri, P. 2007. CFD modeling of binary-fluidized suspensions and investigation of role of particle-particle drag on mixing and segregation. *AIChE Journal* 53, 1924-1940.
- Özcan, G., Tüzün. U. 2006. Gas Fluidisation of Nano-particle Assemblies: Modified Geldart classification to account for multiple-scale fluidisation of agglomerates and clusters. *KONA Powder and Particle Journal*, 24, 3-14.
- Pallarès, D., Johnsson, F. 2006. A novel technique for particle tracking in cold 2-dimensional fluidized beds—simulating fuel dispersion. *Chemical Engineering Science*, 61, 2710-2720.
- Pallares, D., Diez, P., Johnsson, F. 2007. Experimental Analysis of Fuel Mixing Patterns in a Fluidized bed. 12th International Conference on Fluidization, Vancouver, Canada, 929–936.
- Pallares, D., Johnsson, F. 2008. Modeling of fuel mixing in fluidized bed combustors. *Chemical Engineering Science*, 63, 5663-5671.
- Pan, T. W., Joseph, D. D., Bai, R., Glowinski, R., Sarin, V. 2002. Fluidization of 1204 spheres: simulation and experiments. *Journal of Fluid Mechanics*, 451, 169.
- Partridge, B. A., Rowe, P. N. 1965. Chemical reaction in a bubbling gas-fluidised bed. UK Atomic Energy Authority Research Group.
- Passalacqua, A., Marmo, L., 2009. A critical comparison of frictional stress models applied to the simulation of bubbling fluidized beds. *Chemical Engineering Science* 160, 2795- 2806.
- Patil, D.J., van Sint Annaland, M., Kuipers, J.A.M., 2005a. Critical comparison of hydrodynamic models for gas-solid fluidized beds – part I: bubbling gas-solid fluidized beds operated with a jet. *Chemical Engineering Science*, 60, 57-72.
- Patil, D.J., van Sint Annaland, M., Kuipers, J.A.M., 2005b. Critical comparison of hydrodynamic models for gas-solid fluidized beds – part II: freely bubbling gas-solid fluidized beds. *Chemical Engineering Science*, 60, 73-84.
- Peck, G. C. A., Watkins, S. B. 1956. The flow of fluids through beds of spherical particles. *The Industrial Chemist*, 32, 122-127.
- Peirano, E., Delloume, V., Leckner, B. 2001. Two-or three-dimensional simulations of turbulent gas–solid flows applied to fluidization. *Chemical Engineering Science*, 56, 4787-4799.

Bibliography

- Petersen, I., Werther, J. 2005. Experimental investigation and modeling of gasification of sewage sludge in the circulating fluidized bed. *Chemical Engineering and Processing: Process Intensification*, 44, 717-736.
- Pigford, R., Baron, T. 1965. Hydrodynamic stability of a fluidized bed. *Industrial & Engineering Chemistry Fundamentals*, 4, 81.
- Potter, O. E. 1971. Mixing. In J. F. Davidson & D. Harrison (Eds.), *Fluidization* (p. 293). London: Academic Press.
- Pritchett, J. W., Blake, T. R., Garg, S. K. 1978. A numerical model of gas-fluidized beds. *AIChE Symposium Series*, 176, 134.
- Pyle, D. L., Harrison, D. 1967. The rising velocity of bubbles in two-dimensional fluidised beds. *Chemical Engineering Science*, 22, 531-535.
- Qian, G. H., Pfeffer, R., Shaw, H., Stevens, J. 2001. Fluidization of Group C particles using rotating fluidized beds. *Fluidization X, Engineering Foundation*, 509-516.
- Quintanilla, M. A. S., Valverde, J. M., Castellanos, A., Lepek, D., Pfeffer, R., Dave, R. N. 2008. Nanofluidization as affected by vibration and electrostatic fields. *Chemical Engineering Science*, 63, 5559-5569.
- Reuge, N., Cadoret, L., Coufort-Saudejaud, C., Pannala, S., Syamlal, M., Caussat, B. 2008. Multifluid Eulerian modeling of dense gas–solids fluidized bed hydrodynamics: Influence of the dissipation parameters. *Chemical Engineering Science*, 63, 5540–5551.
- Reuter, H. 1964. On the nature of bubbles in gas and liquid fluidized beds. *Chemical Engineering Progress Symposium Series*, 62, 92-99.
- Riba, J. P., Couderc, J. P. 1977. Expansion de couches fluidisées par des liquides. *Canadian Journal of Chemical Engineering*, 55, 118-121.
- Richardson, J.F., Zaki, W.N., 1954. Sedimentation and Fluidization. *Transactions of the Institution of Chemical Engineers* 32, 35-53.
- Rietema, K. 1967. Application of mechanical stress theory to fluidization. In *Proceedings of International Symposium on Fluidization, Eindhoven*. Netherlands University Press Amsterdam.
- Rietema, K. 1973. The effect of interparticle forces on the expansion of a homogeneous gas-fluidised bed. *Chemical Engineering Science*, 28, 1493-1497.
- Rietema, K., Mutsers, S. M. P. 1973. The effect of interparticle forces on the expansion of a homogeneous gas-fluidised bed. *Proceedings of International Symposium on Fluidization, Toulouse*.
- Rietema, K., Piepers, H. W., 1990. The effect of interparticle forces on the stability of gas-fluidized beds-I. Experimental evidence. *Chemical Engineering Science*, 45, 1627-1639.
- Rietema, K. 1984. Powders, what are they? *Powder Technology*, 37, 5-23.

Bibliography

- Rietema, K. 1991. *The dynamics of fine powders*. Springer Science & Business Media.
- Rhodes, M.J., Zhou, S., Hirama, T., Cheng, H. 1991. Effects of operating conditions on longitudinal solids mixing in a circulating fluidized bed riser. *AIChE Journal*, 37, 1450–1458.
- Rhodes, M.J., Wang, X.S., Nguyen, M., Stewart, P., Liffman, K. 2001. Use of discrete element method simulation in studying fluidization characteristics: influence of interparticle force. *Chemical Engineering Science* 56, 69–76.
- Rong, D.G., Mikami, T., Horio, M. 1999. Particle and bubble movements around tubes immersed in fluidized beds — a numerical study. *Chemical Engineering Science* 54, 5737–5754.
- Rosensweig, R.E. 1979. Fluidization: Hydrodynamic stabilization with a magnetic field. *Science*, 204, 57–60.
- Rowe, P. N. 1965. An X-ray study of bubbles in fluidized beds. *Transactions of the Institution of Chemical Engineers*, 43, T157-T175.
- Rowe, P. N., Partridge, B. A., Cheney, A. G., Henwood, G. A., Lyall, E. 1965. The mechanisms of solids mixing in fluidized beds. *Transactions of the Institution of Chemical Engineers* 43, 211-286.
- Rowe, P. N., Everett, D. J. 1972. Fluidised bed bubbles viewed by X-rays Part II—The transition from two to three dimensions of undisturbed bubbles. *Chemical Engineering Research and Design*, 50, 49–54.
- Rowe, P. N., Widmer, A. J. 1973. Estimation of solids circulation rate in a bubbling fluidised bed. *Chemical Engineering Science*, 28, 979.
- Rowe, P. N., 1987. A convenient empirical equation for estimation of the Richardson & Zaki exponent. *Chemical Engineering Science* 42, 2795.
- Russo, P., Chirone, R., Massimilla, L., Russo, S. 1995. The influence of the frequency of acoustic waves on sound-assisted fluidization of beds of fine particles, *Powder Technology*, 82, 219-230.
- Salam, T. F., Ren, Y., Gibbs, B. M., 1987. Lateral solid and thermal dispersion in fluidized bed combustors. *Proceedings of international Conference on Fluid Bed Combustion*, 9, 541.
- Sanchez-Delgado, S., Almendros-Ibanez, J. A., Garcia-Hernando, N., & Santana, D. 2011. On the minimum fluidization velocity in 2D fluidized beds. *Powder Technology*, 207, 145–153.
- Saxena, S. C., Vadivel, R. 1988. Wall effects in gas-fluidized beds at incipient fluidization. *The Chemical Engineering Journal*, 39, 133–137.
- Schaeffer, D.G., 1987. Instability in evolutions describing incompressible granular flow. *Journal of Differential Equations* 66, 19-50.
- Schiller, L., Naumann, A. 1935. A drag coefficient correlation. *Vdi Zeitung*, 77(318), 51.

Bibliography

- Schlichthaerle, P., Werther, J. 2001. Solids mixing in the bottom zone of a circulating fluidized bed. *Powder Technology*, 120, 21-33.
- Savage, S. B. 1982. Granular flows down rough inclines – review and extension. In *Proc. of U.S. – Japan Seminar on New Models and Constitutive Relations in the Mechanics of Granular Materials*. Jenkins J. T. & Satake M. Eds. Elsevier.
- Seville, J. P. K., Willett, C. D., Knight, P. C. 2000. Interparticle forces in fluidisation: a review. *Powder Technology*, 113, 261-268.
- Shabanian, J., Jafari, R., Chaouki, J. 2012. Fluidization of ultrafine powders. *International Review of Chemical Engineering*, 4, 2035 – 1755.
- Shen, L., Zhang, M., Xu, Y. 1995. Solids mixing in fluidized beds. *Powder Technology*, 84, 207–212.
- Shen, L., Zhang, M. 1998. Effect of particle size on solids mixing in bubbling fluidized beds. *Powder technology*, 97, 170-177.
- Shi, Y. F., Fan, L. T. 1984. Lateral mixing of solids in batch gas-solids fluidized beds. *Industrial & Engineering Chemistry Process Design and Development*, 23, 337-341.
- Simpson H. C., Rodger, B. W. 1961. The fluidization of light solids by gases under pressure and heavy solids by water. *Chemical Engineering Science*, 16, 153 - 180.
- Sitnai, O. 1981. Solids mixing in a fluidized bed with horizontal tubes. *Industrial and Engineering Chemistry Process Design and Development*, 20, 533-538.
- Sitnai, O., Whitehead, A.B. 1985. Immersed tubes and other internals in Fluidization, Davidson, J.F., Clift, R., & Harrison, D. (eds). (Academic Press, London, UK).
- Song, L., Zhou, T., Yang, J. 2009. Fluidization behaviour of nanoparticles by adding coarse particles. *Advanced Powder Technology*, 20, 366-370.
- Srivastava, A., Sundaresan, S. 2002. Role of wall friction in fluidization and standpipe flow. *Powder Technology*, 124, 45-54.
- Srivastava, A., Sundaresan, S., 2003. Analysis of a frictional–kinetic model for gas–particle flow. *Powder Technology* 129, 72–85
- Steinour, H. H. 1944b. Rate of sedimentation—suspensions of uniform-size angular particles. *Industrial Engineering Chemistry*, 36, 840 – 847.
- Subbarao, D., Basu, P. 1986. A model for heat transfer in circulating fluidized beds. *International journal of heat and mass transfer*, 29, 487-489.
- Sun, J., Battaglia, F. 2006. Hydrodynamic modelling of particle rotation for segregation in bubbling gas-fluidized beds. *Chemical Engineering Science*, 61, 1470.
- Sun, J., Battaglia, F., Subramaniam, S. 2007. Hybrid two-fluid DEM simulation of gas-solid fluidized beds. *Journal of Fluids Engineering*, 129, 1394-1403.

Bibliography

- Sundaresan, S. 2003. Instabilities in fluidized beds. *Annual review of fluid mechanics*, 35, 63-88.
- Syamlal, M., Rogers, W.A., O'Brien, T.J. MFIx Documentation and Theory Guide, DOE/METC94/1004, NTIS/DE94000087, Electronically available from: <http://www.mfix.org>, 1993.
- Syamlal, M. 1987. The particle-particle drag term in a multiparticle model of fluidization (No. DOE/MC/21353-2373). EG and G Washington Analytical Services Center, Inc., Morgantown, WV (USA).
- Tailby, S. R., Cocquerel, M. A. T. 1961. Some studies of solids mixing in fluidized beds. *Transactions of the Institution of Chemical Engineers*, 39, 195.
- Talmor, E., Benenati, R. F. 1963. Solids mixing and circulation in gas-fluidized beds. *AIChE Journal*, 9, 536-540.
- Tasirin, S. M., Anuar, N. 2001. Fluidization Behaviour of Vibrated and Aerated Beds of Starch Powders. *Chemical Engineering Journal*, 34, 1251 – 1258.
- Tian, F., Zhang, M., Fan, H., Gu, M., Wang, L., Qi, Y. 2007. Numerical studies on microscopic mixing characteristics in fluidized beds via DEM. *Fuel Processing Technology*, 88, 187 – 198.
- Toomey, R. D., Johnstone, H. F., 1952. Gaseous fluidization of solid particles. *Chemical Engineering Progress* 48, 220-226.
- Tong, H., Qiu, O., Li, H. 2004. Fluidization Characteristics of Ultrafine Particles in Conical Bed. *Fluidization IX*, Engineering Foundation, 715-722.
- Trupp, A. C. 1968. Dynamics of liquid fluidised beds of spheres. *International Chemical Engineering Symposium Series*, 30, 182 – 189.
- Tsinontides, S.C., Jackson, R. 1993. The mechanics of gas-fluidized beds with an interval of stable fluidization, *Journal of Fluid Mechanics*, 255, 237-274.
- Tsuji, Y., Tanaka, T., Ishida, T. 1992. Lagrangian numerical-simulation of plug flow of cohesionless particles in a horizontal pipe. *Powder Technology*, 71, 239–250.
- Tsuji, Y., Kawaguchi, T., Tanaka, T. 1993. Discrete particle simulation of two-dimensional fluidized bed. *Powder technology*, 77, 79-87.
- Tsuo, Y. P., Gidaspow, D. 1990. Computation of flow patterns in circulating fluidized beds. *AIChE Journal*, 36, 885-896.
- Tsutsui, T., Miyauchi, T. 1979. Fluidity and its influence on behaviour in a fluidized bed with fine particles, *Kagaku Kogaku Ronbunshu*, 5, 40 – 46.
- Valenzuela, J. A., Glicksman, L. R. 1984. An experimental study of solids mixing in a freely bubbling two-dimensional fluidized bed. *Powder technology*, 38, 63-72
- Valverde, J. M., Ramos, A., Castellanos, A., Watson, P. K. 1998. The tensile strength of cohesive powders and its relationship to consolidation, free volume and cohesivity. *Powder Technology*, 97, 237 – 245.

Bibliography

- Valverde, J. M., Quintanilla, M. A. S., Castellanos, A., Mills, P. 2001. The settling of fine cohesive powders. *Europhysics Letters*, 54, 329.
- Valverde, J.M., Quintanilla, M.A.S., Castellanos, A., Mills, P. 2003. Experimental study on the dynamics of gas-fluidized beds. *Physical Review Letter*, 67, 016303.
- Valverde, J. M., Castellanos, A. 2006. Effect of vibration on agglomerate particulate fluidization. *AIChE Journal*, 52, 1705-1714.
- Valverde, J. M., Quintanilla, M. A. S., Espin, M. J., Castellanos, A. 2008. Nanofluidization electrostatics. *Phys. Review*, E 77, 031301.
- Van Deemter, J. J. 1967. The counter-current flow model of a gas-solids fluidized bed. In *Proceedings of the International Symposium on Fluidization*. Netherlands University Press.
- Van der Hoef, M. A., Ye, M., van Sint Annaland, M., Andrews, A. T., Sundaresan, S., Kuipers, J. A. M. 2006. Multiscale modeling of gas-fluidized beds. *Advances in chemical engineering*, 31, 65-149.
- Van Wachem, B. G. M., Almstedt, A. 2003. Methods for multiphase computational fluid dynamics. *Chemical Engineering Journal*. 96, 81-98.
- Van Wachem, B. G. M., Yu. X., Hsu, T. 2010. A 3D Eulerian-Lagrangian numerical model for sediment transport. 7th International Conference on Multiphase Flow. ICMF. Vol. 2010.
- Van Wachem, B.G.M., Zastawny, M., Zhao, F., Mallouppas, G. 2015. Modelling of gas-solid turbulent channel flow with non-spherical particles with large stokes numbers. *International Journal of Multiphase Flow*, 68, 80 – 92.
- Venkatesh, R. D., Chaouki, J., Klvana, D. 1996. Fluidization of cryogels in a conical column. *Powder Technology*, 89, 179-186.
- Verloop, J., Heertjes, P. M. 1970. Shock waves as a criterion for the transition from homogeneous to heterogeneous fluidization. *Chemical Engineering Science*, 25, 825.
- Visser, J. 1989. Van der Waals and other cohesive forces affecting powder fluidization. *Powder Technology*, 58, 1-10.
- Volpicelli, G., Massimilla, L. Zenz, F. A. 1966. Nonhomogeneities in solid-liquid fluidization. *Chemical Engineering Progress Symposium Series*, 62, 42-50.
- Vu-Quoc, L., Zhang, X. 1999. An elastoplastic contact force-displacement model in the normal direction: Displacement-driven version. *Proceedings of the Royal Society of London, Series A—Mathematical Physical and Engineering Sciences*, 455(1991), 4013–4044.
- Wallis, G. B. 1962. *One-dimensional Waves in Two-component Flow: With Particular Reference to the Stability of Fluidised Beds* Reactor Development Division, Atomic Energy Establishment, 162.
- Wallis, G .B. 1969. *One-dimensional two-phase flow*. McGraw-Hill.

Bibliography

- Walton, O. R., Braun, R. L. 1986. Viscosity, granular-temperature, and stress calculations for shearing assemblies of inelastic, frictional disks. *Journal of Rheology*, 30, 949–980.
- Wang, C., Bouillard, J. X. 1993. Hydrodynamics/heat-transfer/erosion computer predictions for a cold small-scale CFBC. In *Circulating Fluidized Bed Technology IV*, 359-366.
- Wang, H., Zhou, T., Yang, J. S., Wang, J. J., Kage, H., Mawatari, Y. 2010. Model for Calculation of Agglomerate Sizes of Nanoparticles in a Vibro-fluidized Bed. *Chemical Engineering Technology*, 33, 388-394.
- Wank, J. R., George, S. M., Weimer, A. W. 2001. Vibro-fluidization of fine boron nitride powder at low pressure, *Powder Technology*, 121, 195-204.
- Watson, P.K., Valverde, J.M., Castellanos, A., 2001. The tensile strength and free volume of cohesive powders compressed by gas flow. *Powder Technology* 115, 45 – 50.
- Wen, C. Y., Yu, Y. H. 1966. A generalized method for predicting the minimum fluidization velocity. *AIChE Journal*, 12, 610–612.
- Wilhelm, R. H., Kwauk, M. 1948. Fluidization of solid particles. *Chemical Engineering Progress*, 44, 201.
- Winaya, I. N. S., Shimizu, T., Yamada, D. 2007. A new method to evaluate horizontal solid dispersion coefficient in a bubbling fluidized bed. *Powder Technology*, 178, 173–178.
- Wischnewski, R., Ratschow, L., Hartge, E. U., Werther, J. 2010. Reactive gas–solids flows in large volumes—3D modeling of industrial circulating fluidized bed combustors. *Particuology*, 8, 67-77.
- Xiao, P., Yan, G., Wang, D. 1998. Investigation on horizontal mixing of particles in dense bed in circulating fluidized beds (CFB). *Journal of Thermal Science*, 7, 78
- Xiang, Q., Huang, G., Ni, M., Cen, K., Tao, T., 1987. Lateral dispersion of large coal particles in an industrial-scale fluidized. *Proceedings of International Conference on Fluid Bed Combustion*, 9, 546.
- Xie, N., Battaglia, F., Pannala, S. 2008. Effects of using two-versus three-dimensional computational modelling of fluidized beds: part I, hydrodynamics. *Powder Technology*, 182, 1-13.
- Xie, N., Battaglia, F., Pannala, S. 2008. Effects of using two- versus three-dimensional computational modeling of fluidized beds: part II, budget analysis, *Powder Technology*, 182,14–24.
- Xu, B. H., Yu, A. B. 1997. Numerical simulation of the gas-solid flow in a fluidized bed by combining discrete particle method with computational fluid dynamics. *Chemical Engineering Science*, 52, 2785–2809.
- Xu, C., Cheng, Y., Zhu, J. 2004. Fine particle fluidization-effects of mechanical/acoustic vibration. *Fluidization XI*, 627–634.

Bibliography

- Yamazaki, R., Ueda, N., Jimbo, G. 1986. Mechanism of incipient fluidization in fluidized bed at elevated temperature. *Journal of chemical engineering of Japan*, 19, 251-257.
- Yang, W. C. 2005. Fluidization of fine cohesive powders and nanoparticles-a review. *Journal of Chinese Institute of Chemical Engineers*, 36, 1– 15.
- Yates, Y. G., Cheesman, D. J., & Sergeev, Y. A. (1994). Experimental observations of voidage distribution around bubbles in a fluidized bed. *Chemical engineering science*, 49(12), 1885-1895.
- Ye, M., van der Hoef, M.A., Kuipers, J.A.M. 2005. The effects of particle and gas properties on the fluidization of Geldart a particles. *Chemical Engineering Science*, 60, 4567 – 4580.
- Zhang, W., Zhao, M. 2010. Fluidisation behaviour of silica nanoparticles under horizontal vibration, *Journal of Experimental Nanoscience*, 5, 69-82.
- Zhou, T., Li, H. 1999. Effects of adding different size particles on fluidization of cohesive particles, *Powder Technology*, 102, 215-220.
- Zhou, H., Flamant, G., Gauthier D., Flitris, Y. 2003. Simulation of coal combustion in a bubbling fluidized bed by distinct element method. *Chemical Engineering Research and Design*, 81, 1144.
- Zhou, H., Flamant, G., Gauthier, D., Lu, J. 2004. Numerical simulation of the turbulent gas–particle flow in a fluidized bed by an LES-DPM model. *Chemical Engineering Research and Design*, 82, 918–926.
- Zhu, Q. S., Li, H.Z. 1994. Fluidization of group C powder with external magnetic force. *Fifth China-Japan Symposium on Fluidization*, Nagoya, Japan.
- Zhu, Q. Li, H. 1996. Study on magnetic fluidization of group C powders. *Powder Technology*, 86, 179-185.
- Zhu, R. R., Zhu, W. B., Xing, L. C., Sun, Q. Q. 2011. DEM simulation on particle mixing in dry and wet particles spouted bed. *Powder Technology*, 210, 73 – 81.

Publications

Refereed journal publications

1. Oke, O., van Wachem, B.G.M., Mazzei, L. 2016. Lateral solid mixing in gas-fluidized beds: computational fluid dynamics (CFD) and discrete element method (DEM) studies. *Chemical Engineering Research and Design*. Submitted for publication.
2. Oke, O., Lettieri, P., Salatino, P., Mazzei, L. 2015. Eulerian modelling of lateral solid mixing in gas-fluidized suspensions, *Procedia Engineering*, 102, 1491 – 1499.
3. Oke, O., Lettieri, P., Mazzei, L. 2015. An investigation on the mechanics of homogeneous expansion in gas-fluidized beds. *Chemical Engineering Science*, 127, 95-105.
4. Oke, O., Lettieri, P., Solimene, R., Salatino, P., Mazzei, L. 2014. Numerical simulations of lateral solid mixing in gas-fluidized bed. *Chemical Engineering Science*, 120, 117-129.

Refereed conference publications

1. Oke, O., Lettieri, P., Mazzei, L. 2015. 2D and 3D CFD simulations of lateral solid mixing in gas-fluidized beds. Submitted for oral presentation at the *15th International conference on fluidization, Quebec, Canada*.
2. Oke, O., Lettieri, P., Salatino, P., Mazzei, L. 2014. CFD simulations of lateral solid mixing in fluidized beds. *Proceedings of the 11th international conference on fluidized bed technology*, Beijing, China, 287-292.
3. Oke, O., Lettieri, P., Salatino, P., Mazzei, L. 2014. Eulerian modelling of lateral solid mixing in gas-fluidized fluidized suspensions. *Proceedings of the 7th World Congress on Particle Technology*, Beijing, China.
4. Oke, O., Mazzei, L. and Lettieri, P. 2014. Theoretical and experimental Investigation of the Behavior of Cohesive Homogeneous Gas-Fluidized Beds. *13th International Conference on Multiphase Flow in Industrial Plant*, Genova, Italy.

Publications

5. Oke, O., Lettieri, P., Salatino, P., Mazzei, L. 2014. CFD simulations of lateral solid mixing in gas-fluidized beds. ChemengDay 2014, Manchester, United Kingdom.
6. Oke, O., Mazzei, L. and Lettieri, P. 2013. Theoretical Investigation of the Behavior of Cohesive Homogeneous Gas-Fluidized Beds. *Proceedings of the 14th international conference on fluidization – From Fundamentals to Products*, Eds, ECI Symposium Series, Volume (2013).